
Influence of Coulomb interaction and spatial inhomogeneities on two-dimensional materials

Christina Steinke



Influence of Coulomb interaction and spatial inhomogeneities on two-dimensional materials

Dissertation
zur Erlangung des akademischen Grades

**Doktor der Naturwissenschaften
(Dr. rer. nat.)**

am Fachbereich Physik und Elektrotechnik
der Universität Bremen

vorgelegt von
Christina Steinke
aus Bremen

Erstgutachter:

Prof. Dr. Tim Wehling

Zweitgutachter:

Prof. Dr. Gerd Czycholl

Datum des Kolloquiums:

26. April 2019

Bremen, 7. März 2019

Abstract

Nowadays a large variety of two-dimensional (2d) materials ranging from (functionalized) graphene, graphene analogues like hexagonal boron nitride to metallic, semiconducting or superconducting transition metal dichalcogenides are studied theoretically and experimentally. Their remarkable material features, resulting from the unique two-dimensional physics, as well as flexibility in tuning of their properties made them interesting for various applications. For example regarding electronic devices novel kinds of heterostructures were created with the possibility for on demand tailoring through the stacking of different layered materials.

Coulomb interaction effects play a major role in characterizing 2d materials. Due to the low dimensionality of the systems, the interaction effects are enhanced and highly sensitive to external screening. In this thesis we make use of these peculiar interaction effects to create lateral heterojunctions within otherwise *homogeneous* monolayers through the external manipulation of the Coulomb interaction. Therefore we study the band gap modulation in semiconducting transition metal dichalcogenides placed on laterally structured substrates and show spatially sharp band gap transitions on the order of a few unit cells. Contrary to other kinds of heterostructures, the proposed mechanism is non-invasive leaving the active material of the heterojunction untouched. With respect to optical properties we study the response of the exciton to tuning of the Coulomb interaction and find that the lowest energy excited state is nearly unaffected by dielectric environments. However, higher energy excitations can be strongly manipulated.

For the construction of optimal tailor-made devices a comprehensive understanding of the underlying Coulomb interaction effects is necessary. However, interaction effects are often not well understood and can be difficult to describe. To this end we utilize models based on ab-initio calculations which include the main features of the investigated materials and suitable descriptions of the screening effects.

To find optimal candidates for these kind of heterostructures we compare the effect of external dielectric environments on different semiconducting transition metal dichalcogenides. All materials under investigation show the same relative changes in the band gap for increasing dielectric screening rendering this class of materials equally suitable for further applications.

Not only the dielectric but also the chemical environment, e.g. different gaseous atmospheres, can alter the material properties of a 2d material. Finally we investigate the influence of O₂ adsorption on (doped) monolayer MoS₂ as a promising candidate for sensing applications.

Contents

1. Introduction	1
2. Theory and Methods	3
2.1. Many-body theory	3
2.1.1. Many-body Hamiltonian	3
2.1.2. Tight-binding model	6
2.1.3. Maximally localized Wannier functions	9
2.2. Density Functional Theory	13
2.2.1. Hohenberg and Kohn Theorems	14
2.2.2. Kohn-Sham equations	16
2.2.3. Exchange-correlation potential	19
2.2.4. Plane wave basis and Pseudopotentials	20
2.3. Coulomb interaction and screening	23
2.3.1. Screening in classical electrodynamics	23
2.3.2. Random phase approximation	26
2.3.3. Constrained random phase approximation	29
2.4. Many-Body Perturbation Theory	31
2.4.1. Green's functions	32
2.4.2. Hedin's equations	37
2.4.3. GW approximation	38
2.5. Excitons	41
2.5.1. Wannier equation	43
3. Transition Metal Dichalcogenides	47
3.1. Material properties	47
3.1.1. Lattice structure	48
3.1.2. Electronic properties	50
3.1.3. Optical properties	51
3.2. Coulomb interaction in 2d materials	53
3.2.1. Coulomb engineering: Tuning the band gap	55
3.3. Minimal tight-binding model	56
4. 2D Heterojunctions from Non-local Manipulations of the Interactions	59
4.1. Introduction	59
4.2. Real space extent of the self-energy	61

4.3.	Heterostructures induced by heterogeneous dielectric environments . .	63
4.3.1.	Minimal semiconductor tight-binding model for MoS ₂	63
4.3.2.	Including the Coulomb interaction	65
4.3.3.	Local density of states for heterostructure induced by laterally structured environment	66
4.3.4.	Length scale over which band-gap variations can be realized .	67
4.4.	Conclusions	69
5.	Non-invasive control of excitons	71
5.1.	Introduction	71
5.2.	Methods	73
5.2.1.	Modelling spatially resolved optical properties	73
5.2.2.	Tight-binding models for 2d semiconductors	74
5.3.	Results	75
5.3.1.	Monolayer of a semiconductor embedded in homogeneous dielectric environment	75
5.3.2.	Response of lowest-energy exciton to dielectric screening . . .	77
5.3.3.	Excitonic properties of a semiconductor monolayer embedded in laterally structured environment	79
5.4.	Conclusions	81
6.	Material realistic description of Coulomb engineered heterostructures	83
6.1.	Full ab-initio description of Coulomb engineered heterostructures . .	84
6.1.1.	Monolayer MoS ₂ in laterally structured dielectrics	84
6.2.	Material realistic modeling	85
6.2.1.	The G Δ W approach	86
6.2.2.	Modeling the Coulomb interaction	89
6.2.3.	Influence of dielectric substrates on TMDCs	91
6.2.4.	Length scale of self-energy	93
6.2.5.	Coulomb engineered heterostructures	94
6.3.	Conclusions	95
7.	Effects of the Fermi Level Energy on the Adsorption of O₂ to Monolayer MoS₂	97
7.1.	Introduction	97
7.2.	Methods	98
7.3.	Electronic states of MoS ₂ upon adsorption of O ₂	99
7.4.	Measurements of photoluminescence and conductivity	100
7.5.	Conclusion	103
8.	Conclusions	105

A. Appendix	107
A.1. Transition Metal Dichalcogenides	107
A.1.1. Lattice parameter and band structures of TMDCs	107
A.2. 2D Heterojunctions from Non-local Manipulations of the Interactions	109
A.2.1. Computational details	109
A.2.2. Tight-binding model parameter	109
A.2.3. Treating the Coulomb interaction	109
A.2.4. Screening model	111
A.2.5. Calculation of the local density of states	112
A.2.6. Hartree and Fock contributions to the band gap	113
A.2.7. Heterogeneous substrate	113
A.3. Non-invasive control of excitons	115
A.3.1. Electron-Hole Hamiltonian	115
A.3.2. Dipole matrix elements	116
A.3.3. Many-body eigenstates	117
A.3.4. Semiconductor tight-binding models	117
A.3.5. Bohr radius	118
A.3.6. Local density of states for heterostructure	118
A.4. Material realistic description of Coulomb engineered heterostructures	121
A.4.1. Computational details for ab-initio description of heterostructure	121
A.4.2. Calculation details for homogeneous monolayer TMDCs	121
A.4.3. G_0W_0 convergence	122
A.4.4. Fit parameter and band gaps for investigated TMDCs	122
A.4.5. $G\Delta W$ convergence	123
A.4.6. GW self-energy	124
A.4.7. Finding the characteristic length of the interface	125
A.4.8. Substrate dielectric constants	125
A.5. Effects of the Fermi Level Energy on the Adsorption of O_2 to Monolayer MoS_2	127
A.5.1. Band structure of MoS_2 in absence/presence of O_2	127
Bibliography	129
List of publications	157
Conference contributions	159
Acknowledgements	161

1. Introduction

Semiconductors play a major role in modern optoelectronics. Especially heterojunctions, i.e. materials which show a band gap transition between different regions, are building blocks of electronic and information technology and are used for example in transistors, diodes and solar cells. The industrial standard nowadays is Silicon based technology utilizing p-n-junctions with different doping regimes [1]. Additionally heterostructures, which are interfaces of materials with different band gaps, are widely used in various applications [2, 3].

The rising interest in the field of two-dimensional (2d) materials, starting with the first isolation of graphene [4], has opened new ways for building and investigating heterostructures. Nowadays a large variety of atomically thin materials besides graphene are studied. 2d materials inherit great potential not only for understanding fundamental physics but also for the application in (opto-)electronic devices [5] as they offer a great flexibility in tuning their electronic properties [6]. For the creation of heterostructures they provide a large variety of possible materials in addition to bulk crystals. Atomically thin 2d materials [7] including semiconducting transition metal dichalcogenides (TMDCs) have been assembled into structures like lateral [8–11] or vertical [12–18] heterojunctions. In those so-called van-der-Waals heterostructures different materials can be stacked on top of each other connected with weak interlayer interactions. In contrast to conventional epitaxially grown heterostructures, their lattices do not need to match yielding numerous possible material combinations.

We will propose a third unique way to create band gap modulations within a 2d material based on the peculiar 2d Coulomb interaction. The screening in 2d systems is reduced leading to enhanced interaction effects. Changes in the environment of 2d materials result in different screening which directly influences the interaction. This renormalizes the band gap [19–21] and thus opens up the possibility to engineer the properties non-invasively. Although Coulomb interaction effects play a major role in determining material properties of 2d materials they are often not well understood and by far not easy to describe. However, to find optimal tailor-made devices a comprehensive understanding of these effects is needed.

The scope of this work is to investigate how manipulating the Coulomb interaction can alter the material properties of widely studied semiconducting 2d TMDC and how this can be used for applications, e.g. for heterojunctions. We give the first description [22] of a heterojunction induced in a homogeneous monolayer by a laterally structured environment and discuss the peculiar optical properties of such a

system. Additionally we study which semiconducting TMDC MX_2 with $\text{M} \in \{\text{Mo}, \text{W}\}$ and $\text{X} \in \{\text{S}, \text{Se}\}$ is the optimal candidate for future devices.

Since treating the full Coulomb interaction of a many-body system is an arbitrarily difficult task, we will turn to models based on ab-initio calculations which include the main features of the investigated materials and appropriate descriptions of the screening effects. The ab-initio calculations utilize many-body perturbation theory on top of density functional theory. To describe the self-energy, which includes the important Coulomb induced interaction effects we will use the Hartree-Fock and *GW* approximation.

In Chapter 2 we give an overview of the theoretical concepts and methods used in this work. Therefore, we present the many-body Hamiltonian and describe the methods used to solve the non-interacting problem, like the tight-binding approach, and the interacting problem like density functional theory and many-body perturbation theory. Moreover, we shortly explain the concept of excitons as they strongly influence the optical properties of a material.

Chapter 3 introduces TMDCs, showing the lattice structure of the investigated materials as well as basic electronic and optical properties. Furthermore, we discuss Coulomb interaction in 2d materials and explain the idea of Coulomb engineering in which the band gap is manipulated through dielectric environments. At last we derive the model on which all following chapters are based on.

In Chapter 4 we follow the idea of a Coulomb engineered heterostructure and show that a spatially structured environments induces a heterojunction like band gap modulation in an otherwise homogeneous monolayer. Therefore, we turn to a minimal tight-binding description including the inhomogeneous environment through a model screening function in Hartree-Fock approximation. The optical properties of such a system are investigated in Chapter 5 exhibiting interesting potential energy landscapes, where higher energy states are trapped but lower energy states move almost freely or are even expelled from the trapping regions.

At last we turn to a material realistic description of Coulomb engineered heterostructures in Chapter 6. We investigate which of the semiconducting TMDCs under investigation are most sensitive to external manipulation of the band gap. Due to the long-ranged Coulomb interaction there will be an interface region between the regions with different band gaps. We will discuss the *intrinsic* length scale of this interface and show that still sharp band gap modulations can be realized.

Not only manipulation of the Coulomb interaction alters the material properties of a 2d material. They are also sensitive to changes in their *chemical* environment, e.g. molecular adsorbates, rendering them interesting for gas sensors. We study the possible application of MoS_2 in such gas sensing devices in Chapter 7. For that reason we show ab-initio calculations for O_2 adsorbed on doped monolayer MoS_2 to support experimental analysis of monolayer MoS_2 field effect transistors exposed to oxygen.

2. Theory and Methods

In the following chapter a brief introduction to the used theoretical framework for the calculations in this work is given. Thereby we start with a short introduction into many-body physics in Section 2.1 recalling the tight-binding method to solve the non-interacting many-body Hamiltonian. Afterwards we introduce Density Functional Theory in Section 2.2 as a first approach to describe ground-state properties of interacting electrons. In Section 2.3 we show approximations to treat the full Coulomb interaction which are needed for a more sophisticated ab-initio description of interacting electrons within Many-Body-Perturbation-Theory as described in Section 2.4. Lastly, we shortly discuss the electron-hole excitations, namely excitons in Section 2.5.

This chapter shall only give a brief overview of the used methods. Further details can be found in many textbooks and reviews. The main references used for the descriptions in this work are given at the beginning of every chapter. The interested reader is referred to the books by Czycholl [23], Martin [24, 25], Mahan [26] and Bruus and Flensberg [27] to name just a few examples for further insights into many-body theory.

2.1. Many-body theory

2.1.1. Many-body Hamiltonian

The following introduction to the many-body Hamiltonian is based on the corresponding chapter in the book by Czycholl [23]. Similar discussions can be found in a variety of textbooks dealing with condensed matter physics like Refs. [26–28].

For the quantum mechanical description of any system the time-dependent Schrödinger's equations

$$H |\Psi(t)\rangle = i\hbar\partial_t |\Psi(t)\rangle \quad (2.1.1)$$

has to be solved, in which the Hamiltonian H incorporates all relevant energy terms for the problem at hand. In this work H is always a many-body Hamiltonian describing the investigated material system and $|\Psi(t)\rangle$ the corresponding many-body wave function. For a time independent problem the time evolution of $|\Psi(t)\rangle$ is given by

$$|\Psi(t)\rangle = |\psi\rangle e^{-i\frac{E}{\hbar}t}. \quad (2.1.2)$$

This simplifies Eq. (2.1.1) to the stationary Schrödinger's equation

$$H|\psi\rangle = E|\psi\rangle \quad (2.1.3)$$

for the stationary wave function $|\psi\rangle$ and the eigenenergy E .

Without considering relativistic effects and (time-dependent) external fields we can write the Hamiltonian for a system of interacting electrons and nuclei as

$$H = T_{\text{nuc}} + T_e + V_{\text{nuc-nuc}} + V_{\text{e-e}} + V_{\text{e-nuc}}, \quad (2.1.4)$$

where the operators T_{nuc} and T_e describe the kinetic energy of the nuclei and electron, respectively. The pairwise interaction between the particles are given by $V_{\text{nuc-nuc}}$ (nuclei-nuclei interaction), $V_{\text{e-e}}$ (electron-electron interaction) and $V_{\text{e-nuc}}$ (electron-nuclei interaction). For N_e electrons with mass m_e and charge $-e$ at the position \mathbf{r}_i and N_{nuc} nuclei with mass M_I and charge $Z_I e$ at the position \mathbf{R}_I , Eq. (2.1.4) can be explicitly written as

$$H = \underbrace{-\sum_i^{N_e} \frac{\hbar^2}{2m_e} \Delta_i}_{T_e} - \underbrace{\sum_I^{N_{\text{nuc}}} \frac{\hbar^2}{2M_I} \Delta_I}_{T_{\text{nuc}}} + \underbrace{\frac{1}{2} \sum_{I \neq J}^{N_{\text{nuc}}} \frac{Z_I Z_J e^2}{|\mathbf{R}_I - \mathbf{R}_J|}}_{V_{\text{nuc-nuc}}} + \underbrace{\frac{1}{2} \sum_{i \neq j}^{N_e} \frac{e^2}{|\mathbf{r}_i - \mathbf{r}_j|}}_{V_{\text{e-e}}} - \underbrace{\sum_I^{N_{\text{nuc}}} \sum_i^{N_e} \frac{Z_I e^2}{|\mathbf{r}_i - \mathbf{R}_I|}}_{V_{\text{e-nuc}}} \quad (2.1.5)$$

where we used the electron momenta $p_i = -i\hbar\nabla_i$ and nuclei momenta $P_I = -i\hbar\nabla_I$. To get the full many-body wave functions and energies for a solid state, Eq. (2.1.4) has to be solved for approximately 10^{23} particles. This is a highly complex problem which needs the application of various approximations.

One of the most fundamental approximations is the adiabatic *Born-Oppenheimer-approximation* [29] in which the nuclei and electron dynamics are decoupled. This is based on the assumption that the light electrons move much faster than the much heavier atomic cores and thus can follow the motion of the nuclei instantaneously. As a result the electronic and the lattice wave functions can be treated separately and the complete wave function is written as $|\Psi\rangle = |\Psi_e\rangle \otimes |\Psi_{\text{nuc}}\rangle$ with the electron wave function $|\Psi_e\rangle$ and the atomic wave function $|\Psi_{\text{nuc}}\rangle$.

In Born-Oppenheimer approximation the atomic positions $\{\mathbf{R}_I\}$ appear in the electronic problem only as stationary parameters and the electronic part of the Hamiltonian is written as

$$H_{\text{el}} = - \sum_i^{N_e} \frac{\hbar^2}{2m} \Delta_i + \sum_i^{N_e} V(\mathbf{r}_i) + \frac{1}{2} \sum_{i \neq j}^{N_e} \frac{e^2}{|\mathbf{r}_i - \mathbf{r}_j|}, \quad (2.1.6)$$

in which the electrons move within a translational invariant static potential of the atoms

$$V(\mathbf{r}_i) = \sum_I^{N_{\text{nuc}}} \frac{Z_I e^2}{|\mathbf{r}_i - \mathbf{R}_I|}. \quad (2.1.7)$$

As we are mainly interested in the electronic properties in this thesis, we will only consider the electronic part H_{el} of the Hamiltonian when discussing H and thus will often drop the subscript. The Born-Oppenheimer-approximation reduces the complexity of the full problem, nevertheless H_{el} is still not solvable due to the electron-electron interaction. Further approximations have to be made to calculate energy spectra from Eq. (2.1.6) which we will introduce in the following chapters.

Even though we will always treat systems with interacting electrons it is still useful to discuss the non-interacting part of H_{el} , the so called *single-particle operator*

$$H_0 = - \sum_i^{N_e} \frac{\hbar^2}{2m} \Delta_i + \sum_i^{N_e} V(\mathbf{r}_i), \quad (2.1.8)$$

which is a sum of operators describing single electrons. Thus for every particle the *single-particle Schrödinger's equation* can be solved separately

$$\left(-\frac{\hbar^2}{2m} \Delta_i + V(\mathbf{r}_i) \right) \psi_n(\mathbf{r}_i) = E_n^0 \psi_n(\mathbf{r}_i). \quad (2.1.9)$$

Then the eigenfunction of H_0 is the antisymmetric product of the single-particle states $\psi_n(\mathbf{r}_i)$. Due to the translation invariance of the lattice, these single-particle states have to obey the *Bloch theorem* [30]

$$\psi_n(\mathbf{r}_i + \mathbf{R}_j) = e^{i\mathbf{k} \cdot \mathbf{R}_j} \psi_n(\mathbf{r}_i), \quad (2.1.10)$$

where \mathbf{R}_j is a lattice vector and \mathbf{k} a wave vector of the first Brillouin zone. Consequently $\psi_n(\mathbf{r}_i)$ can be written as *Bloch functions*

$$\psi_{n\mathbf{k}}(\mathbf{r}_i) = \frac{1}{\sqrt{V}} e^{i\mathbf{k} \cdot \mathbf{R}_j} u_{n\mathbf{k}}(\mathbf{r}_i) \quad (2.1.11)$$

with a lattice periodic function $u_{n\mathbf{k}}(\mathbf{r})$ meaning the eigenfunctions of the single-particle Hamiltonian are plane waves with wave vector \mathbf{k} modulated with $u_{n\mathbf{k}}(\mathbf{r})$.

In solid-state physics a convenient way to write Hamiltonians is the use of *second quantization* or occupation number representation. In this representation the Hamiltonian (2.1.6) can be written as

$$H = \underbrace{\sum_{k_1 k_2} \varepsilon_{k_1 k_2} c_{k_1}^\dagger c_{k_2}}_{H_0} + \frac{1}{2} \sum_{k_1 k_2 k_3 k_4} U_{k_1 k_2 k_3 k_4} c_{k_1}^\dagger c_{k_2}^\dagger c_{k_3} c_{k_4}. \quad (2.1.12)$$

The operators $c_{k_i}^{(\dagger)}$ annihilate (create) a fermion within the single-particle state $|k_i\rangle$. The single-particle operator matrix elements

$$\varepsilon_{k_1 k_2} = \langle k_1 | H_0 | k_2 \rangle = \int d^3 r \varphi_{k_1}^*(\mathbf{r}) H_0(\mathbf{r}) \varphi_{k_2}(\mathbf{r}) \quad (2.1.13)$$

include the kinetic energy T_e and the effective potential $V(\mathbf{r})$ of the atomic cores. The matrix elements of the two-particle operator

$$\begin{aligned} U_{k_1 k_2 k_3 k_4} &= \langle k_1 | \langle k_2 | V_{e-e}(\mathbf{r} - \mathbf{r}') | k_3 \rangle | k_4 \rangle \\ &= \int d^3 r \int d^3 r' \varphi_{k_1}^*(\mathbf{r}) \varphi_{k_2}^*(\mathbf{r}') V_{e-e}(\mathbf{r} - \mathbf{r}') \varphi_{k_3}(\mathbf{r}') \varphi_{k_4}(\mathbf{r}) \end{aligned} \quad (2.1.14)$$

describe the electron-electron coupling strength due to the Coulomb interaction V_{e-e} . In general any single-particle basis can be used. Often the eigenbasis of H_0 in reciprocal space is chosen, because then $\varepsilon_{k_1 k_2}$ becomes diagonal and $\varepsilon_{\mathbf{k}}$ is the single-particle band structure.

2.1.2. Tight-binding model

In this chapter we will introduce the *tight-binding model* to describe non-interacting electrons within a periodic potential. It is mainly based on the corresponding chapters in Refs. [23, 31]. A detailed description can be found in Ref. [32].

Within the tight-binding model we are solving the non-interacting Hamiltonian from Eq. (2.1.8). As described in the previous section, the solutions to the single-particle Schrödinger's equation are plane waves or Bloch states with the collective band index n $\psi_{n\mathbf{k}} \equiv \langle \mathbf{r} | n\mathbf{k} \rangle$. Within a tight-binding model these eigenstates are now written in a basis of localized functions. One possible orthonormal basis set are the

so called *Wannier functions* [33] $w_n(\mathbf{r} - \mathbf{R}) \equiv \langle \mathbf{r} | n\mathbf{R} \rangle$, which can be derived from the Bloch states via a discrete Fourier transformation and vice versa¹

$$w_n(\mathbf{r} - \mathbf{R}) = \frac{1}{\sqrt{N}} \sum_{\mathbf{k}} e^{-i\mathbf{k}\cdot\mathbf{R}} \psi_{n\mathbf{k}} \quad (2.1.15)$$

$$\psi_{n\mathbf{k}} = \frac{1}{\sqrt{N}} \sum_{\mathbf{R}} e^{i\mathbf{k}\cdot\mathbf{R}} w_n(\mathbf{r} - \mathbf{R}). \quad (2.1.16)$$

Here, N is the number of atoms within the crystal. Wannier functions are localized at the atom positions \mathbf{R} and due to their orthonormality fulfill the condition:

$$\langle n\mathbf{R} | n'\mathbf{R}' \rangle = \delta_{nn'} \delta_{\mathbf{R}\mathbf{R}'}. \quad (2.1.17)$$

The single-particle Hamiltonian in second quantization from Eq. (2.1.12) can be written in Wannier representation as

$$H_0 = \sum_{\mathbf{R}\mathbf{R}'n} \langle n\mathbf{R} | H_0 | \mathbf{R}'n \rangle c_{n\mathbf{R}}^\dagger c_{n\mathbf{R}'} \equiv \sum_{\mathbf{R}\mathbf{R}'n} t_n^{\mathbf{R}\mathbf{R}'} c_{n\mathbf{R}}^\dagger c_{n\mathbf{R}'} \quad (2.1.18)$$

with the so called *hopping matrix elements* $t_n^{\mathbf{R}\mathbf{R}'}$, which are the probability amplitudes for an electron in band n to hop from the atom at position \mathbf{R} to an atom at position \mathbf{R}' . For $\mathbf{R} = \mathbf{R}'$ this matrix element is the on-site energy. The operator $c_{n\mathbf{R}}^{(\dagger)}$ annihilates (creates) an electron in band n at the atomic position \mathbf{R} . If the hopping matrix elements are known, the band structure $\varepsilon_n(\mathbf{k})$ can be directly calculated and vice versa

$$\varepsilon_n(\mathbf{k}) = \frac{1}{N} \sum_{\mathbf{R}\mathbf{R}'} t_n^{\mathbf{R}\mathbf{R}'} e^{i\mathbf{k}\cdot(\mathbf{R}-\mathbf{R}')} \quad (2.1.19)$$

$$t_n^{\mathbf{R}\mathbf{R}'} = \frac{1}{N} \sum_{\mathbf{k}} \varepsilon_n(\mathbf{k}) e^{-i\mathbf{k}\cdot(\mathbf{R}-\mathbf{R}')}. \quad (2.1.20)$$

So far this description only relied on the basis transformation from plane waves to a localized real space basis. In the tight-binding approximation we try to find good approximations to the (not known) Wannier functions. One especially demonstrative approach is the so called *linear combination of atomic orbitals* (LCAO) ansatz, which tries to find approximate eigenfunctions in the subspace of atomic orbitals. It uses the solution to the atomic Schrödinger's equation, i.e., localized atomic orbitals $\varphi_\alpha(\mathbf{r} - \mathbf{R})$ as basis set. Here, α is a collective orbital index which can absorb all relevant quantum numbers. This is based on the assumption, that electrons are tightly bound to the atom (thus the name) and move only slowly through the crystal.

¹It should be noted that the definition of the Wannier functions is not unique as the Bloch functions exhibit a gauge freedom. We will discuss this issue in Section 2.1.3.

2. Theory and Methods

As atomic orbitals do not fulfill the Bloch theorem Eq. (2.1.10), suitable linear combinations have to be found. One possible combination is the *Bloch sum*

$$\langle \mathbf{r} | \chi_{\alpha \mathbf{k}} \rangle = \chi_{\alpha \mathbf{k}}(\mathbf{r}) = \frac{1}{\sqrt{N}} \sum_{\mathbf{R}} e^{i\mathbf{k} \cdot \mathbf{R}} \varphi_{\alpha}(\mathbf{r} - \mathbf{R}). \quad (2.1.21)$$

This Bloch sum assumes that the orbitals are localized at a position of the Bravais lattice ($\mathbf{R} = \mathbf{R}_j$). For more than one atom within a unit cell, additional terms would occur. However, they would not alter the basic considerations of the LCAO ansatz, so due to reasons of simplicity we will consider only a single atom per unit cell here.

In general, Bloch sums are not orthonormal because of the non-orthonormal atomic orbitals. Thus they have a finite overlap [31]

$$\langle \chi_{\alpha \mathbf{k}} | \chi_{\alpha' \mathbf{k}'} \rangle = \frac{1}{N} \sum_{\mathbf{R}, \mathbf{R}'} e^{-i\mathbf{k} \cdot \mathbf{R}} e^{i\mathbf{k}' \cdot \mathbf{R}'} \int d^3r \varphi_{\alpha}^*(\mathbf{r} - \mathbf{R}) \varphi_{\alpha'}(\mathbf{r} - \mathbf{R}'). \quad (2.1.22)$$

Nevertheless it is possible to orthogonalize atomic states with the *Löwdin transformation* without changing spatial symmetries [34]. As the exact form of the orbitals is not of importance in this work, we will use orthonormalized orbitals which have an atomic character in the following, i.e.:

$$\int d^3r \varphi_{\alpha}^*(\mathbf{r} - \mathbf{R}) \varphi_{\alpha'}(\mathbf{r} - \mathbf{R}') = \delta_{\mathbf{R}\mathbf{R}'} \delta_{\alpha\alpha'}. \quad (2.1.23)$$

The Bloch sums are in fact not eigenstates of the single-particle Hamiltonian but can be used as basis functions to construct Bloch functions

$$|\psi_{n\mathbf{k}}\rangle = \sum_{\lambda} c_{\lambda}^n(\mathbf{k}) |\chi_{\lambda\mathbf{k}}\rangle \quad (2.1.24)$$

$$= \frac{1}{\sqrt{N}} \sum_{\mathbf{R}} e^{i\mathbf{k} \cdot \mathbf{R}} \underbrace{\sum_{\lambda} c_{\lambda}^n(\mathbf{k}) \varphi_{\lambda}(\mathbf{r} - \mathbf{R})}_{w_n(\mathbf{r} - \mathbf{R})}, \quad (2.1.25)$$

where the expansion coefficients c_{λ}^n are chosen such that the single-particle Schrödinger's equation is solved. Now it becomes evident that we use linear combinations of atomic orbitals to construct a local Wannier basis for our Hamiltonian.

The matrix representation of the single-particle Schrödinger's equation within this basis is

$$\sum_{\alpha'} H_{\alpha\alpha'}(\mathbf{k}) c_{\alpha'}^n(\mathbf{k}) = E_n^0(\mathbf{k}) c_{\alpha}^n(\mathbf{k}) \quad (2.1.26)$$

with the tight-binding matrix

$$H_{\alpha\alpha'}(\mathbf{k}) = \langle \chi_{\alpha\mathbf{k}} | H_0 | \chi_{\alpha'\mathbf{k}} \rangle = \frac{1}{N} \sum_{\mathbf{R}, \mathbf{R}'} e^{i\mathbf{k} \cdot (\mathbf{R} - \mathbf{R}')} \underbrace{\langle \alpha\mathbf{R} | H_0 | \mathbf{R}'\alpha' \rangle}_{t_{\mathbf{R}\mathbf{R}'}^{\alpha\alpha'}}. \quad (2.1.27)$$

Since the crystal is translational invariant we can set one vector to the origin $\mathbf{R} = 0$ and sum N times over all distance vectors resulting in a more convenient form of the tight-binding matrix

$$H_{\alpha\alpha'}(\mathbf{k}) = \sum_{\mathbf{R}} e^{i\mathbf{k} \cdot \mathbf{R}} \langle \mathbf{0}, \alpha | H_0 | \mathbf{R}, \alpha' \rangle = \sum_{\mathbf{R}} e^{i\mathbf{k} \cdot \mathbf{R}} t_{\alpha\alpha'}(\mathbf{R}). \quad (2.1.28)$$

The hopping matrix elements describe now the probability amplitude of an electron to hop from orbital α to α' in distance \mathbf{R} .

The band structure can be calculated by diagonalizing the tight-binding matrix. Usually further approximations are applied when the tight-binding Hamilton matrix is set up. Often, the Bloch sums are restricted to a finite number of orbitals as well as the \mathbf{R} vectors are limited to a small number of neighbors. Most of the times only hopping between nearest and next nearest neighbors are considered due to the localized basis functions: the farther apart the electron hops, the smaller will be the probability amplitude. When the hopping matrix elements are determined three center integrals have to be calculated. They depend on three different positions: the positions of the orbitals α , α' and the position of the ionic potential. A frequently used approximation is the so called *two-center-approximation* [32], where every integral dependent on three pairwise distinct positions will be neglected due to the strong localization of orbitals. Moreover, in many cases the hopping matrix elements are not calculated but empirical parameters which can be fitted to experimental or ab-initio data. In this work we will use hopping matrix elements fitted to ab-initio data.

2.1.3. Maximally localized Wannier functions

In the previous section, we introduced Wannier functions as a local basis set to describe the electronic properties of a solid. In this chapter we want to show a different approach than the LCAO ansatz to calculate the Wannier functions. Most of the following derivations can be found in Ref. [35] and the presented procedure is implemented in the `Wannier90` Code [36], which we use frequently in this work.

As shown in Eq. (2.1.16) the Wannier functions are the Fourier transformation of the Bloch functions $|\psi_{n\mathbf{k}}\rangle$. However, this definition is not unique as the Bloch states have a gauge freedom, i.e. a rotation with a phase factor like

$$|\tilde{\psi}_{n\mathbf{k}}\rangle = e^{i\varphi_n(\mathbf{k})} |\psi_{n\mathbf{k}}\rangle \quad (2.1.29)$$

2. Theory and Methods

does not change the physical properties as long as $\varphi_n(\mathbf{k})$ is a real function and periodic in \mathbf{k} -space. For J bands the rotation from Eq. (2.1.29) can be generalized with a J dimensional unitary matrix $U_{nm}^{\mathbf{k}}$ which is periodic in \mathbf{k} to:

$$|\tilde{\psi}_{n\mathbf{k}}\rangle = \sum_{m=1}^J U_{mn}^{\mathbf{k}} |\psi_{m\mathbf{k}}\rangle. \quad (2.1.30)$$

This leads to a gauge freedom in the construction of Wannier functions

$$|\mathbf{R}n\rangle = \frac{V}{(2\pi)^3} \int_{\text{BZ}} d^3k e^{-i\mathbf{k}\cdot\mathbf{R}} \sum_{m=1}^J U_{mn}^{\mathbf{k}} |\psi_{m\mathbf{k}}\rangle. \quad (2.1.31)$$

The choice of Wannier functions is thus arbitrary. Marzari and Vanderbilt [37] suggested to choose $U_{mn}^{\mathbf{k}}$ such that the real space spread of the resulting function is minimal yielding *maximally localized* Wannier functions (MLWF). Selecting a specific type of Wannier function will automatically determine the Bloch functions $|\tilde{\psi}_{n\mathbf{k}}\rangle$ by fixing the gauge. For this reason MLWF lead to maximally smooth states in reciprocal space.

For maximal localization, we define a localization functional

$$\Omega = \sum_{n=1}^J [\langle \mathbf{0}n | \mathbf{r}^2 | \mathbf{0}n \rangle - \langle \mathbf{0}n | \mathbf{r} | \mathbf{0}n \rangle^2] = \sum_{n=1}^J f [\langle \mathbf{r}^2 \rangle_n - \bar{\mathbf{r}}_n^2], \quad (2.1.32)$$

which measures the sum of quadratic spreads of the the J Wannier functions. Then, Ω is a localization criterion and has to be minimized to find an optimal $U_{nm}^{\mathbf{k}}$.

Ω can be decomposed into a gauge-invariant and gauge-dependent part

$$\Omega = \Omega_I + \tilde{\Omega} \quad (2.1.33)$$

with

$$\Omega_I = \sum_n \left[\langle \mathbf{0}n | \mathbf{r}^2 | \mathbf{0}n \rangle - \sum_{\mathbf{R}m} |\langle \mathbf{R}m | \mathbf{r} | \mathbf{0}n \rangle|^2 \right] \quad \text{and} \quad \tilde{\Omega} = \sum_n \sum_{\mathbf{R}m \neq \mathbf{0}n} |\langle \mathbf{R}m | \mathbf{r} | \mathbf{0}n \rangle|^2. \quad (2.1.34)$$

The gauge invariant part Ω_I is invariant under any arbitrary unitary transformation [35, 37] of Bloch states, so the task of minimizing Ω is reduced to minimizing only the gauge-dependent part $\tilde{\Omega}$.

Since eventually the minimization procedure will be carried out in momentum space, a \mathbf{k} -space representation of Ω is needed. We will not discuss the details of the

derivations, which can be found in Ref. [35], but only give the results. The gauge invariant part can be written as

$$\Omega_I = \frac{1}{N} \sum_{\mathbf{k}, \mathbf{b}} \left(w_{\mathbf{b}} (J - \sum_{mn} |M_{mn}^{(\mathbf{k}, \mathbf{b})}|^2) \right), \quad (2.1.35)$$

where N is the number of \mathbf{k} points, \mathbf{b} the connection vector between neighboring \mathbf{k} vectors and $w_{\mathbf{b}}$ a weighting factor. The matrix

$$M_{mn}^{(\mathbf{k}, \mathbf{b})} = \langle u_{m\mathbf{k}} | u_{n\mathbf{k}+\mathbf{b}} \rangle \quad (2.1.36)$$

is the overlap between Bloch orbitals $u_{n\mathbf{k}}(\mathbf{r}) = \sqrt{N} e^{-i\mathbf{k}\cdot\mathbf{r}} \psi_{n\mathbf{k}}(\mathbf{r})$ at neighboring \mathbf{k} points and can be derived from electronic structure calculations. The gauge dependent part is reformulated to

$$\tilde{\Omega} = \frac{1}{N} \sum_{\mathbf{k}, \mathbf{b}} w_{\mathbf{b}} \sum_{m \neq n} |M_{mn}^{(\mathbf{k}, \mathbf{b})}|^2 + \frac{1}{N} \sum_{\mathbf{k}, \mathbf{b}} w_{\mathbf{b}} \sum_n (-\text{Im} \ln M_{nn}^{(\mathbf{k}, \mathbf{b})} - \mathbf{b} \cdot \bar{\mathbf{r}}_n)^2 \quad (2.1.37)$$

with

$$\bar{\mathbf{r}}_n = -\frac{1}{N} \sum_{\mathbf{k}, \mathbf{b}} w_{\mathbf{b}} \mathbf{b} \text{Im} \ln M_{nn}^{(\mathbf{k}, \mathbf{b})}. \quad (2.1.38)$$

As the localization is expressed in terms of $M_{mn}^{(\mathbf{k}, \mathbf{b})}$, which are dependent on the gauge factor U_{nm} , these overlap matrix elements play a central role in the formalism. For J bands, the minimization process is now reduced to numerically minimizing $\tilde{\Omega}$ and find an optimal U_{nm} with the help of $M_{mn}^{(\mathbf{k}, \mathbf{b})}$. Often this is done by using a steepest decent or a conjugate gradient algorithm. For further details on the computational algorithms see Ref. [37].

The minimization of $\tilde{\Omega}$ can only be carried out for J *isolated* Bloch bands. Unfortunately, in many cases the bands of interest within a certain energy window overlap and hybridize with bands from outside of the window. The bands are *entangled*. Hence, before the minimization of $\tilde{\Omega}$, the Bloch states have to be *disentangled*. In the following we want to briefly outline the disentanglement method by Souza et al. For further details on the procedure the reader is referenced to Ref. [38].

For the disentanglement an energy window which includes the J bands of interest is chosen. At each \mathbf{k} -point there are $J_{\mathbf{k}} \geq J$ bands within the energy window resulting in a $J_{\mathbf{k}}$ -dimensional Hilbert space $\mathcal{F}(\mathbf{k})$ spanned by the Bloch orbitals $u_{n\mathbf{k}}$ belonging to the bands within the energy window. At some \mathbf{k} points, there will be exactly the number of target states $J_{\mathbf{k}} = J$, then nothing has to be done. For $J_{\mathbf{k}} > J$ an optimal J -dimensional subspace $\mathcal{S}(\mathbf{k}) \subseteq \mathcal{F}(\mathbf{k})$ has to be found where $\mathcal{S}(\mathbf{k})$ should

be *optimally smooth*. This means the difference between neighboring subspaces $\mathcal{S}(\mathbf{k})$ and $\mathcal{S}(\mathbf{k} + \mathbf{b})$ should be as small as possible which will be true if Ω_I is minimal.

As it can be seen from Eq. (2.1.35) Ω_I is small whenever $M_{mn}^{(\mathbf{k}, \mathbf{b})}$ is large, i.e., whenever the overlap between states at neighboring \mathbf{k} points is large. This becomes even more evident when Ω_I is rewritten with the projector $\hat{P}_{\mathbf{k}} = \sum_n |u_{n\mathbf{k}}\rangle \langle u_{n\mathbf{k}}|$ onto $\mathcal{S}(\mathbf{k})$ and the complement $\hat{Q}_{\mathbf{k}} = 1 - \hat{P}_{\mathbf{k}}$:

$$\Omega_I = \text{tr}[\hat{P}_{\mathbf{k}} \hat{Q}_{\mathbf{k}+\mathbf{b}}]. \quad (2.1.39)$$

The product of $\hat{P}_{\mathbf{k}} \hat{Q}_{\mathbf{k}+\mathbf{b}}$ will be zero if $\hat{P}_{\mathbf{k}} = \hat{P}_{\mathbf{k}+\mathbf{b}}$, which means that the subspaces $\mathcal{S}(\mathbf{k})$ and $\mathcal{S}(\mathbf{k} + \mathbf{b})$ are the same. Thus, Ω_I indeed measures how strong neighboring subspaces differ. Hence, a minimal Ω_I means minimal mismatch between neighboring subspaces resulting in smooth changes between subspaces. Additionally, we can see in Eq. (2.1.39) that Ω_I is really gauge invariant as any unitary transformation $U_{nm}^{\mathbf{k}}$ acting on the Bloch orbitals $u_{n\mathbf{k}}$ will not change the projectors. Consequently to find optimal subspaces Ω_I has to be minimized. Then, with a new set of disentangled Bloch states $\tilde{\Omega}$ can be minimized for a maximal localization of the Wannier functions as described above.

By introducing the disentanglement scheme further constraints can be included. For example often we want to exactly reproduce the eigenenergies of the Bloch states within a certain energy window which is part of the outer disentanglement window. For that, a "frozen" energy window can be introduced in which certain states are fixed.

For the minimization process of Ω_I an initial guess for the subspace is needed. Therefore, we can use N localized trial functions $g_{\alpha}(\mathbf{r})$ as for example Gaussian functions or hydrogen orbitals localized at the site of the Wannier functions. On $g_{\alpha}(\mathbf{r})$ the $J_{\mathbf{k}}$ Bloch states are projected

$$|\Phi_{\alpha\mathbf{k}}^{\text{proj}}\rangle = \sum_{m=1}^{J_{\mathbf{k}}} A_{m\alpha} |\psi_{m\mathbf{k}}\rangle \quad (2.1.40)$$

using the projection matrix

$$A_{m\alpha}^{\mathbf{k}} = \langle \psi_{m\mathbf{k}} | g_{\alpha} \rangle \quad (2.1.41)$$

which can be calculated in advance from ab-initio calculations. With the Löwdin transformation [34] these projected states are orthogonalized

$$|\Phi_{\beta\mathbf{k}}^{\text{orth}}\rangle = \sum_{\alpha=1}^N \left| \Phi_{\alpha\mathbf{k}}^{\text{proj}} \right\rangle (S_{\mathbf{k}}^{-1/2})_{\alpha\beta} \quad (2.1.42)$$

with $(S_{\mathbf{k}})_{\alpha\beta} = \langle \Phi_{\alpha\mathbf{k}}^{\text{proj}} | \Phi_{\beta\mathbf{k}}^{\text{proj}} \rangle = (A_{\mathbf{k}}^\dagger A_{\mathbf{k}})_{\alpha\beta}$. The state $|\Phi_{\beta\mathbf{k}}^{\text{orth}}\rangle$ is the starting point of the minimization of Ω_I .

Throughout this work we use the `Wannier90` code [36] to derive tight-binding models based on ab-initio calculations. We utilize these models to calculate the band structures of GW calculations, which we will introduce in Section 2.4.3, on a fine \mathbf{k} -grid or as starting point for further investigations on the material of interest. We do not perform the maximal localization step but use only the disentanglement procedure to keep the symmetry of the trial orbitals for our tight-binding models.

2.2. Density Functional Theory

In this section *Density Functional Theory* (DFT) is introduced, an approach to find solutions to the *interacting* many-body problem from Eq. (2.1.6) within the Born-Oppenheimer approximation. The chapter closely follows the book by Martin[24] and is complemented by the lecture notes from Blöchl[39].

The main idea of DFT is that any property of a system of interacting particles can be viewed as a functional of the ground state density. In other words, a scalar function can determine all information of the many-body wave function. The original idea was proposed by Thomas [40] and Fermi [41] in 1927. The modern formulation was developed forty years later by Hohenberg, Kohn and Sham in 1964 [42] and 1965 [43] leading to a Nobel prize in chemistry for W. Kohn in 1998. With the ansatz by Kohn and Sham it is possible to approximate the ground state of a many-body system by solving effective single-particle equations. Therefore, they introduced an auxiliary system of independent particles casting all many-body effects in an unknown exchange-correlation functional. The used approximative functionals work surprisingly well for a large variety of materials and with increasing computational power even large scaled systems became accessible. This has lead to a huge success of DFT in the description of the ground state of (weakly correlated) electrons in solid states. Still, it is not suitable to treat all systems. Especially strongly correlated electrons are not described well.

In the following the main ideas of DFT will be outlined and a short introduction to the exchange-correlation potentials and pseudopotentials used in this thesis are given. Throughout this work, for DFT calculations we employ the *Vienna Ab initio Simulation Package* (VASP) [44–47].

2.2.1. Hohenberg and Kohn Theorems

In DFT, the many-body Hamiltonian under consideration for interacting electrons in Born-Oppenheimer approximation is written in a generalized form:

$$H = -\frac{\hbar^2}{2m_e} \sum_i \nabla_i^2 + \sum_i v_{\text{ext}}(\mathbf{r}_i) + \frac{1}{2} \sum_{i \neq j} \frac{e^2}{|\mathbf{r}_i - \mathbf{r}_j|} \quad (2.2.1)$$

in which the external potential $V_{\text{ext}}(\mathbf{r}) = \sum_i v_{\text{ext}}(\mathbf{r})$ includes not only the interaction between electron and fixed nuclei as in Eq. (2.1.6) but can also describe external fields. Density Functional Theory is based on the idea to use the ground state density

$$n_0(\mathbf{r}) = \int d^3r_1 \dots \int d^3r_{N_e} \Psi^*(\mathbf{r}_1, \dots, \mathbf{r}_{N_e}) \underbrace{\sum_{i=1}^{N_e} \delta(\mathbf{r} - \mathbf{r}_i)}_{\hat{n}(\mathbf{r})} \Psi(\mathbf{r}_1, \dots, \mathbf{r}_{N_e}) \quad (2.2.2)$$

as basic variable for a many-body system instead of the many-body wave function $\Psi(\mathbf{r})$, i.e. all properties of the system can be considered to be unique functionals of the ground state density. This has the advantage that the ground state density is just a scalar function of the position \mathbf{r} whereas the many-body wave function is a linear combination of Slater determinants and depends on all electronic positions \mathbf{r} . That this is indeed the case was shown by Hohenberg and Kohn with their famous *Hohenberg and Kohn Theorems*, which are the base of modern DFT formulations. They apply to all many-body electrons described by the Hamiltonian (2.2.1) in an external potential V_{ext} . As these theorems are essential to the understanding of DFT we will also show their proofs in the following.

Theorem 1 *For any system of interacting particles in an external potential V_{ext} , the external potential is determined uniquely by the ground state density $n_0(\mathbf{r})$.*

To proof this theorem, we make use of the definition of the electron density operator $n(\mathbf{r}) = \sum_{i=1}^{N_e} \delta(\mathbf{r} - \mathbf{r}_i)$ to describe the external potential

$$V_{\text{ext}} = \int d^3r n(\mathbf{r}) v_{\text{ext}}(\mathbf{r}) = \int d^3r \sum_i \delta(\mathbf{r} - \mathbf{r}_i) v_{\text{ext}}(\mathbf{r}) = \sum_i v_{\text{ext}}(\mathbf{r}_i). \quad (2.2.3)$$

Now, suppose we have two different external potentials $V_{\text{ext}}^{(1)} \neq V_{\text{ext}}^{(2)}$ (which differ by more than a constant) with the same ground state density $n_0(\mathbf{r})$. These two potentials belong to different Hamiltonians $H^{(1)} \neq H^{(2)}$ with different ground state wave functions $\Psi^{(1)}$ and $\Psi^{(2)}$. Both wave functions are assumed to have the same

ground state density. As $\Psi^{(2)}$ is not the ground of state of $H^{(1)}$ and vice versa it follows from Ritz variational principle:

$$\begin{aligned}\langle \Psi^{(1)} | H^{(1)} | \Psi^{(1)} \rangle &= E_1 < \langle \Psi^{(2)} | H^{(1)} | \Psi^{(2)} \rangle \\ \langle \Psi^{(2)} | H^{(2)} | \Psi^{(2)} \rangle &= E_2 < \langle \Psi^{(1)} | H^{(2)} | \Psi^{(1)} \rangle.\end{aligned}\quad (2.2.4)$$

We can use Eq. (2.2.1) and Eq. (2.2.3) to write the expectation values as

$$\begin{aligned}\langle \Psi^{(2)} | H^{(1)} | \Psi^{(2)} \rangle &= \langle \Psi^{(2)} | H^{(2)} | \Psi^{(2)} \rangle + \langle \Psi^{(2)} | H^{(1)} - H^{(2)} | \Psi^{(2)} \rangle \\ &= E_2 + \int d^3r \left[v_{\text{ext}}^{(1)}(\mathbf{r}) - v_{\text{ext}}^{(2)}(\mathbf{r}) \right] n_0(\mathbf{r})\end{aligned}\quad (2.2.5)$$

$$\begin{aligned}\langle \Psi^{(1)} | H^{(2)} | \Psi^{(1)} \rangle &= \langle \Psi^{(1)} | H^{(1)} | \Psi^{(1)} \rangle + \langle \Psi^{(1)} | H^{(2)} - H^{(1)} | \Psi^{(1)} \rangle \\ &= E_1 + \int d^3r \left[v_{\text{ext}}^{(2)}(\mathbf{r}) - v_{\text{ext}}^{(1)}(\mathbf{r}) \right] n_0(\mathbf{r}).\end{aligned}\quad (2.2.6)$$

This can be used to reformulate the inequalities from Eq. (2.2.4) as

$$E^{(1)} < E^{(2)} + \int d^3r \left[v_{\text{ext}}^{(1)}(\mathbf{r}) - v_{\text{ext}}^{(2)}(\mathbf{r}) \right] n_0(\mathbf{r})\quad (2.2.7)$$

$$E^{(2)} < E^{(1)} + \int d^3r \left[v_{\text{ext}}^{(2)}(\mathbf{r}) - v_{\text{ext}}^{(1)}(\mathbf{r}) \right] n_0(\mathbf{r})\quad (2.2.8)$$

and add both equation

$$E_1 + E_2 < E_1 + E_2\quad (2.2.9)$$

resulting in a contradictory inequality. Hence, there cannot be two different external potentials differing by more than a constant with the same ground state density meaning $n_0(\mathbf{r})$ uniquely defines $V_{\text{ext}}(\mathbf{r})$ and thus the complete Hamiltonian. Consequently n_0 not only determines the external potential but *all* material properties of the system.

Theorem 2 *There exists a functional $E[n(\mathbf{r})]$ of the charge density $n(\mathbf{r})$ which is minimized by the ground state density $n_0(\mathbf{r})$.*

Since all properties of the system are uniquely defined by $n(\mathbf{r})$, every property can be viewed as functional of $n(\mathbf{r})$, e.g. the energy functional:

$$E_{\text{HK}}[n(\mathbf{r})] = \underbrace{T[n(\mathbf{r})] + V_{\text{ee}}[n(\mathbf{r})]}_{F_{\text{HK}}} + \int d^3r v_{\text{ext}}(\mathbf{r})n(\mathbf{r})\quad (2.2.10)$$

where we define a universal, i.e. the same for all electron systems, functional F_{HK} . It includes the electron kinetics $T[n(\mathbf{r})]$ and the electron-electron interaction $V_{\text{ee}}[n(\mathbf{r})]$

and shall solely depend on the charge density. We now consider a system with the ground state density $n_0(\mathbf{r})$, which is directly linked to the ground state wave function Ψ belonging to H . Then the functional (2.2.10) is equal to the expectation value of the Hamiltonian H in the ground state

$$E_0 = E_{\text{HK}}[n_0(\mathbf{r})] = \langle \Psi | H | \Psi \rangle. \quad (2.2.11)$$

According to the first Theorem, a different density $n_0^{(1)}(\mathbf{r})$ must correspond to a different wave function $\Psi^{(1)}$ and thus it follows:

$$E_0 = \langle \Psi | H | \Psi \rangle < \langle \Psi^{(1)} | H | \Psi^{(1)} \rangle \quad (2.2.12)$$

which leads directly to

$$E_{\text{HK}}[n_0(\mathbf{r})] < E_{\text{HK}}[n_0^{(1)}(\mathbf{r})]. \quad (2.2.13)$$

As a result the functional E_{HK} is minimized by the ground state density $n_0(\mathbf{r})$. If F_{HK} was known minimizing the total energy of a system with respect to $n_0(\mathbf{r})$ would be sufficient to find the exact ground state density and energy. So far there are no analytic expressions of F_{HK} known for interacting electrons, hence approximations are needed. The very first approximation was introduced by Thomas [40] and Fermi [41] forty years before Hohenberg and Kohn proofed their theorems. They assumed the kinetic energy to be a functional of the local density of a non-interacting electron gas including only Hartree energies and with that neglecting exchange effects. However, the involved approximations were too crude to reliably describe solid states.

Nowadays, the minimization of Eq. (2.2.10) is done by using an auxiliary single-particle system introduced by Kohn and Sham. We will present this approach and more suitable approximations to the involved functionals in the following sections.

2.2.2. Kohn-Sham equations

The idea of Kohn and Sham [43] replaces the interacting system with an auxiliary single-particle system which is easier to solve. In their ansatz they assume that the ground state density of the interacting system is equal to the density of an effective non-interacting system. Then solving this independent particle equation with all difficult many-body terms incorporated in an *exchange-correlation functional* would automatically also solve the many-body problem.

The reformulated Hamiltonian has the form

$$H_{\text{KS}} = -\frac{\hbar^2}{2m_e} \nabla^2 + v_{\text{KS}} \quad (2.2.14)$$

with the effective Kohn-Sham potential v_{KS} which has to be constructed in a way that the resulting ground state density of H_{KS} equals the ground state density of the many-body problem. The density of the auxiliary system

$$n(\mathbf{r}) = \sum_i^{N_e} |\psi_i(\mathbf{r})|^2 \quad (2.2.15)$$

is defined by the *Kohn-Sham orbitals* $\psi_i(\mathbf{r})$, the single-particle wave functions of the auxiliary system. The non-interacting form of the Hohenberg-Kohn functional from Eq. (2.2.10) can be written as

$$E_{\text{KS}}[n(\mathbf{r})] = T_S[n(\mathbf{r})] + \int d^3r v_{\text{ext}} n(\mathbf{r}) + E_{\text{Hartree}}[n(\mathbf{r})] + E_{\text{XC}}[n(\mathbf{r})]. \quad (2.2.16)$$

Here, we use the kinetic energy of the independent particle

$$T_S[n(\mathbf{r})] = -\frac{\hbar^2}{2m_e} \sum_{i=1}^{N_e} \int d^3r |\nabla \psi_i|^2 \quad (2.2.17)$$

and the (classical) Hartree energy functional

$$E_{\text{Hartree}}[n(\mathbf{r})] = \frac{1}{2} \int d^3r d^3r' \frac{n(\mathbf{r})n(\mathbf{r}')}{|\mathbf{r} - \mathbf{r}'|}. \quad (2.2.18)$$

The exchange-correlation potential includes all many-body interaction, thus all exchange and correlation energies. Because the density of the auxiliary system should be equal to the true ground state density, we can compare Eq. (2.2.10) and Eq. (2.2.16) and find

$$\begin{aligned} E_{\text{XC}}[n(\mathbf{r})] &= F_{\text{HK}}[n(\mathbf{r})] - (T_S[n(\mathbf{r})] + E_{\text{Hartree}}[n(\mathbf{r})]) \\ &= \langle T \rangle - T_S[n(\mathbf{r})] + \langle V_{\text{ee}} \rangle - E_{\text{Hartree}}[n(\mathbf{r})]. \end{aligned} \quad (2.2.19)$$

The expectation values in E_{XC} describe the *full* kinetic and interaction energies, thus have to be evaluated with the many-body wave function. The exchange-correlation potential is the difference between the kinetic and electron-electron interaction energies of the many-body system and the energies from the independent particle system. If the exchange-correlation functional was known, the exact many-body ground state could be found by solving the independent particle system. But as this is not possible, approximations to the exchange-correlation functional have to be found (see Section 2.2.3).

To find the ground state density $n_0(\mathbf{r})$ we have to minimize Eq. (2.2.16) with respect to the density $n(\mathbf{r})$ under the constraint of constant particle number N_e .

2. Theory and Methods

Equivalently we can minimize it with respect to ψ_i (c.f. Eq. (2.2.15)) under the constraint of normalized wave functions $\langle \psi_i | \psi_j \rangle = \delta_{ij}$:

$$\delta_{\psi_i^*(\mathbf{r})} \left\{ E_{\text{KS}}[n(\mathbf{r})] - \sum_j \varepsilon_j \left(\int d^3r |\psi_j|^2 - 1 \right) \right\} = 0. \quad (2.2.20)$$

With $\delta_{\psi_i^*(\mathbf{r})} \dots = \frac{\delta(\dots)}{\delta\psi_i^*(\mathbf{r})}$ we describe the functional derivative with respect to $\psi_i^*(\mathbf{r})$ and ε_j are Lagrangian multipliers. The functional derivative of the Kohn-Sham functional can be evaluated with the chain rule

$$\frac{\delta E_{\text{KS}}}{\delta\psi_i^*(\mathbf{r})} = \frac{\delta T_S}{\delta\psi_i^*(\mathbf{r})} + \left[\frac{\delta E_{\text{ext}}}{\delta n(\mathbf{r})} + \frac{\delta E_{\text{Hartree}}}{\delta n(\mathbf{r})} + \frac{\delta E_{\text{XC}}}{\delta n(\mathbf{r})} \right] \frac{\delta n(\mathbf{r})}{\delta\psi_i^*(\mathbf{r})} \quad (2.2.21)$$

using

$$\frac{\delta T_S}{\delta\psi_i^*(\mathbf{r})} \stackrel{(2.2.17)}{=} -\frac{\hbar^2}{2m_e} \nabla^2 \psi_i(\mathbf{r}) \quad \text{and} \quad \frac{\delta n(\mathbf{r})}{\delta\psi_i^*(\mathbf{r})} \stackrel{(2.2.15)}{=} \psi_i(\mathbf{r}). \quad (2.2.22)$$

The derivative of the constraints results in

$$\delta_{\psi_i^*(\mathbf{r})} \sum_j \varepsilon_j \left(\int d^3r |\psi_j|^2 - 1 \right) = \varepsilon_i \psi_i(\mathbf{r}). \quad (2.2.23)$$

Altogether this yields a single-particle Schrödinger equation also known as *Kohn-Sham equation*

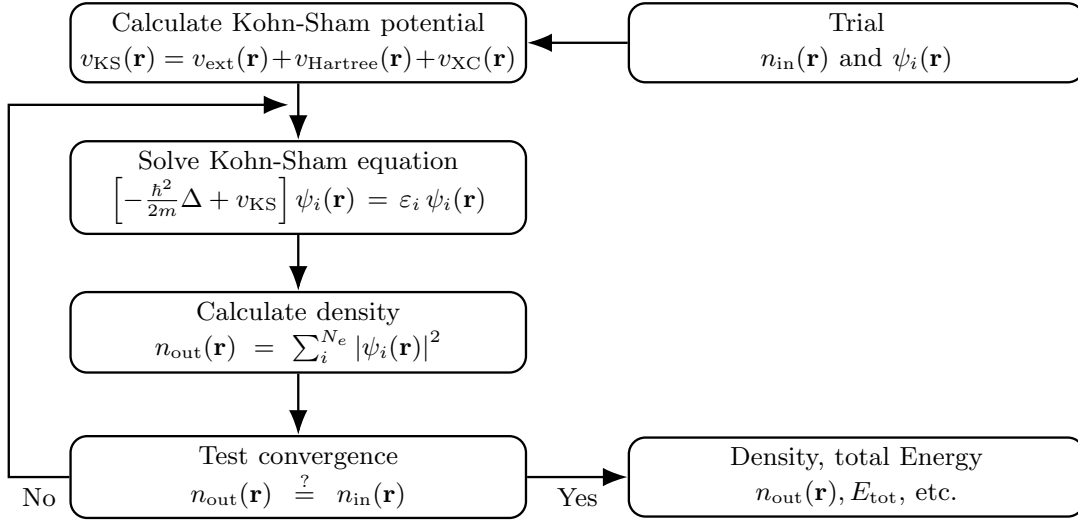
$$\left[-\frac{\hbar^2}{2m_e} \nabla^2 + v_{\text{KS}} - \varepsilon_i \right] \psi_i(\mathbf{r}) = [H_{\text{KS}} - \varepsilon_i] \psi_i(\mathbf{r}) = 0 \quad (2.2.24)$$

with the single-particle Kohn-Sham energies ε_i and the Kohn-Sham potential

$$\begin{aligned} v_{\text{KS}}(\mathbf{r}) &= \frac{\delta E_{\text{ext}}}{\delta n(\mathbf{r})} + \frac{\delta E_{\text{Hartree}}}{\delta n(\mathbf{r})} + \frac{\delta E_{\text{XC}}}{\delta n(\mathbf{r})} \\ &= v_{\text{ext}}(\mathbf{r}) + v_{\text{Hartree}}(\mathbf{r}) + v_{\text{XC}}(\mathbf{r}). \end{aligned} \quad (2.2.25)$$

In Eq. (2.2.25) v_{Hartree} and v_{ext} are known, whereas for the exchange-correlation potential v_{XC} approximations have to be found, which will be discussed in the following section.

The Kohn-Sham equation (2.2.24) is an independent particle equation which has to be solved self-consistently to find the ground state density as shown in Fig. 2.2.1. We start with a trial wave function respectively a trial ground state density. With that the Kohn-Sham potential from Eq. (2.2.25) can be derived and the solutions to the Kohn-Sham equation from Eq. (2.2.24) are found. From the resulting wave

**Figure 2.2.1.**

Self-consistency cycle for the solution of the Kohn-Sham equations. Starting from trial wave functions respectively a trial ground state density, the Kohn-Sham potential is calculated. The solutions to the Kohn-Sham equations are used to calculate a new ground state density which can be compared to the trial density. This is repeated until self-consistency is reached.

functions a new density is generated and compared with the trial density. This is repeated until the self-consistency cycle converges.

2.2.3. Exchange-correlation potential

The exact form of the exchange-correlation potential v_{XC} is not known, but it is often approximated as a local or nearly local functional of the density

$$E_{XC}[n(\mathbf{r})] = \int d^3r n(\mathbf{r}) \varepsilon_{XC}[n(\mathbf{r})] \quad (2.2.26)$$

where ε_{XC} describes the energy per electron at \mathbf{r} only depending on the density $n(\mathbf{r})$ in proximity of \mathbf{r} .

The widely used *Local Density Approximation* (LDA) is a quite simple but surprisingly well working approximation. It assumes a completely local exchange-correlation potential from the homogeneous electron gas as:

$$E_{xc}^{LDA}[n(\mathbf{r})] = \int d^3r n(\mathbf{r}) \varepsilon_{XC}^{hom}[n(\mathbf{r})]. \quad (2.2.27)$$

The exchange-correlation energy $\varepsilon_{\text{XC}}^{\text{hom}}$ can be divided in the exchange $\varepsilon_{\text{X}}^{\text{hom}}$ and correlation part $\varepsilon_{\text{C}}^{\text{hom}}$. While the correlation part is not easy to derive, the exchange part is known analytically from the homogeneous electron gas:

$$\varepsilon_{\text{X}}^{\text{hom}} = -\frac{3e^2}{4\pi} (3\pi^2 n(\mathbf{r}))^{1/3}. \quad (2.2.28)$$

For $\varepsilon_{\text{C}}^{\text{hom}}$ several interpolated expressions [48–50] are used throughout the literature, which are fitted to quantum Monte Carlo calculations of the spin-unpolarized electron gas [51].

In some situations experimental data cannot be reproduced within the LDA. Especially for chemical applications it can hardly be used due to overestimation of bond energies in molecules. To take care of the large variations of the density in real materials, the *generalized gradient approximation* (GGA) was developed. Within the GGA the exchange-correlation potential is not only dependent on the local density but also on its gradient

$$E_{\text{XC}}^{\text{GGA}}[n(\mathbf{r})] = \int d^3r n(\mathbf{r}) \varepsilon_{\text{XC}}^{\text{hom}}[n(\mathbf{r}), \nabla n(\mathbf{r})]. \quad (2.2.29)$$

Within this approximation numerous formulations of E_{XC} have been proposed (e.g. PW91 [52], B88 [53] or LYP [54] to name just a few). In this work we always use the functional of Perdew-Burke-Enzerhof (PBE) [55].

In materials, where electrons tend to be localized and strongly interacting (as for example in transition metal oxides or rare earth elements), LDA and GGA are not capable to reproduce experimental findings. All systems which exhibit (strong) correlations phenomena need different approaches to describe the electrons for example LDA+U [56, 57] or dynamical mean field theory (DMFT)[58].

In LDA and GGA the band gap is usually underestimated [59]. Hence the formulation of in particular non-local exchange-correlation functionals is still an active area of research. Especially in the chemistry community *hybrid* functionals are used because, depending on the system, they describe binding energies, band gaps and reaction energies more accurately [60–62]. These functionals incorporate some of the exact exchange from Hartree-Fock theory combined with other exchange-correlation functionals from for example LDA or GGA. However, they are computationally much more expensive and choosing a suitable potential can be a difficult task.

2.2.4. Plane wave basis and Pseudopotentials

To solve the Kohn-Sham equation (2.2.24) in practice, the problem is written in a single-particle basis to get a matrix representation of H_{KS} . Then, diagonalizing this matrix gives the eigenenergies ε_i and the eigenstates $\psi_i(\mathbf{r})$ in the chosen basis.

Due to the translational invariance in solids, plane waves $\chi_{\mathbf{k}}(\mathbf{r})$ are often used as a possible basis set. The plane wave expansion of the eigenstates yields

$$\psi_i^{\mathbf{k}}(\mathbf{r}) = \sum_m c_{i,\mathbf{k}+\mathbf{G}_m} \chi_{\mathbf{k}+\mathbf{G}_m}(\mathbf{r}) = \frac{1}{\sqrt{\Omega}} \sum_m c_{i,\mathbf{k}+\mathbf{G}_m} e^{i(\mathbf{k}+\mathbf{G}_m)\cdot\mathbf{r}} \quad (2.2.30)$$

with the reciprocal lattices vectors \mathbf{G}_m , the crystal volume Ω and the expansion coefficients $c_{i,\mathbf{k}+\mathbf{G}_m}$ of the wave function. With that the Kohn-Sham equation (2.2.24) becomes a matrix equation

$$\sum_{m'} H_{m,m'}(\mathbf{k}) c_{i,m'}(\mathbf{k}) = \varepsilon_i(\mathbf{k}) c_{i,m}(\mathbf{k}) \quad (2.2.31)$$

with the Hamilton matrix

$$H_{m,m'}(\mathbf{k}) = \frac{\hbar^2}{2m_e} |\mathbf{k} + \mathbf{G}_m|^2 \delta_{m,m'} + v_{\text{KS}}(\mathbf{G}_m - \mathbf{G}_{m'}). \quad (2.2.32)$$

In theory the sum over m has to be infinite, but is in practice truncated by an energy cutoff

$$\frac{\hbar^2}{2m_e} |\mathbf{k} + \mathbf{G}_m|^2 < E_{\text{cut}}. \quad (2.2.33)$$

The computational effort is thus directly linked to the number of involved basis functions. The basis set should on the one hand be able to describe the wave functions near the nuclei, where they show strong oscillations and on the other hand describe the rather smooth area in the bonding regions between the atoms. However, for the description of the strong oscillations near the nuclei a larger number of basis functions is needed for the plane wave expansion resulting in a large computational effort. To reduce the needed computational power mainly two strategies are used: *augmented plane waves* (APW) or *pseudopotentials* (PP).

In the augmented wave methods, which have been introduced 1937 by Slater [63], the space is divided into atom-centered spheres (*augmentation spheres*) and interstitial regions between the atoms (comparable to a muffin-tin). In the region between the atoms, the smoothly varying parts of the wave functions are represented by so called envelope functions, which are plane waves or other smooth functions. Within the augmentation sphere atom-like functions, e.g. spherical harmonics times radial functions, are utilized as basis functions. The partial solutions of both regions are then matched at the interface to compose the complete basis functions.

The method of pseudopotentials is based on the orthogonalized plane wave method by Herring [64] and was further developed by Philipps [65] and Antončík [66]. The main idea is to remove the oscillating structure of the wave function around the core. Therefore, the strong Coulomb potential of the nucleus and the effects of the bound

core electrons are replaced by an effective potential which results in nodeless wave functions around the nuclei while the wave functions outside this region are completely reproduced. With that the valence electrons can be treated with a reasonable amount of plane waves. One further advantage is, that core electrons can also be included in the PP. As a result the number of treated electrons in DFT can be even more reduced. This is possible, when the material properties depend only slightly on the core electrons and are primarily described by the valence electrons which is the case for a wide range of solids.

The PP can be constructed with an all-electron DFT calculation for a spherical atom yielding atomic potentials and wave functions $\Phi_l(\mathbf{r})$. To describe the valence electrons, so called pseudo wave functions $\tilde{\Phi}_l(\mathbf{r})$ are generated, which are nodeless within the core region and the same as $\Phi_l(\mathbf{r})$ anywhere else. To be transferable, i.e. the PP constructed for single atoms can also describe molecules and solids, $\tilde{\Phi}_l(\mathbf{r})$ should have the same norm as $\Phi_l(\mathbf{r})$, thus they should be norm-conserving [24, 67, 68]. From the pseudo wave functions $\tilde{\Phi}_l(\mathbf{r})$ the effective pseudopotential can be derived [39]. There are many PP constructed and studied in detail by for example Haman, Schlüter and Chiang [67], Kerker [69] or Troullier and Martins [70] to name just a few.

In order to be numerically reasonable, PP should not only be transferable but also smooth in the sense, that the number of expansion components needed is minimal. Transferability usually needs a small radius of the core region while smooth functions need a larger radius. Norm-conserving PP have quite accurate results but often have to sacrifice the smoothness of the function. Especially when valence states at the beginning of an atomic shell (1s, 2p, 3d, etc.) are treated, norm-conserving PP are difficult to find.

A different approach to overcome this problem was introduced by Vanderbilt [71, 72] with the so called *ultrasoft* PP where he generalized the PP method to non norm-conserving pseudopotentials leading to accurate and smooth pseudo wave functions.

Another way to deal with the oscillations in the core region introduced by Blöchl [73] is the *projector augmented waves* (PAW) method which combines ideas from the augmented wave method and pseudopotential approach. Using local projectors within an augmentation sphere, the full all-electron wave function is mapped onto smooth, numerically convenient pseudo wave functions. Outside of the sphere, the pseudo wave function coincides with the true wave function. Thus, all involved evaluations of integrals can be carried out as a combination of integrals of smooth functions and localized contributions within an augmentation sphere. If a suitable projection is found, the pseudo wave functions can be expanded in a basis like plane waves. All physical properties can be evaluated after the reconstruction of the true wave functions.

In this work the DFT calculations were performed using the PAW formalism as it was implemented in VASP [47].

2.3. Coulomb interaction and screening

For *interacting* many-body systems like solids a good description of the electron-electron interaction is essential. In a *full* microscopic description of Eq. (2.1.4) considering *all* charges, the use of the bare Coulomb interaction between two electrons at \mathbf{r} and \mathbf{r}'

$$U = \frac{e^2}{|\mathbf{r} - \mathbf{r}'|} \quad (2.3.1)$$

or in q -space for two and three dimensions

$$U^{3D} = \frac{4\pi e^2}{q^2} \quad \text{and} \quad U^{2D} = \frac{2\pi e^2}{q} \quad (2.3.2)$$

would lead to correct many-body eigenvalues and eigenstates.

As already discussed before, a full description using the Hamiltonian (2.1.4) is not possible. However, *screened* Coulomb interactions offer an efficient way to tackle this problem in principle exactly (see e.g. Hedin's equations in Section 2.4.2) or in approximative theories. This means one electron only feels a reduced Coulomb potential of a second electron due to the presence of other charges (e.g. electrons, nuclei or even external fields). In the following chapters we will shortly recapitulate some basic definitions from classical electrodynamics and then introduce methods to derive the microscopic dielectric function within the *random-phase approximation* and *constrained random-phase approximation*. This chapter follows the Refs. [23, 26, 74].

2.3.1. Screening in classical electrodynamics

In this chapter we want to give the most important equations for the understanding of screening and the dielectric function. For a complete introduction and overview the interested reader is referred to Refs. [75–77] and the references therein or other textbooks on electrodynamics.

We define the charge density $\varrho(\mathbf{r})$, which is directly connected to the particle density $n(\mathbf{r})$ via the elementary charge e , and the electrostatic potential $\Phi(\mathbf{r})$:

$$\varrho(\mathbf{r}) = en(\mathbf{r}) \quad (2.3.3)$$

$$\Phi(\mathbf{r}) = \int d^3r' \frac{\varrho(\mathbf{r}')}{|\mathbf{r} - \mathbf{r}'|}. \quad (2.3.4)$$

The Coulomb interaction is the potential energy of the electron and can be written as

$$V(\mathbf{r}) = e\Phi(\mathbf{r}). \quad (2.3.5)$$

The Maxwell equation for constant magnetic fields ($\dot{\mathbf{B}} = 0$) shows that the charge $\varrho(\mathbf{r})$ is the source of the electric field $\mathbf{E} = -\nabla\Phi$ yielding

$$\nabla \cdot \mathbf{E}(\mathbf{r}) = \frac{1}{\varepsilon_0} \varrho(\mathbf{r}), \quad (2.3.6)$$

where ε_0 is the vacuum permittivity. This leads to the Poisson equation in real space respectively in Fourier space:

$$\Delta\Phi(\mathbf{r}) = -\frac{1}{\varepsilon_0} \varrho(\mathbf{r}) \quad \text{and} \quad \Phi(\mathbf{q}) = \frac{1}{\varepsilon_0 q^2} \varrho(\mathbf{r}). \quad (2.3.7)$$

The Maxwell equation (2.3.6) is only valid in vacuum, i.e. there are no other charges than ϱ . In presence of a material or dielectric, the *free* or *external* charge ϱ^{ext} will influence the material and induce a charge ϱ^{ind} . The complete charge associated with the electric field is then $\varrho = \varrho^{\text{ext}} + \varrho^{\text{ind}}$ yielding

$$\nabla \cdot \mathbf{E}(\mathbf{r}) = \frac{1}{\varepsilon_0} [\varrho^{\text{ext}}(\mathbf{r}) + \varrho^{\text{ind}}(\mathbf{r})]. \quad (2.3.8)$$

For an easier description, the dielectric displacement $\mathbf{D}(\mathbf{r})$ is introduced

$$\mathbf{D}(\mathbf{r}) = \varepsilon_0 \mathbf{E}(\mathbf{r}) + \mathbf{P}(\mathbf{r}) \quad (2.3.9)$$

in which the polarization \mathbf{P} resulting from the induced dipoles due to the external charges is taken into account. The Maxwell equation then becomes

$$\nabla \cdot \mathbf{D}(\mathbf{r}) = \varrho^{\text{ext}}(\mathbf{r}), \quad (2.3.10)$$

which means that the source of the dielectric displacement is the external charge and thus it is independent of the material itself (contrary to the electric field). For an isotropic and homogeneous medium the polarization is proportional to the electric field with the *susceptibility* as proportional constant

$$\mathbf{P}(\mathbf{r}) = \chi \varepsilon_0 \mathbf{E}(\mathbf{r}). \quad (2.3.11)$$

Thus, the susceptibility measures how strong a material can be polarized. But many materials are not isotropic and some are even inhomogeneous which leads to a non local susceptibility $\chi(\mathbf{r}, \mathbf{r}')$ in the polarization

$$\mathbf{P}(\mathbf{r}) = \varepsilon_0 \int d^3r' \chi(\mathbf{r}, \mathbf{r}') \mathbf{E}(\mathbf{r}'). \quad (2.3.12)$$

For time dependent fields and materials which do not polarize instantaneously, the polarization becomes even more complex. A frequently used assumption is a linear response to the field:

$$\mathbf{P}(\mathbf{r}, t) = \varepsilon_0 \int \int d^3r' dt' \chi(\mathbf{r}, \mathbf{r}', t - t') \mathbf{E}(\mathbf{r}', t'). \quad (2.3.13)$$

Inserting Eq. (2.3.13) combined with Eq. (2.3.9) in Eq. (2.3.10) results in the the first Maxwell equation in presence of a polarizable material

$$\nabla_{\mathbf{r}} \int \int d^3r' dt' \delta(\mathbf{r} - \mathbf{r}') \delta(t - t') + \chi(\mathbf{r}, \mathbf{r}', t - t') \mathbf{E}(\mathbf{r}', t') = \frac{\rho^{\text{ext}}(\mathbf{r}, t)}{\varepsilon_0}. \quad (2.3.14)$$

If we consider homogeneous systems, χ only depends on the position differences $\mathbf{r} - \mathbf{r}'$ and we can perform a Fourier transform in spatial and time coordinates

$$q^2 [1 + \chi(\mathbf{q}, \omega)] \Phi(\mathbf{q}, \omega) = \frac{\rho^{\text{ext}}(\mathbf{q}, \omega)}{\varepsilon_0}, \quad (2.3.15)$$

which finally defines the *dielectric function* $\varepsilon(\mathbf{q}, \omega) = 1 + \chi(\mathbf{q}, \omega)$ or the *screening function*. With the Poisson equation (2.3.7) we can define the external potential Φ^{ext} associated with ρ^{ext} and calculate the complete potential Φ

$$\Phi(\mathbf{q}, \omega) = \frac{\Phi^{\text{ext}}(\mathbf{q}, \omega)}{\varepsilon(\mathbf{q}, \omega)}. \quad (2.3.16)$$

This means, the potential Φ associated with the electric field \mathbf{E} is defined by the external field reduced by the screening function ε .

We can now find (formal) expressions for the screening. Therefore, we use that the total potential (associated with \mathbf{E}) is the sum of external potential and induced potential and compare it with Eq. (2.3.16)

$$\Phi(\mathbf{q}, \omega) = \Phi^{\text{ext}}(\mathbf{q}, \omega) + \Phi^{\text{ind}}(\mathbf{q}, \omega) = \frac{\Phi^{\text{ext}}(\mathbf{q}, \omega)}{\varepsilon(\mathbf{q}, \omega)}. \quad (2.3.17)$$

Utilizing the Poisson equation for Φ^{ind} , the dielectric function can be defined in various ways

$$\varepsilon(\mathbf{q}, \omega) = \frac{\Phi^{\text{ext}}(\mathbf{q}, \omega)}{\Phi^{\text{ext}}(\mathbf{q}, \omega) + \Phi^{\text{ind}}(\mathbf{q}, \omega)} = 1 - \frac{\Phi^{\text{ind}}(\mathbf{q}, \omega)}{\Phi^{\text{ext}}(\mathbf{q}, \omega) + \Phi^{\text{ind}}(\mathbf{q}, \omega)} \quad (2.3.18)$$

$$= 1 - \frac{1}{\varepsilon_0 q^2} \frac{\rho^{\text{ind}}(\mathbf{q}, \omega)}{\Phi(\mathbf{q}, \omega)}. \quad (2.3.19)$$

In solids we can describe the interaction between two electrons with a screened Coulomb interaction $V = e\Phi$, which includes all effects of every other electrons, ions and even external fields. Therefore, we have to find ε within a microscopic theory, which we will do in the following chapters.

2.3.2. Random phase approximation

There are numerous (approximate) methods to derive the microscopic dielectric function. One of the first approaches was introduced by Thomas and Fermi [40, 41] in the static ($\omega = 0$) and long-wavelength ($\mathbf{q} \rightarrow \infty$) limit. Lindhard [78] used quantum mechanical perturbation theory to develop a more generic but still static approximation. A generalization to the whole Brillouin zone and all frequencies is the *random phase approximation* (RPA) firstly introduced by Bohm and Pines [79–81]. Even though there are more sophisticated approximations taking so called *vertex corrections* into account [26], RPA is still a widely used approach. Commonly there are two ways to derive the RPA: firstly Green's functions² are utilized to add up so called *bubble diagrams* to get the polarization function introduced in the previous section. For further details on this method see for example Ref. [25–27]. Secondly, and the way we will use in this chapter, in the *self-consistent field* method [82] equations of motions are used to derive the dielectric function.

Within RPA electrons respond to the total potential $V(\mathbf{r}, t) = e\Phi^{\text{ext}}(\mathbf{r}, t) + e\Phi^{\text{ind}}(\mathbf{r}, t)$ which is the sum of the external and induced potential. While Φ^{ext} is generally assumed to be known, the unknown potential of the induced charge has to be calculated self-consistently. For the derivation we use the effective Hamiltonian of the perturbed electron gas

$$H = \sum_{\mathbf{k}, \sigma} \varepsilon_{\mathbf{k}, \sigma} c_{\mathbf{k}, \sigma}^\dagger c_{\mathbf{k}, \sigma} + \frac{1}{\Omega} \sum_{\mathbf{q}} e\Phi(\mathbf{q}, \omega) n(\mathbf{q}), \quad (2.3.20)$$

²For a short introduction in the methodology of Green's functions see Section 2.4.1.

where Ω is the unit cell volume, $\Phi(\mathbf{q}, \omega)$ the fourier transform of $\Phi(\mathbf{r}, t)$ and $n(\mathbf{q})$ the density operator

$$n(\mathbf{q}) = \sum_{\mathbf{k}, \sigma} c_{\mathbf{k}+\mathbf{q}, \sigma}^\dagger c_{\mathbf{k}, \sigma} \quad (2.3.21)$$

which can be used to calculate the induced charge density [26]

$$\rho^{\text{ind}}(\mathbf{q}) = e \langle n(\mathbf{q}) \rangle. \quad (2.3.22)$$

The first term of Eq. (2.3.20) describes the kinetics of the electrons and the second term their interaction with the self-consistent potential $\Phi(\mathbf{q}, \omega)$. The two-particle Coulomb interaction is assumed to be included indirectly via the dielectric screening which is part of Φ . With this approximation only screening effects are considered but correlation and exchange effects are neglected.

Now we assume the time dependence of the external potential as a classical oscillation with a single frequency switched on adiabatically $\rho^{\text{ext}}(\mathbf{q}, t) = \rho^{\text{ext}}(\mathbf{q})e^{-i(\omega+i\delta)t}$. Then also the average of the density operator depends on ω [26]

$$\langle n(\mathbf{q}, t) \rangle = n(\mathbf{q}, \omega)e^{-i(\omega+i\delta)t}. \quad (2.3.23)$$

To calculate the reaction of $\Phi(\mathbf{q}, \omega)$ to the external perturbation we need the time evolution of $c_{\mathbf{k}+\mathbf{q}, \sigma}^\dagger c_{\mathbf{k}, \sigma}$ for which we employ the Heisenberg equation of motion:

$$-i\hbar \frac{d}{dt} c_{\mathbf{k}+\mathbf{q}, \sigma}^\dagger c_{\mathbf{k}, \sigma} = \left[H, c_{\mathbf{k}+\mathbf{q}, \sigma}^\dagger c_{\mathbf{k}, \sigma} \right]. \quad (2.3.24)$$

The commutator is evaluated piecewise for both terms of Eq. (2.3.20) yielding

$$\sum_{\mathbf{k}'\sigma'} \varepsilon_{\mathbf{k}}' \left[c_{\mathbf{k}'+\mathbf{q}, \sigma'}^\dagger c_{\mathbf{k}', \sigma'}, c_{\mathbf{k}+\mathbf{q}, \sigma}^\dagger c_{\mathbf{k}, \sigma} \right] = (\varepsilon_{\mathbf{k}+\mathbf{q}} - \varepsilon_{\mathbf{k}}) c_{\mathbf{k}+\mathbf{q}, \sigma}^\dagger c_{\mathbf{k}, \sigma} \quad (2.3.25)$$

and

$$\begin{aligned} \frac{1}{\Omega} \sum_{\mathbf{q}'\mathbf{k}'\sigma'} e\Phi(\mathbf{q}', \omega) \left[c_{\mathbf{k}'+\mathbf{q}', \sigma'}^\dagger c_{\mathbf{k}', \sigma'}, c_{\mathbf{k}+\mathbf{q}, \sigma}^\dagger c_{\mathbf{k}, \sigma} \right] &= \frac{1}{\Omega} \sum_{\mathbf{q}'} e\Phi(\mathbf{q}', \omega) \left(c_{\mathbf{k}+\mathbf{q}+\mathbf{q}', \sigma}^\dagger c_{\mathbf{k}, \sigma} - c_{\mathbf{k}+\mathbf{q}, \sigma}^\dagger c_{\mathbf{k}-\mathbf{q}', \sigma} \right) \\ &\approx \frac{1}{\Omega} e\Phi(\mathbf{q}, \omega) \left(c_{\mathbf{k}\sigma}^\dagger c_{\mathbf{k}\sigma} - c_{\mathbf{k}+\mathbf{q}, \sigma}^\dagger c_{\mathbf{k}+\mathbf{q}, \sigma} \right). \end{aligned} \quad (2.3.26)$$

The last term was approximated by considering only terms of the summation for $\mathbf{q}' = -\mathbf{q}$. This may be justified by the fact, that for any \mathbf{q}' the matrix elements of $c_{\mathbf{k}+\mathbf{q}+\mathbf{q}, \sigma}^\dagger c_{\mathbf{k}\sigma}$ and of $c_{\mathbf{k}+\mathbf{q}, \sigma}^\dagger c_{\mathbf{k}-\mathbf{q}', \sigma}$ are complex values with non correlated phase factors.

For a sum over all \mathbf{q}' it is assumed that they average out to zero except for $\mathbf{q}' = -\mathbf{q}$ which gives this approach the name random phase approximation.

Due to the oscillating time dependence (c.f. Eq. (2.3.23)) we can write the time evolution of the expectation value of the annihilation/creation operators as [26]

$$\begin{aligned} -i\hbar \frac{d}{dt} \langle c_{\mathbf{k}+\mathbf{q},\sigma}^\dagger c_{\mathbf{k},\sigma} \rangle &= \hbar(\omega + i\delta) \langle c_{\mathbf{k}+\mathbf{q},\sigma}^\dagger c_{\mathbf{k},\sigma} \rangle \\ &= (\varepsilon_{\mathbf{k}+\mathbf{q}} - \varepsilon_{\mathbf{k}}) \langle c_{\mathbf{k}+\mathbf{q},\sigma}^\dagger c_{\mathbf{k},\sigma} \rangle + \frac{1}{\Omega} e\Phi(\mathbf{q}, \omega) \left(\langle c_{\mathbf{k}\sigma}^\dagger c_{\mathbf{k}\sigma} \rangle - \langle c_{\mathbf{k}+\mathbf{q},\sigma}^\dagger c_{\mathbf{k}+\mathbf{q},\sigma} \rangle \right). \end{aligned} \quad (2.3.27)$$

Introducing the Fermi function $f_{\mathbf{k}\sigma} = \langle c_{\mathbf{k},\sigma}^\dagger c_{\mathbf{k},\sigma} \rangle$ this simplifies to

$$\langle c_{\mathbf{k}+\mathbf{q},\sigma}^\dagger c_{\mathbf{k},\sigma} \rangle = \frac{1}{\Omega} e\Phi(\mathbf{q}, \omega) \left(\frac{f_{\mathbf{k},\sigma} - f_{\mathbf{k}+\mathbf{q},\sigma}}{\varepsilon_{\mathbf{k}} - \varepsilon_{\mathbf{k}+\mathbf{q}} + \hbar\omega + i\delta} \right). \quad (2.3.28)$$

At last we can calculate the induced charge density from Eq. (2.3.22)

$$\rho^{\text{ind}}(\mathbf{q}, \omega) = e^2 \frac{\Phi(\mathbf{q}, \omega)}{\Omega} \sum_{\mathbf{k},\sigma} \left(\frac{f_{\mathbf{k},\sigma} - f_{\mathbf{k}+\mathbf{q},\sigma}}{\varepsilon_{\mathbf{k}} - \varepsilon_{\mathbf{k}+\mathbf{q}} + \hbar\omega + i\delta} \right) \quad (2.3.29)$$

and get Φ^{ind} from the Poisson equation (2.3.7)

$$\Phi^{\text{ind}}(\mathbf{q}, \omega) = \frac{1}{\varepsilon_0 q^2} \rho^{\text{ind}}(\mathbf{q}, \omega) = \frac{e^2}{\varepsilon_0 q^2} \frac{\Phi(\mathbf{q}, \omega)}{\Omega} \sum_{\mathbf{k},\sigma} \left(\frac{f_{\mathbf{k},\sigma} - f_{\mathbf{k}+\mathbf{q},\sigma}}{\varepsilon_{\mathbf{k}} - \varepsilon_{\mathbf{k}+\mathbf{q}} + \hbar\omega + i\delta} \right). \quad (2.3.30)$$

Equivalently we can write the interaction as

$$V^{\text{ind}}(\mathbf{q}, \omega) = \frac{e^2}{\varepsilon_0 q^2} \langle n(\mathbf{q}, \omega) \rangle. \quad (2.3.31)$$

If we use the bare Coulomb potential $v_q = \frac{e^2}{\varepsilon_0 q^2}$, the total potential $V(\mathbf{q}, \omega)$ and the polarization function $\Pi^0(\mathbf{q}, \omega)$ we can reformulate this to

$$V^{\text{ind}} = v_q V(\mathbf{q}, \omega) \Pi^0(\mathbf{q}, \omega) \quad (2.3.32)$$

for which the RPA polarization function is defined as

$$\Pi^0(\mathbf{q}, \omega) = \frac{1}{\Omega} \sum_{\mathbf{k},\sigma} \frac{f_{\mathbf{k},\sigma} - f_{\mathbf{k}+\mathbf{q},\sigma}}{\varepsilon_{\mathbf{k}} - \varepsilon_{\mathbf{k}+\mathbf{q}} + \hbar\omega + i\delta}. \quad (2.3.33)$$

Finally, the total perturbing potential yields

$$\begin{aligned} V(\mathbf{q}, \omega) &= V^{\text{ext}}(\mathbf{q}, \omega) + V^{\text{ind}}(\mathbf{q}, \omega) = V^{\text{ext}}(\mathbf{q}, \omega) + v_{\mathbf{q}}\Pi^0(\mathbf{q}, \omega)V(\mathbf{q}, \omega) \\ &= \frac{V^{\text{ext}}(\mathbf{q}, \omega)}{1 - v_{\mathbf{q}}\Pi^0(\mathbf{q}, \omega)} \end{aligned} \quad (2.3.34)$$

and the dielectric function is defined as

$$\varepsilon^{\text{RPA}}(\mathbf{q}, \omega) = 1 - v_{\mathbf{q}}\Pi^0(\mathbf{q}, \omega). \quad (2.3.35)$$

Thus the macroscopic dielectric function can be calculated microscopically just by knowing the band structure of the material: it is independent of the external perturbation and with that a pure material property.

As mentioned already, this result can also be obtained using Green's functions and Feynman diagrams through a diagrammatic expansion of the screened Coulomb interaction. As this expansion is not limited to the homogeneous electron gas, this derivation is more general but yields similar results as we have shown. The resulting *screened* Coulomb interaction is

$$V(\mathbf{q}, \omega) = \frac{v_{\mathbf{q}}}{1 - v_{\mathbf{q}}\Pi(\mathbf{q}, \omega)} \quad (2.3.36)$$

which is the same as we have found in Eq. (2.3.34) if the external potential is the bare Coulomb interaction $v_{\mathbf{q}}$ and the complete polarization function is approximated with the RPA polarization. For real materials a single band model is often not sufficient. Hence, a multi band and multi orbital description is needed in which the polarization becomes a fourth rank tensor. Using an orbital basis it can be written as [74, 83]

$$\Pi_{\alpha\beta\gamma\delta}^0(\mathbf{q}, \omega) = \sum_{\mathbf{k}, \sigma, \lambda_1, \lambda_2} M_{\lambda_1, \lambda_2}^{\alpha\beta\gamma\delta} \frac{f_{\mathbf{k}, \sigma}^{\lambda_1} - f_{\mathbf{k}+\mathbf{q}, \sigma}^{\lambda_2}}{\hbar\omega + i\eta + \varepsilon_{\mathbf{k}, \sigma}^{\lambda_1} - \varepsilon_{\mathbf{k}+\mathbf{q}, \sigma}^{\lambda_2}} \quad (2.3.37)$$

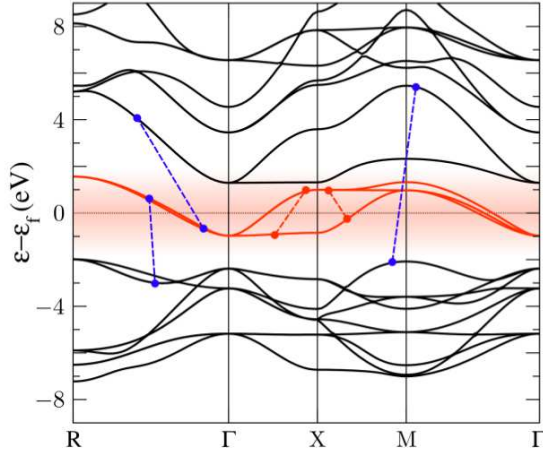
with the orbital indices $\alpha, \beta, \gamma, \delta$, the band indices λ_i and the overlap matrix elements

$$M_{\lambda_1, \lambda_2}^{\alpha\beta\gamma\delta} = (c_{\mathbf{k}, \lambda_1}^{\alpha})^* (c_{\mathbf{k}+\mathbf{q}, \lambda_2}^{\beta})^* c_{\mathbf{k}+\mathbf{q}, \lambda_2}^{\gamma} c_{\mathbf{k}, \lambda_1}^{\delta} \quad (2.3.38)$$

where the scalars $c_{\alpha, \mathbf{k}}^{\lambda}$ are the expansion coefficient of the eigenfunctions $|\Psi_{\lambda, \mathbf{k}}\rangle = \sum_{\alpha} c_{\alpha, \mathbf{k}}^{\lambda} |\mathbf{k}, \alpha\rangle$.

2.3.3. Constrained random phase approximation

The Coulomb interaction is essential to describe the material properties of a system on a realistic level. Especially the correct description of screening processes is important. Often, to simplify the problem, a material is modeled by restricting the description


Figure 2.3.1

LDA band structure of SrVO₃ from [91] with adaptations from [74]. The red bands mark the chosen subspace and the dashed lines virtual excitations. Blue lines correspond to the polarization of the rest and red lines belong to the model polarization.

to a subspace, i.e., only certain orbitals or bands are described [84]. The rest of the system is only considered through an *effective* screening. As the screening within the subspace is treated most of the time explicitly, to avoid double counting it has to be excluded from the effective Coulomb interaction. For this Aryasetiawan et al. [85] developed the *constrained random phase approximation* (cRPA) in 2004. We will just give a short introduction to the main ideas concerning cRPA. For further details, especially for the practical implementation, see Refs. [84, 86–90].

Screening processes can be understood as virtual transitions between all occupied and unoccupied states. In the cRPA the polarization function is separated in a model polarization, which only includes virtual transitions in the chosen subspace and the rest polarization including all other transitions

$$\Pi = \Pi_m + \Pi_r. \quad (2.3.39)$$

In Fig. 2.3.1 the LDA band structure of SrVO₃ is shown. The red area marks a chosen subspace in which a model can be set up for a more detailed investigation. Virtual transitions belonging to Π_m (marked with the red dashed lines) are strictly restricted to the chosen subspace. All other virtual excitations (dashed blue lines) are combined in the rest polarization Π_r .

With such a decomposed polarization function, the fully screened Coulomb interaction from Eq. (2.3.36) can be reformulated to

$$\begin{aligned} V &= \frac{v}{1 - v\Pi} \\ &= \frac{v}{1 - v(\Pi_m + \Pi_r)} = \frac{v}{\varepsilon_r(1 - \varepsilon_r^{-1}v\Pi_m)} \\ &= \frac{W_r}{1 - W_r\Pi_m}. \end{aligned} \quad (2.3.40)$$

Here, we used the dielectric function of the rest subspace $\varepsilon_r = 1 - v\Pi_r$ and the partially screened Coulomb interaction $W_r = \frac{v}{\varepsilon_r}$. If we set up a model in which we calculate or use the polarization of the model subspace, we have to replace the bare Coulomb interaction v with a partially screened Coulomb interaction W_r to include all screening effects from the rest bands properly.

Although Π_r has to be known, often it is more convenient to calculate the full Π and Π_m within RPA and then derive $\Pi_r = \Pi - \Pi_m$ as their difference [86]. Afterwards Π_r can be used to get W_r for further calculations in the model subspace.

It is not always the case that bands of interest are that clearly separated from the rest as it is in SrVO₃. The model subspace can be entangled with the rest of the system which is a similar problem we already described in Section 2.1.3. To disentangle the subspaces several methods were proposed. They either use projection schemes similar to Section 2.1.3 (see e.g. Miyake et al. [87]) or weighting methods to restrict the appearing summations when calculating the polarization functions (as proposed by for example Shih et al. [88] or Şaşıoğlu et al. [89]). Further information on the disentanglement schemes can be found in the mentioned references.

2.4. Many-Body Perturbation Theory

So far we have only discussed effective independent particle solutions to the many-body problem. Often the resulting Kohn-Sham eigenvalues are identified with the band energies of the material which works surprisingly well. Nevertheless, DFT underestimates the true band gap most of the time. On the one hand this is because of the approximations incorporated in the exchange-correlation potentials. On the other hand this is due to the band gap being an excited state property: the bottom of the conduction band is the lowest energy for adding an electron to the N electron system ($E_c = E^{N+1} - E_0^N$) and the top of the valence band is the lowest energy for removing an electron ($E_v = E_0^N - E^{N-1}$). All involved energies are ground state energies for N or $N \pm 1$ electrons, but still they describe *excitation* processes. [25]

Experimentally this is closely linked to photoelectron spectroscopy which measures the density of occupied (photoemission) and unoccupied (inverse photoemission) states [92]. In direct photoelectron spectroscopy an electron with kinetic energy E_{kin} is measured which was removed from the system due to the absorption of a photon with energy $\hbar\omega$. Under the assumption that the electron is decoupled from the system, the energy difference $\varepsilon_i = E_{\text{kin}} - \hbar\omega$ can be interpreted as the energy level of a hole or, in other words, an empty energy state previously occupied by the electron. This is equal to the difference $\varepsilon_i = E_0^N - E_i^{N-1}$ between the energy of the N particle ground state and the energy of the $(N - 1)$ state. In inverse photoelectron spectroscopy electrons are injected and a photon is emitted, yielding a $N + 1$ particle state with the energy difference $\varepsilon_i = E_i^{N+1} - E_0^N$.

The interpretation of photoelectron spectroscopy as density of occupied and unoccupied states (and with that the occupation of some well-defined energy level) is strongly linked to the independent particle picture [25]. In reality, since all electrons are correlated through Coulomb interaction, an addition or removal of an electron is a many-body process and will affect the other electrons (for example leading to relaxation). A nearly independent particle picture can be kept when we consider *quasiparticles*, i.e. due to the presence of the other particles *renormalized* single-particle energy levels. For example if an electron is injected in the sample, a Coulomb hole around this electron will be created due the Coulomb repulsion. The effective interaction between these quasiparticles (the ensemble of electron and Coulomb hole) is screened and thus weaker compared to the bare Coulomb interaction. As a result the quasiparticles are approximately independent from each other.

To describe these processes, we have to use a theory which can link the N -particle and $N \pm 1$ -particle systems. One way is the *Many-Body Perturbation Theory* using time-ordered Green's functions, which will be introduced in the next chapter. After that we will use Hedin's equations to derive the GW approximation to correct the Kohn-Sham eigenvalues. The following chapters are mainly based on the lecture notes by Friedrich and Schindlmayer [93] and complemented by the overviews by Aryasetiawan and Gunnarsson [94] and Onida, Reining and Rubio [92]. We will only give a basic overview of the used method. For further details, see for example the aforementioned overview papers and the book by Martin, Reining and Ceperley [25].

2.4.1. Green's functions

A central quantity for the Green's function formalism is the time-ordered correlation function for operator \hat{A} and \hat{B}

$$G_{AB}(t, t') = -\frac{i}{\hbar} \left\langle \Psi_0 \left| \hat{T} \hat{A}(t) \hat{B}(t') \right| \Psi_0 \right\rangle, \quad (2.4.1)$$

where Ψ_0 is the many-body ground state and \hat{T} is the time-ordering operator. It arranges the operators in order of ascending time arguments from right to left and includes a factor (-1) for every necessary permutation, i.e.

$$\hat{T} \hat{A}(t) \hat{B}(t') = \begin{cases} \hat{A}(t) \hat{B}(t') & \text{for } t > t' \\ -\hat{B}(t') \hat{A}(t) & \text{for } t' > t \end{cases}. \quad (2.4.2)$$

If \hat{A} and \hat{B} are fermionic or bosonic creation and annihilation operators, we will call this correlation function a *time-ordered Green's function*. The field operators $\hat{\psi}^{(\dagger)}(\mathbf{r}t)$

describe the annihilation (creation) of a fermion at position \mathbf{r} and time t . Using these in Eq. (2.4.1) gives the single-particle time-ordered Green function for fermions:

$$G(\mathbf{r}t, \mathbf{r}'t') = -\frac{i}{\hbar} \left\langle \Psi_0^N \left| \hat{T} \hat{\psi}(\mathbf{r}t) \hat{\psi}^\dagger(\mathbf{r}'t') \right| \Psi_0^N \right\rangle, \quad (2.4.3)$$

which describes, depending on the time ordering, the probability amplitude for the propagation of an additional electron ($t > t'$) or hole ($t < t'$) in a many-electron system. In other words: For $t > t'$ an additional electron is created in the N -particle system at \mathbf{r}' and later removed at \mathbf{r} . For $t < t'$ a hole is created at \mathbf{r} and later removed at \mathbf{r}' : the Green function describes the propagation of a hole.

This single-particle Green function contains information about the expectation values of arbitrary single-particle operators or the excitation spectrum of the many-body system. A single-particle operator in second quantization in terms of field operators is given by

$$\hat{O}(t) = \int d^3r d^3r' \langle \mathbf{r}' | \hat{O} | \mathbf{r} \rangle \hat{\psi}^\dagger(\mathbf{r}', t) \hat{\psi}(\mathbf{r}, t) = \int d^3r d^3r' \hat{O}(\mathbf{r}, \mathbf{r}') \hat{\psi}^\dagger(\mathbf{r}', t) \hat{\psi}(\mathbf{r}, t). \quad (2.4.4)$$

Then the expectation value can be written in terms of Green's functions:

$$\langle \hat{O}(t) \rangle = -i\hbar \int d^3r d^3r' \hat{O}(\mathbf{r}, \mathbf{r}') G(\mathbf{r}t, \mathbf{r}'t^+), \quad (2.4.5)$$

where we added an infinitesimal positive number $t^+ = \lim_{\varepsilon \rightarrow 0} t + \varepsilon$ to ensure the correct time ordering of the operators. For example the electron density $n(\mathbf{r})$ can be written in terms of Green's functions:

$$n(\mathbf{r}, t) = \langle \psi_0^N | \hat{\psi}^\dagger(\mathbf{r}t) \hat{\psi}(\mathbf{r}, t) | \psi_0^N \rangle = -i\hbar G(\mathbf{r}t, \mathbf{r}t^+). \quad (2.4.6)$$

For stationary systems with $\tau = t - t'$ it is often convenient to use the *Lehman representation*³ [95]. Therefore we insert the closure relation

$$\sum_i |\Psi_i^{N\pm 1}\rangle \langle \Psi_i^{N\pm 1}| = \mathbb{1}_{N\pm 1} \quad (2.4.7)$$

in Eq. (2.4.3) and perform a Fourier transformation to frequency space

$$G(\mathbf{r}, \mathbf{r}', \omega) = \sum_i \frac{\psi_i(\mathbf{r}) \psi_i^*(\mathbf{r}')}{\hbar\omega - \varepsilon_i + i\eta \text{sgn}(\mu - \varepsilon_i)}. \quad (2.4.8)$$

³A full derivation of the Lehman representation can be found for example in Ref. [93].

2. Theory and Methods

Here, we introduced η as infinitesimal small imaginary part to guarantee the convergence of the Fourier transform and used the chemical potential μ . We define the Lehman amplitudes

$$\psi_i(\mathbf{r}) = \begin{cases} \langle \Psi_i^{N-1} | \hat{\psi}(\mathbf{r}) | \Psi_0^N \rangle & \varepsilon_i < \mu \\ \langle \Psi_0^N | \hat{\psi}(\mathbf{r}) | \Psi_i^{N+1} \rangle & \varepsilon_i > \mu \end{cases} \quad (2.4.9)$$

and the quasiparticle energies

$$\varepsilon_i = \begin{cases} E_0^N - E_i^{N-1} & \varepsilon_i < \mu \\ E_i^{N+1} - E_0^N & \varepsilon_i > \mu \end{cases}, \quad (2.4.10)$$

which are the differences between the ground state energy E_0^N of the N particle system and the energies of $E_i^{N\pm 1}$ of excited states of the $(N \pm 1)$ -particle system. This means they correspond to electron addition and removal energies. In an interacting system quasiparticles are defined as particles which are dressed by a surrounding of virtual electron-hole pairs meaning that correlation effects renormalize the quasiparticle energies. They correspond to excitations of a $(N \pm 1)$ particle system and are the observable accessed in direct and inverse photoelectron spectroscopy [93]. In Eq. (2.4.8) it becomes evident that the Green's function has poles at the quasiparticle energies, so it indeed carries the information of the excitation spectrum and is thus important for describing many-body problems.

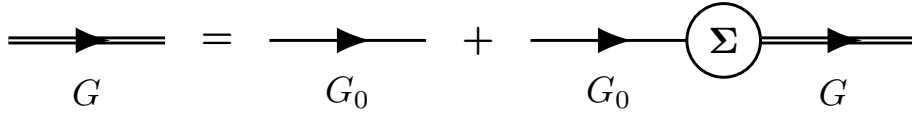
In this context we can define the *spectral function* [92]

$$A(\mathbf{r}, \mathbf{r}', \omega) = \left| \frac{1}{\pi} \text{Im} G(\mathbf{r}, \mathbf{r}', \omega) \right|, \quad (2.4.11)$$

which is the density of the quasiparticle states that contribute to the electron or hole propagation. In contrast to G the spectral function A and with that the quasiparticle spectrum can be measured for example in photoemission experiments. For a detailed derivation see Ref. [93].

For non-interacting systems A would reduce to a series of δ -peaks at the single-particle energies giving the well known density of states. Many-body correlation effects in the interacting system lead to a broadening Γ_i and shift of these peaks to the quasiparticle energies ε_i :

$$A(\mathbf{r}, \mathbf{r}', \omega) = \sum_i \psi_i(\mathbf{r}) \psi_i^*(\mathbf{r}') \frac{\Gamma_i}{(\hbar\omega - \varepsilon_i)^2 + \Gamma_i^2}. \quad (2.4.12)$$


Figure 2.4.1.

Dyson equation in terms of Feynman diagrams. A single line represents the non-interacting Green's function connected with the interacting Green's function (double line) by Σ .

The Green's function of Eq. (2.4.3) includes all correlation effects. Additionally, we can define a non-interacting Green's function

$$G_0(\mathbf{k}, \omega) = \frac{1}{\omega - H_0(\mathbf{k})} \quad (2.4.13)$$

where H_0 describes a non-interacting Hamiltonian (in a mean-field way) as for example from Eq. (2.2.14) minus the exchange-correlation potential. This means H_0 includes the kinetic and external potential as well as the Hartree potential. To connect the full Green function G with G_0 we introduce the self-energy Σ , which contains all interaction and correlation effects. The real part of Σ is directly related to the shifts to the quasiparticle energies in the spectral function Eq. (2.4.12) and the imaginary part is associated with the broadening of the peaks and thus with the lifetime of the quasiparticle. [94] The relation between interacting and non-interacting Green's function is given by the Dyson equation [96] as shown in Fig. 2.4.1 in terms of Feynman diagrams:

$$G(\mathbf{k}, \omega) = G_0(\mathbf{k}, \omega) + G_0(\mathbf{k}, \omega)\Sigma(\mathbf{k}, \omega)G(\mathbf{k}, \omega) \quad (2.4.14)$$

or in real space

$$G(\mathbf{r}, \mathbf{r}', \omega) = G_0(\mathbf{r}, \mathbf{r}', \omega) + \int \int d^3r'' d^3r''' G_0(\mathbf{r}, \mathbf{r}'', \omega)\Sigma(\mathbf{r}'', \mathbf{r}''', \omega)G(\mathbf{r}''', \mathbf{r}', \omega). \quad (2.4.15)$$

This is a self-consistent problem with a non-local, non-hermitian self-energy. If the self-energy was known the full many-body Green function could be calculated and with that the many-body system could be completely described. This turns out to be a difficult task, so approximations, e.g. the so called GW approximation, are needed and will be discussed later. The Dyson equation defines the self-energy as difference of the inverse of both Green's functions:

$$\Sigma(\mathbf{k}, \omega) = G_0^{-1}(\mathbf{k}, \omega) - G^{-1}(\mathbf{k}, \omega). \quad (2.4.16)$$

Using the representation of G_0 from Eq. (2.4.13) and Eq. (2.4.16) the full Green function can be written as

$$G(\mathbf{k}, \omega) = \frac{1}{\omega - H_0(\mathbf{k}) - \Sigma(\mathbf{k}, \omega)}, \quad (2.4.17)$$

which illustrates, that the self-energy indeed renormalizes the non-interacting system due to interaction effects.

Now we turn to derive a *quasiparticle* equation for the interacting system to demonstrate the particle-like behavior of the quasiparticles. Therefore, we use the equation of motion for a Green's function (from which the Dyson equation is the integral form of) [93]

$$i\hbar \frac{\partial}{\partial t} G(\mathbf{r}t, \mathbf{r}'t') = \delta(\mathbf{r} - \mathbf{r}')\delta(t - t') + H_0(\mathbf{r})G(\mathbf{r}t, \mathbf{r}'t') \quad (2.4.18)$$

$$-i\hbar \int v(\mathbf{r}, \mathbf{r}'')G_2(\mathbf{r}''t, \mathbf{r}'t'; \mathbf{r}t, \mathbf{r}'t')d^3r''. \quad (2.4.19)$$

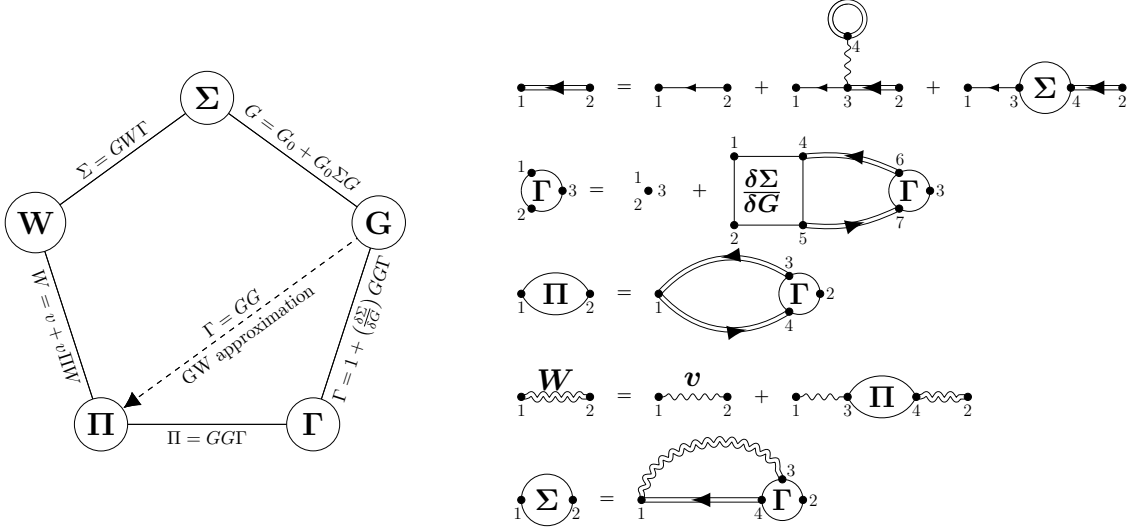
Because the single-particle Green's function depend not only on G but also on the two-particle Green's function G_2 this equation is not closed. A hierarchy of equation of motions is generated which has to be truncated at some point. This can be done by following a functional-derivative method [93, 94, 97] and introducing an external potential, which can be set to zero in the end. This will formally exclude higher order Green's functions and include the self-energy we defined before. A full derivation can be found in Ref. [93, 97]. The resulting equation of motion in the frequency domain (thus for a stationary system) becomes [93]

$$[\hbar\omega - H_0(\mathbf{r})]G(\mathbf{r}, \mathbf{r}', \omega) - \int \Sigma(\mathbf{r}, \mathbf{r}'', \omega)G(\mathbf{r}'', \mathbf{r}', \omega)d^3r'' = \delta(\mathbf{r} - \mathbf{r}'). \quad (2.4.20)$$

Inserting Eq. (2.4.8) and taking the so called quasiparticle limit $\omega \rightarrow \varepsilon_i/\hbar$, yields the quasiparticle equation [93]

$$H_0(\mathbf{r})\psi_i(\mathbf{r}) + \int \Sigma(\mathbf{r}, \mathbf{r}', \varepsilon_i/\hbar)\psi_i(\mathbf{r}')d^3r' = \varepsilon_i\psi_i(\mathbf{r}), \quad (2.4.21)$$

which is a nonlinear differential equation in ε_i (as Σ depends on ε_i). It has the form of a single-particle Schrödinger's equation with a non-local potential namely the self-energy. Since Σ includes all dynamic many-electron processes it is not a mean-field formulation. The eigenvalues are the (complex) quasiparticle energies ε_i and its eigenfunctions are the non-orthogonal quasiparticle states ψ_i . Both quantities have to be understood as properties of the many-electron system. Eq. (2.4.21) just emphasizes the concept of a quasiparticle where single-particle energies are renormalized due to interaction effects.


Figure 2.4.2.

Left: Self-consistency cycle to calculate the full interacting Green's function adapted from Ref. [99]. The dashed arrow mark the *GW* approximation in which vertex corrections are neglected. Right: Feynman diagrams of the Hedin equations from Eq. (2.4.22) - (2.4.26) adapted from Ref. [25]. Double (single) lines represent the (non-)interacting Green's function and single (double) wobbly lines correspond to the bare (fully screened) Coulomb interaction.

2.4.2. Hedin's equations

To derive the quasiparticle energies, we need the self-energy. The *Hedin equations* [97, 98] are a set of closed self-consistent equations to determine Σ which can be in principle used to solve the many-electron system:

$$\Sigma(1, 2) = i\hbar \int d(34)W(1^+3)G(14)\Gamma(423) \quad (2.4.22)$$

$$G(1, 2) = G_0(12) + \int d(34)G_0(13)\Sigma(34)G(42) \quad (2.4.23)$$

$$\Gamma(123) = \delta(12)\delta(13) - \int d(4567)\frac{\delta\Sigma(12)}{\delta G(45)}G(56)\Gamma(67, 3)G(74) \quad (2.4.24)$$

$$\Pi(12) = -i\hbar \int d(34)G(13)\Gamma(342)G(41) \quad (2.4.25)$$

$$W(12) = v(12) + \int d(34)v(13)\Pi(34)W(42) = \int d3\varepsilon^{-1}(13)v(32). \quad (2.4.26)$$

Here, we introduced the abbreviation $1 = (\mathbf{r}_1, t_1)$, with η as infinitesimal small number to ensure the correct time ordering $1^+ = (\mathbf{r}_1, t_1 + \eta)$ and $\delta(12) = \delta(\mathbf{r}_1 - \mathbf{r}_2)\delta(t_1 - t_2)$. The bare Coulomb interaction is $v(12)$.

The self-energy Σ is defined by the *screened* Coulomb interaction W and the *vertex*-correction Γ , a non-local potential which contains information about the exchange-correlation interaction between electron and hole. Eq. (2.4.23) is the already shown Dyson equation. The screened Coulomb interaction depends on the *complete* polarization function Π which includes again the vertex corrections. A visual account of Hedin's equations in terms of Feynman diagrams are shown in Fig. 2.4.2. Straight lines represent the Green's function (a single line meaning the non-interacting G_0 and double lines the full interacting G) and the (double) wiggly lines are the (screened) interactions. The polarization function is represented by the polarization bubble with additional vertex corrections. Also shown in Fig. 2.4.2 is the self-consistency cycle for solving Hedin's equations. With the non-interacting Green function G_0 (for example taken from DFT calculations) the vertex corrections can be calculated. Afterwards the polarization can be evaluated to derive the screened Coulomb interaction which is in turn necessary for the self-energy. With that a interacting Green function G is calculated.

Hedin's equations are in principle exact but very difficult to solve, especially the evaluation of the functional derivative for the vertex correction [25, 92], hence suitable approximations are needed. The simplest and a widely used approach is the *GW* approximation, which shall be discussed in the next chapter.

2.4.3. GW approximation

In the *GW* approximation, vertex corrections are neglected, meaning that

$$\Gamma(123) = \delta(12)\delta(13) \quad (2.4.27)$$

is assumed to be diagonal in space and time. With that electron-hole interactions (meaning excitonic effects) and corrections to the polarization function are not taken into account. Following Hedin's equation the resulting polarization is the polarization function in random phase approximation

$$\Pi(12) = -i\hbar G(12)G(21) \quad (2.4.28)$$

and the self-energy is given by

$$\Sigma(12) = iG(12)W(1^+2). \quad (2.4.29)$$

The assumption that the self-energy only depends on the Green's function and the dynamically screened Coulomb interaction gave the approximation the known name *GW approximation*. The equations to solve are a many-body self-consistent problem

corresponding to the short-cut indicated in the self-consistency cycle from Fig. 2.4.2. The comparatively simple form of the self-energy allows for computing the interacting Green's function from the non-interacting (but still in a mean-field way) G_0 .

The GW self-energy is an extension of the Hartree-Fock self-energy in which the bare Coulomb interaction is replaced with a *dynamical screened* interaction incorporating energy-dependent correlation effects not included in a single-particle picture. This becomes even more evident when the self-energy is separated in two parts: a exchange self-energy $\Sigma_X = iGv$ and a correlation part $\Sigma_{\text{Cor}} = iG\bar{W}$ with $\bar{W} = W - v$. While the exchange self-energy is static, the correlation part is non-Hermitian, non-local and dynamical resulting in the finite lifetimes of the quasiparticle and producing satellite structures in the spectral functions [100].

The first iteration (meaning to use G_0) already yields quite accurate results for electronic properties [92] as, for example, excitation energies and band gaps [94, 101, 102] or quasiparticle life times [103–105]. Actually, it turns out that a self-consistent GW approximation performs worse than just using one iteration [92]. So if improvements beyond GW are needed, approximations to the vertex corrections have to be done which shall not be part of this work. The interested reader is referred to Ref. [25, 92, 94] and the references therein.

Even though the GW approximation is comparatively simpler than the full set of equations, it is still computationally very expensive. To reduce the numerical effort but keep the accuracy of the calculations, often simplifications are used. One possible approach is the static limit of the GW self-energy, first proposed by Hedin himself [97]: The real part of the self-energy is divided in two parts: a screened exchange and a Coulomb hole term, giving the name static *COHSEX* approximation. Formally it can be derived from the real part of the self-energy $\text{Re } \Sigma = \Sigma_{\text{SEX}} + \Sigma_{\text{COH}}$ with [101]

$$\Sigma_{\text{SEX}}(\mathbf{r}, \mathbf{r}', \omega) = - \sum_i^{\text{occ}} \psi_i(\mathbf{r}) \psi_i^*(\mathbf{r}') W(\mathbf{r}, \mathbf{r}', \omega - \varepsilon_i/\hbar) \quad (2.4.30)$$

$$\Sigma_{\text{COH}}(\mathbf{r}, \mathbf{r}', \omega) = \sum_i \psi_i(\mathbf{r}) \psi_i^*(\mathbf{r}') \mathcal{P} \int_0^\infty d\omega' \frac{B(\mathbf{r}, \mathbf{r}', \omega')}{\omega - \varepsilon_i/\hbar - \omega'} \quad (2.4.31)$$

where a spectral representation of the screened interaction [101]

$$W(\mathbf{r}, \mathbf{r}', \omega) = v(\mathbf{r}, \mathbf{r}') + \int_0^\infty d\omega' \frac{2\omega' B(\mathbf{r}, \mathbf{r}', \omega')}{\omega^2 - (\omega' - i\eta^+)^2} \quad (2.4.32)$$

was used. The spectral function $B(\mathbf{r}, \mathbf{r}', \omega')$ is related to the imaginary part of W . The static limit of Eq. (2.4.30) and Eq. (2.4.31) yields [94, 100, 101]

$$\Sigma_{\text{SEX}}^{\text{static}}(\mathbf{r}, \mathbf{r}') = - \sum_i^{\text{occ}} \psi_i(\mathbf{r}) \psi_i(\mathbf{r}') W(\mathbf{r}, \mathbf{r}', \omega = 0) \quad (2.4.33)$$

$$\Sigma_{\text{COH}}^{\text{static}}(\mathbf{r}, \mathbf{r}') = \frac{1}{2} \delta(\mathbf{r} - \mathbf{r}') \overline{W}(\mathbf{r}, \mathbf{r}', \omega = 0). \quad (2.4.34)$$

The screened-exchange part of the self-energy accounts for quantum mechanical exchange effects, while the Coulomb hole term describes a charged hole due to electron removal or addition. The COHSEX approximation gives reasonable results with a reduced numerical effort due to the now local Coulomb hole term. However it overestimates the magnitude of the self-energy [101] resulting in an overestimation of the band gaps compared to GW calculations.

When interested in the quasiparticle energies E_i^{QP} (i.e., the band structure) of a system, often it is more convenient to calculate the energies from the quasiparticle equation Eq. (2.4.21) instead of solving the Dyson equation. Surprisingly, the quasiparticle wave functions $\psi_i(\mathbf{r})$ are quite well approximated by the Kohn-Sham eigenfunctions $\varphi_i^{\text{KS}}(\mathbf{r})$ meaning $\psi_i(\mathbf{r}) \approx \varphi_i^{\text{KS}}(\mathbf{r})$ [101, 106] and thus the Kohn-Sham eigenvalues E_i^{DFT} already give a reasonable estimate of the band structure. Hence the self-energy correction $\Sigma(\mathbf{r}, \mathbf{r}', E_i^{\text{QP}}) - V_{\text{XC}}\delta(\mathbf{r} - \mathbf{r}')$ seems to be small and we can use first-order perturbation theory to approximate the quasiparticle energies:

$$E_i^{\text{QP}} \approx E_i^{\text{DFT}} + \left\langle \varphi_i^{\text{DFT}} \left| \Sigma \left(E_i^{\text{QP}} \right) - V_{\text{XC}} \right| \varphi_i^{\text{DFT}} \right\rangle. \quad (2.4.35)$$

This equation is still non linear and the full energy spectrum have to be known for its solution. We can simplify it with a linear expansion of the self-energy [93, 107]

$$\Sigma \left(E_i^{\text{QP}} \right) \approx \Sigma(E_i^{\text{DFT}}) + \left(E_i^{\text{QP}} - E_i^{\text{DFT}} \right) \left. \frac{\partial \Sigma(E)}{\partial E} \right|_{E=E_i^{\text{DFT}}} \quad (2.4.36)$$

leading to

$$E_i^{\text{QP}} \approx E_i^{\text{DFT}} + Z_i \left\langle \varphi_i^{\text{DFT}} \left| \Sigma \left(E_i^{\text{DFT}} \right) - V_{\text{XC}} \right| \varphi_i^{\text{DFT}} \right\rangle \quad (2.4.37)$$

with the quasiparticle renormalization factor

$$Z_i = \left(1 - \left\langle \varphi_i^{\text{DFT}} \left| \frac{\partial \Sigma(E)}{\partial E} \right|_{E=E_i^{\text{DFT}}} \right| \varphi_i^{\text{DFT}} \right\rangle \right)^{-1}. \quad (2.4.38)$$

Eq. (2.4.37) can be used to calculate the quasiparticle energies as corrections to the DFT eigenenergies resulting from the GW self-energy. This is at least possible for

the first iteration of the self-consistency cycle, which is often called G_0W_0 approximation (with W_0 the screened Coulomb interaction calculated with the non-interacting Green's function G_0).

2.5. Excitons

So far we only discussed how to derive band structures and (quasiparticle) band gaps. However this is not sufficient to explain many phenomena as for example optical properties. Therefore *two-particle correlations* directly resulting from the Coulomb interaction have to be taken into account.

For example, the lowest absorbed light frequency, i.e., the optical band gap, found in absorption spectra is smaller than the quasiparticle band gap. The photon excites electrons from occupied to unoccupied states, leaving a hole in the valence band. Due to the attractive Coulomb interaction between electron and hole an optically active *excitonic* state is formed. The electron and hole do not move independently anymore but form a new quasiparticle which is called *exciton*. In this chapter we want to give a short introduction to their description. The interested reader is referred to Ref. [23, 25, 108] and references therein for a detailed overview of two-particle correlations and optical properties of semiconductors. This chapter is based on the corresponding chapters in Ref. [23] complemented by Ref. [25, 108]. There are several approaches to treat excitonic states (or in general two-particle correlations), two of them will be briefly introduced in the following.

Due to the Coulomb interaction, electron and hole do not move independently, so the problem at hand is a two-particle problem which can be described in general with a two-particle Green's function $G_2(1, 2, 1', 2')$ or a two-particle correlation function

$$L(1, 2, 1', 2') = -G_2(1, 2, 1', 2') + G(1, 1')G(2, 2') \quad (2.5.1)$$

(adopting the notation of the previous chapters). These function inhibits information about the propagation of two particles, which can be electron and hole, but also electron and electron or hole and hole. The Dyson equation of the two-particle correlation function is the *Bethe-Salpeter-equation* [109]

$$L(1, 2, 1', 2') = L_0(1, 2, 1', 2') + \int d3'd3d4d4' L_0(1, 3', 1', 3)\Xi(3, 4, 3', 4')L(4', 2, 4, 2'), \quad (2.5.2)$$

which describes a linear response of the single-particle Green's function to a in general non-local (in space, spin and time) potential [110]. The uncorrelated contribution $L_0(1, 2, 1', 2') = G(1, 2')G(2, 1')$ contains the single-particle Green's function

described by the Dyson equation Eq. (2.4.14) and $i\Xi$ is an interaction kernel which includes information about the many-body interactions in the system

$$\Xi(3, 2, 3', 2') = -i\delta(3, 3')\delta(2^+, 2)v(3^+, 2) + \frac{\delta\Sigma^{\text{XC}}(3, 3')}{\delta G(2', 2)} \quad (2.5.3)$$

with the bare Coulomb interaction v and the exchange-correlation self-energy Σ^{XC} . Treating the Bethe-Salpeter-equation is a very complex and computational demanding task, which is not part of this work. Under well defined assumptions (e.g. neglecting dynamical effects) the Bethe-Salpeter-equation can be reduced to solving an effective hydrogen Schrödinger's equation with effective masses μ of the exciton [25, 111, 112]

$$\left(-\frac{\nabla^2}{2\mu} - \frac{1}{\epsilon r}\right)\Psi(\mathbf{r}) = E\Psi(\mathbf{r}), \quad (2.5.4)$$

which is also known as *Wannier equation* [113].

Additionally, the optical response of a system due to an external field can be described with the *semiconductor Bloch equations* [114] which are equation of motions for the electron/hole distribution $f_{\mathbf{k}}^{e/h}$ and for the macroscopic polarization $P_{\mathbf{k}}$ [108]

$$\frac{\partial}{\partial t}f_{\mathbf{k}}^e = -2\text{Im}(\Omega_{\mathbf{k}}P_{\mathbf{k}}^*) + \left.\frac{\partial f_{\mathbf{k}}^e}{\partial t}\right|_{\text{scatt}} \quad (2.5.5)$$

$$\frac{\partial}{\partial t}f_{\mathbf{k}}^h = -2\text{Im}(\Omega_{\mathbf{k}}P_{\mathbf{k}}^*) + \left.\frac{\partial f_{\mathbf{k}}^h}{\partial t}\right|_{\text{scatt}} \quad (2.5.6)$$

$$\frac{\partial P_{\mathbf{k}}}{\partial t} = -i\tilde{\epsilon}_{\mathbf{k}}P_{\mathbf{k}} - i(f_{\mathbf{k}}^e + f_{\mathbf{k}}^h - 1)\Omega_{\mathbf{k}} + \left.\frac{\partial P_{\mathbf{k}}}{\partial t}\right|_{\text{scatt}} \quad (2.5.7)$$

where we used the renormalized Rabi energy

$$\Omega_{\mathbf{k}} = \frac{1}{\hbar} \left(\mathbf{d} \cdot \mathbf{E} + \sum_{\mathbf{q} \neq \mathbf{k}} V_{\mathbf{k}-\mathbf{q}} P_{\mathbf{q}} \right), \quad (2.5.8)$$

which contains the external electric field \mathbf{E} , the dipole matrix element between the conduction and the valence band \mathbf{d} and the Coulomb matrix element $V_{\mathbf{k}-\mathbf{q}}$. The renormalized carrier energy

$$\tilde{\epsilon}_{\mathbf{k}} = \epsilon_{\mathbf{k}}^e + \epsilon_{\mathbf{k}}^h - \sum_{\mathbf{q} \neq \mathbf{k}} V_{\mathbf{k}-\mathbf{q}}(f_{\mathbf{q}}^e + f_{\mathbf{q}}^h) \quad (2.5.9)$$

contains the single-particle energies of an electron/hole $\epsilon_{\mathbf{k}}^{e/h}$. The *scattering* terms result from a hierarchical coupling to many-body interaction terms. A full deriva-

tion of the semiconductor Bloch equations starting from the two-band Hamiltonian coupled to an external field can be found in Refs. [23, 108]. For a linearized field ($\partial f_{\mathbf{k}}^{e/h}/\partial t = 0$), neglecting scattering terms and within the effective mass approximation, we can derive an inhomogeneous Schrödinger's equation where the homogeneous part is again the Wannier equation Eq. (2.5.4) [23]. As the Wannier equation is an important tool to describe excitons, we want to shortly discuss it in the following chapter.

2.5.1. Wannier equation

Excitons are bound states between electrons in the conduction band and holes in the valence band. To discuss their qualitative properties, we want to utilize a simple model now. In principle the complete many-body Hamiltonian taking into account the full Coulomb interaction has to be considered. To simplify the problem, we use a two-band model and neglect all Coulomb interactions except for the interaction between electrons in the conduction band and electrons in the valence band. That means we disregard the explicit interactions within the bands and put them effectively in the band structure $E_{c/v}$. For the Coulomb matrix elements we only consider direct terms since the exchange terms are only quantitative corrections but do not change the qualitative discussion. Then the Hamiltonian is

$$H_0 = \sum_{\mathbf{k}} \left(E_v(\mathbf{k}) c_{v\mathbf{k}}^\dagger c_{v\mathbf{k}} + E_c(\mathbf{k}) c_{c\mathbf{k}}^\dagger c_{c\mathbf{k}} \right) + \sum_{\mathbf{k}_1 \mathbf{k}_2 \mathbf{k}_3 \mathbf{k}_4} u_{\mathbf{k}_1 \mathbf{k}_2 \mathbf{k}_3 \mathbf{k}_4} c_{v\mathbf{k}_1}^\dagger c_{c\mathbf{k}_2}^\dagger c_{c\mathbf{k}_3} c_{v\mathbf{k}_4}. \quad (2.5.10)$$

with the Coulomb matrix element

$$u_{\mathbf{k}_1 \mathbf{k}_2 \mathbf{k}_3 \mathbf{k}_4} = \int d^3 r \int d^3 r' \varphi_{v\mathbf{k}_1}^*(\mathbf{r}) \varphi_{c\mathbf{k}_2}^*(\mathbf{r}') \frac{e^2}{\varepsilon |\mathbf{r} - \mathbf{r}'|} \varphi_{c\mathbf{k}_3}(\mathbf{r}') \varphi_{v\mathbf{k}_4}(\mathbf{r}), \quad (2.5.11)$$

where we introduce a static dielectric constant ε emanated by the screening from all other electrons and ions in the system. As already mentioned, if an electron is excited to the conduction band, a positively charged hole will remain in the valence band. With that we can introduce creation and annihilation operators for holes

$$h_{\mathbf{k}}^\dagger = c_{v\mathbf{k}} \quad \text{and} \quad h_{\mathbf{k}} = c_{v\mathbf{k}}^\dagger, \quad (2.5.12)$$

which are fermionic quasiparticles with $E_h = -E_v$. In the following we will simplify the notation by writing electron creation and annihilation operators as $e_{\mathbf{k}}^{(\dagger)} = c_{c\mathbf{k}}^{(\dagger)}$. Within the electron-hole picture the Hamiltonian becomes

$$H = \sum_{\mathbf{k}} \left(E_c(\mathbf{k}) e_{\mathbf{k}}^\dagger e_{\mathbf{k}} + E_h(\mathbf{k}) h_{\mathbf{k}}^\dagger h_{\mathbf{k}} \right) - \sum_{\mathbf{k}_1 \mathbf{k}_2 \mathbf{k}_3 \mathbf{k}_4} u_{\mathbf{k}_1 \mathbf{k}_2 \mathbf{k}_3 \mathbf{k}_4} h_{\mathbf{k}_1}^\dagger h_{\mathbf{k}_4} e_{\mathbf{k}_2}^\dagger e_{\mathbf{k}_3} \quad (2.5.13)$$

which emphasizes the attractive Coulomb interaction between electron and hole. In the ground state all valence states are occupied while all conduction band states are unoccupied. With that the many-body ground state can be written as product state

$$|\Phi_0\rangle = \prod_{\mathbf{k}} c_{v\mathbf{k}}^\dagger |0\rangle \quad (2.5.14)$$

with the ground state energy $E_0 = \sum_{\mathbf{k}} E_v(\mathbf{k})$. The simplest excited state is the transition of a single electron from the valence to the conduction band which is the linear combination over all possibilities to create an electron-hole pair

$$|\Phi\rangle = \sum_{\mathbf{k}, \mathbf{k}'} a_{\mathbf{k}\mathbf{k}'} e_{\mathbf{k}}^\dagger h_{\mathbf{k}'}^\dagger |\Phi_0\rangle \quad (2.5.15)$$

with the coefficients $a_{\mathbf{k}\mathbf{k}'}$ chosen such that $|\Phi\rangle$ becomes an eigenstate of Eq. (2.5.13). Calculating $H|\Phi\rangle$ using the fermionic anti-commutator relations yields a homogeneous system of equations for the coefficients:

$$a_{\mathbf{k}\mathbf{k}'}(E_0 - E + E_c(\mathbf{k}) - E_v(\mathbf{k}')) - \sum_{\mathbf{k}_1 \mathbf{k}_3} u_{\mathbf{k}_1 \mathbf{k} \mathbf{k}_3 \mathbf{k}'} a_{\mathbf{k}_1 \mathbf{k}_3} = 0. \quad (2.5.16)$$

Without any interaction the excitation energy would be

$$E - E_0 = E_c(\mathbf{k}) - E_v(\mathbf{k}'). \quad (2.5.17)$$

Consequently the attractive Coulomb interaction decreases the excitation energies in comparison to the band gap E_g . To simplify this model even further, we assume now an effective mass model for the single-particle energies and calculate the Coulomb matrix elements using plane waves instead of Bloch functions. This results in a two-particle Schrödinger's equation [23]

$$\left(-\frac{\hbar^2}{2m_c} \nabla_{\mathbf{r}_1}^2 - \frac{\hbar^2}{2m_v} \nabla_{\mathbf{r}_2}^2 - \frac{e^2}{\varepsilon |\mathbf{r}_1 - \mathbf{r}_2|} \right) \psi(\mathbf{r}_1, \mathbf{r}_2) = \tilde{E} \psi(\mathbf{r}_1, \mathbf{r}_2) \quad (2.5.18)$$

similar to the hydrogen problem. Introducing relative ($\mathbf{r} = \mathbf{r}_1 - \mathbf{r}_2$) and center-of-mass ($\mathbf{X} = \frac{m_c \mathbf{r}_1 + m_v \mathbf{r}_2}{m_c + m_v}$) coordinates we get

$$\left(-\frac{\hbar^2}{2(m_c + m_v)} \nabla_{\mathbf{X}}^2 - \frac{\hbar^2}{2\mu} \nabla_{\mathbf{r}}^2 - \frac{e^2}{\varepsilon r} \right) \psi = \tilde{E} \psi. \quad (2.5.19)$$

This can be solved via a separation of variables resulting in a free particle for the center-of-mass coordinate and the Wannier equation

$$\left(-\frac{\nabla_{\mathbf{r}}^2}{2\mu} - \frac{1}{\varepsilon r}\right) \Psi(\mathbf{r}) = E\Psi(\mathbf{r}), \quad (2.5.20)$$

for the relative coordinate, which is an effective hydrogen problem with the effective mass $\mu = \frac{m_c m_v}{m_c + m_v}$. As a result excitons are often described in the framework of the hydrogen problem with eigenfunctions $\psi_{\kappa,n}(\mathbf{X}, \mathbf{r}) = e^{i\kappa\mathbf{X}}\Psi_n(\mathbf{r})$ with $\Psi_n(\mathbf{r})$ being the hydrogen wave functions and the energy $\tilde{E} = \frac{\hbar^2 \kappa^2}{2(m_c + m_v)} - \frac{E_B}{(n-1/2)^2}$ for a two-dimensional system. The binding energy E_B is an important quantity of the exciton as it defines the energetic position of the lowest excited state E_1 (and with that what is often called the experimental accessible *optical* band gap):

$$E_1 = E_g - E_B \quad (2.5.21)$$

and can be defined analogous to the Rydberg energy

$$E_B = \frac{\mu e^4}{2\varepsilon^2 \hbar^2} = \frac{e^2}{2\varepsilon^2 a_0} \quad (2.5.22)$$

with the *exciton Bohr radius* a_0 which gives the spatial extent of the exciton. Thus, through the Coulomb interaction electron and hole are bound and form a new quasi-particle, the exciton, which lowers the measurable gap.

When deriving the Wannier equation, we used Bloch states, i.e. we assumed free particles and with that delocalized states for the non-interacting electrons and holes which now result in delocalized exciton states. Excitons described by the Wannier equation are also called *Wannier* or *Mott* excitons and have in general a larger spatial extent. Localized excitonic states, i.e. electron and hole are at the same atomic site or at least very close, are called *Frenkel* excitons and are often found in ionic or molecule crystals.

Even though the model shown here is quite simple, often it turns out that excitons can be described surprisingly well with a (modified) hydrogen like problem in bulk [23, 108, 115, 116] as well as in 2d system [117–120]. Sometimes more complex dielectric functions have to be utilized but the picture holds still in many cases.

3. Transition Metal Dichalcogenides

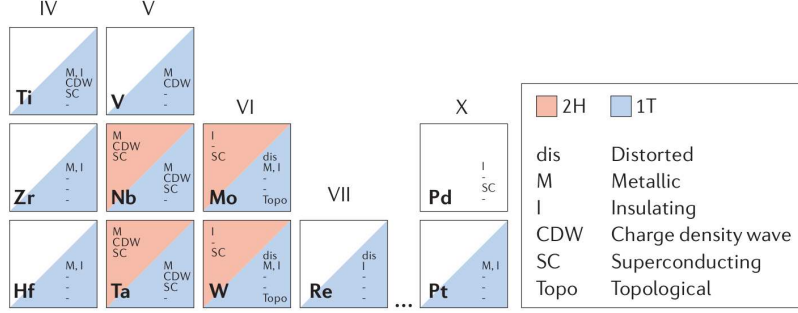
The experimental discovery of graphene [4, 7, 121] and the resulting Nobel prize for Novoselov and Geim in 2010 started an intense research in the field of two-dimensional (2d) materials. Many 2d materials exist in bulk form as *layered* materials with weak van-der-Waals interlayer attraction which allows for mechanically exfoliation [4] into atomically thin monolayers. The synthesis on an even larger scale is possible utilizing chemical vapor deposition [122] making them interesting for technical applications.

A large zoo of 2d materials beyond graphene are intensely studied such as graphene analogues like hexagonal boron nitride (hBN) [123, 124] and phosphorene [125, 126] or the class of transition metal dichalcogenides (TMDC) and titania- and perovskite-based oxides [127, 128]. In particular TMDCs regained interest in the last years as they exhibit promising electronic, optical, mechanical, chemical and thermal properties rendering them important for studying novel fundamental physics as well as for applications in nanoelectronics, nanophotonics or for sensing and actuation at the nanoscale [5, 129–132]. TMDCs have been studied for decades now. Its most prominent member, MoS₂, was investigated for the first time already in 1923 by Dickinson and Pauling [133] followed by extensive studies starting in the 1960s [134–137]. Especially in the last years a strong renaissance of activity in the field of 2d TMDCs have been seen due to the possibility to synthesize high-quality large-area mono crystals [138] allowing a wide range of experimental studies.

In this work we are interested in how many-body interactions, especially the electron-electron interaction, can influence the electronic and optical properties of semiconducting 2d TMDCs. In more detail, we want to find a new and unique way to engineer atomically thin materials. In this chapter, we will give a short overview of the, for this work relevant, electronic and optical properties of semiconducting TMDCs. Additionally we will explain the concept of *Coulomb engineering* which makes use of the peculiar Coulomb interaction in 2d to create a new kind of heterostructure which will be investigated in detail in the subsequent chapters.

3.1. Material properties

We will only outline a few important properties of semiconducting monolayer TMDCs. Thereby, we will give a short overview of the lattice structure and important electronic and optical properties of the ground state. We examine unstrained monolayer MoS₂ without any electron or hole doping as an example for the whole class of semi-


Figure 3.1.1.

Part of the periodic table from Ref. [131] showing the transition metals of known layered TMDCs. The colors mark existing structural phases (2H, 1T or other) and the presence of distorted structural phases and observed electronic phases are shown.

conducting TMDCs. Further details can be found in literature, as for example in Refs. [129–131, 139, 140] and the references therein.

3.1.1. Lattice structure

TMDCs consist of a combination of a transition metal M , mostly from the group IV, V and VI sandwiched between two chalcogen atoms X namely S, Se and Te (c.f. Fig. 3.1.1). In three dimensions strongly bound layers are coupled by weak van-der-Waals interaction. Different polytypes exist in the bulk phase, which differ in stacking order (as shown in Fig. 3.1.2) and metal atom coordination [129]. Depending on the polytype they can be metallic or semiconducting and show interesting phases like superconductivity or charge density waves [129]. Commonly, TMDCs are hexagonal or rhombohedral with either a trigonal prismatic (2H) or a octahedral (1T) coordination of the metal atoms (see Fig. 3.1.2). The transition metal/chalcogen combination defines if the 2H or 1T phase is thermodynamically stable. Nevertheless, the other phase can often be obtained as metastable phase [131].

In this work, we concentrate on semiconducting monolayers of TMDCs, namely MX_2 with $M \in \{W, Mo\}$ and $X \in \{S, Se\}$. They are stable in the hexagonal phase (see Fig. 3.1.2 resulting in a honeycomb lattice (like graphene) with the M atom on sublattice A and the X atom on the sublattice B. The chalcogen atoms are separated in z -direction. In the tetragonal phase, all three atoms are placed on different sublattices (see Fig. 3.1.2). With the lattice constant a_0 the hexagonal Bravais lattice is given by (c.f. Fig. 3.1.3a)

$$\mathbf{a}_1 = a_0 \begin{pmatrix} 1 \\ 0 \\ 0 \end{pmatrix} \quad \mathbf{a}_2 = \frac{a_0}{2} \begin{pmatrix} -1 \\ \sqrt{3} \\ 0 \end{pmatrix} \quad \mathbf{a}_3 = c \begin{pmatrix} 0 \\ 0 \\ 1 \end{pmatrix}. \quad (3.1.1)$$

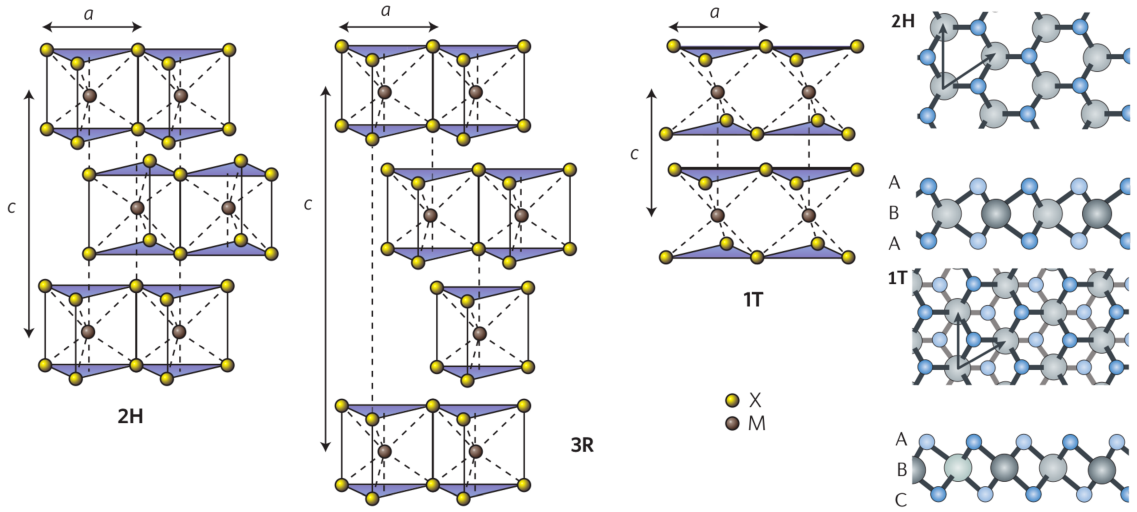


Figure 3.1.2.

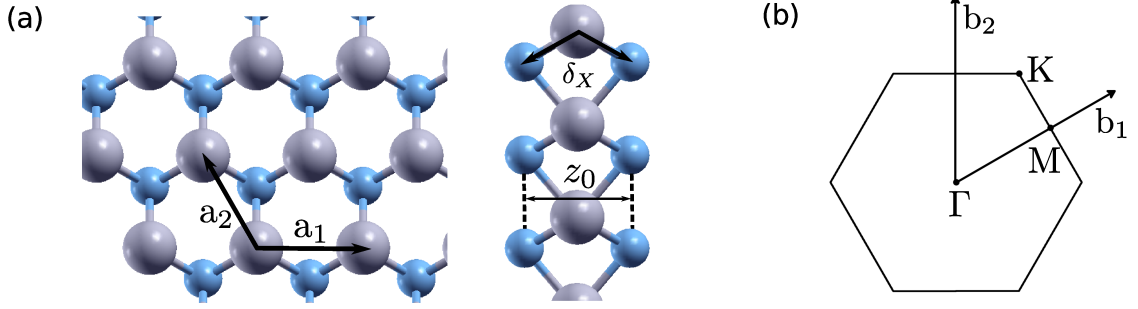
Schematic side view of different stacking order (2H, 3R and 1T) of MX₂ layer in the bulk phases from Ref.[129] and top views of the hexagonal and tetragonal phase of the monolayer from Ref. [131]. Transition metal atoms (M) are marked grey while the chalcogen atoms are colored yellow or blue.

In this basis, the angle between the vectors is chosen to be 120°, but a definition with a 60° angle is also possible. In general a_0 is mainly determined by the chalcogen atom. For example WS₂ has a experimental lattice constant of $a_0 \approx 3.15\text{\AA}$ and MoS₂ of $a_0 \approx 3.16\text{\AA}$, while WSe₂ and MoSe₂ both have $a_0 \approx 3.29\text{\AA}$. [141] The theoretical obtained values of the lattice parameter a_0 and z_0 are shown in Appendix A.1.1. The parameter c defines the supercell height including the vacuum above the monolayer. The atomic positions within the unit cell are (in the basis of the Bravais lattice):

$$\delta_M = \begin{pmatrix} 0 \\ 0 \\ 0 \end{pmatrix}_{\mathbf{a}} \quad \delta_X = \frac{1}{3} \begin{pmatrix} 1 \\ 2 \\ \pm X_z \end{pmatrix}_{\mathbf{a}}, \quad (3.1.2)$$

where $X_z = \frac{3}{2c}z_0$ is the z position of the chalcogen atoms which are separated by the distance z_0 . The 1. Brillouin zone of a hexagonal lattice is again a hexagonal lattice as shown in Fig. 3.1.3b with the reciprocal lattice vectors

$$\mathbf{b}_1 = \frac{2\pi}{a_0\sqrt{3}} \begin{pmatrix} \sqrt{3} \\ 1 \\ 0 \end{pmatrix}, \quad \mathbf{b}_2 = \frac{2\pi}{a_0\sqrt{3}} \begin{pmatrix} 0 \\ 2 \\ 0 \end{pmatrix} \quad \mathbf{b}_3 = \frac{2\pi}{a_0c} \begin{pmatrix} 0 \\ 0 \\ 1 \end{pmatrix} \quad (3.1.3)$$


Figure 3.1.3.

a) Lattice structure of TMDCs with lattice vectors \mathbf{a}_1 and \mathbf{a}_2 spanning the primitive unit cell. The sulfur distance is z_0 and the sulfur position is determined by δ_X . b) 1. Brillouin zone of a hexagonal lattice with reciprocal lattice vectors \mathbf{b}_1 and \mathbf{b}_2 .

and the high symmetry points in the basis of the reciprocal lattice:

$$\mathbf{K} = \frac{1}{3} \begin{pmatrix} 1 \\ 1 \end{pmatrix}_{\mathbf{b}}, \quad \mathbf{M} = \frac{1}{2} \begin{pmatrix} 1 \\ 0 \end{pmatrix}_{\mathbf{b}} \quad \text{and} \quad \mathbf{K}' = \frac{1}{3} \begin{pmatrix} 2 \\ -1 \end{pmatrix}_{\mathbf{b}}. \quad (3.1.4)$$

3.1.2. Electronic properties

As already mentioned in the previous section, depending on the structure and chemical composition, TMDCs can be semiconducting or metallic, exhibiting interesting correlated and topological phases. The four materials under consideration in this work show an indirect to direct band gap transition when going from bulk to the monolayer limit [129, 142, 143]. This is due to quantum confinement [144, 145] and a resulting change of hybridization between the p_z orbitals of the chalcogen atoms and the d orbitals of the metal atoms [142, 144, 146] which shifts the maxima of the valence band at \mathbf{K} and Γ as well as the minima of the conduction band.

All investigated materials show similar electronic properties with direct band gaps of the freestanding monolayer (determined by GW calculations) between 2.1 and 2.55 eV [147] depending on the material. The focus of this chapter will be on the description of MoS_2 as an example crystal for the MoX_2 and WX_2 compounds. The DFT band structure is shown in Fig. 3.1.4. For the band structures of the other materials, see Appendix A.1.1. We find different electron and hole valleys at \mathbf{K} , Γ and Σ in the highest valence and lowest conduction band and a direct (DFT) band gap of 1.7 eV at \mathbf{K} . The orbital characters (marked in color in Fig. 3.1.4) of the bands around the Fermi energy, which describe the *low-energy* states, have predominantly metallic d-orbital character with $m_l = 0$ (d_z^2) and $m_l = \pm 2$ ($d_{xy}, d_{x^2-y^2}$). Furthermore, they are completely decoupled from the other states with $m_l = \pm 1$ (d_{yz}, d_{xz}) due to symmetry reasons. Around Γ there is also weight of the sulfur p orbitals, especially in

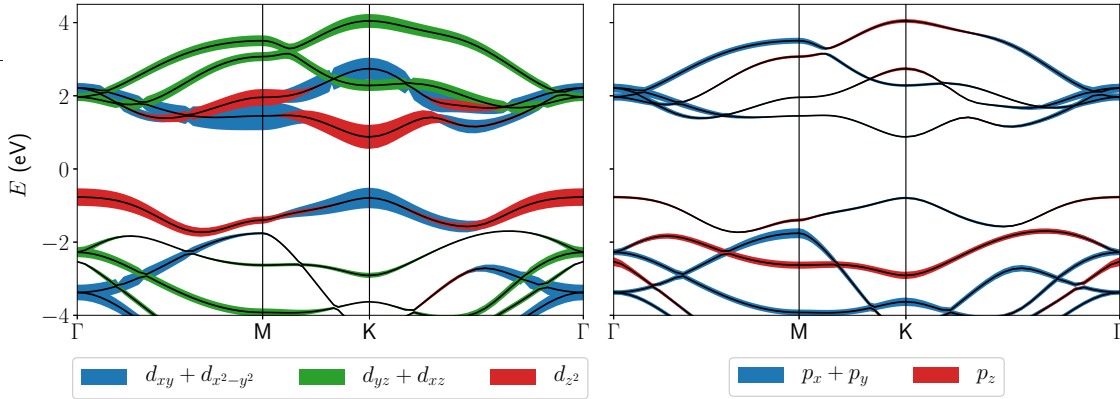


Figure 3.1.4.

Electronic band structure of monolayer MoS_2 in the hexagonal structure obtained from DFT. In the left panel the colored line width correspond to the Mo d orbital weights and in the right panel to the S p orbital weights.

the lowest conduction band (as can be seen in the right panel of Fig. 3.1.4) stemming mainly from the p_x and p_y states. The band gap in TMDCs is opened due to the strong hybridization between the metallic $m_l = \{0, \pm 2\}$ orbitals [137, 148] leading to a strong character variation within the low-energy bands. For example, at Γ the highest valence band has d_{z^2} character while we find this orbital weight in the lowest conduction band at \mathbf{K} .

Another property of 2H-TMDCs is a relatively strong spin-orbit splitting [149–151] of the electronic bands due to the lack of inversion symmetry in the monolayer limit, confinement of the electron motion in a plane and the high mass of the elements. Since \mathbf{K} and \mathbf{K}' are not time-reversal invariant momenta, the spin degeneracy at these points is lifted with an especially strong effect on the valence band. The spin splitting ranges between 0.15 and 0.45 eV [152] with the larger splitting found in the W based materials. Additionally due to the lack of inversion symmetry and the strong spin-orbit coupling a coupling of valley and spin physics is observed [153].

3.1.3. Optical properties

The electronic properties of TMDCs also influence their optical properties. For example is the transition from an indirect to a direct semiconductor in MoS_2 visible in absorption spectra [142] or by an enhancement of the photoluminescence [142, 144] making them promising for optical applications.

The theoretical [147] and experimental [142] absorption spectra are shown in Fig. 3.1.5. We find two sharp absorption peaks around 2 eV corresponding to the direct band gap transitions at the \mathbf{K} and \mathbf{K}' points separated by the spin-orbit splitting. The theoretical data was calculated using the RPA method (blue) and solving

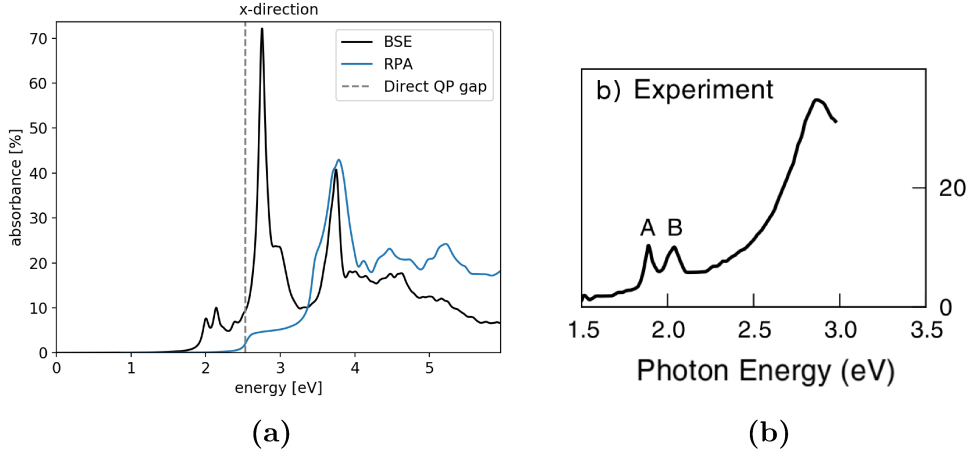
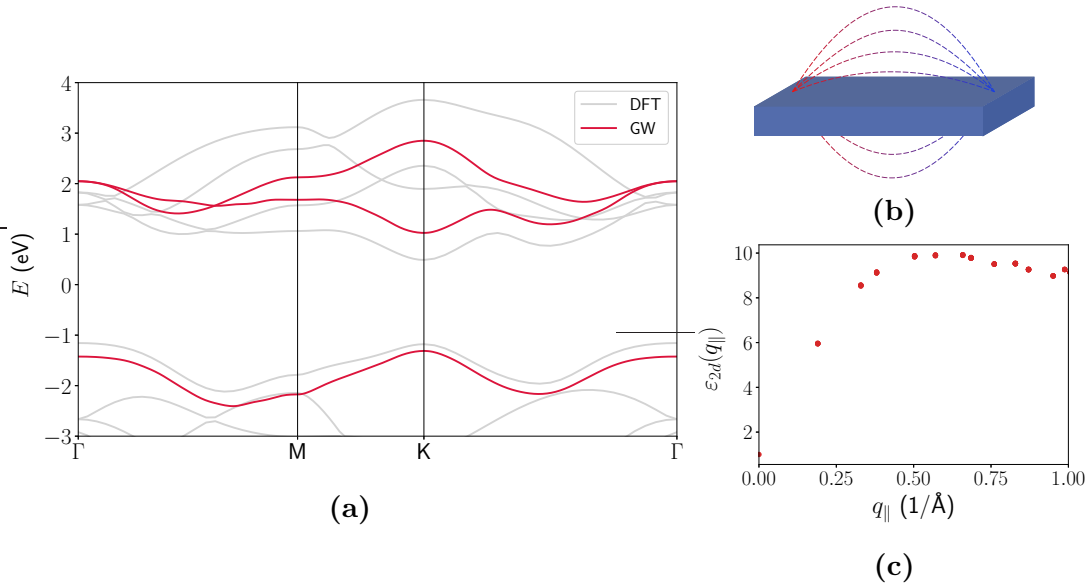


Figure 3.1.5.

(a) Absorption spectrum of MoS₂ calculated with the BSE equation compared to a spectrum derived with RPA. Taken from [147] (b) Experimental absorption spectrum of MoS₂ taken from [142].

the BSE on top of a *GW* input (black). The *GW* quasiparticle band gap is indicated as grey line. As described in Section 2.5 the BSE contain additional many-body effects beyond the *GW* approximation including electron-hole interactions. The absorption edge around 2.6 eV in the RPA data is due to inter-band absorption between the highest valence and lowest conduction band and thus gives the quasiparticle band gap. The peaks around 2 eV are not present in the RPA data, meaning these are excitonic states resulting from bound electron-hole pairs from the **K** and **K'** valleys. For a more detailed discussion on absorption spectra in 2d TMDCs see Refs. [21, 142, 154–156].

Due to the binding of the electron-hole pair the optical measurable band gap respectively the energy of any excitonic states is reduced in comparison to the quasiparticle band gap. The difference between the excitonic energy and the quasiparticle gap is the *exciton binding energy* E_b as introduced in Section 2.5.1. Binding energies in MoS₂ are on the order of several hundred meV, for the lowest exciton even on the order of 1 eV [157, 158] which is one magnitude larger than for conventional bulk systems [159, 160]. These large binding energies can be explained by screening effects in two-dimensional materials. The electron-hole binding results from the attractive Coulomb interaction. In two dimensions the screening is decreased and thus the Coulomb interaction is increased. Hence a stronger interaction yields larger binding energies. [21, 142, 155, 156, 161, 162] A more detailed discussion on the Coulomb interaction in 2d materials can be found in the following section.

**Figure 3.2.1.**

(a) G_0W_0 band structure of MoS₂ for the low-energy bands around the Fermi energy in comparison to the DFT band structure. Most importantly including correlation effects lead to an enhancement of the quasiparticle band gap. (b) Sketch of the electric field lines of a 2d material. (c) Static dielectric function of monolayer MoS₂ for the in-plane wave vectors q_{\parallel} .

3.2. Coulomb interaction in 2d materials

The peculiar Coulomb interaction in 2d materials is responsible for many of the interesting optoelectronic properties of 2d materials as for example excitonic (see Section 3.1.3) or plasmonic effects [83, 163, 164]. In 2d the Coulomb interactions between charge carriers is enhanced [118, 165, 166] compared to bulk materials because of weak internal screening [21, 120, 157]. In a simplified picture sketched in Fig. 3.2.1b this can be explained with field lines between two charges that do not pass only through the material itself as in bulk but also through its environment. The larger the distance of the charges the more field lines go outside of the monolayer. In vacuum this means that the long-range part of the interaction is only weakly if at all screened yielding highly non-local and remarkably strong Coulomb interactions [118, 154, 155, 157]. Thus the dielectric function is strongly \mathbf{q} dependent as shown for monolayer MoS₂ in Fig. 3.2.1c¹. For small wave-vectors \mathbf{q} the polarizability α of an isotropic 2d semiconductor is related to ε with: $\varepsilon(\mathbf{q}) = 1 + |\mathbf{q}|\alpha$ yielding the long wavelength limit $\varepsilon(\mathbf{q} \rightarrow 0) = 1$ [168].

¹The dielectric function was obtained using the Wannier Function Continuum Electrostatics [167] approach, which will be explained in Section 6.2.2

The weak intrinsic screening enhances effects of the self-energy and consequently has a direct influence on the quasiparticle band structure of a 2d material. As already discussed in Section 2.2, DFT calculations underestimate the absolute value of the band gap due to the neglect of Coulomb-interaction induced correlation and in particular non-local exchange effects. In 2d materials this can only be a crude approximation and more sophisticated methods have to be used, e.g. the G_0W_0 approximation introduced in Section 2.4.3. The resulting band structure compared to DFT results is shown in Fig. 3.2.1a for MoS₂. The main effect observed is an enhancement of the native band gap due to a stronger hybridization between the $m_l = \{0, \pm 2\}$ block. This mechanism will be discussed in more detail in Section 4.2.

Different calculations report a range of quasiparticle gaps for MoS₂ from 2.4 to 2.8 eV [19, 154, 157, 168] (without considering spin-orbit couplings) and even 2.3 eV with spin-orbit coupling [147]. A more sophisticated treatment of the Coulomb interaction thus increases the fundamental band gap from DFT calculations on the order of 1 eV.

Yet the wide range of reported quasiparticle band gaps already show that converging G_0W_0 calculations is not a simple task [155, 169]. On the one hand, various calculation parameters as the \mathbf{k} -point sampling or the energy cut-offs to ensure the inclusion of a sufficient number of empty states have to be carefully converged. Often, a compromise between numerical feasibility and converged results has to be found. On the other hand, the long-ranged tail of the Coulomb interaction leads to other numerical problems for G_0W_0 calculations of 2d materials. In practice the monolayer is embedded in a three dimensional cell where adjacent sheets are separated by a large vacuum distance h_{vac} . This *repeated slabs* create artificial screening between the layers and in turn reduce the resulting band gap. Thus, the inclusion of the Coulomb interaction and with that of the dielectric function must be done carefully taking into account that the dielectric function is highly \mathbf{q} dependent [155, 167]. There are several options to overcome this problem. Firstly, the band gaps can be extrapolated for infinite vacuum height from several calculations with different vacuum distances [19, 155]. Secondly, truncated Coulomb interactions are used to suppress the interaction between adjacent sheets [155, 170, 171]. A third approach uses the macroscopic screening properties of the bulk material to correct the long-ranged dielectric function of the monolayer [167]. A detailed description of this method called *Wannier function continuum electrostatics* (WFCE) can be found in Section 6.2.2. More details on the description of dielectric screening in 2d TMDCs are given in Ref. [168, 169].

Most important for our studies is that the interactions between charge carriers are highly sensitive to the local dielectric environments due to the additional screening. Thus in thin layers the Coulomb interaction can be drastically manipulated through external screening influencing the band gap on an electron Volt scale [19–21]. This has become a largely discussed field in the last few years as seen in Refs. [19, 21, 112, 120, 155, 161, 167, 172–187] and many more.

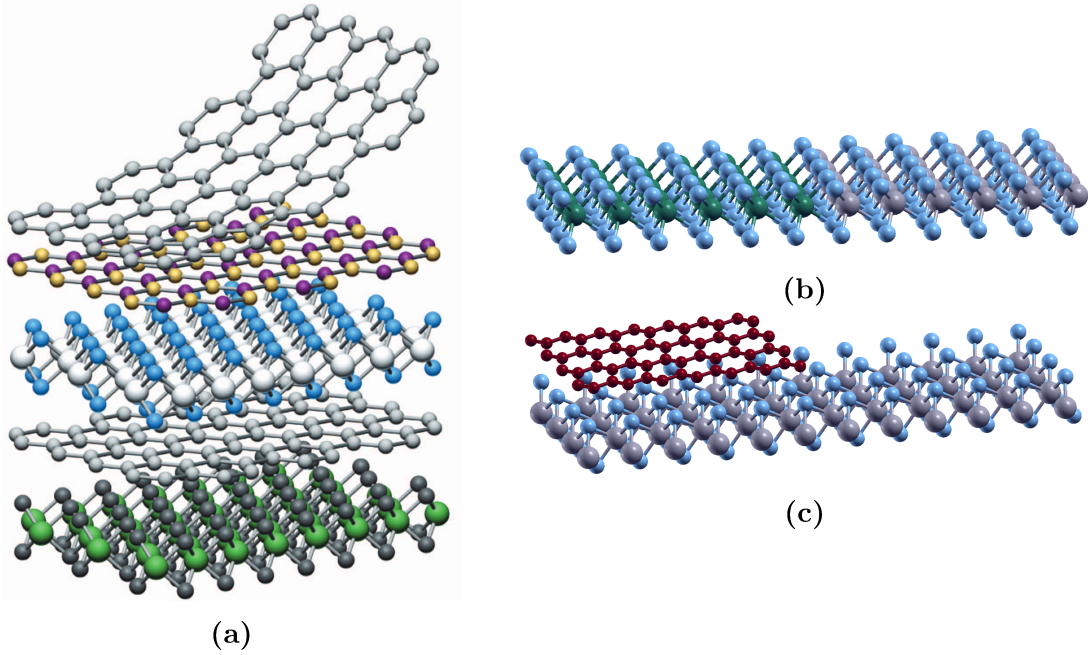


Figure 3.2.2.

Different possible heterostructures in 2d materials. (a) Van-der-Waals heterostructures taken from Ref.[6], where different 2d materials are stacked on top of each other. (b) Lateral heterostructure consisting of MoS_2 (grey spheres) and WS_2 (green spheres) (c) Coulomb engineered heterostructure with a spatially structured dielectric environment of graphene (red atoms) and vacuum.

The dependence of the band gap on screening allows for using substrates as external tuning knob for electronic properties leading to the possibility to induce heterojunction in homogeneous monolayer. This is the foundation for *Coulomb engineered* heterostructures, which will be discussed in more detail in the next chapter and throughout this thesis.

3.2.1. Coulomb engineering: Tuning the band gap

Heterojunctions are building blocks of various technical applications as transistors or solar cells. In 2d materials there are several possibilities to create the desired band gap modulations as depicted in Fig. 3.2.2. Vastly studied are *van-der-Waals*-heterostructures stacking different monolayers on top of each other [6, 12–18, 117] (Fig. 3.2.2a). Another approach especially in TMDCs due to their similar lattice constants are *lateral* heterostructures [8–11] where two materials are grown together parallel to the crystal plane (Fig. 3.2.2b). We make use of the peculiar properties described in the previous section to propose a new kind of heterostructure in which

we introduce laterally structured *environments* as shown in Fig. 3.2.2c to manipulate the quasiparticle band gap.

We introduced this so-called *Coulomb-engineered* heterostructures in 2016 [22]. First experiments supporting our findings followed shortly afterwards [188, 189] and triggered new studies in this field [177, 190–192]. The possibility to use substrates to externally control the band gap as well as excitons [181, 193–199] or plasmons [83, 200], turned out to be a promising new method to tailor new electronic, excitonic and optoelectronic devices.

Next to screening effects the quasiparticle band gap can also be manipulated by mechanical strain or stress [201–203], applied electrical or magnetic fields [204, 205] or electron hole doping [205–207]. In this work we will focus only on the band gap manipulation via screening. We will discuss the electronic and optical properties of Coulomb engineered Heterojunctions using multiscale models in Chapter 4 and 5 and turn to a material realistic description in Chapter 6.

3.3. Minimal tight-binding model

We aim to find simple yet accurate descriptions of the band structures of the TMDCs to obtain material realistic but easy to handle models. In principle all properties of interest, like the influence of external screening, can be calculated by means of full many-body ab-initio methods. However, these methods are numerically very demanding and it can be difficult or even impossible to get converged results for the investigated systems (as we will show in Section 6.1).

The derived models will be the basis of our treatment of additional many-body effects without the necessity to redo computationally demanding ab-initio calculations every time when external parameters change. The relevant physics for the investigations in this thesis are described by the low-energy bands around the Fermi energy. As shown in Fig. 3.1.4 in this energy region the main bands contributing are the highest valence band and the two lowest conduction bands with $m_l = \{0, \pm 2\}$ orbital character. These orbitals can build a minimal basis for a three-band tight-binding Hamiltonian $H_{\alpha\beta}(\mathbf{k})$ [150].

We use a tight-binding Hamiltonian based on band structures resulting from G_0W_0 calculations. The hopping matrix elements are determined with the `Wannier90` [36] code, where the G_0W_0 states are projected onto the three orbitals of the minimal basis. An appropriate inner energy window is chosen to include the highest valence band and as much of the lowest conduction band as possible to ensure the best reproducibility of the G_0W_0 band structure. With that procedure the formally neglected states from the chalcogen p orbitals are indirectly accounted for. We do not perform the maximal localization scheme but use only the disentanglement procedure to maintain the dominant orbital features (as for example the d_{z^2} weights at \mathbf{K}).

All band structures resulting from G_0W_0 calculations shown in this work (c.f. Fig. 3.2.1a) were derived by using Wannier constructions. The derived tight-binding Hamiltonian are used to include additional external effects as described in Section 6.2.1.

The spin-orbit coupling (SOC) can be treated on top of the tight-binding Hamiltonian by considering a Russel-Saunders interaction with a \mathbf{k} -dependent coupling parameter. The Hamiltonian becomes $H_{\alpha\beta}(\mathbf{k}) = H_{\alpha\beta}(\mathbf{k}) \otimes I + H_{\text{SOC}}(\mathbf{k})$ [150, 156] with the 2×2 unity matrix I and

$$H_{\text{SOC}}(\mathbf{k}) = \lambda(\mathbf{k}) \mathbf{L} \cdot \mathbf{S} = \frac{\lambda(\mathbf{k})}{2} \begin{pmatrix} L_z & 0 \\ 0 & L_z \end{pmatrix} \quad (3.3.1)$$

with

$$L_z = \begin{pmatrix} 0 & 0 & 0 \\ 0 & 0 & 2i \\ 0 & -2i & 0 \end{pmatrix}. \quad (3.3.2)$$

The coupling-parameter $\lambda(\mathbf{k})$ is chosen such that the SOC induced splitting at the valence and conduction band matches the splitting resulting from GGA calculations. It additionally accounts for the contribution of the sulfur p orbitals to the effective three-band model reducing the coupling strength throughout the Brillouin zone. With

$$\lambda(\mathbf{k}) = \lambda_0 \cdot e \cdot \left(1 - \frac{|\mathbf{k} - \mathbf{K}|}{|\mathbf{K}|}\right)^2 \cdot e^{-(1 - \frac{|\mathbf{k} - \mathbf{K}|}{|\mathbf{K}|})^2} \quad (3.3.3)$$

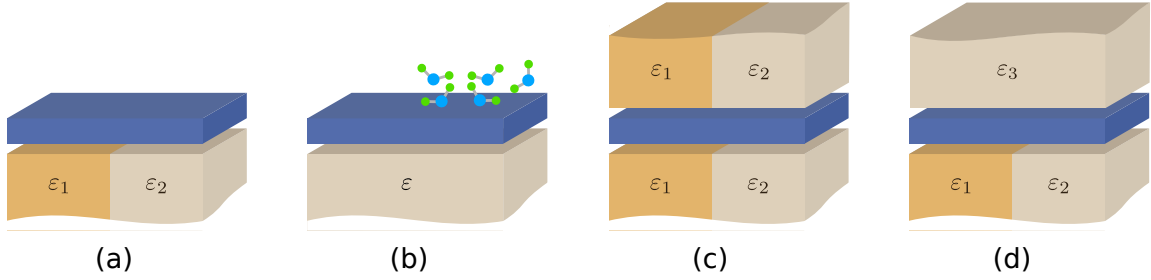
and λ_0 as the spin splitting at the \mathbf{K} point the GGA band structures are reproduced reasonably well [156]. The used λ_0 for the semiconducting TMDCs can be found in Appendix A.1.1.

4. 2D Heterojunctions from Non-local Manipulations of the Interactions

In the following chapter, we will follow the idea of Coulomb engineering introduced in Chapter 3.2.1 and tune the band gap of a 2d material by manipulating the Coulomb interaction through an environment. We use ab-initio calculations to show that Coulomb interaction induced self-energy corrections are sufficiently non-local in real space to be manipulated externally but still local enough to induce spatially sharp interfaces within an otherwise homogeneous monolayer to form heterojunctions. With generic semiconductor models we can create the first Coulomb engineered heterostructures built by monolayers placed in laterally structured dielectric environments. The results shown in this chapter were obtained by M. Rösner and myself and were published in *Nano Lett.* **16**, 2322 (2016) [22]. M. Rösner was responsible for the ab-initio calculations while I performed the model calculations in real space. The manuscript was prepared by M. Rösner and myself with comments and remarks by M. Lorke, C. Gies, F. Jahnke and T. Wehling. The reader will find most parts of the following chapter and its appendix A.2 in the original article.

4.1. Introduction

Heterojunctions are central building blocks of various applications [2, 3] in modern optoelectronics. Apart from planar junctions, which are the basis of light-emitting diodes and solar cells, more complex structures such as quantum wells [208] or quantum dots [209] hold promises in the context of quantum information processing. In the bulk, e.g. in GaAs / InGaAs material systems, heterojunctions are often fabricated by epitaxy, which can be employed up to industrial scales. In addition, also monolayer thin 2d materials including semiconducting TMDCs have been assembled into structures like vertical or lateral heterojunctions as shown in Section 3.2.1. All of these systems rely on interfaces of different materials in order to gain spatial band-gap modulations. The epitaxial fabrication of well defined interfaces with the desired electronic properties underlies constraints due to available materials, and can in practice be very challenging.


Figure 4.1.1.

Sketches of a monolayer (blue) in different heterogeneous dielectric environments. (a), (c) and (d) show situations with structured dielectric substrates while in (b) adsorbed *polarizable* molecules are responsible for the heterogeneous dielectric environment.

In this work we make use of the peculiar properties of Coulomb interaction in 2d semiconductors (see Section 3.2). Since the Coulomb interaction can modify band gaps on an eV scale and is drastically manipulable through external screening [120, 161, 167, 173, 174, 210–213], the band gap can be controlled by the dielectric surroundings of the monolayer.

We propose a new scheme to build heterojunctions within a single *homogeneous* layer of a 2d material based on non-local manipulations of the Coulomb interaction, that is the controlled manipulation of the long-range characteristics of the Coulomb interaction *within* the layered material. By placing a 2d semiconductor into a laterally structured environment (e.g. a substrate with laterally varying dielectric constants as depicted in Fig. 4.1.1), the Coulomb interaction within the 2d material changes spatially and with it, the local band gaps are modulated as well. Thus, band-gap variations like in a heterojunction can be induced externally in a *homogeneous monolayer* by an appropriately structured dielectric environment.

The possible technical relevance of such *Coulomb engineered heterojunctions* is defined by (i) the size of achievable band gap modulations and (ii) the intrinsic length scale over which these modulations take place. We show that changes in the Coulomb interaction can induce band-gap modulations in the range of several 100 meV on the length scale of a few lattice spacings in homogeneous MoS₂. To this end, we consider in a first step a free standing MoS₂ monolayer and analyze Coulomb interaction effects as manifesting in the electronic self-energy in *real space*. Based on *GW* calculations, we demonstrate that the dominant self-energy terms are indeed limited to the length scale of a few unit cells. In order to study heterogeneous systems as shown in Fig. 4.1.1, we switch to a generic 2d semiconductor model that is quantitatively based on our ab-initio *GW* results. Using this model, we demonstrate that a spatially inhomogeneous environment allows to *induce externally* a heterojunction of type-II in MoS₂.

4.2. Real space extent of the self-energy

As discussed in Chapter 3.1.2 the band gap in TMDC and with that also in MoS₂ is opened due to hybridization effects between the d_{z^2} and the $\{d_{xy}, d_{x^2-y^2}\}$ states. To take Coulomb interaction effects into account and investigate the effects to the hybridization mechanism, we perform G_0W_0 (GW) calculations. With that we can study in detail how the band gap is affected by the Coulomb interaction leading to the larger band gaps found in GW calculations (see Chapter 3.2). Additionally, we can examine with a real space description the locality of the Coulomb interaction, which is a crucial internal parameter for spatially sharp band-gap modulations in Coulomb engineered heterostructures.

We derive the corresponding self-energy in *real space* from a comparison of DFT and G_0W_0 calculations (see Appendix A.2.1 for the numeric details) utilizing the Dyson equation (c.f. Eq. (2.4.16)):

$$\Sigma = G_{\text{DFT}}^{-1} - G_{GW}^{-1}, \quad (4.2.1)$$

where G_{DFT} and G_{GW} are the electronic Green functions obtained from corresponding calculations. Within the quasiparticle approximation, the Green functions

$$G_{GW/\text{DFT}}^{-1} = (z + \mu - H_{GW/\text{DFT}}), \quad (4.2.2)$$

can be obtained from the Hamiltonians H_{GW} and H_{DFT} in Wannier basis describing the DFT and G_0W_0 band structures, respectively:

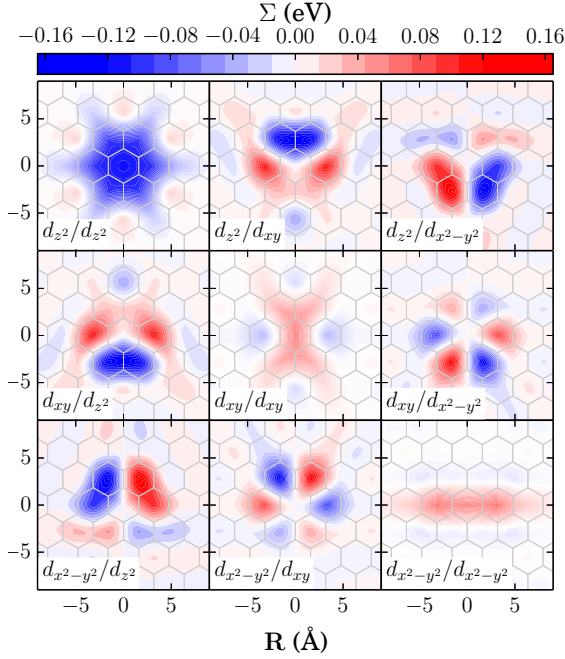
$$H_{\alpha\beta}^{GW/\text{DFT}}(\mathbf{k}) = \sum_{\mathbf{R}} e^{i\mathbf{k}\cdot\mathbf{R}} t_{\alpha\beta}^{GW/\text{DFT}}(\mathbf{R}) \quad (4.2.3)$$

with the quantum numbers $\alpha, \beta \in \{d_{z^2}, d_{xy}, d_{x^2-y^2}\}$ denoting the dominating orbital characters of the wave functions. Then, the real space self-energy is approximated as

$$\Sigma_{\alpha\beta}^{GW}(\mathbf{R}) = t_{\alpha\beta}^{GW}(\mathbf{R}) - t_{\alpha\beta}^{\text{DFT}}(\mathbf{R}) - \Delta\mu \delta_{\mathbf{R}\mathbf{0}}\delta_{\alpha\beta}, \quad (4.2.4)$$

where $\Delta\mu$ aligns the Fermi energies between the DFT and G_0W_0 calculations, which is realized by choosing $\Delta\mu$ such that $\text{Tr}[\Sigma^{GW}(\mathbf{0})] = 0$.

In Fig. 4.2.1 we show a map of $\Sigma_{\alpha\beta}^{GW}(\mathbf{R})$, which visualizes the \mathbf{R} dependent *renormalizations* of the tight-binding hopping matrix elements due to the Coulomb interaction corrections included in GW . These elements can be separated into intra- and inter-orbital contributions arising from induced changes in the intra- ($\alpha \leftrightarrow \alpha$) and inter-orbital ($\alpha \leftrightarrow \beta$) hoppings. In more detail, there are *local* renormalizations $\Sigma_{\alpha\beta}(\mathbf{R} = \mathbf{0})$, and, more importantly, *non-local* self-energy terms $\Sigma_{\alpha\beta}(\mathbf{R} \neq \mathbf{0})$ (the colored cells around the central unit cells in each panel) which result from the non-local character of the Coulomb interaction.


Figure 4.2.1

Real space representation of the GW self-energy $\Sigma_{\alpha\beta}^{GW}(\mathbf{R})$ of MoS_2 within the minimal Mo d basis. The gray lines mark the hexagonal Wigner-Seitz unit cells of the MoS_2 lattice, where the Mo atoms are assumed to be in the center of the cells.

The strongest contributions to the self-energy are non-local inter-orbital exchange terms, which directly increase the hybridization and with that the band gap. Thus the enhanced band gap in GW calculations results from non-local inter-orbital contributions of the Coulomb interaction. Even though we find non-local contributions to Σ , as expected from the long-range character of the Coulomb interaction in 2d, the most sizable contributions are clearly localized within a radius of less than three unit cells. Hence despite the self-energy being non-local, it could still facilitate sharp band-gap modulations in the case of structured dielectric environments, which will be discussed in the following section.

The real space structure of $\Sigma_{\alpha\beta}^{GW}(\mathbf{R})$ is determined by the corresponding orbital symmetries. Since the d_{z^2} orbital is invariant under the operations of the threefold rotation symmetry of the MoS_2 lattice, the self-energy in the d_{z^2}/d_{z^2} panel of Fig. 4.2.1 shows the full symmetry of the lattice. The d_{xy} and $d_{x^2-y^2}$ orbitals belong to a two-dimensional representation of the crystal symmetry point group, which leads to a more complex structure of the corresponding self-energy terms, as seen in the d_{xy} and $d_{x^2-y^2}$ panels in Fig. 4.2.1.

4.3. Heterostructures induced by heterogeneous dielectric environments

Now we turn to structured dielectric environments as depicted in Fig. 4.1.1. Because of the broken translational symmetry GW calculations become numerically extremely demanding. As an alternative, we now use a model system that mimics the essential gap-opening mechanisms and interaction effects present in semiconducting TMDCs and, at the same time allows us to study the influences of a structured dielectric environment on the local density of states (LDOS) and the resulting spatial variation of the band gap.

4.3.1. Minimal semiconductor tight-binding model for MoS_2

To mimic the hybridization effects leading to the gap opening in monolayer MoS_2 , we resort to a two-band model as illustrated in Fig. 4.3.1: We consider a hexagonal double-layer lattice, where the layers A and B mimic the d_{z^2} and $\{d_{xy}/d_{x^2-y^2}\}$ blocks, respectively. The in-plane lattice constants are chosen corresponding to MoS_2 with $a = 3.18 \text{ \AA}$ and the vertical distance is set to $c = a/4$ in the following. The

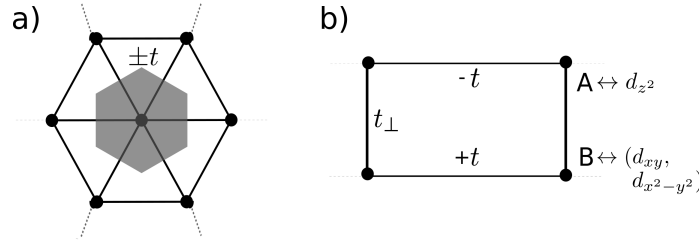


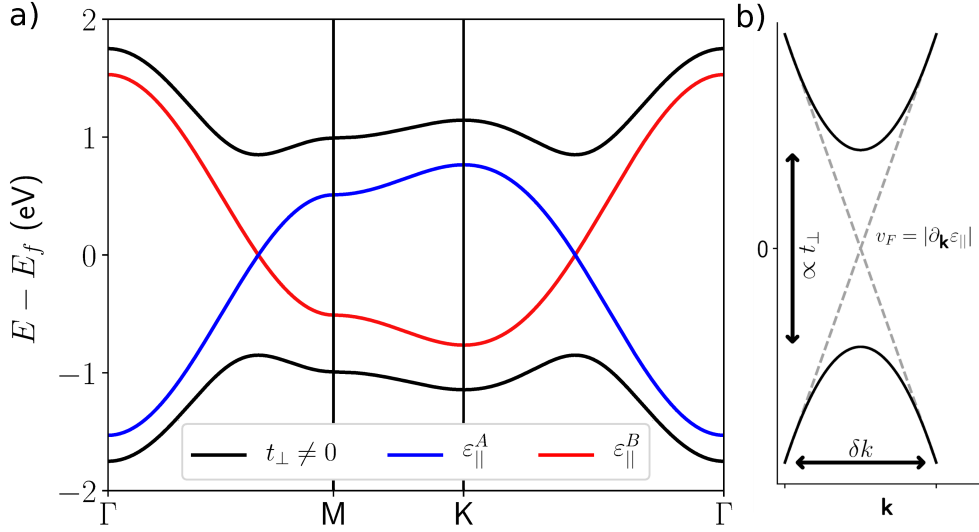
Figure 4.3.1.

a) and b) show top and side view sketches of the hexagonal double-layer lattice used in the minimal model. The lines visualize possible electronic hopping paths. The dots correspond to orbitals from the orbital of $A \leftrightarrow d_{z^2}$ and $B \leftrightarrow \{d_{xy}/d_{x^2-y^2}\}$ type.

corresponding tight-binding Hamiltonian is given by

$$H_{\text{SP}} = \sum_{ij} t_{ij} c_i^\dagger c_j, \quad (4.3.1)$$

where c_i^\dagger (c_i) creates (annihilates) an electron in an orbital at lattice site i . The parameters t_{ij} describe either hybridization $t_{ij} = t_\perp$ between A and B type orbitals inside the same unit cell (which appears like vertical hopping in the illustration of Fig. 4.3.1) or "in-plane" hopping $t_{ij} = t$ (respectively $t_{ij} = -t$) if i and j are nearest


Figure 4.3.2.

a) Tight-binding band structure of the single-particle Hamiltonian with hybridization $t_{\perp} \neq 0$ (black line) and the in-plane dispersions for the two layers mimicking the d-orbital blocks (blue and red line). b) Sketch of the band-gap opening mechanism of the applied model. The \mathbf{k} -region in which the hybridized band structure (black line) differs from the in-plane dispersions (dashed gray lines) is δk . The Fermi velocity $v_F(\mathbf{k}) = |\partial_{\mathbf{k}} \epsilon_{\parallel}(\mathbf{k})|$ is proportional to the slope at \mathbf{k} and thus $\delta k \approx t_{\perp} / v_F(\mathbf{k})$.

neighbors within the A (B) block. As there are two orbitals per unit cell, the resulting \mathbf{k} -space representation of the Hamiltonian is a 2×2 matrix

$$H_{\text{SP}}(\mathbf{k}) = \begin{pmatrix} \epsilon_{\parallel}(\mathbf{k}) & t_{\perp} \\ t_{\perp} & -\epsilon_{\parallel}(\mathbf{k}) \end{pmatrix}. \quad (4.3.2)$$

The in-plane dispersion becomes in this situation the tight-binding dispersion of the 2d hexagonal lattices within nearest neighbor approximation

$$\epsilon_{\parallel}(\mathbf{k}) = t \sum_{j=1}^6 \exp(i\boldsymbol{\delta}_j \cdot \mathbf{k}) \quad (4.3.3)$$

with $\boldsymbol{\delta}_j$ connecting in-plane Mo nearest-neighbors. The hopping parameters (see Appendix A.2.2) are chosen to reproduce the band width ($W_{\parallel} \approx 1.0 \text{ eV}$) and the DFT band gap ($\Delta \approx 2.0 \text{ eV}$) of MoS_2 , which is similar to other semiconducting TMDCs [129]. In Fig. 4.3.2a) we show the band structure obtained from diagonalizing Eq. (4.3.2) with hybridization $t_{\perp} \neq 0$ (black line) and without hybridization $t_{\perp} = 0$ (blue and red line). For $t_{\perp} = 0$ we see two non hybridized bands with opposite

slopes (due to $\varepsilon_{\parallel}^A = -\varepsilon_{\parallel}^B$) and a crossing between Γ and \mathbf{K} and Γ and \mathbf{M} . When we increase $t_{\perp} > 0$ we see a gap opening because of the hybridization at the crossing and a shift by $\pm t_{\perp}$ at Γ . This gap opening, namely hybridization, has the same origin as described before in semiconducting TMDCs. The direct band gap at \mathbf{K} is not reproduced due to neglecting the second $m_l = \pm 2$ band. In fact, Eq. (4.3.2) is the most simple description of a 2d semiconductor.

4.3.2. Including the Coulomb interaction

The Coulomb interaction gives rise to electron-electron, electron-ion and ion-ion interaction terms: $H_{\text{Coulomb}} = H_{\text{ee}} + H_{\text{ei}} + H_{\text{ii}}$. The ions are assumed to have a fixed positive charge $Ze = +1e$ to ensure charge neutrality of the whole system, i.e. $Z = 2\bar{n}$, where \bar{n} is the average electron occupation per spin and orbital. The ionic positions are assumed to be fixed. Thus, H_{ii} leads to a constant shift of the total energy, which will be neglected in the following. The remaining Coulomb terms read [26, 27]

$$H_{\text{ee}} = \frac{1}{2} \sum_{ij\sigma\sigma'} U_{ij} c_{i\sigma}^{\dagger} c_{j\sigma'}^{\dagger} c_{j\sigma'} c_{i\sigma} \quad (4.3.4)$$

$$H_{\text{ei}} = - \sum_{ij\sigma} U_{ij} \hat{n}_{i\sigma} Z, \quad (4.3.5)$$

where $U_{ij} = U(\mathbf{r}_i, \mathbf{r}_j)$ is the interaction energy between electrons or ions at sites \mathbf{r}_i and \mathbf{r}_j , σ labels the electron spin, $c_{i\sigma}^{\dagger}$ ($c_{i\sigma}$) are the corresponding electronic creation (annihilation) operators, and $\hat{n}_{i\sigma} = c_{i\sigma}^{\dagger} c_{i\sigma}$ are electron occupation operators.

The inclusion of the Coulomb interaction in our model induces a correction to the single-particle Hamiltonian. As we show in Section A.2.3 in Hartree Fock approximation the real space Hamiltonian for our model system yields

$$H = \sum_{ij} t_{ij} c_i^{\dagger} c_j + \sum_{ij} \Sigma_{ij} c_i^{\dagger} c_j \quad (4.3.6)$$

with the Hartree-Fock self-energy [27]

$$\Sigma_{ij} = \underbrace{\delta_{ij} \sum_l 2U_{il} \delta n_l}_{\text{Hartree}} - \underbrace{U_{ij} \langle c_j^{\dagger} c_i \rangle}_{\text{Fock}}, \quad (4.3.7)$$

where $\delta n_l = \langle \hat{n}_l \rangle - \bar{n}$ is the deviation from the average occupation \bar{n} . Spin indices are suppressed as Σ_{ij} is spin diagonal.

The environment of the material screens the bare Coulomb potentials v_{ij} via the dielectric function ε_{ij} and correspondingly modifies the interaction matrix elements U_{ij} ,

$$U_{ij} = \int \varepsilon^{-1}(\mathbf{r}_i, \mathbf{r}_l) v(\mathbf{r}_l, \mathbf{r}_j) d^3 r_l. \quad (4.3.8)$$

For heterogeneous environments, as illustrated in Fig. 4.1.1, the corresponding background screened Coulomb interaction can be obtained from a solution of the resulting Poisson equation. In general, numerical schemes need to be employed for this purpose, although analytical results exist for simplified situations. For example for a laterally structured environment as depicted in Fig. 4.1.1c) with zero layer height, we can use the method of mirror charges as shown in Section A.2.4 to derive an analytic expression for the Coulomb matrix elements U_{ij} . For this system, we are able to calculate self-consistently Σ_{ij} from Eq. (4.3.7) and the corresponding local density of states for arbitrary dielectric environments with static dielectric constants ε_1 and ε_2 .

4.3.3. Local density of states for heterostructure induced by laterally structured environment

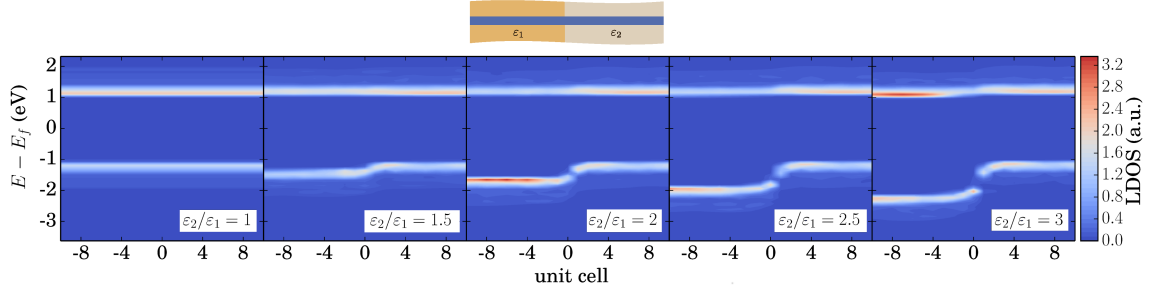


Figure 4.3.3.

Local density of states for different unit cells along a line perpendicular to the dielectric interfaces of the substrates. The dielectric constant $\varepsilon_2 = 15$ is fixed in all panels and ε_1 is varied from 15 to 5 from left to right. Thus the leftmost panel corresponds to a homogeneous environment. Negative unit cells correspond to unit cells lying in the area with ε_1 and positive ones to ε_2 . The model parameters are set to $t = 0.26$ eV, $t_{\perp} = 0.85$ eV, $a = 3.18$ Å (in-plane lattices constant) and $c = a/4$ (layer separation).

In Fig. 4.3.3 we present a direct visual account of the band-gap variation induced by a laterally changing dielectric environment, as indicated by the sketch of the heterostructure. We show the LDOS for substrates with varying $\varepsilon_2/\varepsilon_1$ ratios and fixed $\varepsilon_2 = 15$. The leftmost panel of Fig. 4.3.3 corresponds to a homogeneous environment. In all panels two main characteristics can be clearly seen: The van-Hove singularities

(vHS) as maxima in the LDOS (c.f., Fig. 4.3.2 at the \mathbf{M} point), and spatially dependent band gaps $E_{\text{gap}}(\mathbf{r})$ as energy ranges where the LDOS vanishes between the singularities¹.

The overall variation of the band gaps along the spatial direction is reminiscent of a heterojunction band diagram of type-II. $E_{\text{gap}}(\mathbf{r})$ is clearly reduced in the ε_2 region on the right hand side of each panel ($E_{\text{gap}} \approx 1.9$ eV for $\varepsilon_2 = 15$) compared to the ε_1 area on the left hand side of the panels ($E_{\text{gap}} \approx 2.9$ eV for $\varepsilon_1 = 5$) as a result of stronger external screening effects of the ε_2 substrate and correspondingly reduced Coulomb interaction. For all $\varepsilon_2/\varepsilon_1 > 1$ ratios, we find a nearly vanishing conduction-band offset (CBO), while the different band gaps can be tuned precisely between both regions.

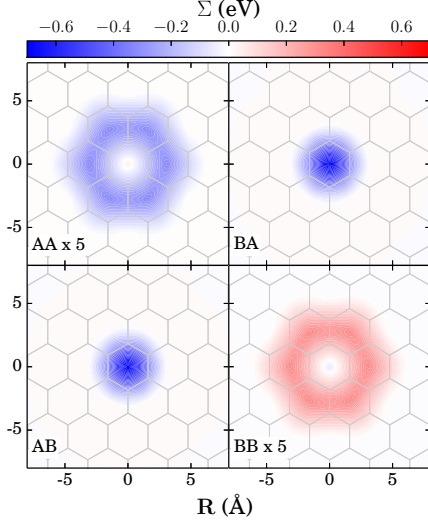
The kind of band diagram shown in Fig. 4.3.3 will arise in all systems shown in Fig. 4.1.1, although the effect of the structured environment is strongest in the setups corresponding to the panels Fig. 4.1.1a and Fig. 4.1.1c. To have a strong effect in the other situations the substrate ε in Fig. 4.1.1b or the capping layer ε_3 in Fig. 4.1.1d should be significantly less polarizable compared to the adsorbed molecules or $\varepsilon_{1/2}$, respectively.

Most importantly for electronic functionalities and particularly regarding electronic transport in these heterojunctions, the band-gap changes within less than 5 unit cells around the interface, which holds for the whole range of $\varepsilon_2/\varepsilon_1$ ratios presented in Fig. 4.3.3. In lateral heterojunctions made from stitching together different TMDCs, a comparable length scale has been reported [9]. Thus, we find a similar behavior with the difference, that here the heterojunction does not arise from different materials, but is induced *externally* by structuring the dielectric substrate.

4.3.4. Length scale over which band-gap variations can be realized

There are intrinsic and extrinsic factors limiting the length scale over which band-gap variations in dielectrically induced heterojunctions can be realized. The major extrinsic factor determining the sharpness of the induced band-gap variation, is the length scale on which the dielectric environment changes, which depends on experimental substrate or adsorbate preparation procedures. There are several experimental ways to realize nearly atomically sharp variations of the dielectric polarizability of the environment of a 2d material. Examples range from the extreme case of substrates containing holes [142, 214, 215], patterned adsorption of polarizable molecules [216–219], and intercalation or adsorption of atoms [220, 221] to self-organized growth of structured dielectrics by epitaxial means [222–225].

¹ Since an artificial broadening $\delta = 5$ meV is involved in the evaluation of the LDOS it never vanishes completely. Therefore we consider values smaller than 0.02 as zero.


Figure 4.3.4

Real space representation of the Hartree-Fock self-energy Σ_{ij} in the $\varepsilon_1 = 5$ area of the system shown in Fig. 4.3.3. The gray lines mark the hexagonal Wigner-Seitz unit cells. Note, the diagonal elements were enhanced by a factor of 5.

A lower intrinsic bound for the length scale, on which the band-gap variation takes place is defined by the spatial extend of the self-energy which can be deduced qualitatively from the underlying model. According to Eq. (4.3.7) the range of the self-energy is limited by the real space decay range of the correlation functions $\langle c_j^\dagger c_i \rangle$ which translates to the region δk in reciprocal space (see Fig. 4.3.2b) in which we find significant changes of the in plane band structure due to hybridization. We can approximate δk using the Wannier Hamiltonian in \mathbf{k} -space representation, Eq. (4.3.2). The hybridization gap is of the order of $\propto t_\perp$ around $\varepsilon_\parallel = 0$ (as shown in Fig. 4.3.2b) in a region extending about $\delta k \approx t_\perp/v_F$. The Fermi velocity $v_f = |\partial_{\mathbf{k}} \varepsilon_\parallel(\mathbf{k})| \approx W_\parallel a$ associated with the in-plane dispersion is proportional to the band width of the dispersion $W_\parallel \propto t$. By the uncertainty principle, the momentum-space extent δk translates into a range $\delta r \sim 1/\delta k \approx W_\parallel a/t_\perp$ of the correlation functions $\langle c_j^\dagger c_i \rangle$ in real space. As a consequence, Σ_{ij} is generically limited to the scale of a few unit cells as long as hybridization (t_\perp) and band width ($W_\parallel \propto t$) are similar in size.

This finding is reflected in the numerical data for the non-local real space self-energy Σ_{ij} depicted in Fig. 4.3.4. In analogy to the discussion of the MoS₂ GW self-energy in the homogeneous case, we show in Fig. 4.3.4 the self-energy in the middle of the $\varepsilon_1 = 5$ area of the heterostructure. Here, the local dielectric environment is essentially homogeneous and thus comparable to the fully homogeneous case. The off-diagonal self-energy terms shown in Fig. 4.3.4 are by definition non-local, as they describe modulations of interlayer couplings (separated by $R_z = c$), but significant contributions are limited to a single unit cell. For orbitals in the same layer (diagonal panels in Fig. 4.3.4), the self-energy is smaller, and substantial contributions are limited to about two unit cells. Hence the real space structure of the model self-energy in this homogeneous-like area of the system is quite similar to the self-energy in MoS₂ obtained from full ab initio calculations (see Fig. 4.2.1),

More specifically, the Hartree contribution of the self-energy Σ^H is diagonal and has hardly any effect on the band structure. Especially the non-local Fock terms Σ^F , as we show in more detail in Section A.2.6, increase the band gap by modifying the hybridization (as seen in Σ_{AB}/Σ_{BA} in Fig. 4.3.4). This tendency is independent of the dielectric constant and inherent to all semiconducting 2d materials where band gaps result from hybridization effects. Consequently, in all materials of this kind, heterojunctions can be induced by an external manipulation of the Coulomb interaction.

4.4. Conclusions

For Coulomb engineered heterojunctions we expect that screening and exchange-interaction induced confinement potentials affect uncorrelated electrons and holes quite differently compared to correlated electron-hole pairs. For instance, optical absorption energies related to the excitation of correlated electron-hole pairs (i.e. excitons) depend on the quasiparticle band gaps but also on the excitonic binding energies which are both decreased by a highly polarizable dielectric environment. Hence, the excitonic absorption energies will change less by external manipulations of the Coulomb interaction [174] than the single-particle properties, which are most relevant for electronic transport. As a consequence, the relation between optical and transport properties in the kind of heterojunctions proposed here will likely differ from heterojunctions created by stitching different materials together. We will discuss the influence of Coulomb engineering on excitonic properties in Chapter 5.

We have demonstrated that in MoS_2 , as a typical 2d TMDC semiconductor, heterostructures can be formed by means of spatially structured dielectric environments. For this purpose, we have used ab-initio calculations and a generic 2d semiconductor model, to show, that the external manipulation of the Coulomb interaction allows for sharp, spatially modulated band gaps. Hence new kinds of heterojunctions can be constructed by placing semiconducting 2d materials on appropriately structured substrates as was later also confirmed experimentally [188, 191]. Similarly, polarizable molecules could be deposited on top of 2d materials to cover parts of the surface to form heterojunctions. Such heterojunctions bring the advantage that only the environment of the active material but not the material itself needs to be structured during the fabrication process. One could thus add the active 2d semiconducting layer to independently pre-structured dielectric layers which is very attractive from a fabrication point of view.

While we consider a single interface in this work, our findings can be generalized to more complex structures. One can for instance use two parallel interfaces to realize a quantum wire-like structure. Finally, with four interfaces (two in the x - and two in the y -direction) or also partial coverage of finite areas with adsorbates quantum dots could be externally induced in monolayers of homogeneous 2d materials.

5. Non-invasive control of excitons

In the previous chapter, we showed the influence of dielectric screening on the quasi-particle band gap and how to create Coulomb engineered heterostructures. As already mentioned in Section 3.1.3, not only the electronic but also the optical properties in 2d TMDCs are of interest. In this chapter we investigate how external screening shapes *excitons* in 2d semiconductors embedded in a laterally structured environment. The results presented have been published in *Phys. Rev. B* *96*, 045431 (2017) [226]. The calculations were done by myself with help of D. Mourad, the manuscript was written by myself and D. Mourad with remarks from T. Wehling. Additional comments were given by M. Rösner, M. Lorke, C. Gies, F. Jahnke and G. Czycholl. The reader will find most of the following text and its appendix A.3 in the original article.

5.1. Introduction

As discussed in detail in Section 3 Coulomb interaction causes pronounced correlation phenomena such as superconductivity [227–231], charge-density waves [232–235], magnetism [236–239] and strong excitonic effects [19, 21, 120, 154, 156, 161, 240] in 2d materials. Monolayers of these materials realize atomically thin electronic systems, where the Coulomb interaction is strongly dependent on the dielectric environment as for instance the substrate of the material. This leads to the exciting opportunity to control interaction driven material properties externally and non-invasively via screening of the substrate or some adsorbates: for instance, laterally structured substrates (see Fig. 5.1.1) can be used to create "junctions" with band gap modulations on the scale of several 100 meV within one and the same material. For independently moving electrons or holes, indeed very sharp potential energy modulations on the scale of a few nm or even less are possible as we have shown in the previous section. However, under optical excitation electrons and holes are known to form strongly bound excitons instead of moving independently in 2d materials. It is thus unclear which optoelectronic material functionalities can be imprinted externally. To change this situation, it is central to understand how and at which length scales excitons are influenced by laterally structured dielectric environments.

In this chapter, we investigate how excitons respond to the tuning of the Coulomb interaction in 2d materials. To this end, we consider two tight-binding model systems, which emulate single semiconducting layers embedded in a dielectric environment.

We study two different kinds of environments as depicted in Fig. 5.1.1: We first analyze the influence of different homogeneous dielectric environments, characterized by the macroscopic dielectric constant ε of the substrate, on our monolayer and show that the size of the exciton Bohr radius a determines how two-particle excitations react to changes in the materials dielectric environment.

Then, we investigate how a spatially structured dielectric environment influences the energy spectrum of an excited system. We show that any exciton which has a considerable spread is strongly affected by the environment, giving rise to the prospect of atomic scale trapping and guiding of higher excited excitons by means of laterally structured dielectric substrates. The only exception holds for the energy of strongly localized excitons, which reveal a non-monotonous behavior leading to interesting possibilities for nanoscale engineering including the creation of novel quantum confined materials. These might serve as building blocks for nanoscale lasers and could help realizing exotic states of excitonic matter (cf. Fig. 5.1.1e for a visual account of a possible potential energy landscape).

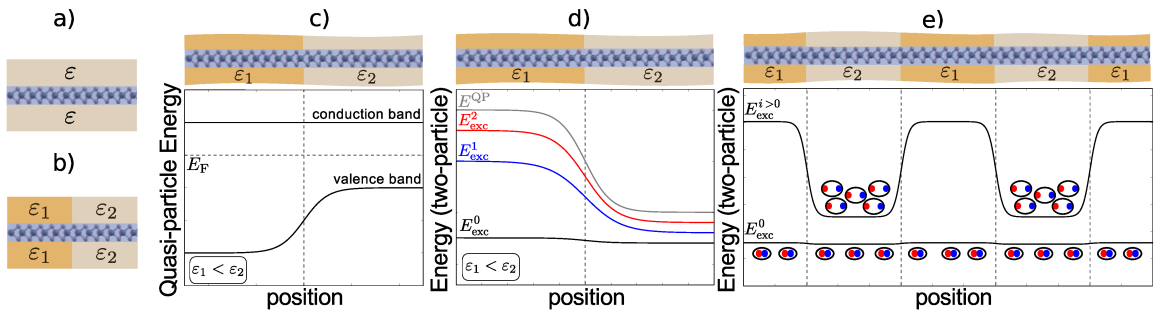


Figure 5.1.1.

Sketches of the electronic quasiparticle and excitonic energies in a homogeneous 2d semiconducting monolayer (blue) embedded in different dielectric environments: a) A homogeneous environment with macroscopic dielectric constant ε . b) A laterally structured dielectric environment with different dielectric constants ε_1 and ε_2 . The heterogeneous environment sketched in b) imprints a potential energy landscape as calculated in Chapter 4 on electronic quasiparticles (panel c) and electron-hole excitations / excitons (panel d). Higher energy excitons are attracted towards regions with higher dielectric constant. The lowest-energy excitons are affected more weakly and can either be attracted towards or expelled from regions with higher dielectric constant. Therefore, nanostructured dielectric substrates allow for the realization of potential energy landscape for excitons as shown in panel e). Under optically pumping, these can yield "inverted" regions where higher energy excitonic states have a higher occupation than the ones at lower energies.

5.2. Methods

5.2.1. Modelling spatially resolved optical properties

To investigate the influence of dielectric environments on excitonic effects in 2d materials we diagonalize a many-body Hamiltonian in the electron-hole picture. We consider a two-band model and the excitation of one electron from the valence to the conduction band. The interaction-free ground-state is described in the tight-binding approximation with a basis set $\{|\mathbf{R}\rangle\}$, where \mathbf{R} is labeling the lattice site on which the orbital is predominantly localized. To account for the electron-electron Coulomb interaction effects on the ground state and on single-particle excitations, we use the Hartree-Fock method and include the screening effects of the spatially structured dielectric environment semi-classically via an electrostatic picture as derived in Chapter 4 (c.f., Section A.2.4). As a basis set for the electron-hole Hamiltonian, we use Slater determinants of dressed electron and hole wave functions which result from the Hartree-Fock calculations. Then, the many-body wave functions of the excited states are linear combinations of these determinants and we are left with a two-particle Schrödinger equation with the electron-hole Hamiltonian

$$H = \sum_i E_i^e e_i^\dagger e_i + \sum_i E_i^h h_i^\dagger h_i - \sum_{ijkl} V_{ijkl}^{ehhe} e_i^\dagger h_j^\dagger h_k e_l. \quad (5.2.1)$$

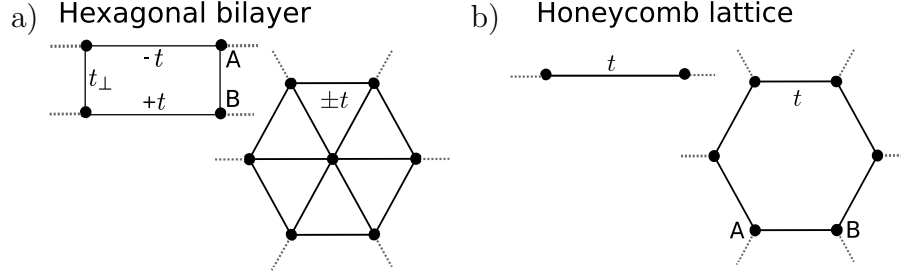
Here, $E_i^{e/h}$ are dressed electron/hole eigenenergies from the Hartree-Fock calculations used in Chapter 4 and V_{ijkl}^{ehhe} are the Coulomb matrix elements between electrons and holes. The operator $(e/h)_i^{(\dagger)}$ annihilates (creates) an electron/hole in the Hartree-Fock eigenstate $|\psi_{(e/h)}^i\rangle$. A detailed description of the construction of Eq. (5.2.1) can be found in Appendix A.3.1.

After diagonalizing the electron-hole Hamiltonian, we obtain the many-body eigenenergies E_λ and eigenstates $|\Psi^\lambda\rangle$. In order to simulate an experimentally easily accessible property, we calculate the linear optical spectrum within the dipole approximation (for details see Appendix A.3.2). The linear absorption spectrum is obtained by Fermi's golden rule:

$$I(E) = \sum_\lambda \frac{2\pi}{\hbar} |\langle \Psi^\lambda | H_d | 0 \rangle|^2 \delta(E_\lambda - E_0 - E). \quad (5.2.2)$$

Here, $|0\rangle$ and $|\Psi^\lambda\rangle$ are the semiconductor vacuum state and many-body final state, respectively, with energies E_0 and E_λ , the former of which will be, as usual, set to zero in the remainder of this paper. E is the absorption/emission energy and

$$H_d = -e\mathbf{E} \sum_{ij} \mathbf{d}_{ij}^{eh} e_i h_j + h.c., \quad (5.2.3)$$


Figure 5.2.1.

The 2d semiconductors are modeled using two different tight-binding models labeled "hexagonal bilayer" and "honeycomb lattice", where the schematic side and top views of the model illustrate the hopping matrix elements.

is the light-matter coupling Hamiltonian to an electromagnetic field \mathbf{E} in dipole approximation (see Appendix A.3.2 for further details).

On similar grounds, we can calculate the total two-particle or "excitonic" density of states (DOS)

$$A(E) = 2\pi \sum_{\lambda} \delta(E - E_{\lambda}), \quad (5.2.4)$$

which includes all possible two-particle excitations regardless of the selection rules, i.e., also accounts for "dark" excitons [241–243]. To investigate excitonic correlations in real space, we use the spatially resolved two-particle DOS, which can be experimentally measured by using a dual-tip scanning tunneling microscope [244–246]:

$$A(E, \mathbf{r}_e, \mathbf{r}_h) = 2\pi \sum_{\lambda} |\Psi^{\lambda}(\mathbf{r}_e, \mathbf{r}_h)|^2 \delta(E - E_{\lambda}). \quad (5.2.5)$$

Here, $\mathbf{r}_{e/h}$ describe the position of the electron/hole. Further details on the calculation of the spatially resolved eigenstates $\Psi^{\lambda}(\mathbf{r}_e, \mathbf{r}_h)$ can be found in Appendix A.3.3.¹

5.2.2. Tight-binding models for 2d semiconductors

In order to emulate 2d semiconductors, we use two different models as shown in Fig. 5.2.1, mimicking different band gap opening mechanism in 2d materials. First, we consider the model described in Section 4.3.1 and shown in Fig. 5.2.1a: a "monolayer" that consists of two hexagonal layers on top of each other (in the following, this model will be called "hexagonal bilayer") embedded in a dielectric environment. The

¹For numerical reasons, the δ -distribution was broadened using a Lorentzian with a full width at half maximum of $\Gamma = 0.01$ eV throughout this work.

coupling between the two layers mimics hybridization effects similar to the d -orbitals in transition metal dichalcogenides like MoS₂. In the tight-binding approach, we only consider an in-plane nearest neighbor hopping $t^{\mathbf{R}\mathbf{R}'} =: t$ and an out-of-plane hopping $t^{\mathbf{R}\mathbf{R}'} =: t_{\perp}$, where $t^{\mathbf{R}\mathbf{R}'}$ gives the energy associated with an electron hopping from state $|\mathbf{R}'\rangle$ to $|\mathbf{R}\rangle$.

An additional class of embedded monolayers is modeled using a honeycomb lattice with broken sublattice symmetry as depicted in Fig. 5.2.1b, which has been widely used to study 2d semiconductors such as hBN [247–249] as well as graphene commensurately stacked with hBN [250–254]. This model leads to a massive Dirac equation in the low energy limit and is in the following referred to as "Honeycomb lattice". Again, we only consider in-plane nearest neighbor hopping t .

As one particular example representative for 2d semiconductors we consider MoS₂. Therefore, the on-site energies and hopping matrix elements are chosen as in Chapter 4 for the hexagonal bilayer ($t = 1.7$ eV) and as in Ref. [255] for the honeycomb lattice ($t = 1.1$ eV). More details and the model parameters of the used models can be found in Appendix A.3.4.

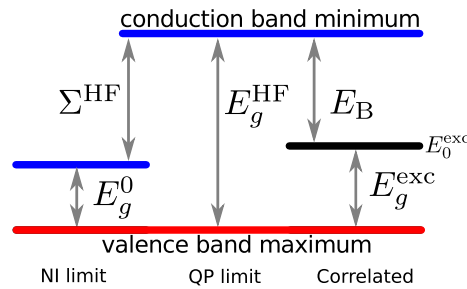
The in-plane hopping t determines how easily electrons can be localized. Thereby, smaller t corresponds to smaller hopping probabilities and thus easier localization. In the following discussion (c.f. Fig. 5.3.2), this case will be referred to as "localized" models in contrast to "delocalized" models with larger t .

5.3. Results

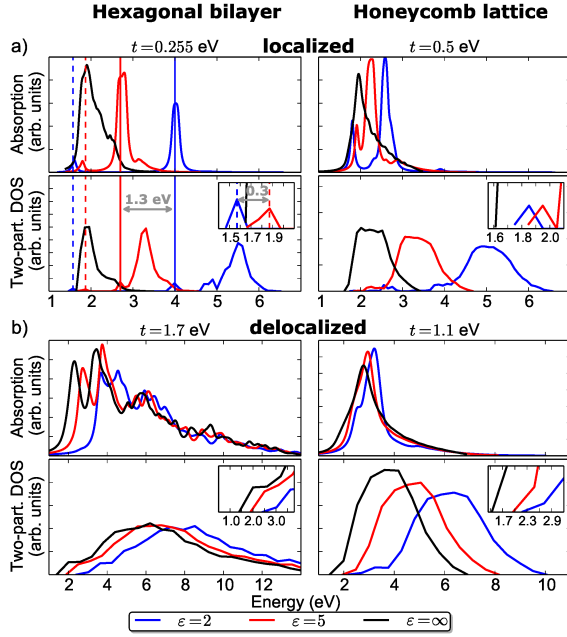
5.3.1. Monolayer of a semiconductor embedded in homogeneous dielectric environment

Figure 5.3.1

Schematic illustration of competing contributions to the excitonic gap E_g^{exc} : the single-particle band gap E_g^0 , is widened to the dressed quasi-particle band gap E_g^{HF} due to the exchange self-energy Σ^{HF} which results from the ground-state electron-electron interaction. The optically measurable excitonic gap is reduced as compared to E_g^{HF} due to the electron-hole binding energy E_B .



For the discussion of environmental influences on a monolayer, it is important to understand the interplay of excitonic binding and exchange self-energy effects.

**Figure 5.3.2**

Linear optical absorption spectra and total excitonic density of states for different dielectric constants of the environment of the monolayer for the localized (a) and delocalized (b) hexagonal bilayer (left panels) and honeycomb lattice (right panels). In the insets of the two-particle DOS the lowest-energy excitations are shown in more detail. High ε correspond to small Coulomb interactions leading in our model systems to the description of independent particles for $\varepsilon = \infty$.

These effects are schematically shown in Fig. 5.3.1. In the non-interacting (NI) limit no Coulomb interaction is considered which results in the band gap being given by the single-particle band gap E_g^0 . This single-particle gap is widened by the exchange self-energy Σ^{HF} that enters the Hartree-Fock ground-state due to electron-electron interaction, resulting in the quasiparticle (QP) band gap E_g^{HF} (QP limit). This is similar to the mechanism yielding larger band gaps in GW calculations compared to DFT calculations. In the presence of Coulomb attraction between electron and hole, the excitonic gap E_g^{exc} is strongly reduced by the exciton binding energy E_B and cancels to some extent the exchange effects of Σ^{HF} as we will discuss in the following.

To investigate the effect of external screening on excited states, we show two quantities of a monolayer embedded in a homogeneous environment in Fig. 5.3.2 : (i) The linear optical absorption spectra obtained according to Eq. (5.2.2), and (ii) the two-particle DOS from Eq. (5.2.4) for a real space supercell of approximate area $(9 \times 10) a^2$ using a lattice constant $a_{\text{latt}} = 3.18 \text{ \AA}$ for MoS_2 for both models.

In general, for different models and in-plane hoppings t we see that external screening, modeled with the dielectric constant ε as described in Appendix A.3.1, has a large impact on both the absorption spectra and two-particle DOS. In all cases, even though in the localized models most pronounced, smaller dielectric constants (i.e., weaker screening / stronger interaction) lead to energetically more extended spectra with spectral weight being shifted towards higher excitation energies. The NI limit is described by $\varepsilon \rightarrow \infty$ and thus yields all possible excitations of non-interacting particles. Then, the lowest-energy transition is the single-particle gap E_g^0 . We see, that the influence of the environment is stronger on the the higher energy states, which

are marked by solid lines in Fig. 5.3.2a. They shift much more upon changes in the dielectric surroundings than the lowest-energy excitation (dashed lines), which are shown in the insets of the two-particle DOS. For example, in the localized hexagonal bilayer, the lowest exciton is shifted by 0.3 eV, which is 1 eV smaller than the shift of one of the higher energy excitations (1.3 eV).

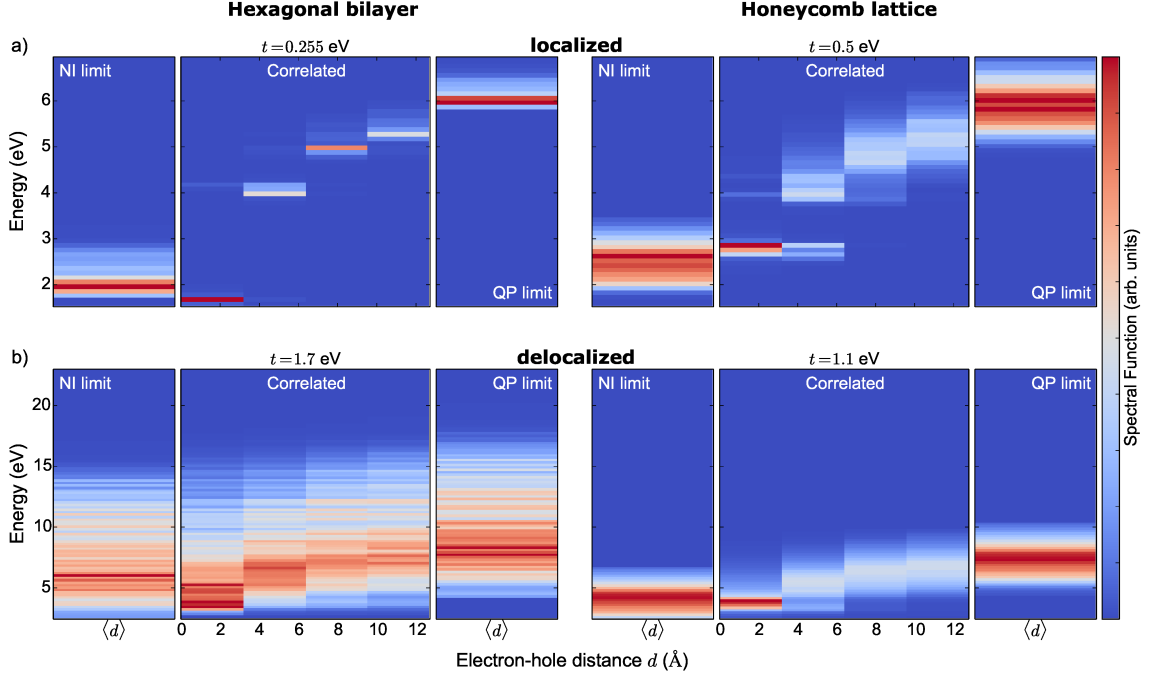
To explain this relation between excitation spectra and dielectric environment, we show the two-particle DOS calculated with Eq. (5.2.5) as function of electron-hole distance of the fully interacting system in Fig. 5.3.3 for $\varepsilon = 2$. We compare this data to the non-interacting two-particle DOS ($\varepsilon \rightarrow \infty$) and to the two-particle DOS in the QP limit for vanishing electron-hole interaction ($V_{ijkl}^{ehhe} = 0$) to show the interplay of excitonic binding E_B and exchange self-energy Σ^{HF} as already discussed for Fig. 5.3.1. In the NI and in QP limit, the figures show the joint DOS, i.e., the DOS of simple electron-hole excitations resulting from the non-interacting and Hartree-Fock calculations. The lowest-energy excitation visible in these joint DOS are then the non-interacting E_g^0 and the HF quasiparticle band gap E_g^{HF} . As the NI and QP limits are always independent of the electron-hole interaction, there is no dependence of the spectral function on the electron-hole distance.

As soon as the Coulomb interaction between the electron and the hole is considered (as shown in panels marked as "correlated") we find (i) a strong dependence on the electron-hole distance and (ii) a, in comparison to the QP band gap E_g^{HF} , reduced excitonic gap E_g^{exc} which can be identified as the lowest peak in all correlated spectra. In more detail, we find that this lowest-excitation belongs to a bound exciton with the electron and hole being in close proximity. With growing electron-hole distance the correlated DOS shows excitonic peaks at elevated energies. Thus, the corresponding excitonic binding energies get smaller with increasing electron-hole distance until the correlated DOS approaches the QP limit.

Consequently, higher energy states belong to two-particle excitations where electrons and holes are not in too close proximity. Since the environmental screening is more effective for larger separations of the electron and the hole, these higher states can generally be easily manipulated by engineering of the dielectric environment as also shown in Ref. [188].

5.3.2. Response of lowest-energy exciton to dielectric screening

The lowest-energy excitation can show a different response to the dielectric screening than the higher excitations as can be seen for example in Fig. 5.3.2a, where the lowest energy exciton shifts in a different direction than the higher ones upon increasing ε . Especially in the localized models, an almost perfect cancellation of the exciton binding and electron-electron exchange effects can occur resulting in an almost static or only slightly shifted peak position. We analyze this behavior by plotting the energetic shift $\delta E = E_g^{\text{exc}} - E_g^0$ of the lowest-energy exciton E_g^{exc} with respect to the non-interacting band gap E_g^0 and the corresponding excitonic Bohr radius a (c.f.,


Figure 5.3.3.

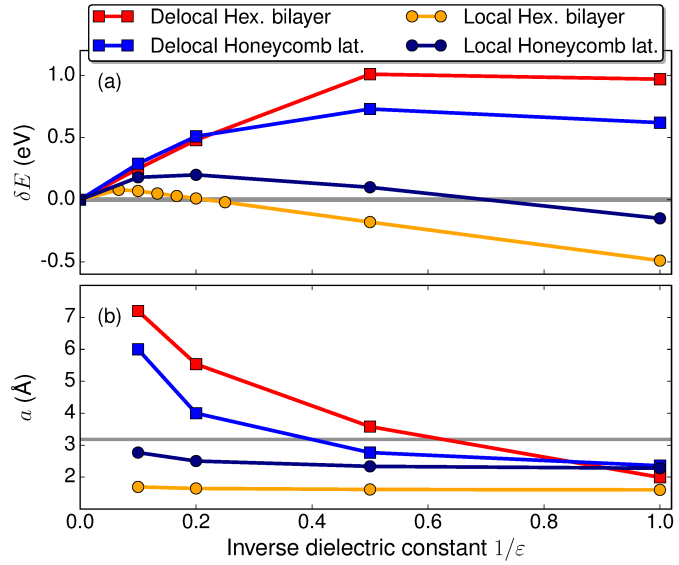
Local two-particle DOS for $\varepsilon = 2$ for different models and in-plane hopping parameters t . A smaller t describes more strongly localized electrons. The quasiparticle (QP) limit corresponds to the case of vanishing electron-hole interaction ($V_{ijkl}^{ehhe} = 0$) but electron-electron interaction being included via the Hartree-Fock self-energy. In addition, the non-interacting (NI) limit $\varepsilon \rightarrow \infty$ is depicted. As the QP and the NI limit show no spatial dependence, the corresponding two-particle DOS are spatially averaged. Note that in the "localized" panels a broadening of $\Gamma = 0.01$ eV and in the "delocalized" panels $\Gamma = 0.1$ eV was used.

Eq. (A.3.12) in Appendix A.3.5) as a function of the inverse environmental dielectric constant in Fig. 5.3.4. In all cases, we see an increase of $\delta E \propto 1/\varepsilon$ at sufficiently weak interactions ($1/\varepsilon \ll 1$) meaning the optical gap shifts to higher energies for smaller ε just like the higher excitonic states. As E_g^{exc} and with it δE depends on the size of the exchange self-energy Σ^{HF} and the binding energy E_B (c.f., Fig. 5.3.1), this directly follows from $\Sigma^{\text{HF}} \propto 1/\varepsilon$ (for $1/\varepsilon \ll 1$) and $E_B \propto 1/\varepsilon^2$ within the Wannier-Mott model for excitons (c.f. Eq. (2.5.22)). In other words for sufficiently weak interactions ($1/\varepsilon \ll 1$) exchange self-energy effects always dominate over electron binding effects, and the lowest-energy exciton shifts similarly upon changes in $1/\varepsilon$ as the higher excitons. However, the dependence of δE on $1/\varepsilon$ changes fundamentally at larger interaction strength being no longer given by a linear increase, but a decreasing energy shift upon increasing interaction. This can be seen exemplary in the delocalized models for $1/\varepsilon > 0.5$ and in the localized models for even smaller

interactions. The corresponding Bohr radii a (see Fig. 5.3.4b) show that this change in the dependence of the excitonic gap on the Coulomb interaction occurs when a and with that the spatial extent of the exciton approaches the length scale of the lattice spacings (marked as gray line). Then, the Wannier-Mott model is no longer a good description of the exciton binding. Thus, for the lowest-energy exciton a subtle interplay between exchange effects and the exciton Bohr radius determines how this exciton reacts on changes in environmental screening and it can either shift towards lower or higher energies upon increasing $1/\varepsilon$.

Figure 5.3.4

a) Energetic shift $\delta E = E_g^{\text{exc}} - E_g^0$ of the lowest-energy exciton E_g^{exc} with respect to the non-interacting band gap E_g^0 as function of the inverse environmental dielectric constant $1/\varepsilon$. b) The Bohr radius a of the lowest-energy exciton as a function of $1/\varepsilon$. The grey line marks the lattice constant.



5.3.3. Excitonic properties of a semiconductor monolayer embedded in laterally structured environment

Now, we investigate how two-particle excitations react to Coulomb engineered heterostructures as proposed and discussed in Chapter 4.

As the forthcoming results do not critically depend on the choice of the model Hamiltonian, we focus on the hexagonal bilayer with $t = 0.255$ eV and include screening effects as introduced in Chapter 4 (c.f. Eq. (A.3.7) in Appendix A.3.1). We use a laterally structured environment with two different dielectrics with $\varepsilon_1 = 5$ and $\varepsilon_2 = 2$.

On the quasiparticle level this setup leads to a heterojunction-like spatial modulation of the band gap with a type-II like band line-up as we discussed in detail in Section 4.3.3 already. For the specific choice of parameters in this chapter the quasiparticle local DOS is shown in Appendix A.3.6. The dielectric interface induces a spatial dependence in the local DOS such that the quasiparticle band gap E_g^{HF} in the region with the higher value of ε is smaller than the band gap in the other region.

The same physics governs the spatial energy landscape experienced by two-particle excitations, as can be seen from the spatially resolved two-particle DOS shown in Fig. 5.3.5. Here, red dots mark the position of the electron (to be more precise, the unit-cell index of the corresponding electron wave function). The unit cell index of the hole is used as a spatial coordinate across the supercell along a line perpendicular to the interface. In addition, we also show the spatially resolved quasiparticle limit of the two-particle DOS in the left panel which simply follows the heterojunction type band gap structure seen in the single-particle DOS of Fig. A.3.1 in the Appendix with the smaller quasiparticle band gap in the region with larger ϵ_1 .²

For the interacting case, shown in the right three panels of Fig. 5.3.5, we find that particularly the higher excitonic states are strongly influenced by the environment. Their energies follow the heterojunction-like band gap profile imprinted by the external dielectric essentially *on an atomic scale*. This means that higher energy two-particle excitations can be trapped and guided on an atomic scale non-invasively by creating a spatial potential energy landscape as, for example, suggested in Fig. 5.1.1e.

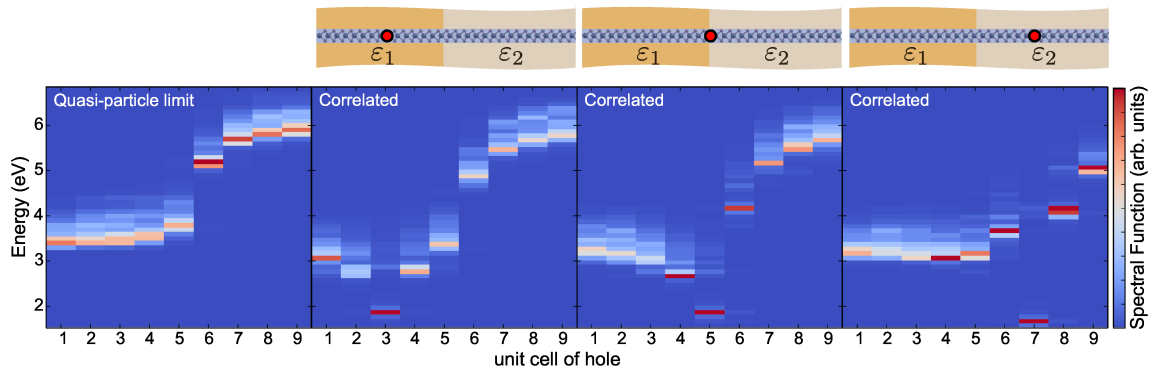


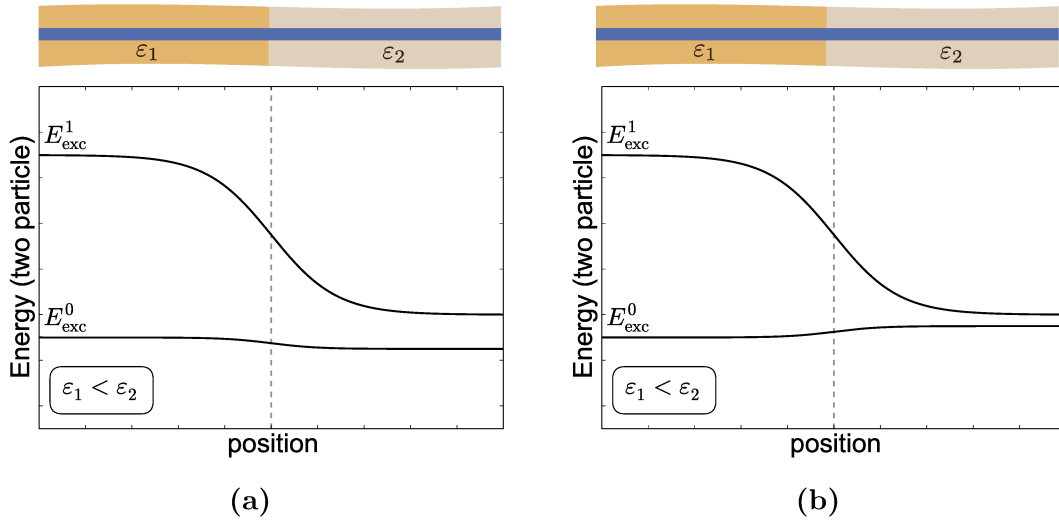
Figure 5.3.5.

Local two-particle DOS for a heterogeneous dielectric environment with $\epsilon_1 = 5$ and $\epsilon_2 = 2$. The x -axis marks the used hole positions whereas the red dot in the picture reveal the chosen electron positions for each subfigure. The quasiparticle limit (left panel) show all possible electron-hole excitations without electron-hole interaction.

The lowest-energy excitations, where electron and hole are closest together, are much less influenced by the dielectric environment, i.e., modulations in the corresponding excitation energies are about one order of magnitude smaller than for the higher energy excitons. Thus, while the higher excitations are trapped, the lowest-energy exciton can move almost freely.

Depending on the characteristics of the system, the energy landscape of the lowest exciton can either follow or be *inverted* with respect to the energy landscape ex-

²As the conduction band states are only weakly modified by the dielectric environment, the two-particle DOS in the quasiparticle limit is almost independent of the electron position and only the dependency on the hole position is shown in the left panel of Fig. 5.3.5.

**Figure 5.3.6.**

Schematic sketch of potential energy landscape when the lowest exciton either (a) follow the higher energy excitons or (b) is inverted with respect to the higher energy exciton for strongly localized excitons.

perceived by the higher energy excitons as sketched in Fig. 5.3.6. Inverted in this context means, that the energies of the lower excitons shift in different directions as compared to their higher energy counterparts. The example considered in Fig. 5.3.5 reveals such an inverted potential energy landscape as the energies of the higher excitons in the region with $\epsilon_1 = 5$ are smaller than in the region with $\epsilon_2 = 2$ but the lowest exciton has a slightly larger energy in the region with ϵ_1 . A comparison with Fig. 5.3.4 reveals that such inverted potential energy landscapes are expected for strongly localized excitons (i.e., Frenkel excitons) but not for Mott-Wannier excitons. Only for Frenkel excitons the lowest-energy excitation shifts towards smaller energies upon decreasing ϵ (increasing $1/\epsilon$) in contrast to the shift of the higher energy excitations.

5.4. Conclusions

We have shown that two-particle excitations in 2d materials show a peculiar response to their dielectric environment. The higher energy states are in general strongly influenced by the dielectric environment, which means that their excitation energies can be tuned at energy scales comparable to the quasiparticle gap at spatial distances of a few lattice constants. This leads to the prospect of trapping and guiding higher energy excitons in 2d materials (including Rydberg excitons, which have been realized

e.g., in MoS₂ [172]) simply via the dielectric landscape of the surrounding medium in a non-invasive way.

For the lowest-energy exciton, which determines by definition the excitonic band gap E_g^{exc} , we have shown that the lowest-energy exciton are less influenced by substrates yielding a less sensitive excitonic gap to the surroundings [180]. A stronger screening reduces the exciton binding energy which is compensated by the screening induced reduction of the quasiparticle band gap. Nevertheless, we see that the Bohr radius in comparison to the lattice spacing determines how E_g^{exc} responds to modulations in the dielectric environment. In the Wannier-Mott limit of delocalized excitons, the excitonic gap follows the trend of the higher energy excited states and, the quasiparticle gap, i.e., the ground-state exciton shifts in the same direction (albeit by a lesser amount) as the higher energy excitons upon changes in the dielectric environment. In the limit of strongly localized excitons, this trend is reversed and the ground-state exciton experiences a potential energy landscape which is inverted with respect to the higher excited states.

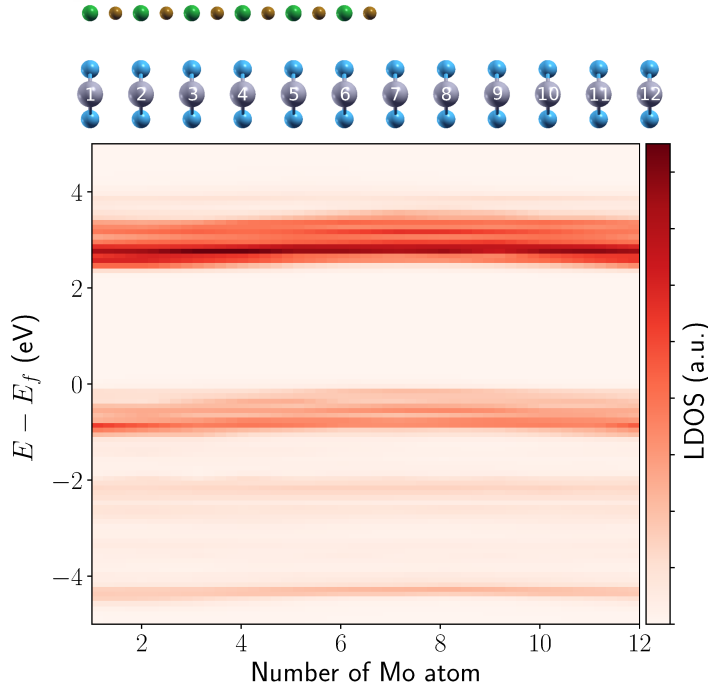
Rather unexpected types of potential energy landscapes can emerge from this different response of two-particle excitations to external dielectrics, where higher energy states are trapped on atomic scale but lower energy states move almost freely or are even expelled from the trapping regions. This opens a large parameter space for dielectric quantum engineering of nanostructures hosting exotic physical states of matter with a variety of imaginable applications. One possible candidate are substrates with periodically modulated dielectric constants such as shown in Fig. 5.1.1e, that would allow for a nanoscale separation of higher energy and ground-state excitons. Locally occupation-inverted regions should occur in these systems already upon weak optical pumping, which would be interesting in context of laser applications.

6. Material realistic description of Coulomb engineered heterostructures

In Section 3.2 we discussed in detail how the Coulomb interaction in 2d materials is enhanced and influences the quasiparticle band gap on the order of 100 meV. By embedding 2d materials in spatially inhomogeneous dielectric environments, the quasiparticle band gaps can be tuned in different regions of the monolayer to create Coulomb engineered (CE) heterostructures [22, 177, 188] as intensely studied in a model system in Chapter 4. In this chapter we turn to a material realistic approach.¹ The possibility to use dielectric environments has become a promising virtue to tailor new electronic, excitonic and optoelectronic devices [181, 187, 190, 191, 193, 195, 256]. To predict suitable 2d materials as well as substrates we need a profound theoretical insight in the processes. Although for describing the important Coulomb effects GW calculations are necessary and the standard way to go nowadays, calculations of full lateral or vertical 2d heterostructures are numerically very demanding as we show in Section 6.1. Therefore, in Section 6.2 we present a modeling scheme based on a combination of $G\Delta W$ [107, 186] and the WFCE [167] approach to systematically investigate material realistically semiconducting transition metal dichalcogenides in their H -phase. From this we want to identify optimal candidates for Coulomb engineering in the class of semiconducting TMDCs and discuss the underlying mechanisms.

Firstly we try to model Coulomb engineered heterostructures by means of full ab-initio G_0W_0 calculations with a supercell approach. We show that numerically reasonable supercell sizes are too small to capture the underlying long-ranged Coulomb effects. Secondly we use the mentioned modeling scheme to investigate how semiconducting TMDCs MX_2 with $M \in \{\text{Mo}, \text{W}\}$ and $X \in \{\text{S}, \text{Se}\}$ react to different dielectric environments. We show that all TMDCs are equally suitable for Coulomb engineering yielding similar *relative* band gap reductions for increasing screening. If absolute band gap changes are of interest, the selenides are weaker influenced due to their larger intrinsic dielectric function. This is supported by previous theoretical calculations [186, 192, 257] showing that the band gap of a monolayer will be stronger

¹The results shown in this chapter, which are in preparation for publication, were obtained in close collaboration with M. Rösner and under the supervision of T. Wehling.

**Figure 6.1.1.**

Side view of supercell with a laterally structured substrate (hBN – vacuum) for MoS₂. The gray and blue spheres are the MoS₂ units. Half of the monolayer is capped with hexagonal boron (green) nitride (gold) leading to different dielectric environments for the left and the right MoS₂ units. Also shown is the spatially resolved local density of states of states of *d*-orbitals of Mo around the Fermi energy for all Mo-atoms in the supercell shown. Maxima in the conduction and valence band of the LDOS correspond the dark red areas.

influenced if their intrinsic screening is small. We show that the length scale of the self-energy is on the order of the lattice parameter for all materials, resulting in a characteristic length scale of the interface of a few unit cells.

6.1. Full ab-initio description of Coulomb engineered heterostructures

6.1.1. Monolayer MoS₂ in laterally structured dielectrics

For a material realistic ab-initio description of Coulomb engineered heterojunctions, we perform G_0W_0 calculations for MoS₂ placed on a substrate consisting of a monolayer of strained hexagonal boron nitride (hBN) and vacuum. The size of the supercell was restricted to twelve primitive unit cells of MoS₂ with six of them covered with hBN (see Fig. 6.1.1) due to computational limits.

To achieve converged G_0W_0 calculations, the vacuum heights and energy cutoffs and with that the number of considered bands are important to consider. However, doing a fully converged calculation² is already difficult for primitive unit cells and becomes even harder for supercell calculations. As a result we choose a sufficiently low number of empty bands and a small vacuum height for a basic primitive unit

²Convergence studies of G_0W_0 calculations are presented in Appendix A.4.3

cell with a substrate, which surprisingly still produce the desired effect qualitatively, i.e. a change of the quasiparticle band gap compared to a freestanding monolayer. For the supercell calculations we scale the parameters ruling the convergence of the system consistently to this primitive cell. In detail this means for the 12×1 supercell we used 12 times the number of bands of the primitive cell with the same vacuum heights and a appropriately reduced \mathbf{k} -grid in the direction of the supercell.

In Fig. 6.1.1 the local density of states (LDOS) of a system with a laterally structured substrate is depicted. We only show the LDOS of the three d -orbitals around the Fermi energy ($d_{xy}, d_{x^2-y^2}, d_{z^2}$) for every Mo atom numbered accordingly to the crystal structure shown in Fig. 6.1.1. Remarkably, there is no clear spatial band gap modulation visible, if at all only a slight bend of the maximum in the conduction band. The quasiparticle band gap seems to be nearly constant through the whole supercell.

For a more detailed investigation we show in Fig. 6.1.2a the LDOS of Mo in the middle of the left (with substrate) and the middle of the right (no substrate) region. Indeed we find a slight shift of the maxima in the conduction and valence band in the different regions, but the band gaps remain unchanged. However, far apart from the interface, a "homogeneous" behavior with band gaps corresponding to systems without any interface should be observed. In Fig. 6.1.2b the LDOS resulting from calculations with corresponding homogeneous substrates are shown, which suggest a band gap difference between the different systems of around 100 meV (marked with the gray dashed line) which we do not find in the calculations for the heterojunction.

These ab-initio results are contradictory to our model calculations discussed in Chapter 4 as well as experimental data [188, 189] which show a band gap shift in distance of the interface. Since VASP uses periodic images of the supercell, in fact this system does not model only one interface in the middle of the cell but two additional ones at the borders. We speculate that the chosen supercell is too small to describe Coulomb engineered heterostructures as effects from the interfaces seem to prevent the expected band gap modulation. That's why we turn to material realistic modeling of the systems of interest in the following sections.

6.2. Material realistic modeling

As we have seen in the previous section, a full ab-initio description for Coulomb engineered heterostructures is numerically very demanding and extremely costly. As a result we turn to a more efficient procedure in the following. When hybridization effects between monolayer and substrate can be neglected, we can circumvent the need for large supercells and strained substrates with the so called $G\Delta W$ [107, 186] approach. Thereby we use a full G_0W_0 ab-initio description of a *freestanding* monolayer and incorporate the environmental screening through a model dielectric function. The main idea of this method is to calculate the *change* of the quasiparti-

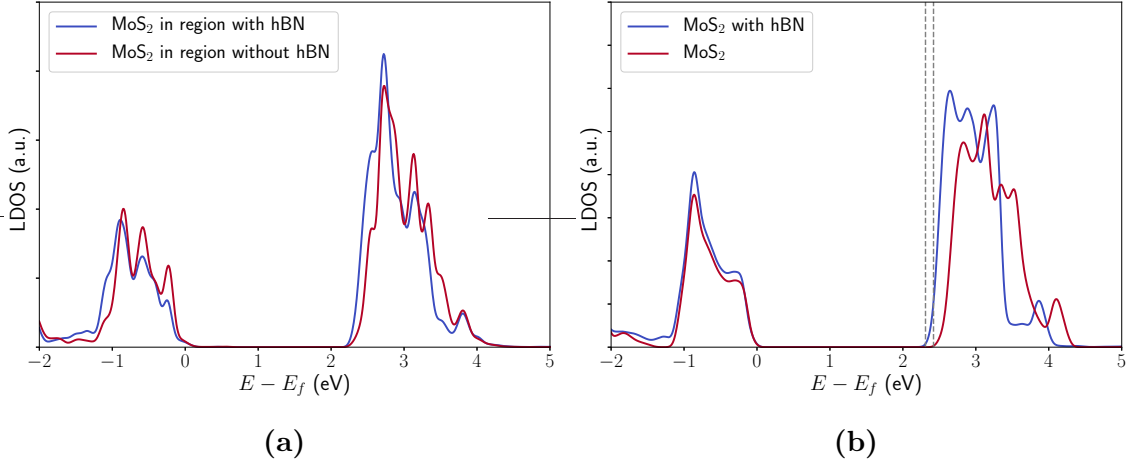


Figure 6.1.2.

(a) Local density of states from atom from region with substrate (red) and without substrate (blue). (b) Density of states of MoS₂ with (red) and without (blue) substrate. The valence band energy is set to zero, so no band alignment was considered in this graph. The grey dashed lines mark the conduction band position and with that the size of the band gap of the systems.

cle energies due to the change of the long-ranged Coulomb interaction resulting from *external* screening (through substrates). The used code was developed by M. Rösner with contributions from R. E. Groenewald, G. Schönhoff and myself [74, 83].

6.2.1. The $G\Delta W$ approach

For the calculation of the quasiparticle energies of a monolayer on a substrate or embedded in a dielectric environment, we have to find the Green's function (c.f., Section 2.4.1)

$$G^\varepsilon(\omega) = (\omega - H_0^{\text{DFT}} - \Sigma^\varepsilon(\omega))^{-1} \quad (6.2.1)$$

in which H_0 is the (in a mean field way) non-interacting Hamiltonian, which we can obtain from DFT calculations. The self-energy Σ^ε includes all additional interaction effects of the monolayer and the substrate. We can rewrite this using the G_0W_0 Hamiltonian of a freestanding monolayer

$$G^\varepsilon(\omega) = (\omega - H_{G_0W_0}^{\text{FS}} - \Delta\Sigma) \quad (6.2.2)$$

while introducing a self-energy in GW approximation

$$\Delta\Sigma = iG_0\Delta W = iG_0(W^\varepsilon - W^{\text{FS}}). \quad (6.2.3)$$

Here, W^{FS} is the fully screened Coulomb interaction of the freestanding monolayer, W^ε the fully screened Coulomb interaction of the monolayer with an external substrate and G_0 the Green function of the freestanding DFT Hamiltonian. Thus this self-energy contains the *renormalization* of the G_0W_0 quasiparticle energies due to external substrate effects. In this work we use the minimal tight-binding model for TMDCs described in Section 3.3 in orbital basis. The self-energy considering only density-density matrix elements $\Sigma^{\alpha\beta\gamma\delta} \approx \Sigma^{\alpha\beta\beta\alpha} \equiv \Sigma^{\alpha\beta}$ in this basis can be written as

$$\Delta\Sigma^{\alpha\beta}(\mathbf{k}, \omega) = \frac{i}{2\pi} \int \frac{d^2q}{(2\pi)^2} \int d\omega' \sum_{\lambda} \Delta W^{\alpha\beta}(\mathbf{q}, \omega) \frac{c_{\alpha}^{\lambda}(\mathbf{k}-\mathbf{q})[c_{\beta}^{\lambda}(\mathbf{k}-\mathbf{q})]^*}{\omega + \omega' - \varepsilon_{\mathbf{k}-\mathbf{q}}^{\lambda} + i\eta^+ \text{sgn}(\varepsilon_{\mathbf{k}-\mathbf{q}}^{\lambda})}, \quad (6.2.4)$$

where $\varepsilon_{\mathbf{k}-\mathbf{q}}^{\lambda}$ are the eigenenergies and $c_{\beta}^{\lambda}(\mathbf{k}-\mathbf{q})$ the coefficients of the eigenfunctions of the DFT Hamiltonian in the orbital basis. That means to treat a system with substrate we have to calculate the DFT and G_0W_0 Hamiltonian in orbital basis³ for a *freestanding* monolayer just once and find ΔW . Therefore we use the cRPA approximation introduced in Section 2.3.3 in matrix representation:

$$\mathbf{W}^{\varepsilon/\text{FS}}(\mathbf{q}, \omega) = \mathbf{U}^{\varepsilon/\text{FS}}(\mathbf{q}, \omega) \cdot [\boldsymbol{\varepsilon}^{\varepsilon/\text{FS}}(\mathbf{q}, \omega)]^{-1}, \quad (6.2.5)$$

where $\mathbf{U}^{\varepsilon/\text{FS}}(\mathbf{q}, \omega)$ is the partially screened Coulomb interaction in orbital basis which includes the screening effects of all other bands not part of the minimal basis and for \mathbf{U}^{ε} additionally the external screening of the environment. The dielectric function is defined as

$$\varepsilon = 1 - \Pi_0 \cdot U \quad (6.2.6)$$

with the RPA polarization function from Eq. (2.3.37) in density density approximation

$$\Pi_0^{\alpha\beta\gamma\delta} \approx \Pi_0^{\alpha\beta} = \sum_{\lambda\lambda'} [c_{\lambda}^{\beta}(\mathbf{k})]^* [c_{\lambda'}^{\alpha}(\mathbf{k}-\mathbf{q})]^* c_{\lambda}^{\alpha}(\mathbf{k}) c_{\lambda'}^{\beta}(\mathbf{k}-\mathbf{q}) \frac{f_{\mathbf{k}-\mathbf{q}}^{\lambda'} - f_{\mathbf{k}}^{\lambda}}{\omega + i\eta^+ + \varepsilon_{\mathbf{k}-\mathbf{q}}^{\lambda'} - \varepsilon_{\mathbf{k}}^{\lambda}}. \quad (6.2.7)$$

How we obtain U is described in Section 6.2.2.

³To get the Hamiltonians in the orbital basis, we use the `Wannier90` code as described in Section 3.3.

As explained in Section 2.4.3 (c.f., Eq. (2.4.30) and Eq. (2.4.31)) the real part of the self-energy can be separated in a screened exchange and Coulomb hole term, which can be written in orbital basis as:

$$\Sigma_{\text{SEX}}^{\alpha\beta}(\mathbf{k}, \omega) = - \int \frac{d^2q}{(2\pi)^2} \sum_{\lambda}^{\text{occ}} \Delta W^{\alpha\beta}(\mathbf{q}, \omega - \varepsilon_{\mathbf{k}-\mathbf{q}}^{\lambda}) c_{\alpha}^{\lambda}(\mathbf{k} - \mathbf{q}) [c_{\lambda'}^{\alpha}(\mathbf{k} - \mathbf{q})]^* \quad (6.2.8)$$

$$\Sigma_{\text{COH}}^{\alpha\beta}(\mathbf{k}, \omega) = \int \frac{d^2q}{(2\pi)^2} \sum_{\lambda} c_{\alpha}^{\lambda}(\mathbf{k} - \mathbf{q}) [c_{\lambda'}^{\alpha}(\mathbf{k} - \mathbf{q})]^* \int_0^{\infty} d\omega' \frac{\Delta B^{\alpha\beta}(\mathbf{q}, \omega)}{\omega - \varepsilon_{\mathbf{k}-\mathbf{q}}^{\lambda} - \omega'} \quad (6.2.9)$$

with $\Delta B^{\alpha\beta}$ the spectral function related to ΔW with (c.f. Eq. (2.4.32))

$$\Delta W^{\alpha\beta}(\mathbf{q}, \omega) = \int_0^{\infty} d\omega' \frac{2\omega' \Delta B^{\alpha\beta}(\mathbf{q}, \omega')}{\omega^2 - (\omega' - i\eta^+)^2}. \quad (6.2.10)$$

Since the polarization function (c.f. Eq. (6.2.7)) is frequency dependent, the Coulomb interaction (and the renormalization of the Coulomb interaction ΔW) has to be depending on ω as well and with that we have to consider a frequency dependent self-energy. However, in a semiconductor with a band gap E_g the polarization function is not strongly depending on ω for small $\omega < E_g$ (in contrast to a metal where we already find strong frequency dependence for small ω). If the active material and the substrate are semiconducting (or insulating) we can assume that the polarization functions for both systems are structure less for ω smaller than the band gaps and hence can approximate $W^{\varepsilon/\text{FS}}(\omega \ll E_g^{\varepsilon/\text{FS}}) \approx W^{\varepsilon/\text{FS}}(\omega = 0)$ yielding $\Delta W(\omega, \mathbf{q}) \approx \Delta W(\omega = 0, \mathbf{q})$. So, as long as ΔW is quite structureless for small ω , we can use the static COHSEX approximation to derive the self-energy:

$$\Delta \Sigma_{\text{SEX}}(\mathbf{q}) = - \int \frac{d^2q}{(2\pi)^2} \sum_{\lambda}^{\text{occ}} \Delta W^{\alpha\beta}(\mathbf{q}, \omega = 0) c_{\alpha}^{\lambda}(\mathbf{k} - \mathbf{q}) [c_{\beta}^{\lambda}(\mathbf{k} - \mathbf{q})]^* \quad (6.2.11)$$

$$\Delta \Sigma_{\text{COH}}(\mathbf{q}) = \frac{1}{2} \int \frac{d^2q}{(2\pi)^2} \sum_{\lambda} \Delta W^{\alpha\beta}(\mathbf{q}, \omega = 0) c_{\alpha}^{\lambda}(\mathbf{k} - \mathbf{q}) [c_{\beta}^{\lambda}(\mathbf{k} - \mathbf{q})]^*. \quad (6.2.12)$$

Thereby we assumed $\Delta W^{\alpha\beta}(\mathbf{q}, \omega - \varepsilon_{\mathbf{k}-\mathbf{q}}^{\lambda}) \approx \Delta W(\mathbf{q}, \omega = 0)$ and $\omega - \varepsilon_{\mathbf{k}-\mathbf{q}}^{\lambda} \ll \omega'$ in Eq. (6.2.8) and Eq. (6.2.9) and used Eq. (6.2.10). The SEX terms only changes occupied states, in other words only the valence band is shifted and with that the band gap changes due to the Coulomb interaction. In TMDCs this means, as discussed in Section 4.2, the hybridization is altered. The Coulomb hole term is added on the valence and conduction bands equivalently yielding a shift of both bands. Within the static COHSEX approximation it is more convenient to perform the RPA step before we include the dielectric environment within our ab-initio step, meaning that we use in Eq. (6.2.5) RPA screened Coulomb matrix elements $U_{\alpha,\beta}^{\varepsilon/\text{FS}}(\mathbf{q}, \omega)$ which

already include all *internal* screening effects. The external screening is then added as described in the following section.

6.2.2. Modeling the Coulomb interaction

We utilize the WFCE approach [167] developed by Rösner et al. to include dielectric environments in the partially screened Coulomb interaction U . Therefore, we fit the *leading eigenvalue* of the bare Coulomb interaction and the dielectric function of freestanding monolayer to ab initio (c)RPA calculations and correct the *leading eigenvalue* of ε . We follow the fitting procedure described by Schönhoff et al. [231].

We start with the bare $V_{\mathbf{q}}^{\alpha\beta}$ and screened Coulomb interaction $U_{\mathbf{q}}^{\alpha\beta}$ in the orbital basis in density-density approximation from ab-initio (c)RPA calculations implemented in VASP by Kaltak [90]. Firstly, we diagonalize the bare interaction $V_{\mathbf{q}}$

$$V_{\mathbf{q}}^{\text{diag}} = V_1(\mathbf{q}) |e_1\rangle \langle e_1| + V_2(\mathbf{q}) |e_2\rangle \langle e_2| + V_3(\mathbf{q}) |e_3\rangle \langle e_3|, \quad (6.2.13)$$

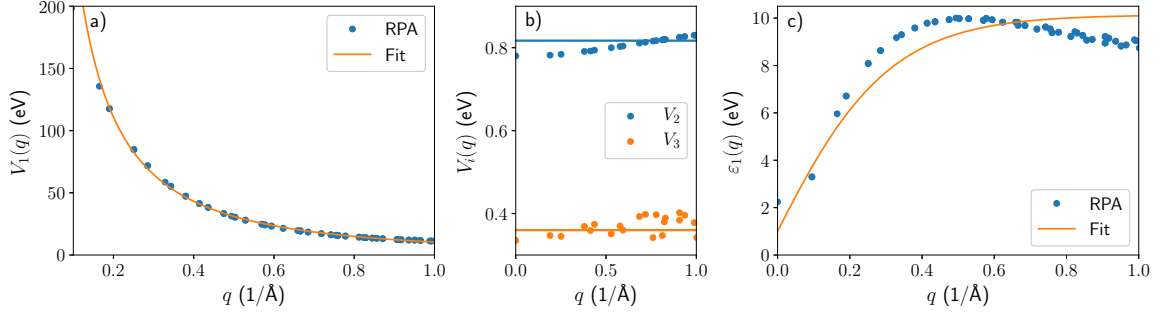
where $V_1(\mathbf{q}) = \langle e_1 | V_{\mathbf{q}} | e_1 \rangle$ is the leading (i.e. largest) eigenvalue and e_i are the eigenvectors of $V_{\mathbf{q}}$ in the long-wavelength limit $q \rightarrow 0$

$$e_1 = \begin{pmatrix} 1/\sqrt{3} \\ 1/\sqrt{3} \\ 1/\sqrt{3} \end{pmatrix}, \quad e_2 = \begin{pmatrix} \sqrt{2/3} \\ -1/\sqrt{6} \\ -1/\sqrt{6} \end{pmatrix}, \quad e_3 = \begin{pmatrix} 0 \\ 1/\sqrt{2} \\ -1/\sqrt{2} \end{pmatrix}. \quad (6.2.14)$$

The leading eigenvalue can be interpreted as charge-density modulations with long wavelength, i.e. the wavelength for which screening effects due to environments are supposed to be strongest. For this limit, a macroscopic treatment with continuum medium electrostatics is possible, thus we can connect the leading eigenvalue to the *macroscopic* properties [167]. The other values $V_{2/3}$ are assumed to be constant [231] and obtained by averaging over the ab-initio values. The macroscopic value of V_1 is fitted with

$$V_1(\mathbf{q}) = \frac{3e^2}{2\varepsilon_0 A} \frac{1}{q(1 + \gamma q)} \quad (6.2.15)$$

where we use the area of the 2d hexagonal unit cell $A = \frac{\sqrt{3}}{2}a^2$ and the form factor γ which describes how the effective height of the orbitals influences short wavelengths. In Fig. 6.2.1a and Fig. 6.2.1b we show the fit for the leading eigenvalue and the other eigenvalues for MoS₂.


Figure 6.2.1.

RPA (dots) and Fits (lines) for MoS₂ for the leading eigenvalue V_1 (a), the other eigenvalues of $V_{2/3}$ (b) and the leading eigenvalue of ε_1 c).

The screened Coulomb matrix $U(\mathbf{q})$ is assumed to have the same eigenbasis as $V(\mathbf{q})$, thus the macroscopic eigenvalue can be determined with $U_1(\mathbf{q}) = \langle e_1 | U(\mathbf{q}) | e_1 \rangle$. With

$$U_i(\mathbf{q}) = [\varepsilon_i(\mathbf{q})]^{-1} V_i(\mathbf{q}) \quad (6.2.16)$$

we can determine the eigenvalues of the dielectric function ε_i . The microscopic local screening effects $\varepsilon_{2/3}$ are similar to the bulk values and unaffected by the dielectric environment. The macroscopic eigenvalue can be corrected with [167, 258]

$$\varepsilon_1(\mathbf{q}, \omega) = \varepsilon_\infty \frac{1 - \beta_1 \beta_2 e^{-2qd}}{1 + (\beta_1 + \beta_2) e^{-qd} + \beta_1 \beta_2 e^{-2qd}}. \quad (6.2.17)$$

The parameter d is set to the interlayer distance from bulk systems and ε_∞ is fitted to the ab-initio (c)RPA calculations of a freestanding monolayer as shown in Fig. 6.2.1c. The factor

$$\beta_i = \frac{\varepsilon_\infty - \varepsilon_{\text{sub},i}(\mathbf{q}, \omega)}{\varepsilon_\infty + \varepsilon_{\text{sub},i}(\mathbf{q}, \omega)} \quad (6.2.18)$$

includes the dielectric functions of the material above and beneath the monolayer $\varepsilon_{\text{sub},i}(\mathbf{q}, \omega)$. As already discussed for small ω we can neglect the frequency dependence of the dielectric function. In the following we additionally neglect the \mathbf{q} dependency of the substrate and assume that the dielectric environment can be described by a constant $\varepsilon_{\text{sub},i}(\mathbf{q}, \omega) = \varepsilon_{\text{sub},i}$. We investigate the influence of a substrate $\varepsilon_{\text{sub},1} \equiv \varepsilon_{\text{sub}}$ and thus set $\varepsilon_{\text{sub},2} = 1$. With the new dielectric function the Coulomb interaction needed for Eq. (6.2.5) can be calculated as shown in Eq. (6.2.16) for arbitrary environments. For MoS₂ the fit to the leading eigenvalue of the dielectric function is shown in Fig. 6.2.1c. The obtained fit values for the TMDCs under investigation

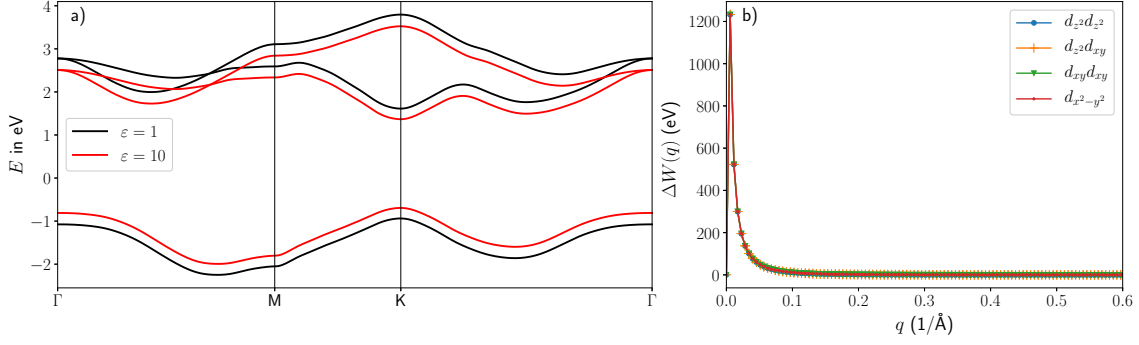


Figure 6.2.2.

a) G Δ W band structure for WS₂ for $\epsilon_{\text{sub}} = 1$ and $\epsilon_{\text{sub}} = 10$ b) $\Delta W(q)$ for WS₂ and $\epsilon = 10$ for different orbital combinations. $\Delta W(q)$ is independent of the orbital combination and strongly peaked around $q = 0$

can be found in Appendix A.4.4. A convergence study of the G Δ W calculations is presented in Appendix A.4.5.

6.2.3. Influence of dielectric substrates on TMDCs

In Fig. 6.2.2a we calculate the band structure for a dielectric substrate with $\epsilon_{\text{sub}} = 10$ for WS₂. We clearly see a band gap reduction as expected due to the stronger screening of the substrate. The band structure in general is nearly untouched, so the screening causes an overall shift of the bands but no changes of the form of the bands. This scissor-like behavior can be explained by looking at the self-energy Eq. (6.2.11) and (6.2.12). For small ω and $\epsilon_{\text{sub}} = \text{const}$ the change in the screened interaction is static and has no orbital structure. It is strongly peaked at $\mathbf{q} = 0$ as shown in Fig. 6.2.2b meaning $\Delta W^{\alpha\beta}(\mathbf{q}, \omega) \approx a\delta(\mathbf{q})$. Inserting this into Eq.(6.2.11) and (6.2.12) yields

$$\Delta\Sigma_{\alpha\beta}(\mathbf{k}) \approx -a \sum_{\lambda}^{\text{occ}} c_{\alpha}^{\lambda}(\mathbf{k}) [c_{\beta}^{\lambda}(\mathbf{k})]^* + a \sum_{\lambda} c_{\alpha}^{\lambda}(\mathbf{k}) [c_{\beta}^{\lambda}(\mathbf{k})]^*. \quad (6.2.19)$$

The self-energy only depends on \mathbf{k} and not on \mathbf{q} which means that it does not couple different \mathbf{k}, \mathbf{k}' anymore. Since a is a simple constant the screened exchange term changes the valence band and the Coulomb hole term shifts *all* bands equally yielding the symmetric alignment of the bands and in general a 'scissor'-like behavior.

Now we will concentrate on how strongly the dielectric environment influences the different TMDCs. For further investigation we calculated the band gaps for

different dielectric constants E_g^ε of the substrate and determined the absolute band gap difference $\Delta E_g = E_g^\varepsilon - E_g^0$ and the relative decrease

$$\Delta = \left(\frac{E_g^\varepsilon - E_g^0}{E_g^0} \right) \quad (6.2.20)$$

as shown in Fig. 6.2.3a and Fig. 6.2.3b in comparison to a freestanding monolayer.

For determining the band gaps spin-orbit coupling (SOC) was considered by a Russell-Saunders coupling with a k-dependent coupling parameter as described in Section 3.3. The coupling parameter is chosen such that the SOC at the valence- and conduction band at high symmetry points matches results of GGA calculations.

As expected we see a significant band gap reduction with increasing screening for all TMDCs. For $\varepsilon_{\text{sub}} = 5$ the band gaps are reduced in an energy range between 0.3 and 0.35 eV depending on the TMDC (c.f. Fig. 6.2.3a). Realistic substrates, as for example SiO_2 or Si have macroscopic dielectric constants of ≈ 3.6 [259] and ≈ 12 [260] respectively, yielding energy reductions up to 0.5 eV in our model.

The selenides are stronger affected with larger absolute changes in the band gap. This is for the Molybdenum based materials also shown by Winther and Thygesen [186], who also see a slightly smaller band gap reduction for MoSe_2 than for MoS_2 for different substrates/environments. This is due to the *intrinsic* screening of the materials. The selenides have a smaller band gap compared to the sulfides and thus they exhibit a larger internal polarisability [186] and with that a larger intrinsic screening. Then, the screening effects of the environment to the whole screening are small in comparison leading to smaller band gap corrections. However, if we consider the relative correction shown in Fig. 6.2.3b all materials show roughly the same reduction of about 15% of the native band gap for $\varepsilon_{\text{sub}} = 5$. This can be explained with the difference in the inverse of the leading eigenvalue of the dielectric function

$$\Delta\varepsilon^{-1} = \frac{\varepsilon^{-1}(\varepsilon_{\text{sub}} = 10) - \varepsilon^{-1}(\varepsilon_{\text{sub}} = 1)}{\varepsilon^{-1}(\varepsilon_{\text{sub}} = 1)} \quad (6.2.21)$$

shown in Fig. 6.2.3c. The band gap reduction is mainly determined by the difference in the Coulomb interaction ΔW , which is primarily influenced by $\Delta\varepsilon^{-1}$. The *difference* in the inverse of the dielectric function is for all investigated TMDCs similar, thus leading to a similar *relative* reduction of the band gaps. As the selenides exhibit a smaller native band gap due to a larger internal polarisability, consequently the absolute band gap reduction is also smaller.

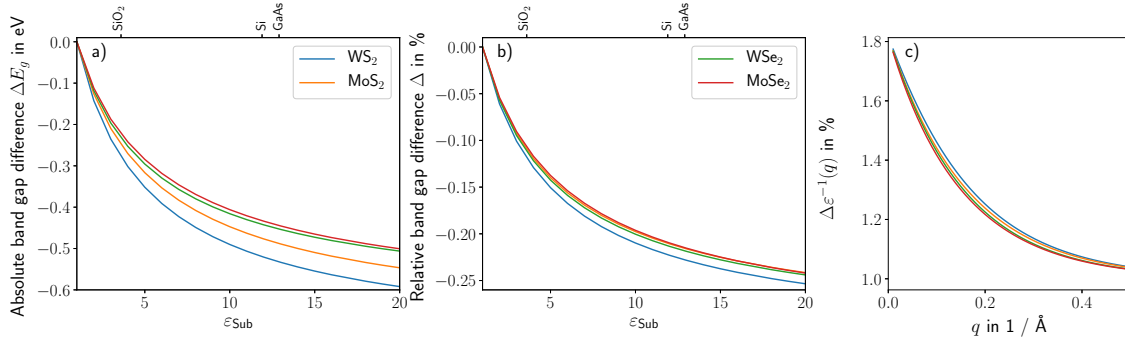


Figure 6.2.3.

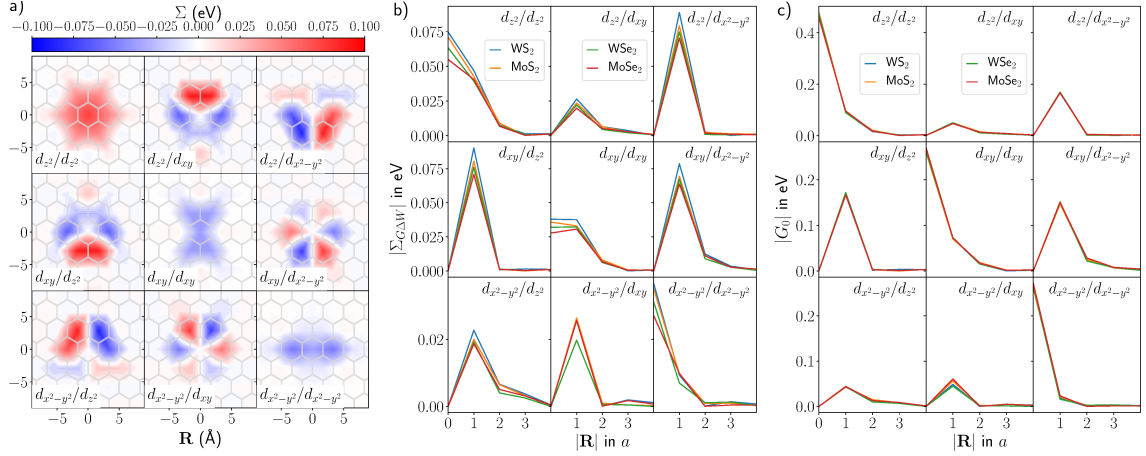
a) Absolute difference of $G\Delta W$ band gaps to the band gap of a freestanding TMDC in dependence of the screening constant ε_{sub} . b) Relative difference of $G\Delta W$ band gaps compared to the freestanding case in dependence of the substrate c) Relative change of the dielectric function $\Delta\varepsilon^{-1}$ for the investigated materials.

6.2.4. Length scale of self-energy

For a technical application of Coulomb engineered heterostructures, not only the band gap reduction but also the *length scale* on which this reduction takes place in the different materials is important. As the extent of the self-energy is an intrinsic measure how sharp an interface in a Coulomb engineered heterostructure can be, we will discuss on which length scale the self-energy for a homogeneous TMDC has significant contributions. The $\Delta\Sigma$ from Eq. (6.2.3) describes the *renormalization* of the Hamiltonian of a freestanding monolayer due to screening effects from an environment. In Fig. 6.2.4 this self-energy is shown in real space for WS_2 and $\varepsilon_{\text{sub}} = 10$ without considering spin-orbit coupling. It is similar to the G_0W_0 self-energy which was already discussed in detail in Chapter 4 and is also comparable to the self-energy resulting from G_0W_0 calculations from a monolayer on top of a substrate (see Fig. A.4.3 in Appendix A.4.6). We see that non-local terms ($\mathbf{R} \neq 0$) are renormalized which is the reason for the band gap change. Still the renormalization is only limited to a few unit cells.

This can also be seen in more detail and for all investigated TMDCs in Fig. 6.2.4b, where we show the absolute value of the self-energy along a line in direction of the basis vector of the hexagonal lattice \mathbf{a}_2 with the lattice constant a . Clearly, for all orbital combinations the largest values for all TMDCs can be found within two unit cells which corresponds to a distance of roughly 6.2 \AA to 6.6 \AA (depending on the material). Most importantly this length scale is similar for all investigated materials.

The self-energy consists of two contributions: the Coulomb interaction ΔW and the non-interacting Green's function G_0 . As ΔW is a peaked function in \mathbf{q} -space it will be nearly constant in real space. Hence, the decrease of the self-energy must result from properties of the Green's function.


Figure 6.2.4.

a) Real space representation of the self-energy of a WS₂ monolayer in an dielectric environment with $\varepsilon = 10$. b) and c) Absolute value of the self-energy and G_0 along a line in dependence of the distance in units of the lattice constant for all investigated TMDCs

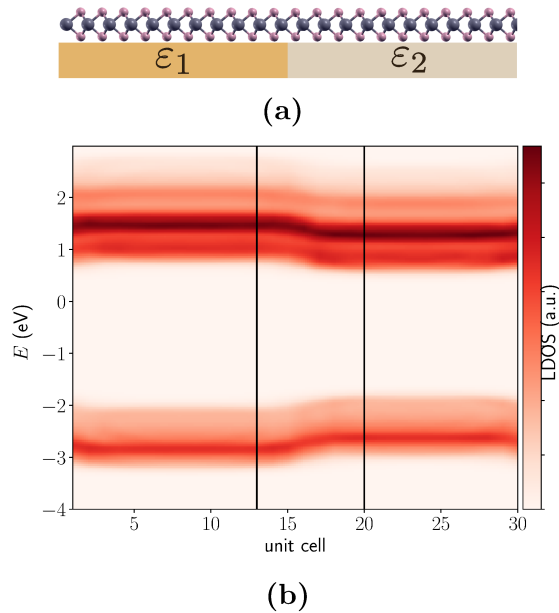
In Fig. 6.2.4c we show $G_0^{\alpha\beta}(\mathbf{R}, \tau = 0^+) = \langle c_{i\alpha}^\dagger c_{0\beta} \rangle$ along the same line as in Fig. 6.2.4b. The general curve characteristics resemble the self-energy and show the same length scale. Thus the spatial extent of the self-energy is determined by the spatial extent of G_0 . However, the band gap reduction is given by the size of the Coulomb interaction.

As G_0 is a purely material specific property the intrinsic length scale of a Coulomb engineered heterostructure is also a purely material specific property. As the semiconducting TMDCs under consideration show similar electronic band structures, they consequently have similar extents of G_0 and with that of the self-energy.

6.2.5. Coulomb engineered heterostructures

Now, we can use the self-energy from Fig. 6.2.4a to construct a model for material realistic Coulomb engineered heterostructures as shown in Fig. 6.2.5a. Therefore, we utilize the self-energy from the different regions and construct the self-energy for the heterostructure according to

$$\Sigma_{\alpha\beta}(\mathbf{R}) = \begin{cases} \Sigma_{\alpha\beta}^{\varepsilon_1} & \text{hopping in } \varepsilon_1 \\ \Sigma_{\alpha\beta}^{\varepsilon_2} & \text{hopping in } \varepsilon_2 \\ \frac{1}{2}(\Sigma_{\alpha\beta}^{\varepsilon_1} + \Sigma_{\alpha\beta}^{\varepsilon_2}) & \text{hopping between } \varepsilon_i \end{cases} \quad (6.2.22)$$

**Figure 6.2.5.**

(a) Model for Coulomb engineered heterostructure with laterally structured substrate with dielectric constants ε_1 and ε_2 (b) Local density of states for a Coulomb engineered heterostructure for WS_2 with $\varepsilon_1 = 1$ and $\varepsilon_2 = 10$.

mimicing an abrupt change of the substrate underneath. With that we get the Hamiltonian for the full heterostructure

$$H_{\alpha\beta}^{\text{het}}(\mathbf{R}) = H_{\alpha\beta}^0(\mathbf{R}) + \Sigma_{\alpha\beta}(\mathbf{R}). \quad (6.2.23)$$

The resulting local density of states (LDOS) in real space is shown in Fig. 6.2.5b. Darker red areas show high density of states whereas the light red area means a nearly zero LDOS marking the gapped region around $E = 0$. The band gap modulation in the different areas is clearly visible. On top of that we see a symmetric band alignment which results directly from the $\omega = 0$ approximation. The change of the band gap from one region to the other is limited to a few unit cells as expected from the extent of the self-energy. As shown in Appendix A.4.7 we define a characteristic length r (indicated by the black vertical lines in Fig. 6.2.5b) which shall be a measure of the interface region. In other words, r is the distance between unit cells in which we see a "homogeneous" behavior in the different regions. We see that the characteristic length that for all four TMDC under investigation is around $r = (7 \pm 1)a$ with a the lattice constant of the TMDC. For WS_2 this leads to $r \approx 22 \text{ \AA}$. Thus intrinsic limits are rather small making extrinsic limitations as the structured substrates more important for the application of Coulomb engineered heterostructures.

6.3. Conclusions

We showed that a full ab-initio description of Coulomb engineered heterostructures is numerically extremely demanding without any approximations to the dielectric

environments. To this end we turned to a more efficient approach with $G\Delta W$ calculations using a model description of the dielectric function within the WFCE framework. All in all we showed that the semiconducting TMDCs under investigation are equally suitable for Coulomb engineering, considering band gap reductions as well as the possibility for rather sharp interface regions considering intrinsic limits. Other influences on the interface region are given by extrinsic measures, e.g. the sharpness of the underlying substrate change. The similarity of the TMDCs is a result of their similar band structures and intrinsic screenings. Even though the selenides are slightly less influenced than the sulfites due to their larger internal polarizability still they all show significant absolute band gap changes.

With a multi-scale approach we showed the local density of states for a material realistic Coulomb engineered heterostructure with a characteristic length scale of the interface around 7 lattice constants for all TMDCs yielding rather small transition regions. This renders the TMDCs as promising candidates for future applications in this field.

Of course for the description of highly frequency dependent substrates as for example graphite[261] or graphene[262], our models have to go beyond the static limit [196]. The next step has to find a suitable description of $\varepsilon_{\text{sub}}(\omega, \mathbf{q})$. The simplest approach would incorporate a plasmon-pole model [263] of the form

$$\frac{1}{\varepsilon_{\text{sub}}(\omega)} = 1 + \frac{A}{\pi [(\omega + i\eta)^2 - \omega_p^2]} \quad (6.3.1)$$

where A is chosen such that for $\omega = 0$ we get the static limit studied in this chapter yielding $A = \pi\omega_p^2 \left(1 - \frac{1}{\varepsilon(\omega=0)}\right)$. Here, ω_p describes the plasmon frequency. Large ω_p would lead to the anti-adiabatic limit $\frac{1}{\varepsilon_{\text{sub}}(\omega)} = \frac{1}{\varepsilon(\omega=0)}$ which is covered by the static COHSEX approximation discussed in the previous section. Small $\omega_p \rightarrow 0$ will give the limit of a freestanding monolayer due to $A(\omega_p \rightarrow 0) \rightarrow 0$ and thus $\varepsilon_{\text{sub}}(\omega) \rightarrow 1$. The interesting ω regime inbetween has to be investigated in future studies.

Additionally substrate specific properties as for example the monolayer-substrate distance [181] (as larger separation decreases the screening) or hybridization effects between substrate and monolayer can become important in some material systems [264] and have to be investigated.

7. Effects of the Fermi Level Energy on the Adsorption of O₂ to Monolayer MoS₂

In the previous chapters, the possibility to manipulate material properties by Coulomb engineering have been discussed in detail. Not only substrates but also molecules adsorbed at surfaces can change the screening of the Coulomb interaction. Additionally, doping could have a significant influence on the non invasive manipulation of a material. However, Coulomb engineering of doped system shall not be part of this work. Instead we investigate the influence of O₂ adsorption on (doped) monolayer MoS₂ as a candidate for sensing applications such as detecting the adsorption of specific gas molecules.

The results presented in this chapter were developed in collaboration with P. Klement, M. Eickhoff and S. Chatterjee and are published in *2D Materials, Volume 5, Number 4 (2018)* [265]. The theoretical calculations were done by myself with help from T. Wehling and the experiments were carried out by P. Klement together with M. Eickhoff and S. Chatterjee. The manuscript was written by P. Klement and myself with additional remarks from T. Wehling, M. Eickhoff and S. Chatterjee. I focused on the theoretical part of this work. The reader will find a significant overlap of the following text, its Appendix A.5 and additional details on the experiments in the original article.

7.1. Introduction

Due to their remarkable electronic and optical properties (see Chapter 3) especially TMDCs have become interesting for applications in field-effect transistors (FETs) [5], chemical sensors [266–268], and optoelectronic devices [269]. Their properties are not only sensitive to changes in their dielectric but also their chemical environments because of large surface-to-volume ratios and the presence of distinct active surface sites such as sulfur vacancies or edge sites [270–272]. Since all atoms in 2d TMDCs are exposed to ambience the chemical reactions between gaseous species and the surface become of fundamental interest. For example the adsorption of specific gas molecules strongly affects the photoluminescence (PL) spectra of such 2d materials [272] rendering them interesting for gas sensing. Consequently different studies

used MoS₂ electrical devices as a proof of principle to detect NO₂, NH₃, acetone, and other solvents [266–268, 273–275]. However, for utilizing MoS₂ in sensing and optoelectronic applications a comprehensive understanding of the interactions between surfaces and its gaseous environment is important.

In this chapter, we show the influence of a variation of the Fermi level energy in monolayer MoS₂ on the adsorption of oxygen as a model system for the interactions between 2d TMDCs and oxidizing gases. Therefore we use first-principles calculations that reveal that an electron transfer from MoS₂ to O₂, required for the ionosorption of O₂, will only take place if the system is sufficiently *n*-doped. These findings support experimental analysis of monolayer MoS₂ FETs on conductive SiO₂/Si substrates, the latter acting as back gates. With these devices the electrical and optical response (such as the channel current in the FET, PL and photocurrent) of monolayer MoS₂ to the exposure to oxygen can be characterized simultaneously. With a variation of the Fermi level energy we can investigate the underlying mechanisms of the adsorption processes. A oxygen-induced reversible increase of PL intensity as well as a decrease of the conductivity of monolayer MoS₂ is observed which helps to identify a charge transfer between MoS₂ and O₂ upon adsorption. Furthermore the manipulation of the PL by external gating is strongly depending on the gaseous environment. This means that the charge transfer between O₂ and MoS₂ is probably more influential than the electrostatic doping shedding new light on earlier reports [276, 277].

7.2. Methods

To simulate the adsorption of O₂ on a monolayer of MoS₂ we performed DFT calculations within the local spin density approximation (LSDA) utilizing VASP [44, 45]. The Projector-augmented wave approach (PAW) [47, 73] with a cutoff energy of 400 eV for the plane wave basis set was used. To avoid interactions between different periodic images of the MoS₂ monolayers we chose a vacuum distance of 15 Å between adjacent periodic images. For modeling the gas adsorption, we use a 4 × 4 supercell of monolayer MoS₂ hosting one O₂ molecule, which results in a distance larger than 12 Å between two gas molecules. The supercell Brillouin zone integrations are performed with a Γ -centered Monkhorst-Pack mesh [278] of 12 × 12 × 1 k-points. Structures were relaxed until forces acting on each ion were less than 0.02 eV/Å. We found an optimized lattice constant for monolayer MoS₂ of $a = 3.12$ Å. As it was suggested by Yue et al. [279], the most favorable adsorption sites for the gas molecules are the so called H-sites, where the center of mass of the molecule is positioned on top of the hexagon, and the T_M site, where the center of mass is on top of a Mo atom. We investigated two different initial molecular orientations of O₂ with the molecular axis parallel (||) or perpendicular (\perp) to the monolayer. For different Sulfur-O distances h , we relaxed all structures and found the most favorable configuration as the T_{M||} site with $h = 2.8$ Å as shown in Fig. 7.2.1.

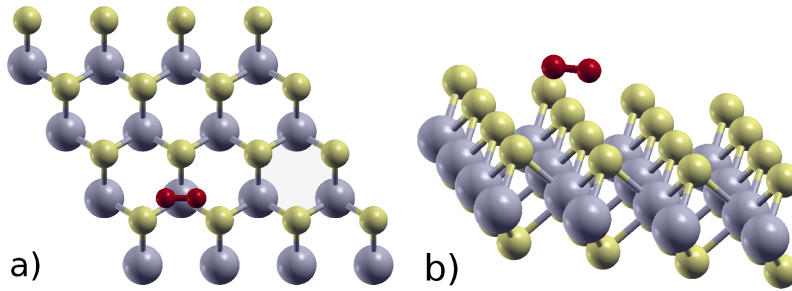


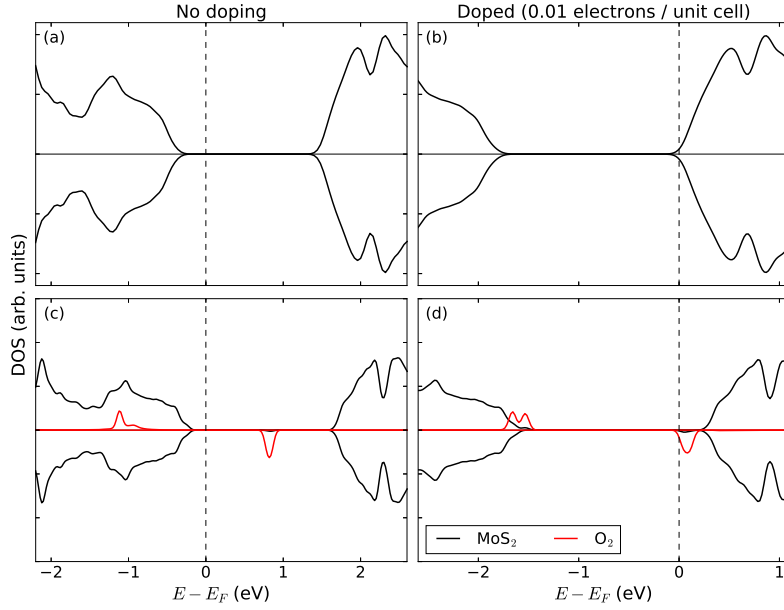
Figure 7.2.1.

Top (a) and side (b) view of the supercell used in the ab-initio DFT calculations. The most favorable adsorption site of O₂ is at the $T_{M\parallel}$ site, where the center of mass mass of the molecule is on top of a Mo atom with the molecular axis parallel to the monolayer.

We discuss the charge transfer in terms of the Fermi level position relative to the density of states as it links directly to the experimentally relevant quantity of free charge carriers and allows us to investigate the effects of doping. To simulate electrostatic n -doping of MoS₂ due to a gate bias and with that a gate controlled manipulation of the Fermi level, we artificially increased the number of electrons in the system while adding homogeneous positive background charge to ensure overall charge neutrality of the system.

7.3. Electronic states of MoS₂ upon adsorption of O₂

In Fig. 7.3.1 the density of states (DOS) of MoS₂ in absence (upper panels) and presence (lower panels) of oxygen for different free electron concentrations, controlled by the gate bias, are shown. The corresponding band structures can be found in Appendix A.5.1. The doping of 0.01 electrons/unit cell corresponds to approximately 10^{13} electrons/cm². In the undoped system without surface adsorbates, the band gap of MoS₂ is clearly visible in the DOS and the Fermi level energy is located inside the gap, as expected for a pristine semiconductor (Fig. 7.3.1a). For increasing number of electrons in the system, the Fermi level shifts to energies within the conduction band of MoS₂ (Fig. 7.3.1b). The oxygen adsorbates change the DOS by contributing a fully occupied molecular orbital in the spin up channel below the valence band edge and an orbital with spin down character within the gap of MoS₂ (Fig. 7.3.1c). Without additional doping of MoS₂, the spin down orbital remains empty. Thus, in absence of free electrons in the conduction band of MoS₂, the number of free carriers remains zero and there is no charge transfer from the extended MoS₂ electronic states to those states localized predominantly in the oxygen orbitals. This situation changes for gate-induced n -doping (Fig. 7.3.1 d). The Fermi level is now above the MoS₂ conduction band edge. Electron transfer from MoS₂ to O₂ occurs and oxygen depletes the MoS₂ conduction band.

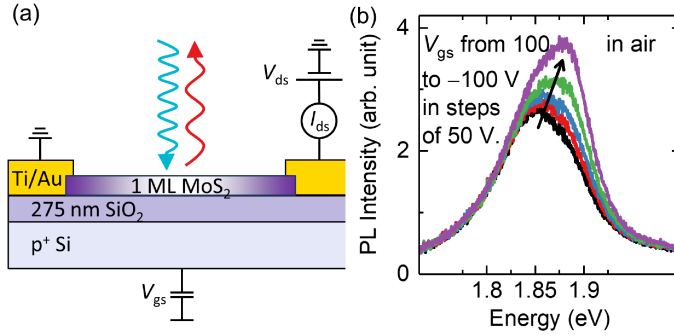
**Figure 7.3.1**

Density of states of free-standing MoS_2 ((a), (b)) and in presence of oxygen ((c), (d)). The black (red) line shows the local density of states of MoS_2 (of the O_2 molecules). Different charge doping levels are accounted for: ((a), (c)), no doping and ((b), (d)), 0.01 electrons per unit cell. The density of states at the positive (negative) ordinate corresponds to spin up (down) states.

Thus an electron transfer from MoS_2 to O_2 , which is required for ionosorption of molecules to the surface, can only take place in sufficiently n -doped systems. This means in experiments an influence of the Fermi level position, i.e. of the back gating, should be observed during adsorption and desorption processes of oxygen molecules to the surface. We will discuss experimental results from photoluminescence and conductivity measurements under O_2 exposition in dependence on the back gate in the following.

7.4. Measurements of photoluminescence and conductivity

To investigate the effect of the Fermi level on the adsorption processes, the PL and PC of monolayer MoS_2 in O_2/N_2 gaseous atmospheres of different O_2 -concentrations were studied. The Fermi level position in the MoS_2 monolayer was varied through different gate biases in the measurement device shown in Fig. 7.4.1a. Thereby, the p^+ -Si-substrate acts as the back gate by applying the gate-to-source voltage V_{gs} . The source contact is grounded and a drain-to-source voltage V_{ds} is applied to the drain contact which results in a drain-to-source current I_{ds} . The PL spectra at room temperature were measured by illuminating the region between the contacts. The results for different back gate biases are shown in Fig. 7.4.1b exhibiting a broad emission peak near 1.85 eV. The peak center shifts to 1.88 eV when the applied negative back gate bias electrically depletes the monolayer. Additionally the intensity increases by 40%.

**Figure 7.4.1.**

(a) Schematic of a back-gated MoS₂ device and the measurement configuration. (b) PL spectra of a monolayer MoS₂ device for different V_{gs} from 100 to +100 V in air. Images from P. Klement

This high-energy peak at 1.88 eV belongs to the recombination of the neutral exciton X^0 while the low-energy peak at 1.85 eV is associated with a negatively charged trion X^- [276]. This is because of an increased density of free electrons for positive back gate bias introducing excess electrons to MoS₂. During PL these electrons can bind to the photo-generated electron-hole pairs forming trions. Thus spectral weight is transferred to the trion, accompanied by a reduction in excitonic PL. In contrast, for negative gate bias, i.e., MoS₂ is depleted of free electrons, less trions (X^-) form and the excitonic X^0 PL is enhanced.

The transients of the PL intensity for different O₂ concentrations are shown in Fig. 7.4.2a. They were obtained by integration of the PL spectra in the energy range around the excitonic peak between 1.7 and 2.0 eV. Upon exposure to O₂ containing atmospheres a reversible increase in PL intensity is found with the magnitude scaling with the oxygen concentrations. Since the PL intensity decreases to approximately the same level in the N₂ intervals (white background in Fig. 7.4.2a), the sample seems to fully recover. Independent of the gaseous environment, PL intensity is increased for negative back gate bias (consistent with Fig. 7.4.1b). However, this enhancement is much more pronounced in the presence of O₂. Thus, the Fermi level position significantly influences the adsorption and desorption processes of oxygen molecules to the surface as we have predicted in our theoretical calculations. Since O₂ has a larger electronegativity compared to N₂, it attracts electrons from the MoS₂ monolayer by charge transfer [270, 272].

In Fig. 7.4.2b the sheet conductivity $\sigma = I_{ds}/V_{ds}$ under illumination is shown which were recorded simultaneously to the PL transients. The source-to-drain current I_{ds} and with that σ is directly related to the density of free carriers. For positive back gate (blue line) a decrease in sheet conductivity during O₂ exposure is observed. This is due to a reduction in the free electron concentration resulting from a charge transfer between MoS₂ and O₂. For high O₂ concentrations (between 100 and 30%),

7. Effects of the Fermi Level Energy on the Adsorption of O₂ to Monolayer MoS₂

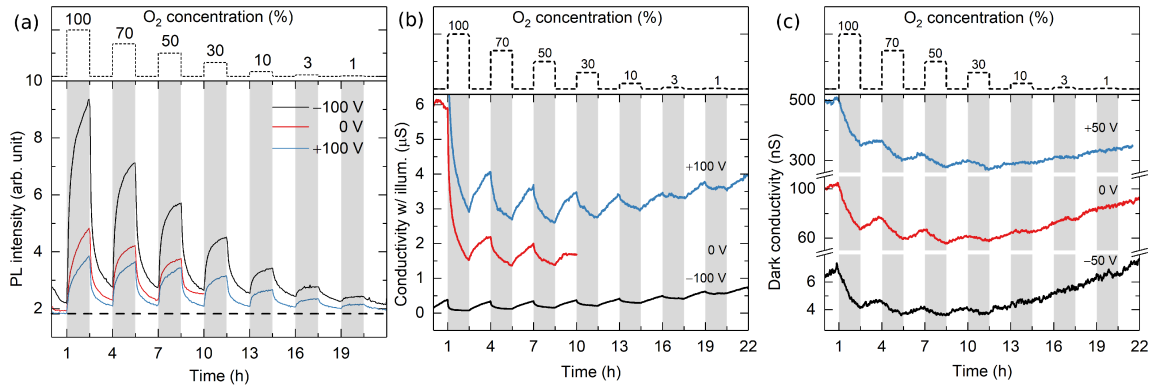


Figure 7.4.2.

Modulation of the photoluminescence intensity (a), sheet conductivity σ with active channel illuminated (b) and in the dark (c) of a monolayer MoS₂ device as a function of the O₂ concentration and back gate bias V_{gs} . The dashed black line indicates the base level. The grey background shows the O₂ intervals. O₂ concentrations in each interval are shown in the upper panels and range from 100 to 1%. For $V_{gs} = 0$ V (red line), the gas input failed after 10 h. Images from P. Klement

σ reaches an approximately constant base level. For lower O₂ (between 10 and 1%) concentrations σ does not reach the base level anymore but higher value in each interval because of fewer available adsorbates resulting in less depletion of MoS₂ and thus an increase in conductivity. During N₂ intervals an increase of σ but no full recovery to the value before oxygen exposure is observed, which is referred to as ‘poisoning’ [267, 280, 281] and indicates chemisorption of O₂ molecules to MoS₂ at room temperature which desorb on a long time scale. The response in conductivity is determined by the modulation in the density of majority carriers (electrons) in contrast to the PL response which is determined by the density of photo-generated minority carriers (holes) decaying on significantly shorter time scales compared to chemisorption processes. Consequently, the PL response completely recovers in the N₂ intervals and σ does not.

For negative or no back gate bias (black and red lines in Fig. 7.4.2b) similar behavior but less pronounced is visible. As the number of free electrons is tuned by the back gate we find the different levels of σ . For a positive back gate the density of electrons is increased and thus the absolute change in σ in the presence of O₂ also increases significantly. This can be understood from the theoretical results shown in the previous chapter: the charge transfer between MoS₂ and O₂ increases with n -doping, i.e. for positive back gate bias.

For other materials it was reported that not only external gating but also visible-light illumination of the device can rise the sensitivity to O₂ [282]. To investigate this effect, the conductivity in the dark σ_{dk} (Fig. 7.4.2c) was measured. Compared to σ under illumination, independent of the bias significantly lower conductivities

are found. This means, the dominant contributions to the drain-to-source current I_{ds} are probably photo-generated carriers. Nevertheless the oxygen exposure affects the properties similarly but only observable for high concentrations above 30%. Below that, σ_{drk} steadily increases and no adsorption effects can be seen anymore. As a result visible-light illumination can not only increase the conductivity through photo-generated carriers but also improves the sensitivity of the device. For negative gate bias σ_{drk} decreases even further. This emphasizes again the importance of free carriers and with that the position of the Fermi level in MoS₂ for O₂ adsorption as shown in the theoretical calculations.

The effect of oxygen adsorption is stronger on the PL intensity compared to the conductivity meaning PL measurements are more sensitive to oxygen exposure. Moreover, the effects of O₂ adsorption are strong in PL intensity irrespective of the back gate. This means when charge carrier transfers are involved, PL are superior to conductivity measurements. A more detailed discussion of the experimental results can be found in the original article [265].

7.5. Conclusion

All in all we have shown with first-principle calculations that the adsorption of O₂ molecules on monolayer MoS₂ is controlled by the Fermi level position. An electron transfer can only take place when the system is sufficiently *n*-doped. These calculations supported experimental measurements of photoluminescence and conductivity of MoS₂ FETs in which the proposed electron transfer from MoS₂ to O₂ upon adsorption [270, 272] was identified and controlled by the Fermi level. The adsorption effects of O₂ are stronger in the PL intensity compared to conductivity measurements rendering PL superior when charge carrier transfers are involved. Furthermore manipulation of the PL intensity through external gating depends on the gaseous environment meaning that the electron transfer between MoS₂ and O₂ upon adsorption seems to be more important than just electrostatic doping which explains earlier results on gated configurations [277].

8. Conclusions

In this work we demonstrated the importance of Coulomb interactions in 2d materials and how the dielectric environment can be used to manipulate electronic properties. We showed first as a proof-of-principle and then in real materials a band gap transition in homogeneous monolayers induced by laterally structured dielectric environments. These Coulomb engineered heterostructures exhibit sharp interface regions on the order of a few unit cells and the two-particle excitations show a peculiar response to the environment. To correctly include internal screening effects we utilized many-body perturbation theory on top of density functional theory. Environmental screening was taken into account by appropriate models for the static dielectric function.

Firstly, we turned to investigate environmental screening effects on the band gap of 2d MoS₂. We proposed a scheme to build Coulomb engineered heterostructures by laterally structured dielectric environments. Furthermore, we investigated the spatial extent of the G_0W_0 self-energy showing that it is non-local and thus able to modify the band gap. Yet it is localized around a few unit cells which allows for sharp interfaces. For spatially structured substrates model calculations based on the Hartree-Fock self-energy showed a spatial band gap change depending on the macroscopic dielectric constant of the region.

Based on this model we studied how excitons respond to the tuning of the Coulomb interaction. The lowest energy excited state (which is a tightly bound exciton) is nearly unaffected by the dielectric environment. However, higher energy states can be strongly manipulated meaning that their excitation energies can be tuned at energy scales comparable to the quasiparticle gap at spatial distances of a few lattice constants. The Bohr radius compared to the lattice spacing determines how the excitonic gap responds to the environment. For delocalized ground state excitons a shift in the same direction as the higher energy excitons upon changes in the dielectric environment was observed. However, in the limit of strongly localized excitons this trend was reversed. We found potential energy landscapes in which higher energy states could be trapped on an atomic scale while the lower energy states move almost freely or were even expelled from the trapping regions.

For the description of Coulomb engineering in semiconducting TMDCs (MoS(e)₂ and WS(e)₂) we turned to a more material realistic approach. Full ab-initio calculations of Coulomb engineered heterostructures turned out to be numerically extremely demanding and costly. Thus we used a more efficient modeling scheme based on a combination of $G\Delta W$ within static COHSEX approximation and the WFCE

approach to incorporate a more material realistic (static) dielectric function. All semiconducting TMDCs under investigation showed a significant band gap reduction upon increasing screening of the dielectric environment. Concerning *absolute* decreases the selenides were a little less influenced by the environment due to stronger internal polarization effects but *relative* changes were roughly the same for all materials. We showed that not only in the simple model approach but also for the material realistic description the length scale of the self-energy, rendering the internal limits for the sharpness of interfaces, is on the order of a few unit cells. This was universal to all investigated materials due to their similarity in their electronic properties. For a material realistic description of a Coulomb engineered heterostructure we turned to a model utilizing the self-energy derived from $G\Delta W$. The band gap modulation were found to be reminiscent of Type-I heterojunction meaning symmetric shifts of the band edges. In conclusion all TMDCs were equally suitable for Coulomb engineering rendering them promising for future devices [188, 191]. With our investigations on Coulomb engineered heterojunctions we opened up a completely new field for tailor made devices.

In this work we only considered dielectric constants to model the substrates. For a more detailed insight into the correlation effects a frequency dependent description will be crucial [196]. In a first step this can be done in the $G\Delta W$ approach by incorporation a plasmon-pole model for the dielectric function. Furthermore, in the material realistic approach we neglected possible charge transfer effects at the interface. To include them, a real space model for the dielectric function has to be used, considering *internal* and *external* screening effects. However, this is not a simple task which needs further investigations.

In terms of possible sensing devices made from TMDCs, we demonstrated that a variation of the Fermi energy in MoS_2 controls the adsorption of O_2 . With density functional theory calculations we supported experimental analysis of monolayer MoS_2 field effect transistors on conductive substrates. We found an oxygen-induced reversible increase of PL intensity dependent on external gating. Through measurements of the PL and conductivity an electron transfer from MoS_2 to O_2 on adsorption controlled by the Fermi level was observed.

A. Appendix

A.1. Transition Metal Dichalcogenides

A.1.1. Lattice parameter and band structures of TMDCs

Table A.1

Relaxed lattice constants a , experimental lattice constant a_{exp} , distance between the chalcogen atoms z_0 and the spin splitting Δ_{SOC} of the valence band at \mathbf{K} .

	a in Å	a_{exp} in Å	z_0 in Å	Δ_{SOC} in eV
MoS ₂	3.18	3.16[141]	3.13	0.148
MoSe ₂	3.32	3.29[141]	3.34	0.186
WS ₂	3.19	3.15[141]	3.15	0.427
WSe ₂	3.32	3.29[141]	3.36	0.464

The ab-initio calculations in this work were performed with the Vienna ab initio simulation package (VASP) [44, 45]. The DFT calculations were carried out within the GGA approximation [59] with a PBE plane wave basis set. The Projector-augmented wave approach (PAW) [47, 73] with a cutoff energy of 350 eV for the plane wave basis set was used. Structures were relaxed with a conjugate gradient algorithm as implemented in VASP on a $18 \times 18 \times 1$ k-mesh till the total free energy change was smaller than 10^{-4} eV. The parameter λ_0 is the spin splitting Δ_{SOC} of the valence band at \mathbf{K} resulting from GGA-PBE calculations considering spin-orbit coupling as implemented in VASP using a $12 \times 12 \times 1$ k-mesh. The resulting parameter are shown in Table A.1. The DFT band structure as well as the G_0W_0 band structures of the low-energy states are presented in Fig. A.1.1. For details on the G_0W_0 calculations see Appendix A.4.2.

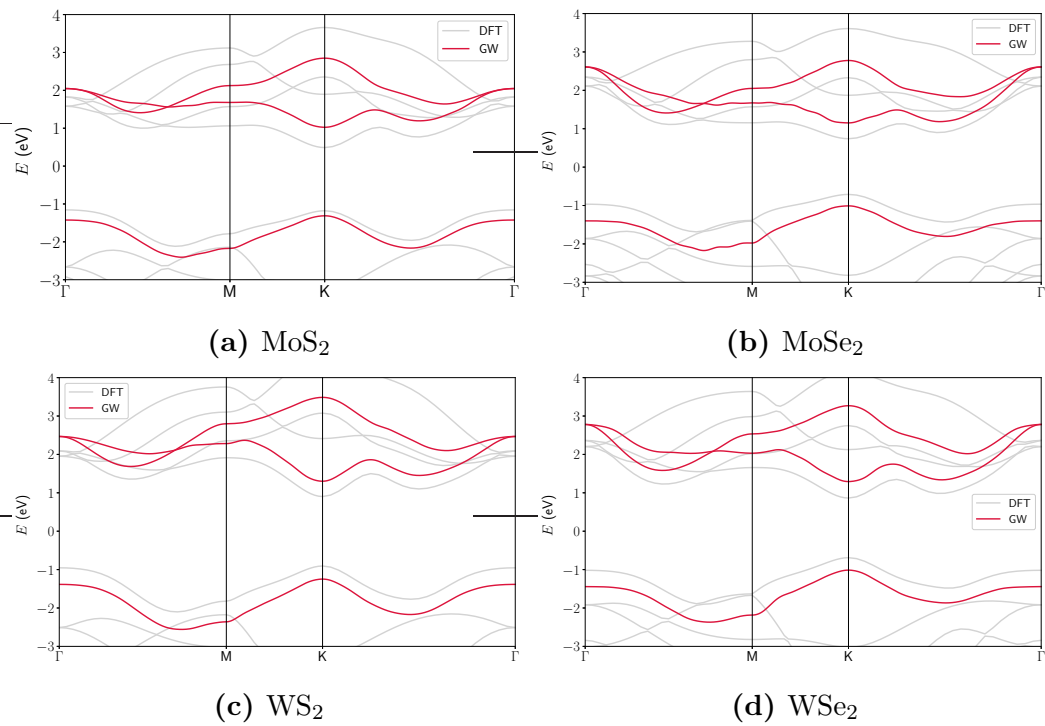


Figure A.1.1.

DFT (grey) and G_0W_0 (red) band structures in the minimal basis set for semiconducting TMDCs investigated in this work.

A.2. 2D Heterojunctions from Non-local Manipulations of the Interactions

A.2.1. Computational details

The DFT and G_0W_0 calculations were performed with VASP [44, 45]. The DFT calculations are carried out in GGA with a PBE plane wave basis set [59] using a $18 \times 18 \times 1$ k-mesh and an energy cut-off of 280 eV. The lattice constant is set to 3.18 Å, the sulfur z -positions are relaxed to ± 1.57 Å. The results are projected onto Mo d_{z^2} , d_{xy} and $d_{x^2-y^2}$ orbitals using Wannier90 [36] to get a minimal tight-binding model as described in Chapter 3.3. Afterwards we stay with the resulting projections without performing a maximal localization. As an extrapolation scheme for treating artificial screening effects due to a periodic image of the monolayer cannot be applied to the resulting hopping element $t_{\alpha\beta}^{GW}$, an interlayer separation of 55 Å is chosen to minimize artificial self-interactions within the supercell approach. For the evaluation of the polarization in the G_0W_0 calculations 192 bands together with an energy cut-off of 150 eV are used.

A.2.2. Tight-binding model parameter

In order to describe MoS₂ with the tight-binding model introduced in Section 4.3.1, we use the parameter given in Tab. A.3 which reproduce the DFT band gap and band width of MoS₂. The in-plane lattice constant is labeled by a and the vertical separation is set to c .

t	t_{\perp}	t_{ii}	a	c
-0.26 eV	-0.85 eV	0.0 eV	3.18 Å	$a/4$

Table A.2.

Tight-binding model parameter for the description of MoS₂

A.2.3. Treating the Coulomb interaction

The Coulomb interaction gives rise to electron-electron, electron-ion and ion-ion interaction terms: $H_{\text{Coulomb}} = H_{ee} + H_{ei} + H_{ii}$. The ions are assumed to have a fixed positive charge $Ze = +1e$ to ensure charge neutrality of the whole system, i.e. $Z = 2\bar{n}$, where \bar{n} is the average electron occupation per spin and orbital. The ionic positions

A. Appendix

are assumed to be fixed. Thus, H_{ii} leads to a constant shift of the total energy, which will be neglected in the following. The remaining Coulomb terms read [26, 27]

$$H_{ee} = \frac{1}{2} \sum_{ij\sigma\sigma'} U_{ij} c_{i\sigma}^\dagger c_{j\sigma'}^\dagger c_{j\sigma'} c_{i\sigma} \quad (\text{A.2.1})$$

$$H_{ei} = - \sum_{ij\sigma} U_{ij} \hat{n}_{i\sigma} Z, \quad (\text{A.2.2})$$

where $U_{ij} = U(\mathbf{r}_i, \mathbf{r}_j)$ is the interaction energy between electrons or ions at sites \mathbf{r}_i and \mathbf{r}_j , σ labels the electron spin, $c_{i\sigma}^\dagger$ ($c_{i\sigma}$) are the corresponding electronic creation (annihilation) operators, and $\hat{n}_{i\sigma} = c_{i\sigma}^\dagger c_{i\sigma}$ are electron occupation operators.

In the Hartree-Fock approximation H_{ee} becomes

$$\begin{aligned} H_{ee}^{\text{HF}} &= \sum_{ij\sigma\sigma'} U_{ij} (c_{i\sigma}^\dagger c_{i\sigma} \langle c_{j\sigma'}^\dagger c_{j\sigma'} \rangle - c_{i\sigma}^\dagger c_{j\sigma'} \langle c_{j\sigma'}^\dagger c_{i\sigma} \rangle) \\ &= \sum_{ij\sigma\sigma'} U_{ij} (\hat{n}_{i\sigma} \langle \hat{n}_{j\sigma'} \rangle - c_{i\sigma}^\dagger c_{j\sigma'} \langle c_{j\sigma'}^\dagger c_{i\sigma} \rangle) \\ &= \sum_{ij\sigma} U_{ij} \left(2\hat{n}_{i\sigma} \langle \hat{n}_j \rangle - c_{i\sigma}^\dagger c_{j\sigma} \langle c_j^\dagger c_i \rangle \right). \end{aligned} \quad (\text{A.2.3})$$

We used the symmetry of the Coulomb matrix $U_{ij} = U_{ji}$ and assumed that the system is non-magnetic, i.e. $\langle \hat{n}_{j\sigma} \rangle = \langle \hat{n}_{j\sigma'} \rangle \equiv \langle \hat{n}_j \rangle$ and $\langle c_{j\sigma'}^\dagger c_{i\sigma} \rangle \equiv \delta_{\sigma'\sigma} \langle c_j^\dagger c_i \rangle$. The factor of 2 in the Hartree term (first term) accounts for spin-degeneracy. Together with the electron-ion interaction $H_{ei} = - \sum_{ij\sigma} U_{ij} \hat{n}_{i\sigma} Z$ from Eq. (A.2.2) and the charge-neutrality condition $Z = 2\bar{n}$ we arrive at

$$\begin{aligned} H_{ee}^{\text{HF}} + H_{ei} &= \sum_{ij\sigma} U_{ij} \left(2\hat{n}_{i\sigma} (\langle \hat{n}_j \rangle - \bar{n}) - \langle c_i^\dagger c_j \rangle c_{j\sigma}^\dagger c_{i\sigma} \right) \\ &= \sum_{ij\sigma} U_{ij} \left(2\hat{n}_{i\sigma} \delta n_j - \langle c_i^\dagger c_j \rangle c_{j\sigma}^\dagger c_{i\sigma} \right), \end{aligned} \quad (\text{A.2.4})$$

where we introduced the deviation from the average occupation $\delta n_j = \langle \hat{n}_j \rangle - \bar{n}$. Eq. (A.2.4) can be expressed according to

$$H_{ee}^{\text{HF}} + H_{ei} = \sum_{ij\sigma} \Sigma_{ij} c_{j\sigma}^\dagger c_{i\sigma} \quad (\text{A.2.5})$$

with the self-energy

$$\Sigma_{ij} = \delta_{ij} \sum_l 2U_{il} \delta n_l - U_{ij} \langle c_j^\dagger c_i \rangle, \quad (\text{A.2.6})$$

where the spin indices are suppressed as Σ_{ij} is spin diagonal.

The self-consistent evaluations of the self-energy are performed by using non-primitive rectangular unit cells, which involve 4 atoms. All supercells consist of 50×30 non-primitive unit cells. We use periodic boundary conditions in the y -direction and fixed boundaries in the x -direction. In the case of the heterostructures, the plane, which separates the different dielectric areas from each other is chosen to be parallel to the y -axis and is placed between the 25th and 26th unit cells on the x -axis.

A.2.4. Screening model

As described in Section 4.3.2, the Poisson equation has to be solved in general numerically to obtain the *screened* Coulomb interaction within the two-dimensional layer. Nevertheless, there are situations in which the resulting problem can be solved analytically, for instance, in the case of two half spaces with different dielectric constants ε_1 and ε_2 and zero film thickness. In this situation, the screened Coulomb potential can be obtained analytically using the method of image charges [76].

Therefore, the electrostatic potential $\phi_{\mathbf{r}_j}(\mathbf{r}_i) = U_{ij}/e$ at position \mathbf{r}_i resulting from a source electron with charge q_j at \mathbf{r}_j is calculated as a superposition of the potential of the source charge and its corresponding image charge. If \mathbf{r}_i and \mathbf{r}_j are in the same subspace, the image charge q_m is placed at \mathbf{r}_m , which is the mirrored position of \mathbf{r}_j with respect to the plane separating the dielectrics. Otherwise the image charge q'_m is positioned at \mathbf{r}_j . The continuity conditions for the electric field \mathbf{E} and the electric displacement field \mathbf{D} lead to $q_m = \pm \frac{\varepsilon_1 - \varepsilon_2}{\varepsilon_1 + \varepsilon_2} q_j$ and $q'_m = \frac{2}{\varepsilon_1 + \varepsilon_2} q_j$ which finally yields the potential¹:

$$U_{ij} = \begin{cases} \frac{1}{\varepsilon_1} \left(v_{ij} + \frac{\varepsilon_1 - \varepsilon_2}{\varepsilon_1 + \varepsilon_2} v_{im} \right) & i, j \in \mathbf{R}_{\varepsilon_1} \\ \frac{1}{\varepsilon_2} \left(v_{ij} + \frac{\varepsilon_2 - \varepsilon_1}{\varepsilon_1 + \varepsilon_2} v_{im} \right) & i, j \in \mathbf{R}_{\varepsilon_2} \\ \frac{2}{\varepsilon_1 + \varepsilon_2} v_{ij} & \text{otherwise.} \end{cases} \quad (\text{A.2.7})$$

Here, $\mathbf{R}_{\varepsilon_1}$ ($\mathbf{R}_{\varepsilon_2}$) is the set of lattice vectors in the area with the dielectric constant ε_1 (ε_2). v_{ij} is an unscreened (bare) Coulomb potential of the form

$$v_{ij} = \frac{e^2}{\sqrt{|\mathbf{r}_i - \mathbf{r}_j|^2 + \delta^2}}, \quad (\text{A.2.8})$$

with e being the elementary charge and δ accounting for the finite spread of the electronic orbitals[283].

¹A complete step-by-step derivation of the resulting potential is given e.g. in Ref. [76]

If $\varepsilon_1 = \varepsilon_2 = \varepsilon$, we end up with a homogeneous environment and the Coulomb interaction reduces to

$$U_{ij} = \frac{1}{\varepsilon} v_{ij}. \quad (\text{A.2.9})$$

In order to implement a situation that is similar to MoS₂, we set $\delta = 1.5 \text{ \AA}$ which leads to a bare on-site potential $U_{ii} \approx 9.6 \text{ eV}$ (i.e. for $\varepsilon = 1$) and corresponds to a bare density-density matrix element of the Coulomb interaction for the d_{z^2} orbitals of MoS₂. The diagonal elements of the bare Coulomb tensor in the basis of the aforementioned three Wannier orbitals vary between 8.9 eV and 9.9 eV.

A.2.5. Calculation of the local density of states

To calculate the local density of states (LDOS) shown in Section 4.3, we use the single-particle Green's function

$$G(E) = \frac{1}{E + i\delta - H}, \quad (\text{A.2.10})$$

with the single-particle Hamiltonian (including the Hartree-Fock contributions) with the eigenenergies E_n and eigenstates $|\psi_n\rangle$. For the full density of states we have to calculate the spectral function (see Chapter 2.4.1) as the trace of the imaginary part of $G(E)$ [284]:

$$D(E) = -\frac{1}{\pi} \text{Tr}(\text{Im}[G(E)]). \quad (\text{A.2.11})$$

We are interested in the *local density of states* $D_\nu(E)$, which is the energy distribution for particles in the single-particle states $|\nu\rangle$. Then, the full DOS is the sum over all local density of states:

$$D(E) = -\frac{1}{\pi} \sum_\nu (\text{Im}[G(E)])_{\nu\nu} = \sum_\nu D_\nu(E), \quad (\text{A.2.12})$$

meaning that the LDOS is proportional to the diagonal elements of the imaginary part of $G(E)$ from Eq. (A.2.10):

$$D_\nu(E) = -\frac{1}{\pi} \text{Im}[G(E)]_{\nu\nu}. \quad (\text{A.2.13})$$

To calculate $G_{\nu\nu} = \langle \nu | G | \nu \rangle$, we use the eigenbasis of the Hamiltonian

$$G_{\nu\nu}(E) = \sum_n \frac{|\langle \nu | \psi_n \rangle|^2}{E + i\delta - E_n}. \quad (\text{A.2.14})$$

The coefficient $\langle \nu | \psi_n \rangle$ are the entries of the eigenvectors in the single-particle basis $\{|\nu\rangle\}$:

$$|\psi_n\rangle = \sum_{\nu} \langle \nu | \psi_n \rangle |\nu\rangle = \sum_{\nu} c_{\nu}^{(n)} |\nu\rangle. \quad (\text{A.2.15})$$

In this work the single-particle basis $\{|\nu\rangle\}$ are the Wannier orbitals of our model system.

A.2.6. Hartree and Fock contributions to the band gap

In Fig. A.2.1 we show the electronic density of states obtained by including different parts of the self-energy using the generic model within a homogeneous dielectric environment ($\varepsilon = 5$) for a 50×30 super cell. Fig. A.2.1a shows the evolution of the band gap by subsequent inclusion of the Hartree (Σ_H) and Fock (Σ_F) terms. The *local* Hartree contribution to the tight-binding gap is negligible, while the Fock terms cause a drastic increase. In more detail, we see in Fig. A.2.1b that this increase is due to the *non-local* Fock contribution only, while the local Fock terms just broaden the bands. Thus, the drastic increase of the band gap within the Hartree-Fock approximation results from a modified hybridization due to non-local interactions.

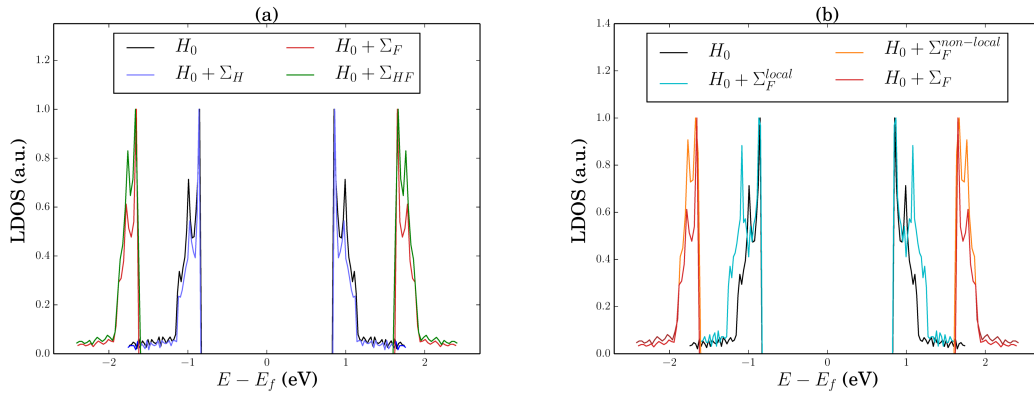


Figure A.2.1.

Hartree-Fock self-energy contributions to the density of states in an homogeneous dielectric environment. (a) Influence of the Hartree and full Fock terms. (b) Local and non-local contributions of the Fock term.

A.2.7. Heterogeneous substrate

In order to illustrate the details of the band-gap overlaps between the areas with different dielectric environments ($\varepsilon_1 = 5$ and $\varepsilon_2 = 15$), we show in Fig. A.2.2 the

local density of states for the unit cells far from the interface shown in Fig. 4.3.3. These unit cells are chosen to lie in regions where the local density of states essentially coincide with the density of states of the corresponding homogeneous systems. Due to the relative shifts of the valance-band maxima and conduction-band minima in each spatial area, the resulting *total* density of states shows a strongly reduced band gap of $\approx 1.8\text{eV}$, which we refer to as the band-gap overlap. The local density of states reveals the typical characteristic of a type-II heterojunction, here.

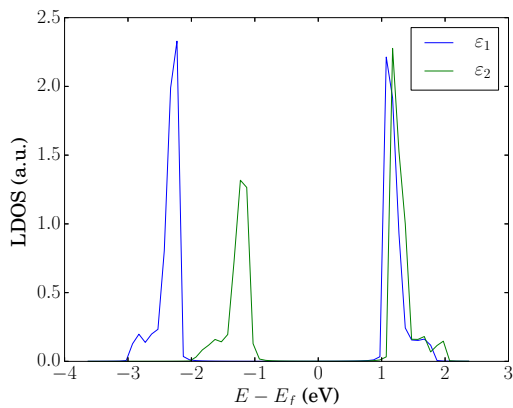


Figure A.2.2

Local density of states for the system considered in Fig. A.2.2 of the main text inside the regions with different dielectric environment ($\epsilon_1 = 5$ and $\epsilon_2 = 15$).

A.3. Non-invasive control of excitons

A.3.1. Electron-Hole Hamiltonian

The many-body wave functions of the excited state in the electron-hole picture can be described as linear combinations of Slater determinants of electron and hole wave functions. Upon single excitation of only one electron-hole pair, all electron-electron (V_{ijkl}^{eeee}) and hole-hole (V_{ijkl}^{hhhh}) interaction terms vanish. If we neglect electron-hole exchange-like terms (which do not contribute to the energy scale discussed in Chapter 5), the many-body Hamiltonian in second quantization is given by Eq. (5.2.1):

$$H = \sum_i E_i^e e_i^\dagger e_i + \sum_i E_i^h h_i^\dagger h_i - \sum_{ijkl} V_{ijkl}^{ehhe} e_i^\dagger h_j^\dagger h_k e_l, \quad (\text{A.3.1})$$

where $E_i^{e/h}$ are dressed electron/hole eigenenergies from the Hartree-Fock calculations which are described in Chapter 4. The operator $(e/h)_i^{(\dagger)}$ annihilates (creates) an electron/hole in the Hartree-Fock eigenstate

$$|\psi_{(e/h)}^i\rangle = \sum_{\mathbf{R}} c_{\mathbf{R},(e/h)}^i |\mathbf{R}\rangle. \quad (\text{A.3.2})$$

In more detail, the coefficients $c_{\mathbf{R},(e/h)}^i$ are the entries of the i -th eigenvector obtained from diagonalizing the Hartree-Fock Hamiltonian within the $\{|\mathbf{R}\rangle\}$ -basis. Then the Coulomb matrix elements V_{ijkl}^{ehhe} between electrons and holes are given by

$$\begin{aligned} V_{ijkl}^{ehhe} &= \sum_{\mathbf{R}_1, \mathbf{R}_2, \mathbf{R}_3, \mathbf{R}_4} c_{\mathbf{R}_1, e}^{i*} c_{\mathbf{R}_2, h}^{j*} c_{\mathbf{R}_3, h}^k c_{\mathbf{R}_4, e}^l \\ &\times \langle \mathbf{R}_1 | \langle \mathbf{R}_2 | U(\mathbf{r} - \mathbf{r}') | \mathbf{R}_3 \rangle | \mathbf{R}_4 \rangle. \end{aligned} \quad (\text{A.3.3})$$

Here, U describes the screened Coulomb interaction. Due to the orthogonality and the localization of the states $|\mathbf{R}\rangle$ we only consider two-center contributions,

$$\begin{aligned} V_{ijkl}^{ehhe} &\approx \sum_{\mathbf{R}, \mathbf{R}'} c_{\mathbf{R}, e}^{i*} c_{\mathbf{R}', h}^{j*} c_{\mathbf{R}', h}^k c_{\mathbf{R}, e}^l \\ &\times \langle \mathbf{R} | \langle \mathbf{R}' | U(\mathbf{r} - \mathbf{r}') | \mathbf{R}' \rangle | \mathbf{R} \rangle. \end{aligned} \quad (\text{A.3.4})$$

For further details see, e.g., Ref. [285] and the references therein. In our lattice-discretized approach, the short-range spatial distribution of the states $|\mathbf{R}\rangle$ is not

explicitly known. Thus, the electron-hole Coulomb matrix elements are approximated by

$$V_{ijkl}^{ehhe} = \sum_{\mathbf{R}, \mathbf{R}'} c_{\mathbf{R},e}^{i*} c_{\mathbf{R}',h}^{j*} c_{\mathbf{R}',h}^k c_{\mathbf{R},e}^l U_{\mathbf{R},\mathbf{R}'}. \quad (\text{A.3.5})$$

The Coulomb matrix elements $U_{\mathbf{R},\mathbf{R}'}$ contain the screening effects of the spatially structured dielectric environment as in Eq. (A.2.9):

$$U_{\mathbf{R},\mathbf{R}'} = \frac{1}{\varepsilon_{\mathbf{R},\mathbf{R}'}} \frac{e^2}{\sqrt{(\mathbf{R} - \mathbf{R}')^2 + \delta^2}}. \quad (\text{A.3.6})$$

Here, e is the elementary charge and the parameter δ takes into account the finite spread of the orbitals $|\mathbf{R}\rangle$ for $\mathbf{R} = \mathbf{R}'$. To emulate MoS₂ we choose $\delta = 1.5 \text{ \AA}$ as in Chapter 4. The macroscopic dielectric function $\varepsilon_{\mathbf{R},\mathbf{R}'}$ includes the screening effects of the environment. For a homogeneous environment it is set to a constant value $\varepsilon_{\mathbf{R},\mathbf{R}'} = \varepsilon$, whereas in a heterogeneous environment the interface is included as described in Section A.2.4 using image charges at the lattice sites \mathbf{R}_m , yielding

$$\varepsilon_{\mathbf{R},\mathbf{R}'} = \begin{cases} \frac{1}{\varepsilon_1} \left(1 + \frac{\varepsilon_1 - \varepsilon_2}{\varepsilon_1 + \varepsilon_2} \frac{\sqrt{(\mathbf{R} - \mathbf{R}')^2 + \delta^2}}{\sqrt{(\mathbf{R} - \mathbf{R}_m)^2 + \delta^2}} \right) & \mathbf{R}, \mathbf{R}' \in \mathbf{R}_{\varepsilon_1} \\ \frac{1}{\varepsilon_2} \left(1 + \frac{\varepsilon_2 - \varepsilon_1}{\varepsilon_1 + \varepsilon_2} \frac{\sqrt{(\mathbf{R} - \mathbf{R}')^2 + \delta^2}}{\sqrt{(\mathbf{R} - \mathbf{R}_m)^2 + \delta^2}} \right) & \mathbf{R}, \mathbf{R}' \in \mathbf{R}_{\varepsilon_2} \\ \frac{2}{\varepsilon_1 + \varepsilon_2} & \text{otherwise} \end{cases}. \quad (\text{A.3.7})$$

A.3.2. Dipole matrix elements

To directly investigate experimentally easily accessible optical properties, we calculate the linear optical absorption spectrum. In the dipole approximation, the light-matter coupling can be described by the dipole Hamiltonian:

$$H_d = -e\mathbf{E} \sum_{ij} \underbrace{\langle \psi_e^i | \mathbf{r} | \psi_h^j \rangle}_{\mathbf{d}_{ij}^{eh}} e_i h_j + h.c. \quad (\text{A.3.8})$$

Its matrix elements, that contain the optical selection rules can unambiguously be obtained from matrix elements of the position operator \mathbf{r} between the quasiparticle electron and hole states $|\psi_{(e/h)}^i\rangle$ from Eq. (A.3.2):

$$\mathbf{d}_{ij}^{eh} = e \langle \psi_e^i | \mathbf{r} | \psi_h^j \rangle. \quad (\text{A.3.9})$$

Here e is the electron charge and \mathbf{r} is (in consistency with the spatial resolution on a lattice scale) approximated by the lattice operator $\mathbf{r} \approx \sum_{\mathbf{R}} |\mathbf{R}\rangle \mathbf{R} \langle \mathbf{R}|$ [286], thus neglecting the short range contributions that are not accessible in the tight-binding

model. Depending on the polarization of the electric field vector of the incident light, different vectorial components are projected out of \mathbf{d}_{ij}^{eh} in Eq. (5.2.2). We simulate the case of unpolarized light via an equally weighted superposition of $I(\mathbf{E} = [100])$, $I(\mathbf{E} = [010])$ and $I(\mathbf{E} = [001])$.

A.3.3. Many-body eigenstates

For the spatially resolved two-particle DOS, Eq. (5.2.4), we calculate the eigenstates $\Psi^\lambda(\mathbf{r}_e, \mathbf{r}_h)$ of the electron-hole Hamiltonian (Eq. (5.2.1)) as a function of the electron and hole position $\mathbf{r}_{(e/h)}$. Therefore, we calculate the eigenstate $|\Psi^\lambda\rangle$ from the many-body Hamiltonian (5.2.1) as linear combination of Slater determinants of electron and hole wave functions build from the Hartree-Fock eigenstates defined by Eq. (A.3.2):

$$\begin{aligned} |\Psi^\lambda\rangle &= \sum_{nm} a_{nm}^\lambda |\psi_{(e)}^n\rangle |\psi_{(h)}^m\rangle \\ &= \sum_{nm} a_{nm}^\lambda \sum_{\mathbf{R}, \mathbf{R}'} c_{\mathbf{R}, e}^n c_{\mathbf{R}', h}^m |\mathbf{R}\rangle |\mathbf{R}'\rangle. \end{aligned} \quad (\text{A.3.10})$$

The expansion coefficients a_{nm}^λ are the entries of the λ -th eigenvector which results from numerically diagonalizing the many-body Hamiltonian. The spatial representation of the eigenstate is then the projection on the electron and hole position $|\mathbf{r}_{(e/h)}\rangle$:

$$\begin{aligned} \Psi^\lambda(\mathbf{r}_e, \mathbf{r}_h) &= \langle \mathbf{r}_e | \langle \mathbf{r}_h | \Psi^\lambda \rangle \\ &= \sum_{nm} \sum_{\mathbf{R}, \mathbf{R}'} a_{nm}^\lambda c_{\mathbf{R}, e}^n c_{\mathbf{R}', h}^m \delta_{\mathbf{r}_e, \mathbf{R}} \delta_{\mathbf{r}_h, \mathbf{R}'} \end{aligned} \quad (\text{A.3.11})$$

A.3.4. Semiconductor tight-binding models

		t	t_{ii}^A	t_{ii}^B	a	t_\perp	c
Hex. bilayer	Localized	0.225 eV	0.0 eV	0.0 eV	3.18 Å	-0.85 eV	$a/4$
	Delocalized	1.7 eV	0.0 eV	0.0 eV	3.18 Å	-0.85 eV	$a/4$
Honeycomb latt.	Localized	0.5 eV	0.83 eV	-0.83 eV	3.19 Å		
	Delocalized	1.1 eV	0.83 eV	-0.83 eV	3.19 Å		

Table A.3.

Tight-binding model parameter for the description of MoS₂ for the "hexagonal bilayer" and the "honeycomb lattice".

From the perspective of tight-binding modeling, several methods exist to open a gap in an initially gapless electronic band structure. The two distinct models we

use shall mimic a hybridization gap ("hexagonal bilayer") and a broken sublattice symmetry ("honeycomb lattice") as described in the main text.

For the hexagonal bilayer, the on-site energies and hopping matrix elements are chosen to reproduce DFT band gaps and band width of MoS₂. For the honeycomb lattice the parameter from Ref. [255] are used. In both models we control how localized the electrons are with the in-plane hopping t . The hopping $t_{ii}^{A/B}$ defines the on-site energy and quantifies the sublattice symmetry breaking. The employed parameters and their notation are presented in Table A.3.

A.3.5. Bohr radius

To analyze the spatial extent of the lowest-energy excitation E_g^{exc} , we calculate the corresponding excitonic Bohr radius a for every dielectric constant ε . Therefore, we use the expectation value of the Coulomb interaction V_0 between electron and hole:

$$\begin{aligned} \langle V_0 \rangle &= \frac{e^2}{\varepsilon a} \\ \Rightarrow a \left(\frac{1}{\varepsilon} \right) &= \frac{e^2}{\langle V_0 \rangle} \frac{1}{\varepsilon}. \end{aligned} \quad (\text{A.3.12})$$

To obtain $\langle V_0 \rangle$, we calculate the expectation value of the Coulomb matrix elements V_{ijkl}^{ehhe} for the excitonic eigenstate $|\Psi^0\rangle$ with the lowest energy E_g^{exc}

$$\langle V_0 \rangle = \langle \Psi^0 | V_{ijkl}^{ehhe} | \Psi^0 \rangle \quad (\text{A.3.13})$$

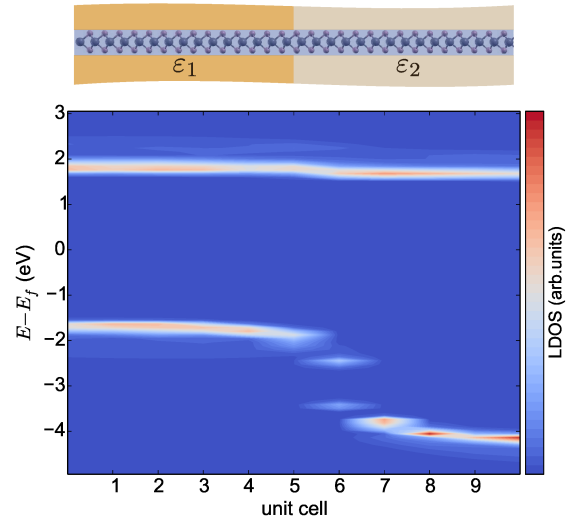
for each model and ε of the homogeneous dielectric environment.

A.3.6. Local density of states for heterostructure

In Fig. A.3.1 we show the local density of states for a supercell which uses a non-primitive rectangular unit cell which involves 4 atoms. The supercell consists of 9×6 non-primitive unit-cells spanning an approximate area of $(9 \times 10)a^2$. The plane which separates the different dielectric areas from each other is chosen to be parallel to the y-axis and placed in 5th unit cell. We chose the dielectric constants to be $\varepsilon_1 = 5$ in the left area and $\varepsilon_2 = 2$ in the right area. The spatial band gap dependence induced by the interface with a smaller band gap in the region with the higher ε (left area) is clearly visible.

Figure A.3.1

One-particle local DOS for different unit cells along a line perpendicular to the dielectric interface of the environment located in the unit cell 5 (left $\varepsilon_1 = 5$ and right $\varepsilon_2 = 2$).



A.4. Material realistic description of Coulomb engineered heterostructures

A.4.1. Computational details for ab-initio description of heterostructure

For the ab-initio calculations of the heterostructure in Section 6.1.1 we performed G_0W_0 with VASP based on GGA-PBE results obtained within a PBE plane wave basis set. A PAW approach with a cutoff energy of 420 eV was used.

The interlayer distance between the substrate and MoS₂ was set to $\approx 5\text{\AA}$ [287] and the vacuum height was chosen to be 20 \AA . For numerical feasibility we used the same lattice constant of hBN as for MoS₂. Since the relaxed lattice constant of hBN is 2.51 \AA [147] compared to 3.18 \AA in MoS₂ this yields a strained substrate. However, in homogeneous calculations of the primitive unit cell (as shown in Fig. 6.1.2b) we already find a band gap reduction, thus for the study of qualitative trends this approach is sufficient.

For numerical feasibility we used a $12 \times 12 \times 1$ \mathbf{k} -grid (for the homogeneous calculations) and correspondingly a $1 \times 12 \times 1$ \mathbf{k} -grid for the supercell calculation of the heterostructure. A GW cutoff energy of 150 eV was utilized and a total number of bands of 80 respectively of 960 for the supercell.

A.4.2. Calculation details for homogeneous monolayer TMDCs

The ab-initio calculations for the results in Chapter 6.2 were performed with VASP. The DFT calculations were carried out within the GGA approximation with a PBE plane wave basis set using a $24 \times 24 \times 1$ \mathbf{k} -mesh. We used the PAW approach with a cutoff energy of 350 eV.

In Table A.1 the used lattice constants and distances between the chalcogen atoms are shown. For the GW calculations we used a total of 280 bands with a ω grid consisting of 200 grid points and a GW energy cutoff of 150 eV.

Since an extrapolation scheme for the individual hopping matrix elements $H_{\alpha\beta}(\mathbf{k})$ (c.f., Section 3.3) is not possible, we chose an interlayer separation of 20 \AA as a compromise between numerical feasibility and minimizing artificial self-interactions within the supercell approach during the G_0W_0 step. This yields slightly underestimated band gaps in comparison to fully converged results. As we are interested in the different reactions of the materials to external screening, the full optimization of the band gap is not the main purpose of this study. Furthermore, in Appendix A.4.5 we show that the absolute band gap changes in $G\Delta W$ do not depend on the vacuum height.

The RPA calculations were carried out utilizing the RPA module implemented in VASP by M. Kaltak [90] in the Wannier basis as presented in Section 3.3. To

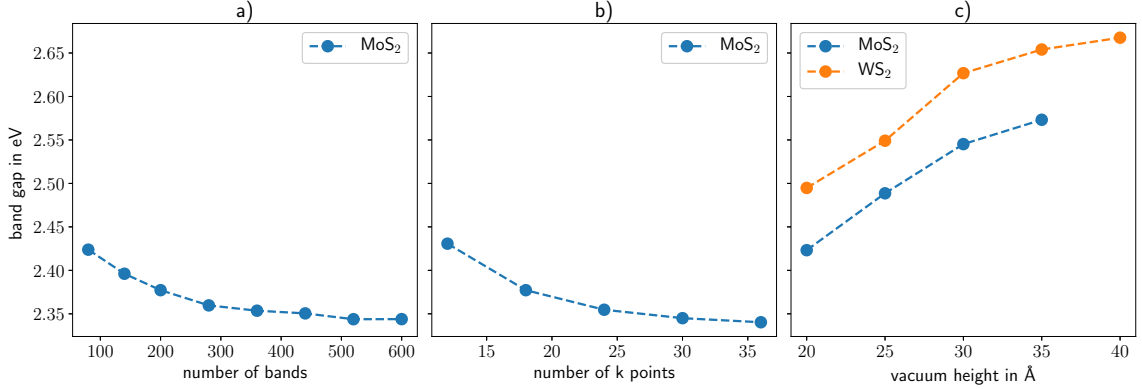


Figure A.4.1.

Convergence plots for the bandgap of a homogeneous monolayer of MoS₂ where the number of bands (a), the number of k-points (b) and the vacuum height (c) were varied.

account for artificial self-interaction within the supercell we performed calculations for different vacuum heights h_{vac} between 15 Å and 40 Å and extrapolated the results to infinite vacuum heights

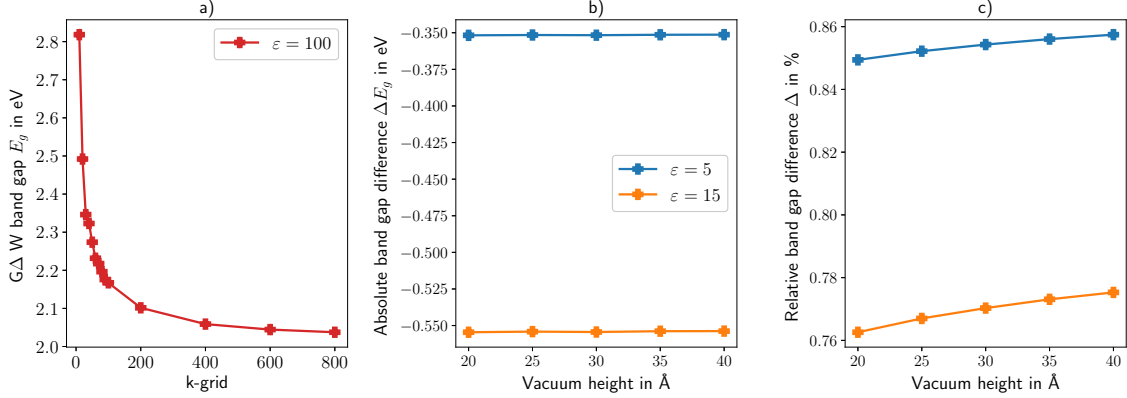
$$U_{\alpha\beta}(\mathbf{q}, h_{\text{vac}}) = U_{\alpha\beta}(\mathbf{q}, \infty) + \frac{b_{\alpha\beta}(\mathbf{q})}{h_{\text{vac}}}.$$

A.4.3. G_0W_0 convergence

In Fig. A.4.1 we show the dependence of the band gap on different calculational parameters. We used MoS₂ as example material for all TMDCs (and for the vacuum heights additionally WS₂ as we used these calculations in Fig. A.4.2). For a fixed number of bands (Fig. A.4.1a) we used a $18 \times 18 \times 1$ \mathbf{k} -grid and 200 bands for a fixed number of \mathbf{k} points (Fig. A.4.1b). The GW energy cutoff was chosen to be 300 eV in these calculations. The vacuum heights (Fig. A.4.1c) were varied for a $12 \times 12 \times 1$ ($24 \times 24 \times 1$) \mathbf{k} -grid and 200 (280) bands for MoS₂ (WS₂). We see a strong dependence of the band gap on the chosen parameter. As a compromise between numerical feasibility and accuracy we chose to use for the $G\Delta W$ calculations a $24 \times 24 \times 1$ grid and 280 bands. The vacuum height was chosen to be rather small with 20 Å but we are mainly interested in the *changes* of the band gap as already mentioned.

A.4.4. Fit parameter and band gaps for investigated TMDCs

In the $G\Delta W$ calculations we incorporate the dielectric environment by substituting the leading eigenvalue of the dielectric function of a freestanding monolayer with Eq. (6.2.17). We fit Eq. (6.2.15) and Eq. (6.2.17) to RPA calculations of a freestanding


Figure A.4.2.

Convergence of band gap in GdW for $\epsilon = 100$ and WS₂

monolayer using the interlayer distance d of the bulk system. The used and resulting parameter and vacuum band gaps are given in Table A.4. For details on the derivation see Section 6.2.2.

	E_g^0 in eV	d in Å	Δ in eV	ϵ_∞	ϵ_2	ϵ_3	γ in Å	V_2 in eV	V_3 in eV
MoS ₂	2.26	6.148 [288]	0.148	10.136	2.637	2.019	1.990	0.817	0.360
MoSe ₂	2.07	6.450 [288]	0.186	11.282	2.307	1.787	1.637	0.867	0.402
WS ₂	2.33	6.162 [289]	0.427	8.565	2.913	2.281	2.169	0.737	0.332
WSe ₂	2.07	6.480 [289]	0.464	9.873	3.097	2.490	2.733	0.647	0.303

Table A.4.

Interlayer distance d and fit parameter of the bare Coulomb interaction (γ , V_2, V_3) as well as for the dielectric function (ϵ_∞ , ϵ_2 , ϵ_3). Additionally, we show the spin-orbit coupling parameter determined from the valence band splitting at \mathbf{K} in GGA calculations.

A.4.5. G Δ W convergence

In Fig. A.4.2a we show G Δ W results for WS₂ for the band gap of a dielectric substrate with $\epsilon = 100$ in dependence on the \mathbf{k} -grid. Throughout this work we use 400×400 k-points in the G Δ W calculations as therefore the change between band gaps is smaller than 0.02 eV when increasing \mathbf{k} . In Fig. A.4.2b and Fig. A.4.2c we show the dependence of the absolute and relative band gap changes for WS₂ for different dielectric constants on the vacuum height of the underlying G₀W₀ calculation. We

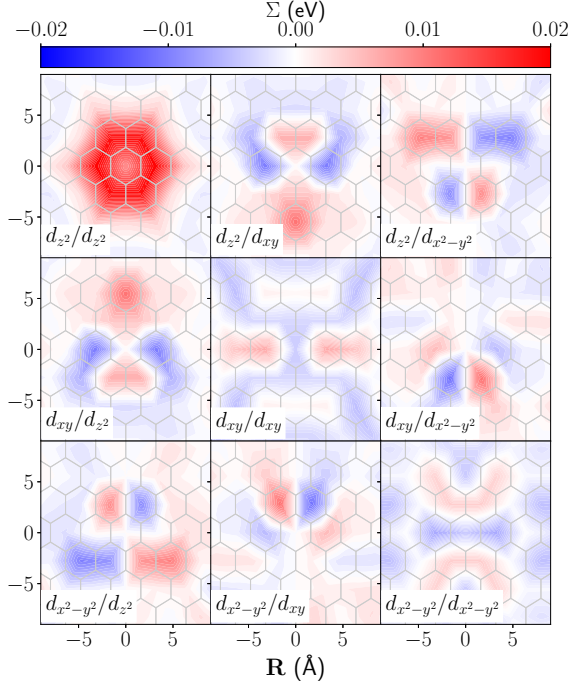


Figure A.4.3

G_0W_0 self-energy for WS_2 with a substrate of strained hexagonal boron nitride. The G_0W_0 self-energy shows similar features as the $G\Delta W$ self-energy.

see nearly no influence on the *absolute* band gap changes and a small influence on the relative changes due to the increasing quasiparticle band gap for increasing vacuum height in G_0W_0 (see Fig. A.4.1c). Since the influence on the absolute changes is small, we chose $c = 20 \text{ \AA}$ for all investigated TMDCs to lower the computational effort in the G_0W_0 step.

A.4.6. GW self-energy

To benchmark our $G\Delta W$ results we performed full G_0W_0 calculations for a monolayer of WS_2 in vacuum and on top of a layer of strained hexagonal boron nitride (hBN). A distance between both monolayers of $\approx 5 \text{ \AA}$ was used. The self-energy was calculated using

$$\Sigma = G_{\text{vacuum}}^{-1} - G_{\text{substrate}}^{-1} \quad (\text{A.4.1})$$

with the Green's function G_{vacuum}^{-1} resulting from G_0W_0 calculations of the free standing and the Green's function $G_{\text{substrate}}^{-1}$ for the system of the monolayer on top of a layer of hBN. The calculational details are presented in Appendix A.4.1. The real space representation of the self-energy is shown in Fig. A.4.3 and shows similar features as the $G\Delta W$ results from Fig. 6.2.4a which is a good benchmark for our modeling approach.

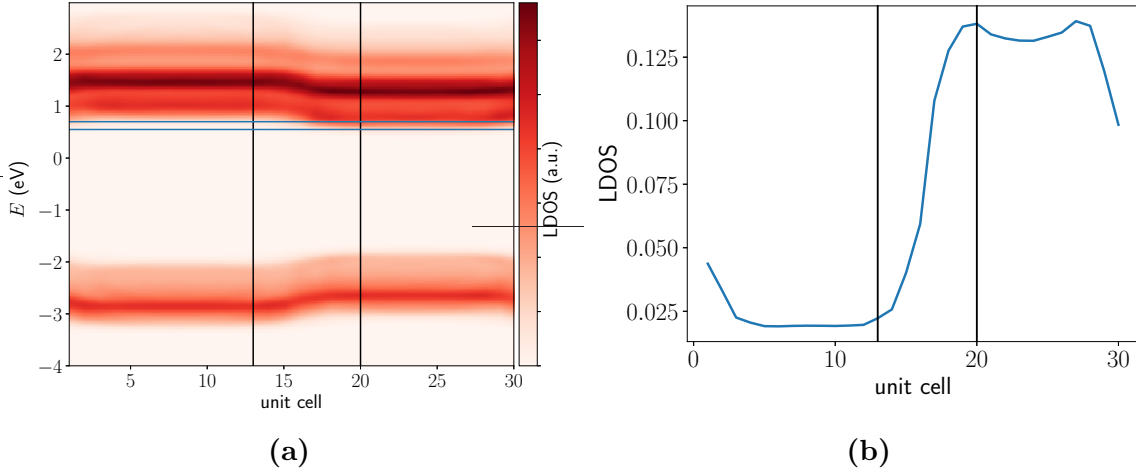


Figure A.4.4.

a) Local density of states for a WS_2 Coulomb engineered heterostructure from Fig. 6.2.5b. Blue lines mark the energy range in which LDOS is averaged shown in (b). We investigate the energy range from 0.55 eV to 0.7 eV. The interface region is marked with black lines.

A.4.7. Finding the characteristic length of the interface

To find a characteristic length r of the interface, we use the local density of states for a specific energy range near the conduction band edge in dependence of the position/unit cell. In Fig. A.4.4b we show the averaged LDOS for a WS_2 heterostructure (from Fig. 6.2.5b) for energies in the energy range from 0.55 eV to 0.7 eV (marked with blue lines in Fig. A.4.4a). Small numbers mean nearly no density of states, i.e. in the left region the studied energies lie within the band gap. To define the characteristic length we seek the unit cells where the change in LDOS becomes small. We define the area of the interface as the region where the LDOS varies strongly. The determined interface region is marked with black lines in Fig. A.4.4

A.4.8. Substrate dielectric constants

We present static dielectric constants for a few typical substrate for 2d materials in Table A.5

substrate	SiO_2	HfO_2	Si	GaAs	hBN
ϵ	≈ 3.6	25	≈ 12	≈ 13	$\approx (1.8 - 3.3)$
Reference	[259]	[259]	[260]	[260]	[290],[291]

Table A.5.

Static dielectric constants for a few typical substrate for 2d materials

A.5. Effects of the Fermi Level Energy on the Adsorption of O_2 to Monolayer MoS_2

A.5.1. Band structure of MoS_2 in absence/presence of O_2

In Fig. A.5.1 the (unfolded) band structures corresponding to the density of states shown in Fig. 7.3.1 of Chapter 7.3 are shown. For the monolayer without adsorbate, we calculated the band structure directly in the first Brillouin zone. For the calculations with the adsorbed molecule we used a 4×4 supercell. Correspondingly, the band structures had to be unfolded, which we performed using the BandUP code [292, 293].

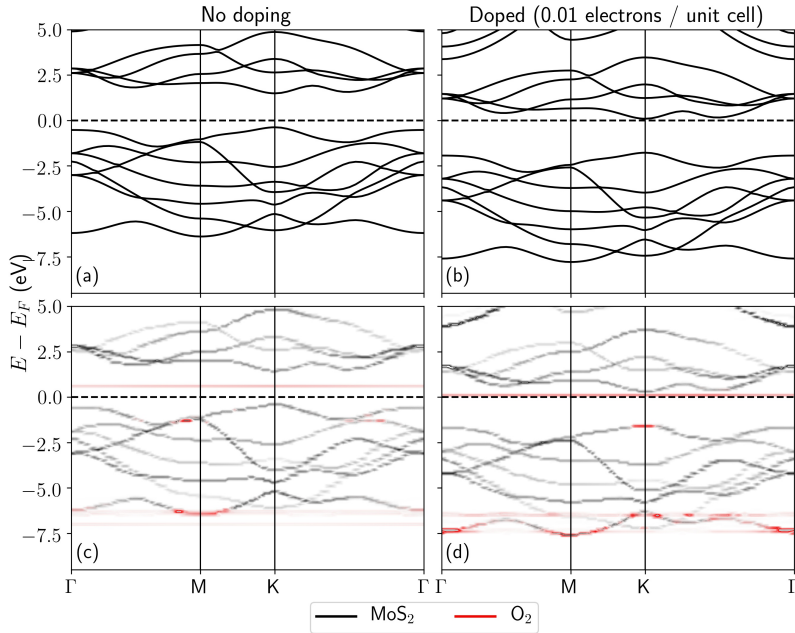


Figure A.5.1.

Band structure of MoS_2 ((a), (b)) and unfolded band structure of MoS_2 in the presence of oxygen ((c), (d)). The black (red) line marks states derived from MoS_2 (O_2 molecules). Different external charge doping levels are accounted for: ((a), (c)), no doping, and ((b), (d)), 0.01 electrons per unit cell.

As in the density of states, we find for the undoped case the Fermi level between the valence and conduction band of MoS_2 (Fig. A.5.1(a) und (c)), leaving the O_2 state unoccupied without doping. When the system is doped with 0.01 electrons/unit cell, which corresponds to approximately 10^{13} electrons/cm², the Fermi level is now at the MoS_2 conduction band edge increasing the number of free carriers. Thus, an electron transfer from MoS_2 to the previously empty orbital localized at O_2 can occur.

Bibliography

- [1] W. Shockley. “The Theory of p-n Junctions in Semiconductors and p-n Junction Transistors”. In: *Bell System Technical Journal* 28.3 (1949), pp. 435–489. DOI: 10.1002/j.1538-7305.1949.tb03645.x.
- [2] H. Kroemer. “Quasi-Electric Fields and Band Offsets: Teaching Electrons New Tricks”. In: *Nobel Lectures in Physics 1996 – 2000* (2000), p. 449.
- [3] Z. I. Alferov. “Nobel Lecture: The double heterostructure concept and its applications in physics, electronics, and technology”. In: *Rev. Mod. Phys.* 73.3 (2001), pp. 767–782. DOI: 10.1103/RevModPhys.73.767.
- [4] K. S. Novoselov. “Electric Field Effect in Atomically Thin Carbon Films”. In: *Science* 306.5696 (2004), pp. 666–669. DOI: 10.1126/science.1102896.
- [5] B. Radisavljevic, A. Radenovic, J. Brivio, V. Giacometti, and A. Kis. “Single-layer MoS₂ transistors”. In: *Nature Nanotechnology* 6.3 (2011), pp. 147–150. DOI: 10.1038/nnano.2010.279.
- [6] A. K. Geim and I. V. Grigorieva. “Van der Waals heterostructures”. In: *Nature* 499.7459 (2013), pp. 419–425. DOI: 10.1038/nature12385.
- [7] K. S. Novoselov et al. “Two-dimensional atomic crystals”. en. In: *Proc. Natl. Acad. Sci. U. S. A.* 102.30 (2005), pp. 10451–10453. DOI: 10.1073/pnas.0502848102.
- [8] X. Duan et al. “Lateral epitaxial growth of two-dimensional layered semiconductor heterojunctions”. en. In: *Nat. Nanotechnol.* 9.12 (2014), pp. 1024–1030. DOI: 10.1038/nnano.2014.222.
- [9] Y. Gong et al. “Vertical and in-plane heterostructures from WS₂/MoS₂ monolayers”. en. In: *Nat. Mater.* 13.12 (2014), pp. 1135–1142. DOI: 10.1038/nmat4091.
- [10] C. Huang et al. “Lateral heterojunctions within monolayer MoSe₂–WSe₂ semiconductors”. en. In: *Nat. Mater.* 13.12 (2014), pp. 1096–1101. DOI: 10.1038/nmat4064.

- [11] M.-Y. Li et al. “Epitaxial growth of a monolayer WSe₂-MoS₂ lateral p-n junction with an atomically sharp interface”. en. In: *Science* 349.6247 (2015), pp. 524–528. DOI: 10.1126/science.aab4097.
- [12] B. Radisavljevic, A. Radenovic, J. Brivio, V. Giacometti, and A. Kis. “Single-layer MoS₂ transistors”. en. In: *Nat. Nanotechnol.* 6.3 (2011), pp. 147–150. DOI: 10.1038/nnano.2010.279.
- [13] L. Britnell et al. “Field-Effect Tunneling Transistor Based on Vertical Graphene Heterostructures”. en. In: *Science* 335.6071 (2012), pp. 947–950. DOI: 10.1126/science.1218461.
- [14] L. Britnell et al. “Strong Light-Matter Interactions in Heterostructures of Atomically Thin Films”. en. In: *Science* 340.6138 (2013), pp. 1311–1314. DOI: 10.1126/science.1235547.
- [15] T. Georgiou et al. “Vertical field-effect transistor based on graphene-WS₂ heterostructures for flexible and transparent electronics”. en. In: *Nat. Nanotechnol.* 8.2 (2013), pp. 100–103. DOI: 10.1038/nnano.2012.224.
- [16] W. J. Yu et al. “Highly efficient gate-tunable photocurrent generation in vertical heterostructures of layered materials”. en. In: *Nat. Nanotechnol.* 8.12 (2013), pp. 952–958. DOI: 10.1038/nnano.2013.219.
- [17] D. Jariwala, V. K. Sangwan, L. J. Lauhon, T. J. Marks, and M. C. Hersam. “Emerging Device Applications for Semiconducting Two-Dimensional Transition Metal Dichalcogenides”. In: *ACS Nano* 8.2 (2014), pp. 1102–1120. DOI: 10.1021/nn500064s.
- [18] F. Withers et al. “Light-emitting diodes by band-structure engineering in van der Waals heterostructures”. en. In: *Nat. Mater.* 14.3 (2015), pp. 301–306. DOI: 10.1038/nmat4205.
- [19] H.-P. Komsa and A. V. Krasheninnikov. “Effects of confinement and environment on the electronic structure and exciton binding energy of MoS₂ from first principles”. In: *Physical Review B* 86.24 (2012). DOI: 10.1103/physrevb.86.241201.
- [20] F. Hüser, T. Olsen, and K. S. Thygesen. “Quasiparticle GW calculations for solids, molecules, and two-dimensional materials”. In: *Phys. Rev. B* 87.23 (2013), p. 235132. DOI: 10.1103/PhysRevB.87.235132.

-
- [21] D. Y. Qiu, F. H. da Jornada, and S. G. Louie. “Optical Spectrum of MoS₂: Many-Body Effects and Diversity of Exciton States”. In: *Physical Review Letters* 111.21 (2013). DOI: 10.1103/physrevlett.111.216805.
- [22] M. Rösner et al. “Two-Dimensional Heterojunctions from Nonlocal Manipulations of the Interactions”. In: *Nano Letters* 16.4 (2016), pp. 2322–2327. DOI: 10.1021/acs.nanolett.5b05009.
- [23] G. Czycholl. *Theoretische Festkörperphysik: von den klassischen Modellen zu modernen Forschungsthemen*. 3., aktualisierte Aufl. Springer-Lehrbuch. Berlin: Springer, 2008.
- [24] R. M. Martin. *Electronic Structure: Basic Theory and Practical Methods*. Cambridge University Press, 2008.
- [25] R. M. Martin, L. Reining, and D. M. Ceperley. *Interacting Electrons: Theory and Computational Approaches*. Cambridge University Press, 2016.
- [26] G. D. Mahan. *Many-Particle Physics (Physics of Solids and Liquids)*. Springer, 2000.
- [27] H. Bruus and K. Flensberg. *Many-body quantum theory in condensed matter physics: an introduction*. Reprinted. Oxford graduate texts. Oxford [u.a.]: Oxford University Press, 2007.
- [28] N. W. Ashcroft and N. D. Mermin. *Solid State Physics*. Cengage Learning, 1976.
- [29] M. Born and R. Oppenheimer. “Zur Quantentheorie der Molekeln”. In: *Annalen der Physik* 389.20 (1927), pp. 457–484. DOI: 10.1002/andp.19273892002.
- [30] F. Bloch. “Über die Quantenmechanik der Elektronen in Kristallgittern”. In: *Zeitschrift für Physik* 52.7-8 (1929), pp. 555–600. DOI: 10.1007/bf01339455.
- [31] D. Mourad. “Empirische Tight-Binding-Modellierung geordneter und ungeordneter Halbleiterstrukturen”. PhD thesis. Universität Bremen, 2010.
- [32] J. C. Slater and G. F. Koster. “Simplified LCAO Method for the Periodic Potential Problem”. In: *Physical Review* 94.6 (1954), pp. 1498–1524. DOI: 10.1103/PhysRev.94.1498.

- [33] G. H. Wannier. “The Structure of Electronic Excitation Levels in Insulating Crystals”. In: *Physical Review* 52.3 (1937), pp. 191–197. DOI: 10.1103/PhysRev.52.191.
- [34] P.-O. Löwdin and H. Shull. “Natural Orbitals in the Quantum Theory of Two-Electron Systems”. In: *Physical Review* 101.6 (1956), pp. 1730–1739. DOI: 10.1103/PhysRev.101.1730.
- [35] N. Marzari, A. A. Mostofi, J. R. Yates, I. Souza, and D. Vanderbilt. “Maximally localized Wannier functions: Theory and applications”. In: *Reviews of Modern Physics* 84.4 (2012), pp. 1419–1475. DOI: 10.1103/RevModPhys.84.1419.
- [36] A. A. Mostofi et al. “An updated version of wannier90: A tool for obtaining maximally-localised Wannier functions”. In: *Computer Physics Communications* 185.8 (2014), pp. 2309–2310. DOI: 10.1016/j.cpc.2014.05.003.
- [37] N. Marzari and D. Vanderbilt. “Maximally localized generalized Wannier functions for composite energy bands”. In: *Physical Review B* 56.20 (1997), pp. 12847–12865. DOI: 10.1103/PhysRevB.56.12847.
- [38] I. Souza, N. Marzari, and D. Vanderbilt. “Maximally localized Wannier functions for entangled energy bands”. In: *Physical Review B* 65.3 (2001), p. 035109. DOI: 10.1103/PhysRevB.65.035109.
- [39] E. Blöchl. “Theory and Practice of Density-Functional Theory”. In: *The LDA+DMFT approach to strongly correlated materials*. Ed. by E. Pavarini, E. Koch, D. Vollhardt, and A. Lichtenstein. Schriften des Forschungszentrums Jülich : Modeling and Simulation, Vol. 1. 2011. Chap. 2.
- [40] L. H. Thomas. “The calculation of atomic fields”. In: *Mathematical Proceedings of the Cambridge Philosophical Society* 23.5 (1927), 542–548. DOI: 10.1017/S0305004100011683.
- [41] E. Fermi. “Un metodo statistico per la determinazione di alcune proprietà dell’atomo”. In: *Rend. Accad. Naz. Lincei* 6 (1927), pp. 602–607.
- [42] P. Hohenberg and W. Kohn. “Inhomogeneous Electron Gas”. In: *Phys. Rev.* 136.3B (1964), B864–B871. DOI: 10.1103/PhysRev.136.B864.
- [43] W. Kohn and L. J. Sham. “Self-Consistent Equations Including Exchange and Correlation Effects”. In: *Phys. Rev.* 140.4A (1965), A1133–A1138. DOI: 10.1103/PhysRev.140.A1133.

-
- [44] G. Kresse and J. Hafner. “Ab initio molecular dynamics for liquid metals”. In: *Phys. Rev. B* 47.1 (1993), pp. 558–561. DOI: 10.1103/PhysRevB.47.558.
- [45] G. Kresse and J. Furthmüller. “Efficiency of ab-initio total energy calculations for metals and semiconductors using a plane-wave basis set”. In: *Computational Materials Science* 6.1 (1996), pp. 15–50. DOI: 10.1016/0927-0256(96)00008-0.
- [46] G. Kresse and J. Furthmüller. “Efficient iterative schemes for ab initio total-energy calculations using a plane-wave basis set”. In: *Phys. Rev. B* 54.16 (1996), pp. 11169–11186. DOI: 10.1103/PhysRevB.54.11169.
- [47] G. Kresse and D. Joubert. “From ultrasoft pseudopotentials to the projector augmented-wave method”. In: *Phys. Rev. B* 59.3 (1999), pp. 1758–1775. DOI: 10.1103/PhysRevB.59.1758.
- [48] J. P. Perdew and A. Zunger. “Self-interaction correction to density-functional approximations for many-electron systems”. In: *Phys. Rev. B* 23.10 (1981), pp. 5048–5079. DOI: 10.1103/PhysRevB.23.5048.
- [49] S. H. Vosko, L. Wilk, and M. Nusair. “Accurate spin-dependent electron liquid correlation energies for local spin density calculations: a critical analysis”. In: *Canadian Journal of Physics* 58.8 (1980), pp. 1200–1211. DOI: 10.1139/p80-159.
- [50] J. P. Perdew and Y. Wang. “Accurate and simple analytic representation of the electron-gas correlation energy”. In: *Physical Review B* 45.23 (1992), pp. 13244–13249. DOI: 10.1103/physrevb.45.13244.
- [51] D. M. Ceperley and B. J. Alder. “Ground State of the Electron Gas by a Stochastic Method”. In: *Phys. Rev. Lett.* 45.7 (1980), pp. 566–569. DOI: 10.1103/PhysRevLett.45.566.
- [52] J. P. Perdew et al. “Atoms, molecules, solids, and surfaces: Applications of the generalized gradient approximation for exchange and correlation”. In: *Phys. Rev. B* 46.11 (1992), pp. 6671–6687. DOI: 10.1103/PhysRevB.46.6671.
- [53] A. D. Becke. “Density-functional exchange-energy approximation with correct asymptotic behavior”. In: *Phys. Rev. A* 38.6 (1988), pp. 3098–3100. DOI: 10.1103/PhysRevA.38.3098.

- [54] C. Lee, W. Yang, and R. G. Parr. “Development of the Colle-Salvetti correlation-energy formula into a functional of the electron density”. In: *Phys. Rev. B* 37.2 (1988), pp. 785–789. DOI: 10.1103/PhysRevB.37.785.
- [55] J. P. Perdew, K. Burke, and M. Ernzerhof. “Generalized Gradient Approximation Made Simple”. In: *Phys. Rev. Lett.* 77.18 (1996), pp. 3865–3868. DOI: 10.1103/PhysRevLett.77.3865.
- [56] V. I. Anisimov, A. I. Poteryaev, M. A. Korotin, A. O. Anokhin, and G. Kotliar. “First-principles calculations of the electronic structure and spectra of strongly correlated systems: dynamical mean-field theory”. In: *Journal of Physics: Condensed Matter* 9.35 (1997), pp. 7359–7367. DOI: 10.1088/0953-8984/9/35/010.
- [57] V. I. Anisimov, J. Zaanen, and O. K. Andersen. “Band theory and Mott insulators: Hubbard U instead of Stoner I”. In: *Phys. Rev. B* 44.3 (1991), pp. 943–954. DOI: 10.1103/PhysRevB.44.943.
- [58] A. Georges, G. Kotliar, W. Krauth, and M. J. Rozenberg. “Dynamical mean-field theory of strongly correlated fermion systems and the limit of infinite dimensions”. In: *Rev. Mod. Phys.* 68.1 (1996), pp. 13–125. DOI: 10.1103/RevModPhys.68.13.
- [59] J. P. Perdew. “Density functional theory and the band gap problem”. In: *International Journal of Quantum Chemistry* 28.S19 (2009), pp. 497–523. DOI: 10.1002/qua.560280846.
- [60] J. Heyd, G. E. Scuseria, and M. Ernzerhof. “Hybrid functionals based on a screened Coulomb potential”. In: *The Journal of Chemical Physics* 118.18 (2003), pp. 8207–8215. DOI: 10.1063/1.1564060.
- [61] A. D. Becke. “A new mixing of Hartree–Fock and local density-functional theories”. In: *The Journal of Chemical Physics* 98.2 (1993), pp. 1372–1377. DOI: 10.1063/1.464304.
- [62] A. D. Becke. “Density-functional thermochemistry. III. The role of exact exchange”. In: *The Journal of Chemical Physics* 98.7 (1993), pp. 5648–5652. DOI: 10.1063/1.464913.
- [63] J. C. Slater. “Wave Functions in a Periodic Potential”. In: *Phys. Rev.* 51.10 (1937), pp. 846–851. DOI: 10.1103/PhysRev.51.846.

-
- [64] C. Herring. “A New Method for Calculating Wave Functions in Crystals”. In: *Phys. Rev.* 57.12 (1940), pp. 1169–1177. DOI: 10.1103/PhysRev.57.1169.
- [65] J. C. Phillips and L. Kleinman. “New Method for Calculating Wave Functions in Crystals and Molecules”. In: *Phys. Rev.* 116.2 (1959), pp. 287–294. DOI: 10.1103/PhysRev.116.287.
- [66] E. Antončík. “Approximate formulation of the orthogonalized plane-wave method”. In: *Journal of Physics and Chemistry of Solids* 10.4 (1959), pp. 314–320. DOI: 10.1016/0022-3697(59)90007-1.
- [67] D. R. Hamann, M. Schlüter, and C. Chiang. “Norm-Conserving Pseudopotentials”. In: *Phys. Rev. Lett.* 43.20 (1979), pp. 1494–1497. DOI: 10.1103/PhysRevLett.43.1494.
- [68] E. L. Shirley, D. C. Allan, R. M. Martin, and J. D. Joannopoulos. “Extended norm-conserving pseudopotentials”. In: *Phys. Rev. B* 40.6 (1989), pp. 3652–3660. DOI: 10.1103/PhysRevB.40.3652.
- [69] G. P. Kerker. “Non-singular atomic pseudopotentials for solid state applications”. In: *Journal of Physics C: Solid State Physics* 13.9 (1980), pp. L189–L194. DOI: 10.1088/0022-3719/13/9/004.
- [70] N. Troullier and J. L. Martins. “Efficient pseudopotentials for plane-wave calculations”. In: *Phys. Rev. B* 43.3 (1991), pp. 1993–2006. DOI: 10.1103/PhysRevB.43.1993.
- [71] D. Vanderbilt. “Soft self-consistent pseudopotentials in a generalized eigenvalue formalism”. In: *Phys. Rev. B* 41.11 (1990), pp. 7892–7895. DOI: 10.1103/PhysRevB.41.7892.
- [72] K. Laasonen, A. Pasquarello, R. Car, C. Lee, and D. Vanderbilt. “Car-Parrinello molecular dynamics with Vanderbilt ultrasoft pseudopotentials”. In: *Phys. Rev. B* 47.16 (1993), pp. 10142–10153. DOI: 10.1103/PhysRevB.47.10142.
- [73] P. E. Blöchl. “Projector augmented-wave method”. In: *Phys. Rev. B* 50.24 (1994), pp. 17953–17979. DOI: 10.1103/PhysRevB.50.17953.
- [74] M. Rösner. “Electronic Structure of Novel Two-dimensional Materials and Graphene Heterostructures”. PhD thesis. University of Bremen, 2016.
- [75] W. Nolting. *Grundkurs Theoretische Physik 3: Elektrodynamik (Springer-Lehrbuch) (German Edition)*. Springer Spektrum, 2013.

- [76] J. D. Jackson. *Klassische Elektrodynamik*. 5. Auflage. Berlin [u.a.]: Walter de Gruyter, 2014.
- [77] D. J. Griffiths. *Elektrodynamik. Eine Einführung*. 3., aktualisierte Aufl. München: Pearson Studium, 2011.
- [78] J. Lindhard. *On the Properties of a Gas of Charged Particles*. Matematisk-fysiske meddelelser. I kommission hos Munksgaard, 1954.
- [79] D. Bohm and D. Pines. “A Collective Description of Electron Interactions. I. Magnetic Interactions”. In: *Phys. Rev.* 82.5 (1951), pp. 625–634. DOI: 10.1103/PhysRev.82.625.
- [80] D. Pines and D. Bohm. “A Collective Description of Electron Interactions: II. Collective vs Individual Particle Aspects of the Interactions”. In: *Phys. Rev.* 85.2 (1952), pp. 338–353. DOI: 10.1103/PhysRev.85.338.
- [81] D. Bohm and D. Pines. “A Collective Description of Electron Interactions: III. Coulomb Interactions in a Degenerate Electron Gas”. In: *Phys. Rev.* 92.3 (1953), pp. 609–625. DOI: 10.1103/PhysRev.92.609.
- [82] H. Ehrenreich and M. H. Cohen. “Self-Consistent Field Approach to the Many-Electron Problem”. In: *Phys. Rev.* 115.4 (1959), pp. 786–790. DOI: 10.1103/PhysRev.115.786.
- [83] R. E. Groenewald, M. Rösner, G. Schönhoff, S. Haas, and T. O. Wehling. “Valley plasmonics in transition metal dichalcogenides”. In: *Phys. Rev. B* 93.20 (2016), p. 205145. DOI: 10.1103/PhysRevB.93.205145.
- [84] F. Aryasetiawan, K. Karlsson, O. Jepsen, and U. Schönberger. “Calculations of Hubbard U from first-principles”. In: *Phys. Rev. B* 74.12 (2006), p. 125106. DOI: 10.1103/PhysRevB.74.125106.
- [85] F. Aryasetiawan et al. “Frequency-dependent local interactions and low-energy effective models from electronic structure calculations”. In: *Phys. Rev. B* 70.19 (2004), p. 195104. DOI: 10.1103/PhysRevB.70.195104.
- [86] F. Aryasetiawan, T. Miyake, and R. Sakuma. “The Constrained RPA Method for Calculating the Hubbard U from First-Principles”. In: *The LDA+DMFT approach to strongly correlated materials*. Ed. by E. Pavarini, E. Koch, D. Vollhardt, and A. Lichtenstein. Schriften des Forschungszentrums Jülich : Modeling and Simulation, Vol. 1. 2011. Chap. 7.

-
- [87] T. Miyake, F. Aryasetiawan, and M. Imada. “Ab initio procedure for constructing effective models of correlated materials with entangled band structure”. In: *Phys. Rev. B* 80.15 (2009), p. 155134. DOI: 10.1103/PhysRevB.80.155134.
- [88] B.-C. Shih, Y. Zhang, W. Zhang, and P. Zhang. “Screened Coulomb interaction of localized electrons in solids from first principles”. In: *Phys. Rev. B* 85.4 (2012), p. 045132. DOI: 10.1103/PhysRevB.85.045132.
- [89] E. Şaşıoğlu, C. Friedrich, and S. Blügel. “Effective Coulomb interaction in transition metals from constrained random-phase approximation”. In: *Phys. Rev. B* 83.12 (2011), p. 121101. DOI: 10.1103/PhysRevB.83.121101.
- [90] M. Kaltak. “Merging GW with DMFT”. PhD thesis. University of Vienna, 2015.
- [91] B. Amadon et al. “Plane-wave based electronic structure calculations for correlated materials using dynamical mean-field theory and projected local orbitals”. In: *Phys. Rev. B* 77.20 (2008), p. 205112. DOI: 10.1103/PhysRevB.77.205112.
- [92] G. Onida, L. Reining, and A. Rubio. “Electronic excitations: density-functional versus many-body Green’s-function approaches”. In: *Reviews of Modern Physics* 74.2 (2002), pp. 601–659. DOI: 10.1103/RevModPhys.74.601.
- [93] C. Friedrich and A. Schindlmayr. “Many-Body Perturbation Theory: The GW Approximation”. In: *Computational Nanoscience: Do It Yourself!* Ed. by J. Grotendorst, S. Blügel, and D. Marx. NIC Series Vol. 31. 2006. Chap. 12.
- [94] F. Aryasetiawan and O. Gunnarsson. “The GW method”. en. In: *Reports on Progress in Physics* 61.3 (1998), p. 237. DOI: 10.1088/0034-4885/61/3/002.
- [95] H. Lehmann. “Über Eigenschaften von Ausbreitungsfunktionen und Renormierungskonstanten quantisierter Felder”. In: *Il Nuovo Cimento* 11.4 (1954), pp. 342–357. DOI: 10.1007/bf02783624.
- [96] F. J. Dyson. “The S Matrix in Quantum Electrodynamics”. In: *Phys. Rev.* 75.11 (1949), pp. 1736–1755. DOI: 10.1103/PhysRev.75.1736.
- [97] L. Hedin. “New Method for Calculating the One-Particle Green’s Function with Application to the Electron-Gas Problem”. In: *Physical Review* 139.3A (1965), A796–A823. DOI: 10.1103/PhysRev.139.A796.

- [98] L. Hedin and S. Lundqvist. “Effects of Electron-Electron and Electron-Phonon Interactions on the One-Electron States of Solids”. In: *Solid State Physics*. Ed. by F. Seitz, D. Turnbull, and H. Ehrenreich. Vol. 23. Academic Press, 1970, pp. 1–181. DOI: 10.1016/S0081-1947(08)60615-3.
- [99] W. G. Aulbur, L. Jönsson, and J. W. Wilkins. “Quasiparticle Calculations in Solids”. In: *Solid State Physics*. Elsevier, 2000, pp. 1–218. DOI: 10.1016/S0081-1947(08)60248-9.
- [100] F. Bruneval, N. Vast, and L. Reining. “Effect of self-consistency on quasiparticles in solids”. In: *Phys. Rev. B* 74.4 (2006), p. 045102. DOI: 10.1103/PhysRevB.74.045102.
- [101] M. S. Hybertsen and S. G. Louie. “Electron correlation in semiconductors and insulators: Band gaps and quasiparticle energies”. In: *Physical Review B* 34.8 (1986), pp. 5390–5413. DOI: 10.1103/PhysRevB.34.5390.
- [102] R. W. Godby, M. Schlüter, and L. J. Sham. “Accurate Exchange-Correlation Potential for Silicon and Its Discontinuity on Addition of an Electron”. In: *Phys. Rev. Lett.* 56.22 (1986), pp. 2415–2418. DOI: 10.1103/PhysRevLett.56.2415.
- [103] I. Campillo, J. M. Pitarke, A. Rubio, E. Zarate, and P. M. Echenique. “Inelastic Lifetimes of Hot Electrons in Real Metals”. In: *Phys. Rev. Lett.* 83.11 (1999), pp. 2230–2233. DOI: 10.1103/PhysRevLett.83.2230.
- [104] W.-D. Schöne, R. Keyling, M. Bandic, and W. Ekardt. “Calculated lifetimes of hot electrons in aluminum and copper using a plane-wave basis set”. In: *Phys. Rev. B* 60.12 (1999), pp. 8616–8623. DOI: 10.1103/PhysRevB.60.8616.
- [105] V. M. Silkin, T. Balasubramanian, E. V. Chulkov, A. Rubio, and P. M. Echenique. “Surface-state hole decay mechanisms: The Be(0001) surface”. In: *Phys. Rev. B* 64.8 (2001), p. 085334. DOI: 10.1103/PhysRevB.64.085334.
- [106] P. Duffy, D. P. Chong, M. E. Casida, and D. R. Salahub. “Assessment of Kohn-Sham density-functional orbitals as approximate Dyson orbitals for the calculation of electron-momentum-spectroscopy scattering cross sections”. In: *Phys. Rev. A* 50.6 (1994), pp. 4707–4728. DOI: 10.1103/PhysRevA.50.4707.
- [107] M. Rohlfing and S. G. Louie. “Electron-hole excitations and optical spectra from first principles”. In: *Phys. Rev. B* 62.8 (2000), pp. 4927–4944. DOI: 10.1103/PhysRevB.62.4927.

-
- [108] H. Haug and S. W. Koch. *Quantum theory of the optical and electronic properties of semiconductors*. Fifth edition. xiii, 469 Seiten : Diagramme. Hackensack, NJ: World Scientific, [2009]2009.
- [109] E. E. Salpeter and H. A. Bethe. “A Relativistic Equation for Bound-State Problems”. In: *Phys. Rev.* 84.6 (1951), pp. 1232–1242. DOI: 10.1103/PhysRev.84.1232.
- [110] L. Reining. “Linear Response and More: the Bethe-Salpeter Equation”. In: *Quantum Materials: Experiments and Theory*. Ed. by E. Pavarni, E. Koch, J. van den Brink, and G. Sawatzky. Schriften des Forschungszentrums Jülich : Modeling and Simulation, Vol. 6. 2011. Chap. 2.
- [111] S. Latini and K. Thygesen. “Excitons in van der Waals Heterostructures: A theoretical study”. English. PhD thesis. 2016.
- [112] S. Latini, T. Olsen, and K. S. Thygesen. “Excitons in van der Waals heterostructures: The important role of dielectric screening”. In: *Phys. Rev. B* 92.24 (2015), p. 245123. DOI: 10.1103/PhysRevB.92.245123.
- [113] G. H. Wannier. “The Structure of Electronic Excitation Levels in Insulating Crystals”. In: *Phys. Rev.* 52.3 (1937), pp. 191–197. DOI: 10.1103/PhysRev.52.191.
- [114] M. Lindberg and S. W. Koch. “Effective Bloch equations for semiconductors”. In: *Phys. Rev. B* 38.5 (1988), pp. 3342–3350. DOI: 10.1103/PhysRevB.38.3342.
- [115] A. D’Andrea and R. D. Sole. “Wannier-Mott excitons in semi-infinite crystals: Wave functions and normal-incidence reflectivity”. In: *Phys. Rev. B* 25.6 (1982), pp. 3714–3730. DOI: 10.1103/PhysRevB.25.3714.
- [116] J. Tilchin et al. “Hydrogen-like Wannier-Mott Excitons in Single Crystal of Methylammonium Lead Bromide Perovskite”. In: *ACS Nano* 10.6 (2016), pp. 6363–6371. DOI: 10.1021/acsnano.6b02734.
- [117] K. Andersen, S. Latini, and K. S. Thygesen. “Dielectric Genome of van der Waals Heterostructures”. In: *Nano Letters* 15.7 (2015). PMID: 26047386, pp. 4616–4621. DOI: 10.1021/acs.nanolett.5b01251.
- [118] T. C. Berkelbach, M. S. Hybertsen, and D. R. Reichman. “Theory of neutral and charged excitons in monolayer transition metal dichalcogenides”. In: *Phys. Rev. B* 88.4 (2013), p. 045318. DOI: 10.1103/PhysRevB.88.045318.

- [119] T. Olsen, S. Latini, F. Rasmussen, and K. S. Thygesen. “Simple Screened Hydrogen Model of Excitons in Two-Dimensional Materials”. In: *Phys. Rev. Lett.* 116.5 (2016), p. 056401. DOI: 10.1103/PhysRevLett.116.056401.
- [120] A. Chernikov et al. “Exciton Binding Energy and Nonhydrogenic Rydberg Series in Monolayer WS₂”. In: *Physical Review Letters* 113.7 (2014). DOI: 10.1103/physrevlett.113.076802.
- [121] A. H. Castro Neto, F. Guinea, N. M. R. Peres, K. S. Novoselov, and A. K. Geim. “The electronic properties of graphene”. In: *Rev. Mod. Phys.* 81.1 (2009), pp. 109–162. DOI: 10.1103/RevModPhys.81.109.
- [122] X. Li et al. “Large-Area Synthesis of High-Quality and Uniform Graphene Films on Copper Foils”. In: *Science* 324.5932 (2009), pp. 1312–1314. DOI: 10.1126/science.1171245.
- [123] D. Pacilé, J. C. Meyer, Ç. O. Girit, and A. Zettl. “The two-dimensional phase of boron nitride: Few-atomic-layer sheets and suspended membranes”. In: *Applied Physics Letters* 92.13 (2008), p. 133107. DOI: 10.1063/1.2903702.
- [124] C. R. Dean et al. “Boron nitride substrates for high-quality graphene electronics”. In: *Nature Nanotechnology* 5.10 (2010), pp. 722–726. DOI: 10.1038/nnano.2010.172.
- [125] L. Li et al. “Black phosphorus field-effect transistors”. In: *Nature Nanotechnology* 9.5 (2014), pp. 372–377. DOI: 10.1038/nnano.2014.35.
- [126] H. Liu et al. “Phosphorene: An Unexplored 2D Semiconductor with a High Hole Mobility”. In: *ACS Nano* 8.4 (2014), pp. 4033–4041. DOI: 10.1021/nn501226z.
- [127] M. Osada and T. Sasaki. “Two-Dimensional Dielectric Nanosheets: Novel Nanoelectronics From Nanocrystal Building Blocks”. In: *Advanced Materials* 24.2 (2011), pp. 210–228. DOI: 10.1002/adma.201103241.
- [128] A. Ayari, E. Cobas, O. Ogundadegbe, and M. S. Fuhrer. “Realization and electrical characterization of ultrathin crystals of layered transition-metal dichalcogenides”. In: *Journal of Applied Physics* 101.1 (2007), p. 014507. DOI: 10.1063/1.2407388.
- [129] Q. H. Wang, K. Kalantar-Zadeh, A. Kis, J. N. Coleman, and M. S. Strano. “Electronics and optoelectronics of two-dimensional transition metal dichalco-

- genides”. In: *Nature Nanotechnology* 7.11 (2012), pp. 699–712. DOI: 10.1038/nnano.2012.193.
- [130] E. M. Vogel and J. A. Robinson. “Two-dimensional layered transition-metal dichalcogenides for versatile properties and applications”. In: *MRS Bulletin* 40.07 (2015), pp. 558–563. DOI: 10.1557/mrs.2015.120.
- [131] S. Manzeli, D. Ovchinnikov, D. Pasquier, O. V. Yazyev, and A. Kis. “2D transition metal dichalcogenides”. In: *Nature Reviews Materials* 2.8 (2017), p. 17033. DOI: 10.1038/natrevmats.2017.33.
- [132] S. Das, J. A. Robinson, M. Dubey, H. Terrones, and M. Terrones. “Beyond Graphene: Progress in Novel Two-Dimensional Materials and van der Waals Solids”. In: *Annual Review of Materials Research* 45.1 (2015), pp. 1–27. DOI: 10.1146/annurev-matsci-070214-021034.
- [133] R. G. Dickinson and L. Pauling. “THE CRYSTAL STRUCTURE OF MOLYBDENITE”. In: *Journal of the American Chemical Society* 45.6 (1923), pp. 1466–1471. DOI: 10.1021/ja01659a020.
- [134] Frindt R. F., Yoffe A. D., and Bowden Frank Philip. “Physical properties of layer structures : optical properties and photoconductivity of thin crystals of molybdenum disulphide”. In: *Proceedings of the Royal Society of London. Series A. Mathematical and Physical Sciences* 273.1352 (1963), pp. 69–83. DOI: 10.1098/rspa.1963.0075.
- [135] R. F. Frindt. “Optical Absorption of a Few Unit-Cell Layers of MoS_2 ”. In: *Physical Review* 140.2A (1965), A536–A539. DOI: 10.1103/PhysRev.140.A536.
- [136] P. Joensen, R. F. Frindt, and S. R. Morrison. “Single-layer MoS_2 ”. In: *Materials Research Bulletin* 21.4 (1986), pp. 457–461. DOI: 10.1016/0025-5408(86)90011-5.
- [137] L. F. Mattheiss. “Band Structures of Transition-Metal-Dichalcogenide Layer Compounds”. In: *Physical Review B* 8.8 (1973), pp. 3719–3740. DOI: 10.1103/physrevb.8.3719.
- [138] D. Dumcenco et al. “Large-Area Epitaxial Monolayer MoS_2 ”. In: *ACS Nano* 9.4 (2015), pp. 4611–4620. DOI: 10.1021/acsnano.5b01281.

- [139] M. Bernardi, C. Ataca, M. Palummo, and J. C. Grossman. “Optical and Electronic Properties of Two-Dimensional Layered Materials”. In: *Nanophotonics* 6.2 (2017). DOI: 10.1515/nanoph-2015-0030.
- [140] K. F. Mak and J. Shan. “Photonics and optoelectronics of 2D semiconductor transition metal dichalcogenides”. In: *Nature Photonics* 10.4 (2016), pp. 216–226. DOI: 10.1038/nphoton.2015.282.
- [141] W. S. Yun, S. W. Han, S. C. Hong, I. G. Kim, and J. D. Lee. “Thickness and strain effects on electronic structures of transition metal dichalcogenides: 2H-MX₂semiconductors”. In: *Physical Review B* 85.3 (2012). DOI: 10.1103/physrevb.85.033305.
- [142] K. F. Mak, C. Lee, J. Hone, J. Shan, and T. F. Heinz. “Atomically Thin MoS₂: A New Direct-Gap Semiconductor”. In: *Phys. Rev. Lett.* 105.13 (2010), p. 136805. DOI: 10.1103/PhysRevLett.105.136805.
- [143] A. Kuc, T. Heine, and A. Kis. “Electronic properties of transition-metal dichalcogenides”. en. In: *MRS Bulletin* 40.7 (2015), pp. 577–584. DOI: 10.1557/mrs.2015.143.
- [144] A. Splendiani et al. “Emerging Photoluminescence in Monolayer MoS₂”. In: *Nano Letters* 10.4 (2010), pp. 1271–1275. DOI: 10.1021/nl903868w.
- [145] A. Kuc, N. Zibouche, and T. Heine. “Influence of quantum confinement on the electronic structure of the transition metal sulfide TS₂”. In: *Physical Review B* 83.24 (2011). DOI: 10.1103/physrevb.83.245213.
- [146] T. Li and G. Galli. “Electronic Properties of MoS₂Nanoparticles”. In: *The Journal of Physical Chemistry C* 111.44 (2007), pp. 16192–16196. DOI: 10.1021/jp075424v.
- [147] S. Hastrup et al. “The Computational 2D Materials Database: high-throughput modeling and discovery of atomically thin crystals”. In: *2D Materials* 5.4 (2018), p. 042002. DOI: 10.1088/2053-1583/aacfc1.
- [148] J. Wilson and A. Yoffe. “The transition metal dichalcogenides discussion and interpretation of the observed optical, electrical and structural properties”. In: *Advances in Physics* 18.73 (1969), pp. 193–335. DOI: 10.1080/00018736900101307.
- [149] A. Kormányos, V. Zólyomi, N. D. Drummond, and G. Burkard. “Spin-Orbit Coupling, Quantum Dots, and Qubits in Monolayer Transition Metal

- Dichalcogenides”. In: *Physical Review X* 4.1 (2014). DOI: 10.1103/physrevx.4.011034.
- [150] G.-B. Liu, W.-Y. Shan, Y. Yao, W. Yao, and D. Xiao. “Three-band tight-binding model for monolayers of group-VIB transition metal dichalcogenides”. In: *Physical Review B* 88.8 (2013). DOI: 10.1103/physrevb.88.085433.
- [151] N. Zibouche, A. Kuc, J. Musfeldt, and T. Heine. “Transition-metal dichalcogenides for spintronic applications”. In: *Annalen der Physik* 526.9-10 (2014), pp. 395–401. DOI: 10.1002/andp.201400137.
- [152] Z. Y. Zhu, Y. C. Cheng, and U. Schwingenschlögl. “Giant spin-orbit-induced spin splitting in two-dimensional transition-metal dichalcogenide semiconductors”. In: *Physical Review B* 84.15 (2011). DOI: 10.1103/physrevb.84.153402.
- [153] D. Xiao, G.-B. Liu, W. Feng, X. Xu, and W. Yao. “Coupled Spin and Valley Physics in Monolayers of MoS₂ and Other Group-VI Dichalcogenides”. In: *Physical Review Letters* 108.19 (2012). DOI: 10.1103/physrevlett.108.196802.
- [154] A. Ramasubramanian. “Large excitonic effects in monolayers of molybdenum and tungsten dichalcogenides”. In: *Physical Review B* 86.11 (2012). DOI: 10.1103/physrevb.86.115409.
- [155] F. Hüser, T. Olsen, and K. S. Thygesen. “How dielectric screening in two-dimensional crystals affects the convergence of excited-state calculations: Monolayer MoS₂”. In: *Physical Review B* 88.24 (2013). DOI: 10.1103/physrevb.88.245309.
- [156] A. Steinhoff, M. Rösner, F. Jahnke, T. O. Wehling, and C. Gies. “Influence of Excited Carriers on the Optical and Electronic Properties of MoS₂”. In: *Nano Letters* 14.7 (2014), pp. 3743–3748. DOI: 10.1021/nl500595u.
- [157] T. Cheiwchanamngij and W. R. L. Lambrecht. “Quasiparticle band structure calculation of monolayer, bilayer, and bulk MoS₂”. In: *Physical Review B* 85.20 (2012). DOI: 10.1103/physrevb.85.205302.
- [158] H. Shi, H. Pan, Y.-W. Zhang, and B. I. Yakobson. “Quasiparticle band structures and optical properties of strained monolayer MoS₂ and WS₂”. In: *Physical Review B* 87.15 (2013). DOI: 10.1103/physrevb.87.155304.

- [159] C. Kittel and S. Hunklinger. *Einführung in die Festkörperphysik*. 14., überarb. und erw. Aufl. München: Oldenbourg, 2006.
- [160] M. Dvorak, S.-H. Wei, and Z. Wu. “Origin of the Variation of Exciton Binding Energy in Semiconductors”. In: *Physical Review Letters* 110.1 (2013). DOI: 10.1103/physrevlett.110.016402.
- [161] M. M. Ugeda et al. “Giant bandgap renormalization and excitonic effects in a monolayer transition metal dichalcogenide semiconductor”. In: *Nature Materials* 13.12 (2014), pp. 1091–1095. DOI: 10.1038/nmat4061.
- [162] K. He et al. “Tightly Bound Excitons in MonolayerWSe₂”. In: *Physical Review Letters* 113.2 (2014). DOI: 10.1103/physrevlett.113.026803.
- [163] Y. Liu, R. F. Willis, K. V. Emtsev, and T. Seyller. “Plasmon dispersion and damping in electrically isolated two-dimensional charge sheets”. In: *Phys. Rev. B* 78.20 (2008), p. 201403. DOI: 10.1103/PhysRevB.78.201403.
- [164] K. Andersen and K. S. Thygesen. “Plasmons in metallic monolayer and bilayer transition metal dichalcogenides”. In: *Phys. Rev. B* 88.15 (2013), p. 155128. DOI: 10.1103/PhysRevB.88.155128.
- [165] L.V. Keldysh. “Coulomb interaction in thin semiconductor and semimetal films”. In: 29.29 (1979), p. 658.
- [166] P. Cudazzo, I. V. Tokatly, and A. Rubio. “Dielectric screening in two-dimensional insulators: Implications for excitonic and impurity states in graphane”. In: *Physical Review B* 84.8 (2011). DOI: 10.1103/physrevb.84.085406.
- [167] M. Rösner, E., C. Friedrich, S. Blügel, and T. O. Wehling. “Wannier function approach to realistic Coulomb interactions in layered materials and heterostructures”. In: *Phys. Rev. B* 92.8 (2015), p. 085102. DOI: 10.1103/PhysRevB.92.085102.
- [168] K. S. Thygesen. “Calculating excitons, plasmons, and quasiparticles in 2D materials and van der Waals heterostructures”. In: *2D Materials* 4.2 (2017), p. 022004. DOI: 10.1088/2053-1583/aa6432.
- [169] D. Y. Qiu, F. H. da Jornada, and S. G. Louie. “Screening and many-body effects in two-dimensional crystals: MonolayerMoS₂”. In: *Physical Review B* 93.23 (2016). DOI: 10.1103/physrevb.93.235435.

-
- [170] C. A. Rozzi, D. Varsano, A. Marini, E. K. U. Gross, and A. Rubio. “Exact Coulomb cutoff technique for supercell calculations”. In: *Physical Review B* 73.20 (2006). DOI: 10.1103/physrevb.73.205119.
- [171] S. Ismail-Beigi. “Truncation of periodic image interactions for confined systems”. In: *Physical Review B* 73.23 (2006). DOI: 10.1103/physrevb.73.233103.
- [172] H. M. Hill et al. “Observation of Excitonic Rydberg States in Monolayer MoS₂ and WS₂ by Photoluminescence Excitation Spectroscopy”. In: *Nano Letters* 15.5 (2015), pp. 2992–2997. DOI: 10.1021/nl504868p.
- [173] C.-H. Park, F. Giustino, C. D. Spataru, M. L. Cohen, and S. G. Louie. “First-Principles Study of Electron Linewidths in Graphene”. In: *Phys. Rev. Lett.* 102.7 (2009), p. 076803. DOI: 10.1103/PhysRevLett.102.076803.
- [174] Y. Lin et al. “Dielectric Screening of Excitons and Trions in Single-Layer MoS₂”. In: *Nano Letters* 14.10 (2014), pp. 5569–5576. DOI: 10.1021/nl501988y.
- [175] F. Chen, J. Xia, D. K. Ferry, and N. Tao. “Dielectric Screening Enhanced Performance in Graphene FET”. In: *Nano Letters* 9.7 (2009), pp. 2571–2574. DOI: 10.1021/nl900725u.
- [176] C.-H. Park, F. Giustino, C. D. Spataru, M. L. Cohen, and S. G. Louie. “Angle-Resolved Photoemission Spectra of Graphene from First-Principles Calculations”. In: *Nano Letters* 9.12 (2009), pp. 4234–4239. DOI: 10.1021/nl902448v.
- [177] J. Ryou, Y.-S. Kim, S. Kc, and K. Cho. “Monolayer MoS₂ Bandgap Modulation by Dielectric Environments and Tunable Bandgap Transistors”. en. In: *Scientific Reports* 6 (2016), p. 29184. DOI: 10.1038/srep29184.
- [178] A. J. Bradley et al. “Probing the Role of Interlayer Coupling and Coulomb Interactions on Electronic Structure in Few-Layer MoSe₂ Nanostructures”. In: *Nano Letters* 15.4 (2015), pp. 2594–2599. DOI: 10.1021/acs.nanolett.5b00160.
- [179] Q. Zhang et al. “Bandgap renormalization and work function tuning in MoSe₂/hBN/Ru(0001) heterostructures”. In: *Nature Communications* 7 (2016), p. 13843.

- [180] A. V. Stier, N. P. Wilson, G. Clark, X. Xu, and S. A. Crooker. “Probing the Influence of Dielectric Environment on Excitons in Monolayer WSe₂: Insight from High Magnetic Fields”. In: *Nano Letters* 16.11 (2016), pp. 7054–7060. DOI: 10.1021/acs.nanolett.6b03276.
- [181] M. Florian et al. “The Dielectric Impact of Layer Distances on Exciton and Trion Binding Energies in van der Waals Heterostructures”. In: *Nano Letters* 18.4 (2018), pp. 2725–2732. DOI: 10.1021/acs.nanolett.8b00840.
- [182] M. L. Trolle, T. G. Pedersen, and V. Véniard. “Model dielectric function for 2D semiconductors including substrate screening”. In: *Scientific Reports* 7.1 (2017). DOI: 10.1038/srep39844.
- [183] C.-H. Park, F. Giustino, C. D. Spataru, M. L. Cohen, and S. G. Louie. “First-Principles Study of Electron Linewidths in Graphene”. In: *Phys. Rev. Lett.* 102.7 (2009), p. 076803. DOI: 10.1103/PhysRevLett.102.076803.
- [184] Y. Lin et al. “Dielectric Screening of Excitons and Trions in Single-Layer MoS₂”. In: *Nano Letters* 14.10 (2014), pp. 5569–5576. DOI: 10.1021/nl501988y.
- [185] A. Bruix et al. “Single-layer MoS₂ on Au(111): Band gap renormalization and substrate interaction”. In: *Physical Review B* 93.16 (2016). DOI: 10.1103/physrevb.93.165422.
- [186] K. T. Winther and K. S. Thygesen. “Band structure engineering in van der Waals heterostructures via dielectric screening: the G Delta W method”. In: *2D Materials* 4.2 (2017), p. 025059. DOI: 10.1088/2053-1583/aa6531.
- [187] Y. Cho and T. C. Berkelbach. “Environmentally sensitive theory of electronic and optical transitions in atomically thin semiconductors”. In: *Phys. Rev. B* 97.4 (2018), p. 041409. DOI: 10.1103/PhysRevB.97.041409.
- [188] A. Raja et al. “Coulomb engineering of the bandgap and excitons in two-dimensional materials”. In: *Nature Communications* 8 (2017), p. 15251. DOI: 10.1038/ncomms15251.
- [189] N. Krane, C. Lotze, J. M. Läger, G. Reecht, and K. J. Franke. “Electronic Structure and Luminescence of Quasi-Freestanding MoS₂ Nanopatches on Au(111)”. In: *Nano Letters* 16.8 (2016), pp. 5163–5168. DOI: 10.1021/acs.nanolett.6b02101.

-
- [190] S. Borghardt et al. “Engineering of optical and electronic band gaps in transition metal dichalcogenide monolayers through external dielectric screening”. In: *Physical Review Materials* 1.5 (2017). DOI: 10.1103/physrevmaterials.1.054001.
- [191] M. I. B. Utama et al. “A dielectric-defined lateral heterojunction in a monolayer semiconductor”. In: *Nature Electronics* 2.2 (2019), pp. 60–65. DOI: 10.1038/s41928-019-0207-4.
- [192] D. Y. Qiu, F. H. da Jornada, and S. G. Louie. “Environmental Screening Effects in 2D Materials: Renormalization of the Bandgap, Electronic Structure, and Optical Spectra of Few-Layer Black Phosphorus”. In: *Nano Letters* 17.8 (2017), pp. 4706–4712. DOI: 10.1021/acs.nanolett.7b01365.
- [193] P. Steinleitner et al. “Dielectric Engineering of Electronic Correlations in a van der Waals Heterostructure”. In: *Nano Letters* 18.2 (2018), pp. 1402–1409. DOI: 10.1021/acs.nanolett.7b05132.
- [194] L. Meckbach, T. Stroucken, and S. W. Koch. “Influence of the effective layer thickness on the ground-state and excitonic properties of transition-metal dichalcogenide systems”. In: *Phys. Rev. B* 97.3 (2018), p. 035425. DOI: 10.1103/PhysRevB.97.035425.
- [195] G. Gupta, S. Kallatt, and K. Majumdar. “Direct observation of giant binding energy modulation of exciton complexes in monolayer MoSe₂”. In: *Physical Review B* 96.8 (2017). DOI: 10.1103/physrevb.96.081403.
- [196] A. Steinhoff, T. O. Wehling, and M. Rösner. “Frequency-dependent substrate screening of excitons in atomically thin transition metal dichalcogenide semiconductors”. In: *Physical Review B* 98.4 (2018). DOI: 10.1103/physrevb.98.045304.
- [197] S. Park et al. “Direct determination of monolayer MoS₂ and WSe₂ exciton binding energies on insulating and metallic substrates”. In: *2D Materials* 5.2 (2018), p. 025003. DOI: 10.1088/2053-1583/aaa4ca.
- [198] G. Y. Jia, Y. Zhou, Y. Z. Niu, S. B. Huang, and Y. P. Cao. “Screening Effect of Ultrathin Gold Films on Excitons in Monolayer WS₂”. In: *Plasmonics* (2019). DOI: 10.1007/s11468-018-00894-6.
- [199] M. Drüppel, T. Deilmann, P. Krüger, and M. Rohlfiing. “Diversity of trion states and substrate effects in the optical properties of an MoS₂ monolayer”. In: *Nature Communications* 8.1 (2017). DOI: 10.1038/s41467-017-02286-6.

- [200] P. A. D. Gonçalves, L. P. Bertelsen, S. Xiao, and N. A. Mortensen. “Plasmon-exciton polaritons in two-dimensional semiconductor/metal interfaces”. In: *Physical Review B* 97.4 (2018). DOI: 10.1103/physrevb.97.041402.
- [201] E. Scalise, M. Houssa, G. Pourtois, V. Afanas’ev, and A. Stesmans. “Strain-induced semiconductor to metal transition in the two-dimensional honeycomb structure of MoS₂”. In: *Nano Research* 5.1 (2011), pp. 43–48. DOI: 10.1007/s12274-011-0183-0.
- [202] H. Peelaers and C. G. Van de Walle. “Effects of strain on band structure and effective masses in MoS₂”. In: *Phys. Rev. B* 86.24 (2012), p. 241401. DOI: 10.1103/PhysRevB.86.241401.
- [203] H. J. Conley et al. “Bandgap Engineering of Strained Monolayer and Bilayer MoS₂”. In: *Nano Letters* 13.8 (2013), pp. 3626–3630. DOI: 10.1021/nl4014748.
- [204] H. Rostami, A. G. Moghaddam, and R. Asgari. “Effective lattice Hamiltonian for monolayer MoS₂: Tailoring electronic structure with perpendicular electric and magnetic fields”. In: *Phys. Rev. B* 88.8 (2013), p. 085440. DOI: 10.1103/PhysRevB.88.085440.
- [205] T. Brumme, M. Calandra, and F. Mauri. “First-principles theory of field-effect doping in transition-metal dichalcogenides: Structural properties, electronic structure, Hall coefficient, and electrical conductivity”. In: *Phys. Rev. B* 91.15 (2015), p. 155436. DOI: 10.1103/PhysRevB.91.155436.
- [206] J. T. Ye et al. “Superconducting Dome in a Gate-Tuned Band Insulator”. In: *Science* 338.6111 (2012), pp. 1193–1196. DOI: 10.1126/science.1228006.
- [207] Y. Ge and A. Y. Liu. “Phonon-mediated superconductivity in electron-doped single-layer MoS₂: A first-principles prediction”. In: *Phys. Rev. B* 87.24 (2013), p. 241408. DOI: 10.1103/PhysRevB.87.241408.
- [208] J. H. Smet et al. “Gate-voltage control of spin interactions between electrons and nuclei in a semiconductor”. en. In: *Nature* 415.6869 (2002), pp. 281–286. DOI: 10.1038/415281a.
- [209] S. Buckley, K. Rivoire, and J. Vučković. “Engineered quantum dot single-photon sources”. en. In: *Rep. Prog. Phys.* 75.12 (2012), p. 126503. DOI: 10.1088/0034-4885/75/12/126503.

-
- [210] Keldysh L.V. “Coulomb interaction in thin semiconductor and semimetal films”. In: 29.29 (1979), p. 658.
- [211] C.-H. Park, F. Giustino, C. D. Spataru, M. L. Cohen, and S. G. Louie. “Angle-Resolved Photoemission Spectra of Graphene from First-Principles Calculations”. In: *Nano Letters* 9.12 (2009), pp. 4234–4239. DOI: 10.1021/nl902448v.
- [212] C.-H. Park and S. G. Louie. “Tunable Excitons in Biased Bilayer Graphene”. en. In: *Nano Lett.* 10.2 (2010), pp. 426–431. DOI: 10.1021/nl902932k.
- [213] C. Zhang, H. Wang, W. Chan, C. Manolatou, and F. Rana. “Absorption of light by excitons and trions in monolayers of metal dichalcogenide MoS₂: Experiments and theory”. In: *Phys. Rev. B* 89.20 (2014), p. 205436. DOI: 10.1103/PhysRevB.89.205436.
- [214] N. M. Perney et al. “Tuning localized plasmons in nanostructured substrates for surface-enhanced Raman scattering”. en. In: *Opt. Express* 14.2 (2006), p. 847. DOI: 10.1364/OPEX.14.000847.
- [215] C. Lee, X. Wei, J. W. Kysar, and J. Hone. “Measurement of the Elastic Properties and Intrinsic Strength of Monolayer Graphene”. en. In: *Science* 321.5887 (2008), pp. 385–388. DOI: 10.1126/science.1157996.
- [216] H. Sirringhaus et al. “Two-dimensional charge transport in self-organized, high-mobility conjugated polymers”. en. In: *Nature* 401.6754 (1999), pp. 685–688. DOI: 10.1038/44359.
- [217] M. de Wild et al. “A Novel Route To Molecular Self-Assembly: Self-Intermixed Monolayer Phases”. en. In: *ChemPhysChem* 3.10 (2002), pp. 881–885. DOI: 10.1002/1439-7641(20021018)3:10<881::AID-CPHC881>3.0.CO;2-P.
- [218] M De Wild et al. “Molecular Assembly and Self-Assembly: Molecular Nanoscience for Future Technologies”. en. In: *Ann. N. Y. Acad. Sci.* 1006.1 (2003), pp. 291–305. DOI: 10.1196/annals.1292.020.
- [219] K. Suto, S. Yoshimoto, and K. Itaya. “Two-Dimensional Self-Organization of Phthalocyanine and Porphyrin: Dependence on the Crystallographic Orientation of Au”. In: *J. Am. Chem. Soc.* 125.49 (2003), pp. 14976–14977. DOI: 10.1021/ja038857u.
- [220] M. Petrović et al. “The mechanism of caesium intercalation of graphene”. en. In: *Nat. Commun.* 4 (2013), p. 2772. DOI: 10.1038/ncomms3772.

- [221] S. Ulstrup et al. “Sequential oxygen and alkali intercalation of epitaxial graphene on Ir(111): enhanced many-body effects and formation of pn -interfaces”. en. In: *2D Mater.* 1.2 (2014), p. 025002. DOI: 10.1088/2053-1583/1/2/025002.
- [222] R. F. Klie, Y. Zhu, E. I. Altman, and Y. Liang. “Atomic structure of epitaxial SrTiO₃-GaAs(001) heterojunctions”. In: *Appl. Phys. Lett.* 87.14 (2005), p. 143106. DOI: 10.1063/1.2077837.
- [223] Q. Qiao, R. F. Klie, S. Ögüt, and J. C. Idrobo. “Atomic and electronic structures of SrTiO₃/GaAs heterointerfaces: An 80-kV atomic-resolution electron energy-loss spectroscopy study”. In: *Phys. Rev. B* 85.16 (2012), p. 165406. DOI: 10.1103/PhysRevB.85.165406.
- [224] M. K. Hudait et al. “Integration of SrTiO₃ on Crystallographically Oriented Epitaxial Germanium for Low-Power Device Applications”. In: *ACS Appl. Mater. Interfaces* 7.9 (2015), pp. 5471–5479. DOI: 10.1021/am5091726.
- [225] L. Mazet, S. M. Yang, S. V. Kalinin, S. Schamm-Chardon, and C. Dubourdieu. “A review of molecular beam epitaxy of ferroelectric BaTiO₃ films on Si, Ge and GaAs substrates and their applications”. In: *Sci. Technol. Adv. Mater.* 16.3 (2015), p. 036005. DOI: 10.1088/1468-6996/16/3/036005.
- [226] C. Steinke et al. “Noninvasive control of excitons in two-dimensional materials”. In: *Phys. Rev. B* 96.4 (2017), p. 045431. DOI: 10.1103/PhysRevB.96.045431.
- [227] R. B. Somoano, V. Hadek, A. Rembaum, S. Samson, and J. A. Woollam. “The alkaline earth intercalates of molybdenum disulfide”. In: *The Journal of Chemical Physics* 62.3 (1975), pp. 1068–1073. DOI: 10.1063/1.430548.
- [228] N. E. Staley et al. “Electric field effect on superconductivity in atomically thin flakes of NbSe₂”. In: *Physical Review B* 80.18 (2009), p. 184505. DOI: 10.1103/PhysRevB.80.184505.
- [229] W. Shi et al. “Superconductivity Series in Transition Metal Dichalcogenides by Ionic Gating”. In: *Scientific Reports* 5 (2015), p. 12534. DOI: 10.1038/srep12534.
- [230] S. Jo, D. Costanzo, H. Berger, and A. F. Morpurgo. “Electrostatically Induced Superconductivity at the Surface of WS₂”. In: *Nano Letters* 15.2 (2015), pp. 1197–1202. DOI: 10.1021/nl504314c.

-
- [231] G. Schönhoff, M. Rösner, R. E. Groenewald, S. Haas, and T. O. Wehling. “Interplay of screening and superconductivity in low-dimensional materials”. In: *Physical Review B* 94.13 (2016), p. 134504. DOI: 10.1103/PhysRevB.94.134504.
- [232] X. Xi et al. “Strongly enhanced charge-density-wave order in monolayer NbSe₂”. en. In: *Nature Nanotechnology* 10.9 (2015), pp. 765–769. DOI: 10.1038/nnano.2015.143.
- [233] J. A. Wilson, F. J. Di Salvo, and S. Mahajan. “Charge-Density Waves in Metallic, Layered, Transition-Metal Dichalcogenides”. In: *Physical Review Letters* 32.16 (1974), pp. 882–885. DOI: 10.1103/PhysRevLett.32.882.
- [234] A. H. Castro Neto. “Charge Density Wave, Superconductivity, and Anomalous Metallic Behavior in 2D Transition Metal Dichalcogenides”. In: *Physical Review Letters* 86.19 (2001), pp. 4382–4385. DOI: 10.1103/PhysRevLett.86.4382.
- [235] K. Rossnagel. “On the origin of charge-density waves in select layered transition-metal dichalcogenides”. en. In: *Journal of Physics: Condensed Matter* 23.21 (2011), p. 213001. DOI: 10.1088/0953-8984/23/21/213001.
- [236] X.-L. Wei, Z.-K. Tang, G.-C. Guo, S. Ma, and L.-M. Liu. “Electronic and magnetism properties of two-dimensional stacked nickel hydroxides and nitrides”. In: *Scientific Reports* 5 (2015), p. 11656. DOI: 10.1038/srep11656.
- [237] S. Tongay, S. S. Varnoosfaderani, B. R. Appleton, J. Wu, and A. F. Hebard. “Magnetic properties of MoS₂: Existence of ferromagnetism”. In: *Applied Physics Letters* 101.12 (2012), p. 123105. DOI: 10.1063/1.4753797.
- [238] N. M. R. Peres, F. Guinea, and A. H. Castro Neto. “Coulomb interactions and ferromagnetism in pure and doped graphene”. In: *Physical Review B* 72.17 (2005), p. 174406. DOI: 10.1103/PhysRevB.72.174406.
- [239] M. A. McGuire, H. Dixit, V. R. Cooper, and B. C. Sales. “Coupling of Crystal Structure and Magnetism in the Layered, Ferromagnetic Insulator CrI₃”. In: *Chemistry of Materials* 27.2 (2015), pp. 612–620. DOI: 10.1021/cm504242t.
- [240] F. Ceballos, Q. Cui, M. Z. Bellus, and H. Zhao. “Exciton formation in monolayer transition metal dichalcogenides”. In: *Nanoscale* 8.22 (2016), pp. 11681–11688. DOI: 10.1039/C6NR02516A.

- [241] E. Poem et al. “Accessing the dark exciton with light”. en. In: *Nature Physics* 6.12 (2010), pp. 993–997. DOI: 10.1038/nphys1812.
- [242] T. K. Mullenbach, I. J. Curtin, T. Zhang, and R. J. Holmes. “Probing dark exciton diffusion using photovoltage”. en. In: *Nature Communications* 8 (2017), p. 14215. DOI: 10.1038/ncomms14215.
- [243] Z. Ye et al. “Probing excitonic dark states in single-layer tungsten disulphide”. en. In: *Nature* 513.7517 (2014), pp. 214–218. DOI: 10.1038/nature13734.
- [244] Q. Niu, M. C. Chang, and C. K. Shih. “Double-tip scanning tunneling microscope for surface analysis”. In: *Physical Review B* 51.8 (1995), pp. 5502–5505. DOI: 10.1103/PhysRevB.51.5502.
- [245] H. Okamoto and D. Chen. “An ultrahigh vacuum dual-tip scanning tunneling microscope operating at 4.2 K”. In: *Review of Scientific Instruments* 72.12 (2001), pp. 4398–4403. DOI: 10.1063/1.1416113.
- [246] H. Grube, B. C. Harrison, J. Jia, and J. J. Boland. “Stability, resolution, and tip–tip imaging by a dual-probe scanning tunneling microscope”. In: *Review of Scientific Instruments* 72.12 (2001), pp. 4388–4392. DOI: 10.1063/1.1416120.
- [247] A. Catellani, M. Posternak, A. Baldereschi, and A. J. Freeman. “Bulk and surface electronic structure of hexagonal boron nitride”. In: *Phys. Rev. B* 36.11 (1987), pp. 6105–6111. DOI: 10.1103/PhysRevB.36.6105.
- [248] T. Galvani et al. “Excitons in boron nitride single layer”. In: *Phys. Rev. B* 94.12 (2016), p. 125303. DOI: 10.1103/PhysRevB.94.125303.
- [249] G. Fugallo et al. “Exciton energy-momentum map of hexagonal boron nitride”. In: *Phys. Rev. B* 92.16 (2015), p. 165122. DOI: 10.1103/PhysRevB.92.165122.
- [250] G. Giovannetti, P. A. Khomyakov, G. Brocks, P. J. Kelly, and J. van den Brink. “Substrate-induced band gap in graphene on hexagonal boron nitride: Ab initio density functional calculations”. In: *Phys. Rev. B* 76.7 (2007), p. 073103. DOI: 10.1103/PhysRevB.76.073103.
- [251] B. Sachs, T. O. Wehling, M. I. Katsnelson, and A. I. Lichtenstein. “Adhesion and electronic structure of graphene on hexagonal boron nitride substrates”. In: *Phys. Rev. B* 84.19 (2011), p. 195414. DOI: 10.1103/PhysRevB.84.195414.

-
- [252] M. Bokdam, T. Amlaki, G. Brocks, and P. J. Kelly. “Band gaps in incommensurable graphene on hexagonal boron nitride”. In: *Phys. Rev. B* 89.20 (2014), p. 201404. DOI: 10.1103/PhysRevB.89.201404.
- [253] J. Sławińska, I. Zasada, and Z. Klusek. “Energy gap tuning in graphene on hexagonal boron nitride bilayer system”. In: *Physical Review B* 81.15 (2010). DOI: 10.1103/physrevb.81.155433.
- [254] N. Kharche and S. K. Nayak. “Quasiparticle Band Gap Engineering of Graphene and Graphone on Hexagonal Boron Nitride Substrate”. In: *Nano Letters* 11.12 (2011), pp. 5274–5278. DOI: 10.1021/nl202725w.
- [255] D. Xiao, G.-B. Liu, W. Feng, X. Xu, and W. Yao. “Coupled Spin and Valley Physics in Monolayers of MoS₂ and Other Group-VI Dichalcogenides”. In: *Physical Review Letters* 108.19 (2012), p. 196802. DOI: 10.1103/PhysRevLett.108.196802.
- [256] I. C. Gerber and X. Marie. “Dependence of band structure and exciton properties of encapsulated WSe₂ monolayers on the hBN-layer thickness”. In: *Physical Review B* 98.24 (2018). DOI: 10.1103/physrevb.98.245126.
- [257] L. Li et al. “Direct observation of the layer-dependent electronic structure in phosphorene”. In: *Nature Nanotechnology* 12.1 (2016), pp. 21–25. DOI: 10.1038/nnano.2016.171.
- [258] A. Emelyanenko and L. Boinovich. “On the effect of discrete charges adsorbed at the interface on nonionic liquid film stability: charges in the film”. In: *Journal of Physics: Condensed Matter* 20.49 (2008), p. 494227. DOI: 10.1088/0953-8984/20/49/494227.
- [259] J. Robertson. “High dielectric constant oxides”. In: *The European Physical Journal Applied Physics* 28.3 (2004), pp. 265–291. DOI: 10.1051/epjap:2004206.
- [260] S. Sze and K. K. Ng. *Physics of Semiconductor Devices*. John Wiley and Sons, Inc., 2006. DOI: 10.1002/0470068329.
- [261] M. F. Lin, C. S. Huang, and D. S. Chuu. “Plasmons in graphite and stage-1 graphite intercalation compounds”. In: *Phys. Rev. B* 55.20 (1997), pp. 13961–13971. DOI: 10.1103/PhysRevB.55.13961.

- [262] E. H. Hwang, R. E. Throckmorton, and S. D. Sarma. “Plasmon-pole approximation for many-body effects in extrinsic graphene”. In: *Physical Review B* 98.19 (2018). DOI: 10.1103/physrevb.98.195140.
- [263] G. E. Engel and B. Farid. “Generalized plasmon-pole model and plasmon band structures of crystals”. In: *Physical Review B* 47.23 (1993), pp. 15931–15934. DOI: 10.1103/physrevb.47.15931.
- [264] M. Dendzik et al. “Substrate-induced semiconductor-to-metal transition in monolayer WS₂”. In: *Phys. Rev. B* 96.23 (2017), p. 235440. DOI: 10.1103/PhysRevB.96.235440.
- [265] P. Klement, C. Steinke, S. Chatterjee, T. O. Wehling, and M. Eickhoff. “Effects of the Fermi level energy on the adsorption of O₂ to monolayer MoS₂”. In: *2D Materials* 5.4 (2018), p. 045025. DOI: 10.1088/2053-1583/aadc24.
- [266] F. K. Perkins et al. “Chemical Vapor Sensing with Monolayer MoS₂”. In: *Nano Letters* 13.2 (2013), pp. 668–673. DOI: 10.1021/nl3043079.
- [267] D. J. Late et al. “Sensing Behavior of Atomically Thin-Layered MoS₂ Transistors”. In: *ACS Nano* 7.6 (2013), pp. 4879–4891. DOI: 10.1021/nl400026u.
- [268] R. Samnakay, C. Jiang, S. L. Rumyantsev, M. S. Shur, and A. A. Balandin. “Selective chemical vapor sensing with few-layer MoS₂ thin-film transistors: Comparison with graphene devices”. In: *Applied Physics Letters* 106.2 (2015), p. 023115. DOI: 10.1063/1.4905694.
- [269] J. S. Ross et al. “Electrically tunable excitonic light-emitting diodes based on monolayer WSe₂ p–n junctions”. In: *Nature Nanotechnology* 9.4 (2014), pp. 268–272. DOI: 10.1038/nnano.2014.26.
- [270] H. Nan et al. “Strong Photoluminescence Enhancement of MoS₂ through Defect Engineering and Oxygen Bonding”. In: *ACS Nano* 8.6 (2014), pp. 5738–5745. DOI: 10.1021/nl500532f.
- [271] H. Qiu et al. “Electrical characterization of back-gated bi-layer MoS₂ field-effect transistors and the effect of ambient on their performances”. In: *Applied Physics Letters* 100.12 (2012), p. 123104. DOI: 10.1063/1.3696045.
- [272] S. Tongay et al. “Broad-Range Modulation of Light Emission in Two-Dimensional Semiconductors by Molecular Physisorption Gating”. In: *Nano Letters* 13.6 (2013), pp. 2831–2836. DOI: 10.1021/nl4011172.

- [273] B. Liu et al. “High-Performance Chemical Sensing Using Schottky-Contacted Chemical Vapor Deposition Grown Monolayer MoS₂ Transistors”. In: *ACS Nano* 8.5 (2014), pp. 5304–5314. DOI: 10.1021/nm5015215.
- [274] Q. He et al. “Fabrication of Flexible MoS₂Thin-Film Transistor Arrays for Practical Gas-Sensing Applications”. In: *Small* 8.19 (2012), pp. 2994–2999. DOI: 10.1002/smll.201201224.
- [275] M. Donarelli et al. “Response to NO₂ and other gases of resistive chemically exfoliated MoS₂-based gas sensors”. In: *Sensors and Actuators B: Chemical* 207 (2015), pp. 602–613. DOI: 10.1016/j.snb.2014.10.099.
- [276] K. F. Mak et al. “Tightly bound trions in monolayer MoS₂”. In: *Nature Materials* 12.3 (2012), pp. 207–211. DOI: 10.1038/nmat3505.
- [277] A. Newaz et al. “Electrical control of optical properties of monolayer MoS₂”. In: *Solid State Communications* 155 (2013), pp. 49–52. DOI: 10.1016/j.ssc.2012.11.010.
- [278] H. J. Monkhorst and J. D. Pack. “Special points for Brillouin-zone integrations”. In: *Physical Review B* 13.12 (1976), pp. 5188–5192. DOI: 10.1103/physrevb.13.5188.
- [279] Q. Yue, Z. Shao, S. Chang, and J. Li. “Adsorption of gas molecules on monolayer MoS₂ and effect of applied electric field”. In: *Nanoscale Research Letters* 8.1 (2013), p. 425. DOI: 10.1186/1556-276x-8-425.
- [280] H. Li et al. “Fabrication of Single- and Multilayer MoS₂ Film-Based Field-Effect Transistors for Sensing NO at Room Temperature”. In: *Small* 8.1 (2011), pp. 63–67. DOI: 10.1002/smll.201101016.
- [281] F. Schedin et al. “Detection of individual gas molecules adsorbed on graphene”. In: *Nature Materials* 6.9 (2007), pp. 652–655. DOI: 10.1038/nmat1967.
- [282] S.-W. Fan, A. K. Srivastava, and V. P. Dravid. “UV-activated room-temperature gas sensing mechanism of polycrystalline ZnO”. In: *Applied Physics Letters* 95.14 (2009), p. 142106. DOI: 10.1063/1.3243458.
- [283] K. Ohno. “Some remarks on the Pariser-Parr-Pople method”. en. In: *Theoret. Chim. Acta* 2.3 (1964), pp. 219–227. DOI: 10.1007/BF00528281.
- [284] E. N. Economou. *Green’s functions in quantum physics*. Springer series in solid-state sciences 7. Berlin: Springer, 1979.

- [285] S. Schulz, S. Schumacher, and G. Czycholl. “Tight-binding model for semiconductor quantum dots with a wurtzite crystal structure: From one-particle properties to Coulomb correlations and optical spectra”. In: *Physical Review B* 73.24 (2006), p. 245327. DOI: 10.1103/PhysRevB.73.245327.
- [286] K. Leung and K. B. Whaley. “Electron-hole interactions in silicon nanocrystals”. In: *Physical Review B* 56.12 (1997), pp. 7455–7468. DOI: 10.1103/PhysRevB.56.7455.
- [287] S. Latini, K. T. Winther, T. Olsen, and K. S. Thygesen. “Interlayer Excitons and Band Alignment in MoS₂/hBN/WSe₂ van der Waals Heterostructures”. In: *Nano Letters* 17.2 (2017), pp. 938–945. DOI: 10.1021/acs.nanolett.6b04275.
- [288] R. Coehoorn et al. “Electronic structure of MoSe₂, MoS₂, and WSe₂. I. Band-structure calculations and photoelectron spectroscopy”. In: *Physical Review B* 35.12 (1987), pp. 6195–6202. DOI: 10.1103/physrevb.35.6195.
- [289] W. Schutte, J. D. Boer, and F. Jellinek. “Crystal structures of tungsten disulfide and diselenide”. In: *Journal of Solid State Chemistry* 70.2 (1987), pp. 207–209. DOI: 10.1016/0022-4596(87)90057-0.
- [290] L. Wang, Y. Pu, A. K. Soh, Y. Shi, and S. Liu. “Layers dependent dielectric properties of two dimensional hexagonal boron nitridenanosheets”. In: *AIP Advances* 6.12 (2016), p. 125126. DOI: 10.1063/1.4973566.
- [291] A. Laturia, M. L. V. de Put, and W. G. Vandenberghe. “Dielectric properties of hexagonal boron nitride and transition metal dichalcogenides: from monolayer to bulk”. In: *npj 2D Materials and Applications* 2.1 (2018). DOI: 10.1038/s41699-018-0050-x.
- [292] P. V. C. Medeiros, S. Stafström, and J. Björk. “Effects of extrinsic and intrinsic perturbations on the electronic structure of graphene: Retaining an effective primitive cell band structure by band unfolding”. In: *Physical Review B* 89.4 (2014). DOI: 10.1103/physrevb.89.041407.
- [293] P. V. C. Medeiros, S. S. Tsirkin, S. Stafström, and J. Björk. “Unfolding spinor wave functions and expectation values of general operators: Introducing the unfolding-density operator”. In: *Physical Review B* 91.4 (2015). DOI: 10.1103/physrevb.91.041116.

List of publications

Published in peer-reviewed journals

- [1] P. Klement, C. Steinke, S. Chatterjee, T. O. Wehling, and M. Eickhoff. “Effects of the Fermi level energy on the adsorption of O₂ to monolayer MoS₂”. In: *2D Materials* 5.4 (2018), p. 045025. DOI: 10.1088/2053-1583/aadc24.
- [2] C. Steinke, D. Mourad, M. Rösner, M. Lorke, C. Gies, F. Jahnke, G. Czycholl, and T. O. Wehling. “Noninvasive control of excitons in two-dimensional materials”. In: *Phys. Rev. B* 96.4 (2017), p. 045431. DOI: 10.1103/PhysRevB.96.045431.
- [3] N. Néel, C. Steinke, T. O. Wehling, and J. Kröger. “Inelastic electron tunneling into graphene nanostructures on a metal surface”. In: *Phys. Rev. B* 95.16 (2017), p. 161410. DOI: 10.1103/PhysRevB.95.161410.
- [4] M. Rösner, C. Steinke, M. Lorke, C. Gies, F. Jahnke, and T. O. Wehling. “Two-Dimensional Heterojunctions from Nonlocal Manipulations of the Interactions”. In: *Nano Letters* 16.4 (2016), pp. 2322–2327. DOI: 10.1021/acs.nanolett.5b05009.

In preparation

- [5] C. Steinke, M. Rösner, and T. O. Wehling. “Material realistic description of Coulomb engineered two-dimensional materials”. in preparation. 2019.
- [6] L. Waldecker, A. Raja, M. Rösner, C. Steinke, R. J. Koch, A. Bostwick, C. Jozwiack, T. Taniguchi, K. Watanabe, E. Rotenberg, T. O. Wehling, and T. F. Heinz. “The effect of dielectric screening on the bandstructure of two-dimensional semiconductors”. in preparation. 2019.

Conference contributions

1. Poster: *Material Realistic Description of Coulomb Engineering and Defect Potentials in Two-dimensional Materials*
C. Steinke, N. Witt, M. Rösner, and T. O. Wehling
Cecam Workshop: "Correlated electron physics beyond the Hubbard model", Bremen (2019)
2. Poster: *Material Realistic Description of Coulomb Engineering and Defect Potentials in Two-dimensional Materials*
C. Steinke, N. Witt, M. Rösner, and T. O. Wehling
Cecam Workshop: "Reliable and quantitative prediction of defect properties in Ga-based semiconductors", Bremen (2018)
3. Talk (together with E. Kapetanovic): *P3: Many-body approaches to realistic quantum impurity models and Coulomb engineering*
C. Steinke, E. Kapetanovic, N. Witt, B. Shao, G. Czycholl, T. O. Wehling
Midterm Workshop Research Training Group "Quantum Mechanical Materials Modelling", Etelsen (2018)
4. Poster: *Material Realistic Description of Coulomb Engineered 2D Materials*
C. Steinke, M. Rösner, D.A. Ryndyk and T. O. Wehling
Flatlands beyond graphene, Leipzig (2018)
5. Talk: *Material Realistic Description of Coulomb Engineered Two-dimensional Materials*
C. Steinke, M. Rösner, D. A. Ryndyk, T. O. Wehling
DPG Frühjahrstagung, Berlin (2018)
6. Poster: *Coulomb engineered two-dimensional materials: non-invasive control of band gaps and excitons*
C. Steinke, D. Mourad, M. Rösner, M. Lorke, C. Gies, F. Jahnke, and T. O. Wehling
Graphene Flagship WP1 meeting, Teddington/UK (2018)
7. Talk: *Coulomb engineered two-dimensional materials: non-invasive control of band gaps and excitons*
C. Steinke, D. Mourad, M. Rösner, M. Lorke, C. Gies, G. Czycholl, F. Jahnke, T. O. Wehling
USC Seminar, Los Angeles/USA (2018)
8. Poster: *Coulomb engineered two-dimensional materials: non-invasive control of band gaps and excitons*

- C. Steinke, D. Mourad, M. Rösner, M. Lorke, C. Gies, F. Jahnke, and T. O. Wehling
Cecam Workshop: "Charge carrier dynamics in nanostructures: optoelectronic and photo-stimulated processes", Bremen (2017)
9. Talk: *Coulomb engineered two-dimensional materials: non-invasive control of band gaps and excitons*
C. Steinke, D. Mourad, M. Rösner, M. Lorke, C. Gies, G. Czycholl, F. Jahnke, T. O. Wehling
Flatlands beyond Graphene, Lausanne/CH (2017)
10. Talk: *2d Heterojunctions and its two-particle properties from non-local manipulation of the Interactions*
C. Steinke, D. Mourad, M. Rösner, M. Lorke, C. Gies, G. Czycholl, F. Jahnke, T. O. Wehling
DPG Frühjahrstagung, Dresden (2017)
11. Poster: *Real-space view of electron correlations in two-dimensional materials*
C. Steinke, D. Mourad, M. Rösner, M. Lorke, C. Gies, F. Jahnke, and T. O. Wehling
Cecam Workshop: "Computational insight into photo-induced processes at interfaces", Bremen (2016)
12. Talk: *2d Heterojunctions from Non-local Manipulations of the Interactions*
C. Steinke, M. Rösner, M. Lorke, C. Gies, F. Jahnke, T. O. Wehling
DPG Frühjahrstagung, Regensburg (2016)
13. Poster: *Two-Dimensional Heterojunctions from Nonlocal Manipulations of the Interactions*
C. Steinke, M. Rösner, M. Lorke, C. Gies, F. Jahnke, and T. O. Wehling
Cecam Workshop: "Tailor-made 2D-materials and functional devices", Bremen (2016)

Acknowledgements

I would like to use the last page to thank the numerous people who made this work possible with their endless patience and motivation.

First of all I want to thank Tim Wehling for giving me the opportunity to work on this thesis. Without his help, motivation and time for many discussions this would not have been possible. I am very grateful to have been part of his group not only because of the great working atmosphere but also for the fun we all had together outside from university. In this context I am also thankful to the whole working group for the nice company during the last years. Additionally I would like to thank Gerd Czycholl for acting as a second referee and always giving great lectures which, in the end, brought me to theoretical physics.

Furthermore I would like to thank Malte Rösner, who, starting during my Bachelor's thesis, always answered any questions I had. I am really grateful for the ongoing collaborations and help even when he moved to the United States (and back). Without him, some problems I encountered during the last years would have brought me to despair. I am grateful that because of him (and Stephan Haas) I had the opportunity to visit Los Angeles.

I would like to thank Daniel Mourad for helping me tackle the tight-binding description of excitons and additionally emphasizing the importance of programming skills for my future career. Thanks for all the great discussions - about physics and not so much about physics.

Many thanks also to Andreas Beuthner and Klaus Bove for helping with all hardware and software related issues at the ITP. Additional thanks to Sarah Farley for all the administrative work. Also, I would like to thank Niklas Witt for the many nice conversations and proof reading some parts of this thesis. Thanks to all the students of the Research Training Group for the many fruitful discussions.

Many thanks to Philip Mirbach, which whom I not only shared my office for a year but who is also a really good friend starting from our first semester. Additional thanks to all of my friends, especially Saskia, Tanja, Christian, Jakob and and Patricia who always supported me during the last years. Special thanks to Sanja for not only proof reading part of this thesis without knowing anything about physics, but also for always having a sympathetic ear for me and keeping me sane.

And lastly, but most importantly, I want to thank my family and in particular Patrick. We have been through a rough time in the last years. Thank you for being there for me even though you have been struggling with so much other stuff. Without you, not a single page would have been written. Thank you for taking care of me all the time.

Furthermore, financial support from the European Graphene Flagship, the Research Training Group "Quantum Mechanical Materials Modeling" GRK 2247 and computational resources from the HLRN is greatly acknowledged.